Exploring two-dimensional physics with Bose gases in box potentials: phase ordering and dynamical symmetry

Raphaël Saint-Jalm

To cite this version:

Raphaël Saint-Jalm. Exploring two-dimensional physics with Bose gases in box potentials: phase ordering and dynamical symmetry. Quantum Physics [quant-ph]. Université Paris Sciences et Lettres, 2019. English. NNT : . tel-02464649

HAL Id: tel-02464649
https://theses.hal.science/tel-02464649

Submitted on 3 Feb 2020

PSL
UNIVERSITÉ PARIS

THÈSE DE DOCTORAT
DE L'UNIVERSITÉ PSL

Préparée à l'École normale supérieure

Exploring two-dimensional physics with Bose gases in box potentials: phase ordering and dynamical symmetry

Soutenue par
Raphaël Saint-Jalm
Le 3 octobre 2019

École doctorale n°564
Physique en Île-de-France

Spécialité
Physique Quantique

Composition du jury :

Vincent Josse Institut d'Optique	*Rapporteur*
Wilhelm Zwerger Technische Universität München	*Rapporteur*
Anna Minguzzi Université Grenoble Alpes	*Présidente du jury*
Robert Smith University of Oxford	*Examinateur*
Jean Dalibard Collège de France	*Directeur de thèse*
Jérôme Beugnon Sorbonne Université	*Invité*

ENS | PSL

Laboratoire Kastler Brossel
Physique quantique et applications

COLLÈGE DE FRANCE
1530

ABSTRACT

The thermodynamic properties and the dynamical behaviour of two-dimensional systems differ notably from the ones in three dimensions. This work presents experiments performed with ultracold clouds of uniform weakly interacting bosons confined in two dimensions of space. These experiments explore some specific features of the thermodynamics and the out-of equilibrium dynamics of two-dimensional systems.

Working with ultracold atoms provides the experimentalist with a rich toolbox: geometry, temperature and internal state of the system are well controlled, and various methods to investigate their properties are available. In particular we work with uniform Boses gases in highly tunable geometries. I describe the set-up and our experimental toolbox in a first part.

In a second part I present experiments to investigate the Berezinskii-Kosterlitz-Thouless transition of a two-dimensional Bose gas. It is a topological phase transition for which the system displays a quasi-long range order below the critical temperature. We have developed two experimental schemes to probe this quasi-long range order.

In a third and final part I explain the symmetries that underlie the dynamics of a cloud near zero temperature in a harmonic potential. These symmetries are the hidden symmetries of the two-dimensional non-linear Schrödinger equation, which describes many other physical systems. We could probe these symmetries experimentally, and we also observed initial shapes whose evolution is periodic in a harmonic potential in the presence of a non-linearity. They could constitute new breathers of this non-linear equation.

RÉSUMÉ

Les propriétés thermodynamiques ainsi que l'évolution temporelle des systèmes bidimensionnels sont nettement différentes de celles de systèmes à trois dimensions. Ce travail de thèse présente des expériences réalisées avec des gaz ultrafroids uniformes de bosons en interaction faible, et confinés à deux dimensions d'espace. Ces expériences permettent de mettre en lumière certains traits caractéristiques de l'équilibre thermique et de la dynamique hors équilibre des systèmes à deux dimensions.

Un expérimentateur travaillant avec des atomes froids possède une boîte à outils très fournie: la géométrie, la température, l'état interne des atomes sont très bien contrôlés, et de nombreuses méthodes permettant d'étudier leurs propriétés sont disponibles. En particulier, nous travaillons avec des gaz de densité uniforme dont la géométrie peut être choisie à volonté. Je décris l'installation expérimentale et les outils à notre disposition dans une première partie.

Dans une deuxième partie, je présente une série d'expériences concernant la transition de phase Berezinskii-Kosterlitz-Thouless d'un gaz de Bose bidimensionnel. Il s'agit d'une transition de phase topologique pour laquelle le système présente un ordre à quasi-longue portée en dessous de la température critique. Nous avons développé deux méthodes expérimentales pour sonder cet ordre à quasi-longue portée.

Dans une troisième et dernière partie, je détaille les symétries qui sous-tendent la dynamique d'un gaz proche d'une température nulle dans un piège harmonique. Ces symétries sont les symétries cachées de l'équation de Schrödinger non-linéaire, qui décrit plusieurs autres systèmes physiques. Nous avons testé ces symétries expérimentalement, et nous avons également observé des formes dont l'évolution est périodique dans un potentiel harmonique en présence de non-linéarités. Ces formes géométriques pourraient constituer un nouveau type de solutions périodiques de cette équation non-linéaire.

ACKNOWLEDGMENTS

Le travail de thèse que clôt le présent manuscrit résulte de l'effort combiné de nombreuses personnes avec lesquelles j'ai eu le plaisir de travailler au cours de mes quatre années de thèse. Tout le long de cette période, j'ai également bénéficié de l'entourage et du soutien indéfectible de plusieurs cercles amicaux et familiaux. Les paragraphes qui suivent sont consacrés à toutes ces personnes, et si la part que ces quelques lignes représentent dans un manuscrit est infime, celle qu'ont pris toutes ces individualités dans ma vie de doctorant est immense.

Je souhaite remercier mes deux directeurs de thèse, Jean Dalibard et Jérôme Beugnon de m'avoir accueilli tout d'abord pour mon stage de Master, puis pour ma thèse. Je les remercie de m'avoir confié dès le début la tâche de construire l'accordéon optique, ce qui m'a permis de me convaincre que j'avais toute ma place dans le laboratoire. Leur présence et leur soutien constant durant ces années ont été très précieux. Les discussions avec Jean ont toujours été très profitables, et l'apport qu'il a eu sur les projets présentés dans cette thèse sont incalculables. Jérôme a été un chef d'orchestre impeccable et je te remercie pour sa bonne gestion de l'expérience au quotidien, mais aussi pour ton accueil dans ton bureau pour la rédaction de ce manuscrit lorsque le bureau Rubidium a atteint une surpopulation critique.

Ce duo de directeurs de thèse est complété par Sylvain Nascimbène dont l'implication dans l'expérience est souvent cruciale lorqu'il s'agit de s'attaquer à des questions théoriques ouvertes. Je te remercie pour toutes les discussions fructueuses que j'ai pu avoir avec toi.

Je remercie enfin Antoine Heidmann, directeur du laboratoire, de m'avoir accueilli comme doctorant dans l'équipe Condensats de Bose-Einstein. Merci aussi à Jakob Reichel pour son suivi tout le long de ma thèse.

La majeure partie du temps consacré à cette thèse s'est faite aux côtés de plusieurs postdocs, doctorants, stagiaires avec qui j'ai partagé tous les moments de labeur, de joie, de peine, de détente inhérents à tout travail expérimental. C'est ainsi que je remercie chaleureusement les six thésards avec qui j'ai eu le grand plaisir de travailler: Lauriane, Laura, Jean-Loup, Édouard, Brice et Chloé. Le quotidien au labo a été très agréable à vos côtés, et je dois beaucoup à votre patience et votre enthousiasme. Je remercie également les quatre postdocs qui m'ont beaucoup appris: Tom, Monika, Patricia et Yiquan. Enfin, je souhaite remercier les stagiaires de plus ou moins longue durée qui ont travaillé avec nous, et avec qui j'ai eu beaucoup de plaisir à interagir : Victor, Charlie, Lorenzo, Fabrizio, Marius, Andres et Alexandre.

Je veux ensuite remercier tout le deuxième étage du bâtiment E du Collège de France, à commencer par les chercheurs permanents Fabrice, Alexei et Raphaël, ainsi que les équipes Sodium, Ytterbium, Dysprosium, et Jeunes Chercheurs. Sous ces dénominations se cachent quelques dizaines de doctorants, postdocs, stagiaires avec qui j'ai eu le privilège de partager quelques mois ou années de ma vie. Les liens amicaux qui en ont résulté ont été très importants pour moi. Merci aussi à touts les doctorants et postdocs du LKB avec qui j'ai pu discuter.

Je remercie Carmen pour son soutien administratif sans faille, ainsi que tout le personnel du Collège de France, du Laboratoire Kastler Brossel, de l'ENS et de l'EDPIF qui ont permi à cette thèse de suivre son cours. Merci également aux ateliers mécaniques et électroniques du Collège et du département de physique de l'ENS pour leur aide.

J'ai effectué des missions d'enseignement durant cette thèse et je remercie toutes les personnes qui ont contribué à leur bon déroulement, en particulier Pierre-François Cohadon, Nabil Garroum et François Pétrélis.

J'ai bénéficié durant ces années de thèse d'un entourage familial et amical qui m'a toujours soutenu. Je remercie du fond du cœur toute ma famille proche: mon père, Valérie, toutes mes sœurs, mes grands-parents, Nathalie, Ivan et les cousins. Merci également à toute la troupe du théâtre pour les moments de joie à Paris, Sarrebrück ou Konstanz, merci à toute l'équipe du Ciné-club de l'ENS depuis 2012 pour les mardis et dimanches dans les salles obscures, merci à Aurélien et à Katharina pour leur soutien indispensable.

Je souhaite enfin remercier les deux rapporteurs, Vincent Josse et Wilhelm Zwerger pour leur lecture attentive de ce manuscrit, ainsi que les examinateurs Anna Minguzzi et Rob Smith pour avoir accepté de faire partie de mon jury de thèse et pour leurs questions lors de la soutenance.

CONTENTS

III DYNAMICAL SYMMETRY OF THE 2D BOSE GAS

APPENDICES

ACRONYMS

2D	bidimensional
2D MOT	two-dimensional magneto-optical trap
AOM	acousto-optic modulator
BKT	Berezinskii–Kosterlitz–Thouless
DMD	digital micro-mirror device
EOM	electro-optic modulator
GPE	Gross-Pitaevskii equation
HWHM	half width at half-maximum
KPZ	Kardar-Parisi-Zhang
MOT	magneto-optical trap
PSD	phase-space density
RMS	root mean square

1

INTRODUCTION

In modern physics, symmetries play an important role in the understanding of phenomena. The most spectacular result was found one hundred years ago by Emmy Noether [1], who linked the existence of continuous symmetries to conserved quantities of a system. Symmetries are also at the heart of gauge theories that are used to describe the structure of many physical models, ranging from classical electrodynamics [2] to the Standard Model of particle physics [3].

The symmetries of a system form a mathematical group and, in the case where this group is continuous, one can describe it thanks to Lie's group theory [4]. One important object is the Lie algebra that locally describes the structure of this group and from which many properties of the system can be inferred [5]. In this approach, not only geometrical symmetries are considered, but also symmetries involving the time coordinate and/or the time derivative of the parameters of the system. Such symmetries are thus called 'dynamical symmetries', and they can give a profound insight in the understanding of a system. The most celebrated examples are the Kepler problem [6] and its quantum counterpart, the model of the hydrogen atom [7, 8], where the existence of a dynamical symmetry allows one to demonstrate respectively that the orbit of planets are closed, and that the energy levels of hydrogen are degenerate with respect to the azimuthal quantum number [9].

The symmetry group of a model depends on the dimensionality of its underlying space. While some theories aiming at the description of particle physics rely on a space with more than three dimensions [10, 11], rich symmetries can be found in low-dimensional systems [12]. An interesting example is set by the conformal group of the Euclidean space, which is the group of maps that preserves the angles of this space. In dimensions higher or equal to three, this conformal group is constrained to be a composition of translations, rotations, dilatations and inversions. In two dimensions, the conformal group is much richer and it contains all the holomorphic functions [13]. This conformal group has many applications in physics [14]. Another feature that low-dimensional systems are more prone to exhibiting is the property of integrability. This happens when a system has as many invariants as degrees of freedom [15], and such integrable systems have been the focus of many studies [16].

The dimensionality of a system also affects its properties. Many systems in condensed matter are constrained in one or two dimensions and thus have very interesting features, related for example to the conductivity of heat or of electrons [17, 18]. An important family of problems relies on the particular topology of these systems, such as gases of electrons in two dimensions where the quantum Hall effect [19] and the fractional quantum Hall effect [20–22] have been observed, or the band properties of graphene [23, 24].

Among these two-dimensional systems, a handful of them undergo a topological phase transition that was first predicted by Berezinskii [25] and by Kosterlitz and Thouless [26]. This particular phase transition has triggered many theoretical and experimental studies [27]. It does not stem from the breaking of any symmetry, but it comes from the existence of topological objects called vortices that are paired on one side of the transition and that are unbound on the other side. The transition from one phase to the other is of infinite order, which means that the order parameter and all its derivatives are continuous.

Several experimental systems display this BKT transition: thin films of superfluid ^{4}He [28], two-dimensional arrays of Josephson junctions [29–32], thin superconducting films [33–35], crystals growing on a surface [36], arrays of Bose-Einstein condensates [37], and the weakly-interacting two-dimensional Bose gas [38]. For all these systems, the BKT transition describes how a spatial phase ordering emerges when their temperature is decreased.

An interesting quantity to illustrate this phase ordering is the first-order correlation function $g_1(\boldsymbol{r})$. For systems with long-range order, this function converges to a non-zero value when $\boldsymbol{r} \to \infty$. Above the BKT transition, this correlation function decreases exponentially fast to zero, which indicates a short-range order. Below the transition, $g_1(\boldsymbol{r})$ decreases to zero as well, but as a power-law, which is much slower than an exponential decrease. Such a behaviour is called a quasi-long range order.

The BKT transition has also the particularity of having a superfluid fraction that is discontinuous at the critical point. I describe this phenomenon with the vocabulary that is suited for fluids, but it can be translated for any other system described by this physics. At zero temperature, the whole system is superfluid and the flow of such a fluid around an obstacle can be frictionless if the velocity of the flow is small enough [39]. When the temperature is increased, a fraction of the gas becomes normal and can dissipate energy. The superfluid fraction decreases until the temperature reaches the critical temperature of the BKT transition. At this critical point, the superfluid fraction exhibits a sudden jump to zero when the system is brought right above the transition. When considered in terms of superfluid phase-space density, this jump is universal, which means that it does not depend on the specific model that is considered.

The system of interest in this thesis is the two-dimensional weakly-interacting Bose gas, and it provides a powerful platform to investigate the properties of two-dimensional systems. In particular we will explore the symmetries of this system and the phase-ordering that is described by the BKT transition.

Working with ultracold atoms comes with a rich experimental toolbox that has been developed over the years in the cold-atoms community.

Laser and evaporative cooling [40] allow an ensemble of atoms to reach quantum degeneracy where the thermal de Broglie wavelength becomes larger than the interparticle distance [41]. Bosonic atoms then form a Bose-Einstein condensate [42–45] and fermionic atoms form a degenerate Fermi gas [46, 47]. In this regime, three-dimensional clouds of bosons have a long-range phase coherence [48]. Trapping methods such as magnetic traps [49] and optical traps [50] allow one to shape the potential energy landscape of the atomic cloud. Extremely rich situations can be created, such as harmonic traps, optical lattices with various geometries [51–54], low-dimensional geometries [55–57], disordered potentials [58], flat-bottom box potentials [59]. The interactions between particles can also be tailored at will. Feshbach resonances allow one to vary the s-scattering length of the atoms [60], magnetic atoms can display strong anisotropic dipolar interactions [61], and the coupling of a cloud with a light field in a cavity can lead to the engineering of infinite-range interactions [62].

Ultracold atomic gases thus constitute a very versatile platform and they open many perspectives in the study of many-body physics [63].

Before introducing the content of this thesis and diving into the core of this work, I first mention briefly what is *not* in this manuscript. The building of our experimental set-up has started in 2014, and I arrived in the group in January 2015. At the beginning of my Ph.D. thesis, I was involved in several projects that are not discussed in this manuscript. I briefly summarize here these projects and I refer the reader to the list of publications at the end of this introduction and to the Ph.D. theses of Laura Corman [64] and Jean-Loup Ville [65] for more details.

We first built the experimental set-up to efficiently produce dense uniform pancakes of ultracold rubidium atoms. It is a great experimental advantage to work with uniform samples, especially when the quantities of interest depend on the atomic density, and this approach is followed by more and more experimentalists [66–68]. Another advantage resides in the high versatility of the shapes that we can give to our atomic pancakes [69]. A novelty of the design of our set-up consists in the use of a so-called 'optical accordion' to confine the atoms in two dimensions. The characterisation of the combination of an optical accordion and a box potential is partly presented in this manuscript, and more details can be found in the article that we published.

A first set of projects then aimed at studying some interesting properties of light-matter interaction. Our atomic samples are not as dense as usual solids, but their density is high enough so that the average distance between particles is notably lower than the wavelength λ of their main electronic transitions, which makes these samples interesting to study with resonant light. Several mechanisms can occur. The first one is called multiple scattering: a photon scattered by an atom can be scattered by other atoms. This happens when the optical density of a sample is large compared to 1. The second process is called recurrent scattering: in a classical picture, a photon scattered by an atom can be later scattered by the same atom [70]. This happens when the density n of a sample is large compared to λ^{-3}. In a more realistic picture, neighbouring atoms are coupled by a dipole-dipole interaction and the eigenstates of the system are intrinsically many-body [71]. To understand properly the scattering of light in such a medium, one also has to take into account the polarisation degree of freedom of light [72] and the internal structure of the atoms [73].

Our atomic system is cold, so that the Doppler shift associated with the temperature is much lower than the linewidth of the transitions. This makes the regime of recurrent scattering easier to reach for a given atomic density. In the vertical direction, our sample is thin, and multiple scattering is suppressed. On the contrary, in the horizontal plane, the system is large and one can study multiple scattering in two dimensions. In this respect our experimental system is unique to study light-matter interactions. Previous studies had indeed been done with hot atomic vapours [74], with dilute systems with a large size where the optical density of the cloud is large [75–77], or with very small and non-degenerate systems [78, 79].

In a first study we measured the transmission of near-resonant light of our two-dimensional pancake to see how the single-atom picture of the resonant line was modified when increasing the atomic density. We found that the absorption line measured via the transmission of light is broadened, has an amplitude reduced and experiences a (small) blue shift. In a second study, we could illuminate with near-resonant light only a small central portion of the cloud and we could study radiation trapping by measuring the propagation of photons in the transverse direction. We could demonstrate that this trapping is affected by refractive index effects with opposite behaviours on each side of the resonance frequency.

Another type of experiments probes the mechanisms with which several independent Bose-Einstein condensates merge and reach a global coherence. This question is closely linked to the Kibble-Zurek mechanism [80] where a hot system is cooled down and crosses at a given rate the critical temperature of a phase transition that spontaneously breaks a continuous symmetry. In a uniform system, domains with different values of the order parameter grow, and their size depends on the cooling rate. In the case of Bose-Einstein condensates, the order parameter is the phase of the condensate. In this system, the phase domains formed during a quench subsequently merge and the system relaxes. This coarse-graining dynamics is expected to follow the geodesic rule that states that the phase landscape established after the merging of two condensates follows the path of minimal gradient. During this process, topological defects can be created when the phase landscape whirls by a multiple of 2π around a given point in the gas. The number of defects varies as a power law of the cooling rate, with an exponent that depends notably on the dynamical exponent of the phase transition. Several experiments have been performed with cold atoms to measure dynamical exponents (see [81] and references therein).

We performed experiments to confirm this geodesic rule by merging independent condensates in the shape of a ring and measuring the statistics of supercurrents that are formed when the phase whirls by a multiple of 2π around the ring. We could also measure the time scale on which the phase correlation across the ring emerges. The study of such supercurrents in rings is also very interesting for the development of atomtronic circuits, in continuous rings [82–85] or in lattice rings [86, 87].

A last study focused on the propagation of sound waves in a two-dimensional sample. The propagation of sound had already been measured a few years ago in three-dimensional systems [88–92], but it is interesting to wonder how the thermodynamics in low dimensions and the BKT physics affect this propagation of sound [93]. The propagation of sound relies on the mode coupling between the ‘normal’ and the superfluid part of the gas. Two sound modes emerge from this coupling and their velocity depend on the thermodynamics of the two parts of the fluid. The speed of sound was notably expected to display a discontinuity at the BKT transition, as the superfluid fraction exhibits a sudden jump at this point.

We could measure the velocity of the second sound across the BKT transition. Interestingly, we did not measure any discontinuity. These measurements have been explained theoretically in reference [94], and the sound that we measure above the critical temperature is thought to be a collisionless sound that takes its roots in the mean-field interactions of the gas.

In this thesis, I focus on the last results that we obtained. Two main directions are pursued.

The first one is the investigation of the BKT physics. It aims at measuring the phase ordering across this transition and thus showing how the role of thermal fluctuations is enhanced in a low-dimensional system, as well as pointing out the specificities of this topological phase transition.

The second direction concentrates on the dynamical symmetries of weakly interacting bosons in two dimensions. The symmetry group of this system is very rich due to the low-dimension of space, and it has many consequences on the dynamics of a cloud of atoms when they are placed in a harmonic potential. Our experimental approach sheds light on these consequences, and it also reveals surprising features of the dynamics of clouds with particular initial conditions: wave functions that evolve periodically and that are thus called 'breathers'.

DETAILED CONTENT OF THIS THESIS

This thesis is divided into three parts. In the first one I describe the important technical aspects of our experimental set-up. The second one is dedicated to the study of the spatial phase ordering of a uniform two-dimensional Bose gas across the BKT transition. In the third part is presented the study of the dynamical symmetries of weakly-interacting bosons in two dimensions. Here is a detailed summary of the chapters of each of these parts:

I. Producing and manipulating 2D Bose gases

Chapter 1: I describe the experimental set-up that allows us to produce uniform two-dimensional Bose gases. I detail the important experimental techniques that we use to image the atomic samples, to control their internal degree of freedom and to extract their temperature.

Chapter 2: I characterize in detail a new tool based on Raman beams, with which we can perform manipulations of the internal state of the atoms in a spatially-resolved way. This manipulation can be accompanied with a tunable momentum transfer.

II. Measuring the first correlation function of the 2D Bose gas

Chapter 3: I present the basic theory of the Berezinskii-Kosterlitz-Thouless transition with the XY-model, and I show how it applies to an infinite two-dimensional Bose gas. I then discuss some measurements that have been performed in the last years to measure first-order correlation functions on 2D systems. These measurements raise issues due to the out-of-equilibrium character of systems, to their spatial non-uniformity, and to their finite size.

Chapter 4: I present experiments that we have performed to measure the first-order correlation function of our uniform two-dimensional Bose gases. These experiments are based on the measurement of the momentum distribution of the gas. They provide only a qualitative understanding of how this correlation function evolves across the Berezinskii-Kosterlitz-Thouless transition.

Chapter 5: I present a second set of experiments to have a more quantitative measurement of the first-order correlation function. They rely on interferometric measurement of the relative phase between different points of the gas, and provide a direct and more accurate access to this correlation function.

III. Dynamical symmetry of the 2D Bose gas

Chapter 6: This chapter is dedicated to the theoretical study of the dynamical symmetries of the two-dimensional Bose gas in the presence of a harmonic trap. These symmetries allow one to determine scaling laws linking the dynamics of clouds that do not have the same initial conditions.

Chapter 7: The dynamical symmetries derived in the previous chapter are investigated experimentally in this chapter. The link between the dynamics of clouds initially at rest and with the same initial shape are reconstructed and compared with the theoretical laws.

Chapter 8: In this last chapter I report the observation of two types of wave functions that may be breathers of the two-dimensional Gross-Pitaevskii equation with a harmonic potential. This experimental observation is compared with numerical simulations of the equation.

LIST OF PUBLICATIONS

The several project in which I was involved in at the beginning of my thesis, but which are not discussed in this manuscript have led to the following publications:

- *Loading and compression of a single two-dimensional Bose gas in an optical accordion*, J.-L. Ville, T. Bienaimé, R. Saint-Jalm, L. Corman, M. Aidelsburger, L. Chomaz, K. Kleinlein, D. Perconte, S. Nascimbène, J. Dalibard and J. Beugnon, Phys. Rev. A, **95**, 013632 (Jan. 2017).
- *Relaxation dynamics in the merging of N independent condensates*, M. Aidelsburger, J.-L. Ville, R. Saint-Jalm, S. Nascimbène, J. Dalibard and J. Beugnon, Phys. Rev. Lett **119**, 190403 (Nov. 2017).
- *Transmission of near-resonant light through a dense slab of cold atoms*, L. Corman, J.-L. Ville, R. Saint-Jalm, M. Aidelsburger, T. Bienaimé, S. Nascimbène, J. Dalibard and J. Beugnon, Phys. Rev. A **96**, 053629 (Nov. 2017).
- *Resonant light diffusion in a disordered atomic layer*, R. Saint-Jalm, M. Aidelsburger, J.-L. Ville, L. Corman, Z. Hadzibabic, D. Delande, S. Nascimbène, N. Cherroret, J. Dalibard and J. Beugnon, Phys. Rev. A **97**, 061801(R) (June 2018).
- *Sound propagation in a uniform superfluid two-dimensional Bose gas*, J.-L. Ville, R. Saint-Jalm, É. Le Cerf, M. Aidelsburger, S. Nascimbène, J. Dalibard and J. Beugnon, Phys. Rev. Lett. **121**, 145301 (Oct. 2018).

These articles are reproduced at the end of this manuscript.

The content of the three last chapters of this thesis have been gathered and published in an article:

- *Dynamical symmetry and breathers in a two-dimensional Bose gas*, R. Saint-Jalm, P. C. M. Castilho, É. Le Cerf, B. Bakkali-Hassani, J.-L. Ville, S. Nascimbène, J. Beugnon and J. Dalibard, Phys. Rev. X **9**, 021035 (May. 2019).

Part I

PRODUCING AND MANIPULATING 2D BOSE GASES

2

EXPERIMENTAL SET-UP

The experimental set-up has been designed and built to produce ultracold bidimensional uniform samples of rubidium atoms. This chapter aims at giving an overview of this set-up.

When I arrived in the group, the experiment was being built for several months, and I participated to the end of this building. Thorough descriptions of the structure of the experiment have been delivered by previous Master and Ph.D. students, and the reader can refer to these works to have detailed information:

- The Masterarbeit of Katharina Kleinlein who worked on the early laser system, the vacuum system and the first cooling steps [95].
- The Ph.D. thesis of Laura Corman, who detailed the whole scheme to create a uniform bidimensional (2D) sample [64].
- The Ph.D. thesis of Jean-Loup Ville, who detailed the manipulation of the internal state, as well as important calibrations of our 2D gas [65].

I develop here all the elements that are useful in order to understand the experiments presented in this thesis. In particular I detail some features that were not discussed in these works. In a first part, the basic functioning of the experiment is presented without going too much into the technicalities. The second part details how the cloud is confined in two dimensions and how a uniform density is maintained. Finally, I explain how the internal state and the temperature of the cloud are prepared prior to investigating its properties.

2.1 OVERVIEW OF A COLD ATOM EXPERIMENT

2.1.1 *General features*

2.1.1.1 *Electronic structure of* ^{87}Rb

Rubidium belongs to the alkali group and has a simple electronic structure. Lasers addressing its electronic transitions are easy to access, enabling cooling schemes as well as optical trapping methods. All these advantages make this atom a widely-spread tool in the cold atoms community.

The electronic ground state of the atom is $^2S_{1/2}$ and its first excited state has two fine levels: $^2P_{1/2}$ and $^2P_{3/2}$. The transition $^2S_{1/2} \to {}^2P_{1/2}$ (resp. $^2S_{1/2} \to {}^2P_{3/2}$) is called the D1 (resp. D2) line and has a wavelength of 795 nm (resp. 780 nm).

We are only interested here in the $^2S_{1/2}$ and $^2P_{3/2}$ states, that we use for our cooling scheme. Each of these levels experiences hyperfine splitting due to the coupling between the electron and the spin of the nucleus: the $^2S_{1/2}$ level splits

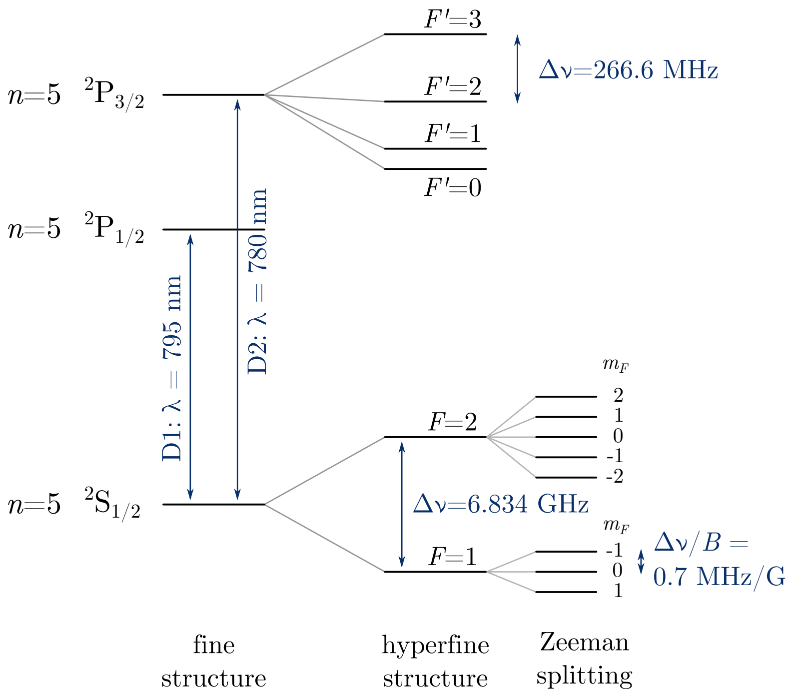

Figure 2.1: Electronic structure of rubidium atoms. The fine, hyperfine and Zeeman structures are detailed only for the levels of interest in this work.

into the $F = 1$ and $F = 2$ level, separated by $\approx 6.834\,\text{GHz}$, and the $^2P_{3/2}$ level splits into four levels labelled from $F' = 0$ to $F' = 3$.

The two hyperfine states of $^2S_{1/2}$ are the ones in which we perform the interesting physics. They experience Zeeman splitting in the presence of a magnetic field B: the $F = 1$ state splits into three levels, labelled with $m_F = -1, 0, 1$, and the $F = 2$ state splits into five levels, labelled with $m_F = -2, -1, 0, 1, 2$. In the low magnetic field regime where the quadratic Zeeman shift is negligible, the displacement of the energy of each level is $\Delta E = \mu_{\mathrm{B}} g_F m_F B$, with μ_{B} the Bohr magneton, and g_F the Landé factor of the hyperfine state of interest. For $F = 1$ (resp. $F = 2$), we have $g_F = -1/2$ (resp. $1/2$). For magnetic fields around a few gauss, these displacements correspond to frequencies on the order of a few megahertz.

All these features of the electronic structure of rubidium are summarized on Fig. 2.1, where only the relevant states are depicted.

2.1.1.2 *Lasers*

We use lasers with four different optical wavelengths to reach the quantum regime from a metallic sample, to trap them in a controlled geometry and to probe the properties of 2D samples.:

- Two lasers at 780 nm to address the D2 line. They are used for the cooling schemes summarized in 2.2.1, and for the imaging of the cloud explained in 2.1.2. We use saturated absorption on a vapour of rubidium to lock the frequency of these lasers with a precision of a few hundreds of kilohertz.

- Two lasers at 1064 nm, red-detuned with respect to the D1 and D2 lines, to create conservative attractive potentials (see 2.2.1), referred to as optical dipole traps.
- A laser at 532 nm, blue-detuned with respect to the D1 and D2 lines, to create conservative repulsive potentials and shape the final geometry of the cloud (see 2.2.2 and 2.2.3).
- A laser at 790 nm, between the D1 and D2 lines, to perform Raman transfers between the two lowest hyperfine states of the atom, as developed in Chapter 3.

2.1.1.3 *Vacuum system*

The experiments are performed in a compact vacuum system where a high vacuum is maintained. All experimental steps are performed in a single rectangular glass cell with high optical access and dimensions $25 \times 25 \times 105$ mm. In particular, the early cooling steps to prepare the atomic sample and the experiments performed on it are done at the same position, which prevents any technical difficulty due to the transport of the cloud between different regions of space.

Using a glass cell also allows to have coils and optical elements very near the atoms and outside the cell. Having these tools near the atoms permits to reach higher magnetic fields and optical numerical apertures, and not having them in the vacuum cell is technically easier to develop.

The glass cell is represented seen from three sides on Fig. 2.2, and as many elements as possible that are described in this chapter are depicted on these drawings.

2.1.1.4 *Magnetic fields*

The magnetic field in the glass cell has to be well-controlled in order to implement some of the cooling stages (see 2.2.1) and to control the energy splitting between Zeeman states of the atoms (see 2.3.1) and reliably address transitions between these states. There are several pairs of coils to achieve these tasks:

- A pair of water-cooled coils in anti-Helmholtz configuration along the vertical (z) axis. They produce a quadrupolar field for our quadrupole magnetic trap with a maximal vertical gradient of 240 G/cm.
- A pair of water-cooled coils in anti-Helmholtz configuration along the y axis. They produce a quadrupolar field for our magneto-optical trap (MOT) with a maximal gradient of 22 G/cm.
- Three pairs of coils in Helmholtz configuration along the three axes, to create bias fields. The pair on the vertical axis (resp. horizontal axes) creates a maximum bias field of 2 G (resp. 1 G). These coils are located around the glass cell, but they are not represented on Fig. 2.2. The intensity is provided by power supplies (Delta Elektronika ES 030-5) with a relative intensity noise of 10^{-4}, which corresponds to a fluctuation of magnetic field of 0.2 (resp. 0.1) mG.

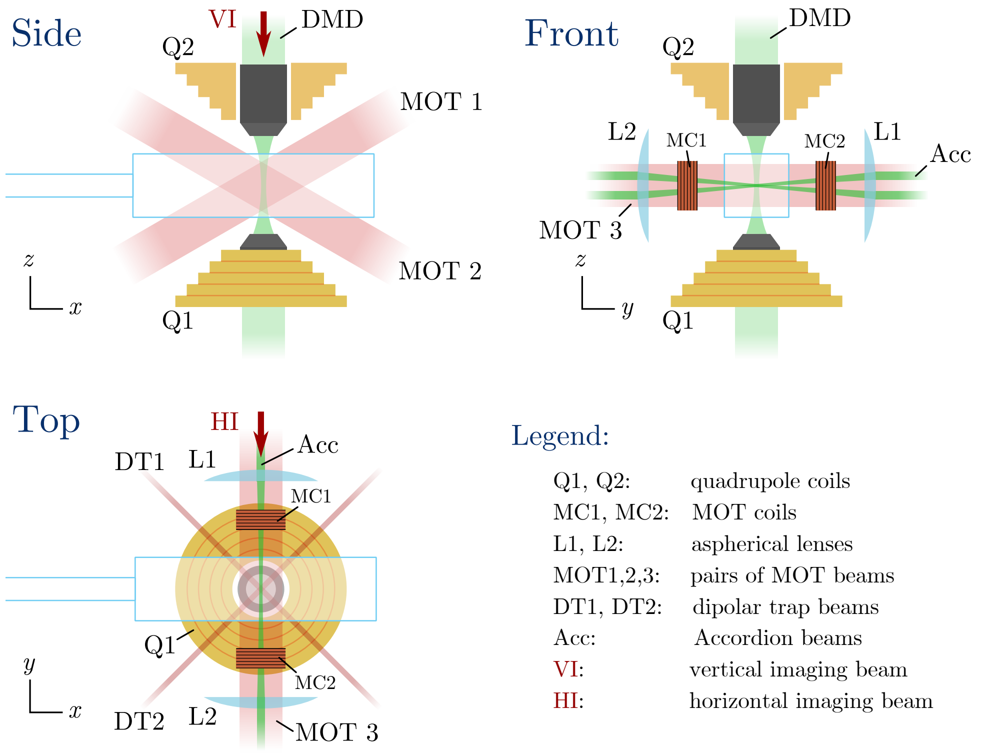

Figure 2.2: Scheme of the experimental set-up: Side, Front and Top views. The glass cell is in the centre of each view (light blue rectangle). The vertical anti-Helmholtz coils are represented in orange (Q1 and Q2). Inside them are placed microscope objectives. On the first two panels, only a cut of the top coils has been represented to better see the top microscope objective. For the sake of clarity, the laser beams are represented only on the panels that contain their propagation axis. The coils for the bias fields are not depicted here.

2.1.1.5 *Control of the experiment*

The whole experiment is computer-controlled. The free software Cicero-Word generator is used to generate a series of instructions. These instructions are transmitted to several National Instruments cards that send ‘analogical’ and digital signals to all the instruments we use (lasers, power supplies, generator, etc.). The different cards are synchronized by a FPGA module that acts as a clock.

The temporal resolution of all the signals is 1 µs, and their temporal accuracy is below 100 ns. The ‘analogical’ signals are in fact digitized with a resolution of approximately 2 mV, and they are bounded between −10 and 10 V. The digital signals provide 0 or 5 V.

2.1.2 *Taking pictures of atoms*

The determination of the density distribution of the cloud is realised via absorption imaging on the state $F = 2$. A laser pulse is tuned on the closed transition from $F = 2$ to $F' = 3$, which has a frequency ω_L, a linewidth Γ and a wavelength $\lambda_\mathrm{L} = 2\pi \mathrm{c}/\omega_\mathrm{L}$ with c the speed of light. It is sent on the atoms during a few tens of microseconds. The atoms scatter photons in all directions of space and a camera collects the remaining ones in the forward direction.

In the regime of low saturation, where the intensity I of the laser probe is small compared to the saturation intensity $I_\mathrm{sat} = \hbar\omega_\mathrm{L}^3\Gamma/(12\pi c^2)$, and in the regime of dilute clouds where the atomic density n_3D is small compared to λ_L^{-3}, the intensity collected on the camera is given by the Beer-Lambert law:

$$I_\mathrm{with} = I \exp\left(-\int \mathrm{d}l\, \sigma\, n_\mathrm{3D}\right) + I_\mathrm{bgd}, \tag{2.1}$$

where σ is the scattering cross-section of the atoms, whose value is discussed in 2.2.3, and the integral is performed along the direction of the probe laser. I_bgd represents any spurious light that can hit the camera and pollute our signal.

Another pulse of light without atoms is then sent to the camera to measure

$$I_\mathrm{without} = I + I_\mathrm{bgd} \tag{2.2}$$

and acts as a reference, and an image is also taken without any light pulse to measure I_bgd.

We then numerically compute the optical density OD of the cloud:

$$\mathrm{OD} = -\ln\left(\frac{I_\mathrm{with} - I_\mathrm{bgd}}{I_\mathrm{without} - I_\mathrm{bgd}}\right), \tag{2.3}$$

and one should get from equation (2.1)

$$\mathrm{OD} = \int \mathrm{d}l\, \sigma\, n_\mathrm{3D}. \tag{2.4}$$

Departing from the low saturation regime $I \ll I_\mathrm{sat}$ broadens the absorption line, and the number of photons each of the atoms scatter is not proportional to I any more, which is an important hypothesis to get the Beer-Lambert law. Moreover, having a too dense cloud where the condition $n_\mathrm{3D}\lambda_\mathrm{L}^3 \ll 1$ is *not* fulfilled can lead the light field to excite collective modes of the cloud mediated by dipole-dipole interactions, and the intensity I_{with} that we would measure can be very different from the single-atom picture given by the Beer-Lambert law. These effects have been studied into more details during the beginning of my Ph.D. They have been the subject of two publications [96, 97] and they are discussed in the two previous Ph.D. works [64, 65].

In this thesis, we restrict ourselves to the regime where the Beer-Lambert law is valid. More precisely, we use a probe light with $I/I_{\text{sat}} < 0.2$, and we measure optical densities that are always smaller than 1.5 to avoid leaving this regime due to collective excitations. In order to do that, the experiments are performed with the atoms in the $F = 1$ state, which is not sensitive to the probe light. A controlled fraction of these atoms is transferred in the $F = 2$ state to be imaged. This fraction is adjusted to limit the optical density to values lower than 1.5. The detail of how these transfers from $F = 1$ to $F = 2$ are done is explained in 2.3.1.

For quantitative measurements, we mainly use a vertical imaging to probe the spatial distribution of the bidimensional cloud in the xy-plane. We use a microscope objective with a numerical aperture of 0.45 to have a diffraction-limited resolution around 1 µm on the atoms. We image the atoms with a magnification of 11 with a low-noise CCD camera (Princeton Instruments, Pixis 1024 Excelon) that has an effective pixel size of 1.15 µm on the atoms. This calibration has been performed by combining the imaging of atoms trapped in a periodic potential and the diffraction of these atoms by a periodic lattice. More details are given in [65].

2.2 HOW TO PRODUCE A UNIFORM 2D BOSE GAS

2.2.1 *Cooling atoms down to quantum degeneracy*

In order to reach the quantum degeneracy from a hot vapour of rubidium, we follow four successive cooling steps briefly detailed here. The geometrical configuration of the various tools are shown on Fig. 2.2.

- In a primary glass cell separated from the science cell by approximately 30 cm, a two-dimensional magneto-optical trap (2D MOT) cools the initial vapour of rubidium in two dimensions of space, y and z. A beam resonant with the D2 line pushes the atoms to the science cell. The rest of the experimental steps are performed in this science cell.
- A MOT confines and cools around 10^9 atoms down to approximately 250 µK. The quadrupolar magnetic field is provided by the horizontal anti-Helmholtz coils. A first pair of laser beams propagates along the y axis, and the two others are in the xz-plane, at an angle of 60° with respect to the vertical axis. After this step, followed by a compressed-MOT step and a molasses step, we are left with $6 \cdot 10^8$ atoms at a temperature of 15 µK, and they are optically pumped in the $F = 1$ state.

- A strong quadrupolar magnetic field provided by the vertical anti-Helmholtz coils is ramped up (vertical gradient of 240 G/cm). Only the atoms in the sub-state $m_F = -1$ are trapped in this magnetic landscape, and their temperature rises to $\approx 200\,\mu$K. We proceed to evaporative cooling by sending a radio-frequency field to couple this sub-state to the other Zeeman sub-states. We ramp the frequency from 35 to 2.5 MHz during 12 s to transfer the most energetic atoms to the non-trapped Zeeman states, eject them and let the residual ones rethermalize. At the end of this step we have $2.5 \cdot 10^7$ atoms at a temperature of $20\,\mu$K.

- A crossed dipolar trap made of two red-detuned lasers located $50\,\mu$m below the centre of the quadrupolar field is turned on. The quadrupolar magnetic field is ramped down and the atoms fall into the optical dipolar trap. We proceed to further evaporative cooling by lowering the depth of this trap. Around $3 \cdot 10^5$ atoms reach quantum degeneracy at a temperature of 200 nK and in the $F = 1, m_F = -1$ state. A vertical magnetic field around 1 G is maintained to keep the atoms polarised in this state.

All these steps last in total 26 s, and a few more seconds are needed to create a 2D gas and probe its properties.

2.2.2 *Confining the gas in two dimensions*

The construction of the vertical confinement of the atoms is crucial to have a 2D gas. The goal is to confine the atoms around a minimum of potential energy in the z direction, to freeze the degrees of freedom along this axis and get a system that effectively evolves in the two other dimensions only. This 2D regime is attained when the vertical frequency ω_z of the confinement corresponds to an energy $\hbar\omega_z$ much larger than both the interaction energy E_{int} and the thermal energy $k_{\text{B}}T$ of the cloud. In that case, the atoms occupy only the lowest state of the vertical potential. Their dynamics is frozen in this direction of space and the gas is in the quasi-2D regime.

2.2.2.1 *An optical accordion*

We chose to build an ‘optical accordion’ following the scheme published in [98], which is also close to the optical set-up described in [99] and implemented with cold atoms in [100]. It consists in creating a vertical optical lattice with two blue-detuned lasers beams interfering with an angle that can be dynamically varied to change the lattice spacing. The same approach has also been used in [101] by reflecting a beam on a surface with a variable angle.

The building and the optical testing of our accordion was the subject of my master internship in the group, and it was followed by its implementation on the experiment in the very beginning of my Ph.D. To our knowledge, it is the first implementation of an optical accordion of this kind to produce 2D ultracold gases.

I describe here the set-up and give some important technical details that were not discussed in the previous Ph.D. theses.

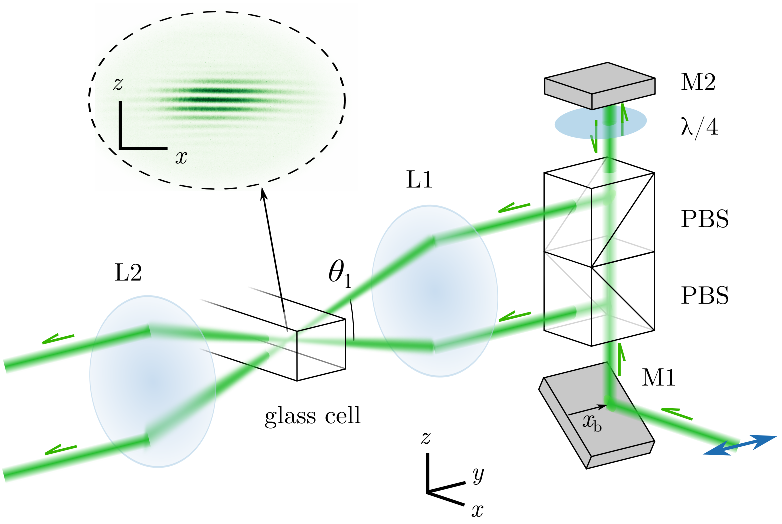

Figure 2.3: Optical set-up of the accordion. Two parallel beams come out of the two polarising beam splitters (PBS) on the right of the figure. Lens L1 focuses them on the atoms and lens L2 is used to image the interference pattern, as shown on the inset. The position x_b of the initial beam on mirror M1 can be varied (blue arrow) and controls the angle of interference θ_1 and the lattice spacing. This is done thanks to a mirror mounted on a motorized translation stage (not represented here). Mirror M2 is mounted on a piezoelectric stack to adjust the relative phase between the two beams.

When using a lattice made of repulsive light (wavelength $\lambda_\mathrm{A} = 532\,\mathrm{nm}$), the atoms sit in the dark fringes of the interference pattern. If the lattice is deep enough, the potential that the atoms experience is well approximated by a harmonic potential, with a vertical frequency

$$\omega_z = \sqrt{\frac{2\pi^2 U}{md^2}}, \tag{2.5}$$

where U is the maximum potential height of the lattice, m is the mass of an atom and d is the distance between two sites of the lattice. In order to have a high confinement, one therefore needs a lattice with a high potential U and a small lattice spacing d. For a given laser wavelength, the value of U depends only on the intensity we use to create the lattice. In our case we are limited to values of U/k_B below $\approx 10\,\mu\mathrm{K}$. If we want to have a vertical confinement of several kilohertz (so that $\hbar\omega_z > k_\mathrm{B}T$), we need to have a fringe spacing d below $4\,\mu\mathrm{m}$, so we aim at having d around 1 or $2\,\mu\mathrm{m}$.

Efficiently loading a large cloud of atoms (size $\approx 10\,\mu\mathrm{m}$) in a single node of a lattice with such a small spacing is a difficult task. The accordion solves this problem with the possibility to dynamically vary the lattice spacing: we load the atoms in a large spacing configuration so that they populate only one site of the lattice, and we adiabatically decrease the spacing to reach a high confinement.

The scheme of the accordion set-up is presented on Fig. 2.3: a single laser beam is separated into two by a first polarising beam splitter. The combination

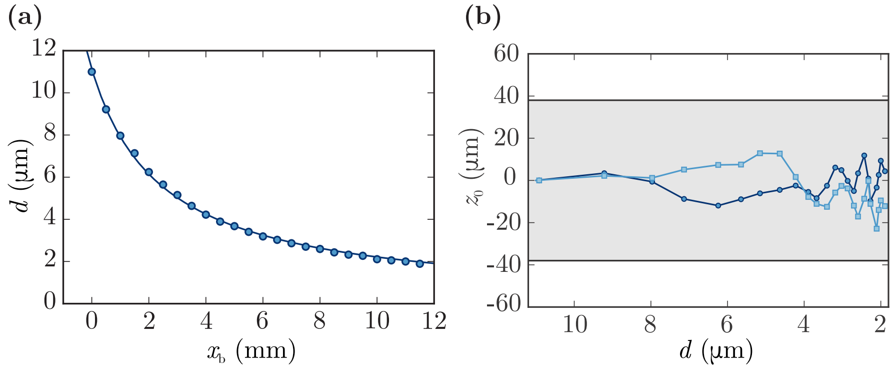

Figure 2.4: Optical measurements on the accordion. (a): Lattice spacing as a function of the position x_b of the translation stage. The solid line is a fit with expression 2.6 with f and $x_{\mathrm{b},0}$ as free parameters. We get $f_\mathrm{fit} = 103(1)\,\mathrm{mm}$, in agreement with the specification of the lens, and $x_{\mathrm{b},0} = -2.46(3)\,\mathrm{mm}$. (b): Vertical position of the centre of the two accordion beams as a function of the lattice spacing: square (circles) correspond to the bottom (top) beam. The shaded area represents the vertical size of the beams $\pm w_z$. Image adapted from [102].

of a mirror, a quarter-wave plate and a second polarising beam splitter makes the two beams parallel. Another polarising beam splitter is added to filter the vertical polarisation and make sure that both beams have the same horizontal polarisation. This element is not represented on Fig. 2.3. The two beams are then sent on an aspherical lens (Asphericon ALL50-100-S-U, labelled 'L1' on the figure) of focal length $f = 100\,\mathrm{mm}$ and they interfere in the glass cell. The waists of the beams at the position of the atoms are $w_z \approx 40\,\mu\mathrm{m}$ in the vertical direction and $w_x \approx 90\,\mu\mathrm{m}$ in the horizontal direction. A second aspherical lens, identical to the first one, is used to image the interference pattern on a control camera. The position x_b of the incoming beam on the beam splitters can be varied thanks to a mirror mounted on a motorized translation stage (PI miCos LS-100), which changes the distance between the two beams before the aspherical lens and then modifies the lattice spacing on the atoms. The angle θ_1 between the two interfering beams can be varied between 3° and 15°. The former is limited by the edge of the two polarising beam splitters, and the latter is limited by the aperture of the MOT coils through which the beams pass. The lattice spacing is

$$d = \frac{\lambda_\mathrm{A}}{2\sin(\theta_1/2)} = \frac{\lambda_\mathrm{A}}{2}\sqrt{1 + \left(\frac{f}{x_\mathrm{b} - x_{\mathrm{b},0}}\right)^2}, \tag{2.6}$$

which varies between 2 and $10\,\mu\mathrm{m}$. In the second expression, the value $x_{\mathrm{b},0}$ corresponds to the position of the stage where the two beams overlap perfectly. We measured the lattice spacing d on the control camera as a function of x_b. The results are presented on Fig. 2.4a.

2.2.2.2 *Limitation due to the quality of the focussing lens*

The most important element in the set-up is the quality of the focussing lens. When realising tests with a doublet, we observed that the aberrations of such a lens did not allow to make two beams with a waist smaller than 100 µm cross at the same position when displacing the incoming beam with the translation stage. We could have such beams overlapping and interfering properly on the whole range of the translation stage only with an aspherical lens that corrects for these aberrations.

For this aspherical lens as well, we observe that the centres of the two beams are not exactly at the same vertical position in the focal plane of the lens when varying the lattice spacing. On Fig. 2.4b are reported these vertical positions as a function of the lattice spacing. The biggest distance between them is $\approx 20\,\mu$m, which is why we chose the vertical waist of the beams w_z to be larger than this value.

The way the centres of the two beams are vertically displaced one with respect to the other is very reproducible and is independent of the speed of the translation stage that displaces the light beam. We found that it mostly depends on the surface of the aspherical lens. We have indeed tested several lenses from the same company and with the same specifications, and we measured different relative motions. More precisely, we have purchased successively one pair of lenses, then another pair, and then an additional single lens. These three sets of lenses have been manufactured separately. When testing them, we found good correlations between two lenses belonging to a pair, and much less correlations between the pairs, and between a lens from a pair and the single lens.

We have also performed a simple numerical simulation to check whether defects of the profile of the lens could lead to deflections of the beams on this order of magnitude. The manufacturer provides the equation of the surface of the lens and specifies the tolerance on this surface. The root mean square (RMS) of the irregularities does not exceed 100 nm and the error on the slope of the surface is smaller than 0.06 mrad.

Thanks to Snell's law, we compute the geometrical path of a ray of light parallel to the optical axis of the lens and hitting it at various positions of the surface and look at the position of the beam in the focal plane of the lens (see Fig. 2.5a). We perform this computation either with the perfect surface profile, or adding to it a small sinusoidal modulation within the specifications of the manufacturer.

On Fig 2.5b we show the results of this computation. We find that the displacement of a beam with respect to the optical axis does not exceed 5 µm, which would translate into a distance smaller than 10 µm between two beams symmetric with respect to the optical axis. This simple picture may not grasp all the effects that we experimentally observe. For example a misalignment between the first and the second aspherical lens that we use may increase the measured displacements.

The conclusion is nevertheless that we have good indications that the minute deviations from the optimal surface of the aspherical lens is limiting the accuracy with which we are able to focus the two beams on the same spot. It also constrains the minimal vertical waist of the accordion beams that we can have in order to always maintain a good interference between the accordion beams and keep the atoms in a dark fringe while varying the spacing of the vertical lattice.

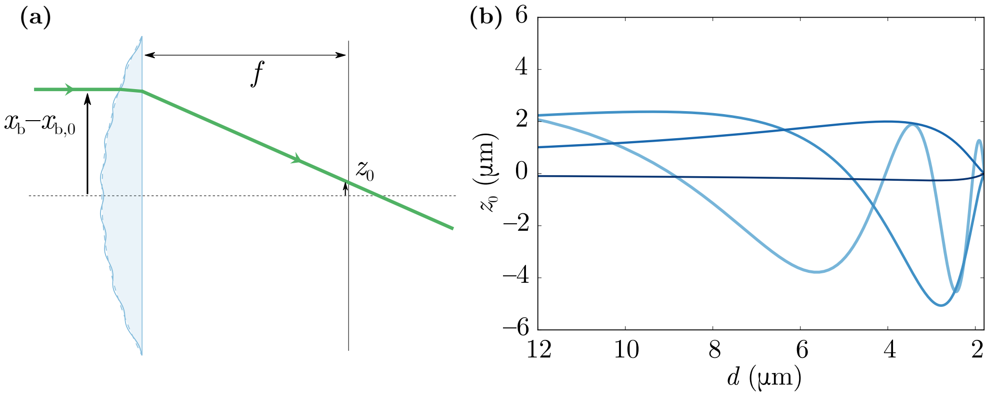

Figure 2.5: Numerical simulations of the aspherical lens. (a): Scheme illustrating the simulations: we compute the vertical position z_0 of one beam on the focal plane of a lens by adding small defects to its ideal surface (solid and dashed line on the scheme). (b): We perform the calculation for the ideal profile (dark-blue line), and for profiles where we add small sinusoidal modulations with different k-vectors. The values for the three examples here are $k/(2\pi) = 0.16, 0.08, 0.04\,\mathrm{mm}^{-1}$ for the three lines with increasing colour intensity. For each value, the amplitude of the sinusoidal modulations is adjusted to meet the specifications of the manufacturer.

2.2.2.3 *Stabilisation of the interference pattern*

Another important parameter to control is the relative phase between the two accordion beams. This phase difference changes the vertical position of the fringes. Since we need to load a cloud of atoms with radius $\approx 10\,\mu\mathrm{m}$ into the dark fringe of a lattice with a spacing of the same order of magnitude, the relative position of the cloud and the dark fringe of the lattice has to be stable to much better than $10\,\mu\mathrm{m}$.

We found that this relative phase drifts with a typical time scale of a few hours. At each experimental sequence, we take a picture of the lattice with the control camera. We select on this image a narrow region corresponding to a full period of the lattice and determine the line of pixels on which the dark fringe is located (see Fig. 2.6a, b and c).

If we monitor the position of this dark fringe, we see it drifting during the day (see Fig. 2.6d, before the dashed line): the relative phase between the accordion beams changes by 2π in approximately four hours. On top of this drift there are oscillations that we correlate with the fluctuations of temperature in the room.

In order to compensate for these variations, the retro-reflecting mirror of the top accordion beam (labelled ‘M2’ on Fig. 2.3) is mounted on a piezo-electric stack. After each experimental sequence we can determine the position p_{min} of the dark fringe on the camera and, if necessary, compensate the mismatch between the measurement and the target by changing the voltage sent to the piezo-electric stack. The target is determined by looking at the atoms in the lattice with an auxiliary horizontal imaging. When the lattice is well aligned with the cloud, we see only one plane of atoms.

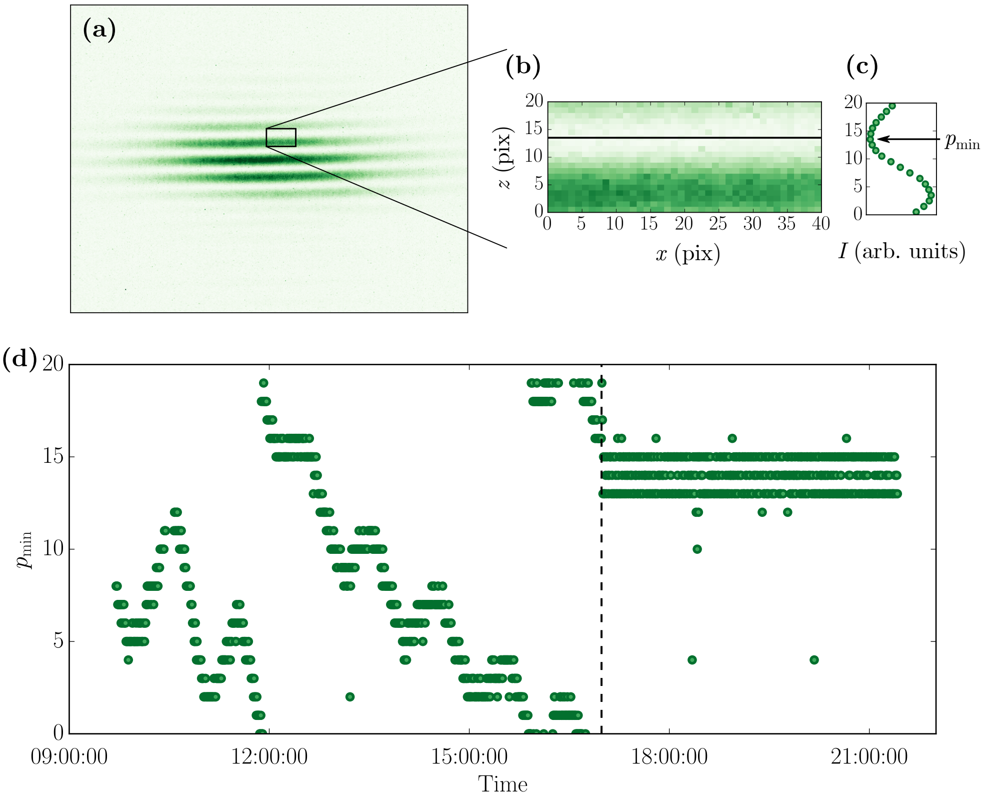

Figure 2.6: Stability of the accordion. (a): After each experimental sequence we take a picture of the vertical lattice. (b): We zoom on a region corresponding to a full period of the lattice. (c): We determine the position $p_{\min}$ of the dark fringe on the region chosen on (b). (d) We monitor $p_{\min}$ as a function of time during the whole day. There is one point every 30 s approximately. On that day, the feedback loop has been off until 5pm. It has then been turned on, indicated by the vertical dashed line, and the position of the dark fringe is stable until the end of the day.

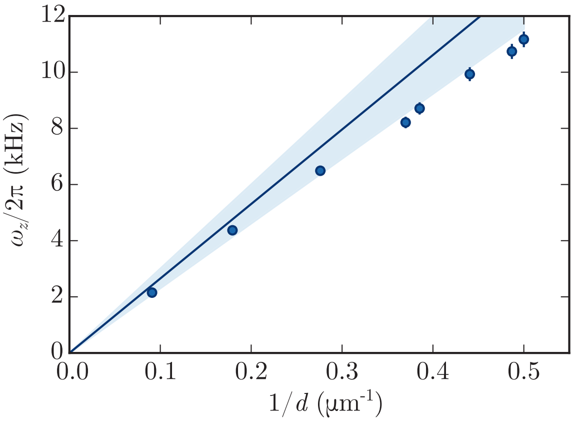

Figure 2.7: Vertical frequency of the accordion as a function of the inverse lattice spacing. The solid line is the theoretical prediction obtained with the parameters of the light beams measured independently. The shaded area represents the uncertainty on these independent calibrations. The data points are below the solid line, possibly because the contrast of the interference pattern between the two beams is not perfect.

On Fig. 2.6(d), after the dashed line that indicates when this feedback loop has been turned on on that day, we see that the dark fringe is stable over several hours, except for a few points. The position of the dark fringe oscillates between three pixels of the camera, but the loading of the atoms in a single node of the lattice is good for all of these three positions.

2.2.2.4 *Dynamical variation of the vertical confinement*

The loading of the cloud in the large spacing lattice is very efficient and the compression of this lattice is performed in a duration $\tau \approx 0.2\,\mathrm{s}$, which corresponds to $\omega_z \tau \gg 1$ with the smallest vertical frequency we use, as we will see.

We measure the vertical frequency ω_z by giving a vertical kick to the cloud and observing its oscillation in the vertical harmonic trap. More precisely we let the cloud evolve in this trap during a variable duration, then we release all traps and let the atoms fall freely. After a few microseconds we look at the vertical position of the atoms which is mostly sensitive to the velocity of the atoms when they are released. A sinusoidal fit of this position as a function of time provides ω_z. On Fig. 2.7 is reported this measurement as a function of the inverse lattice spacing. It is in good agreement with the expectation given by equation 2.5.

In the following, we usually work with a lattice spacing of $d = 2\,\mu\mathrm{m}$, and we reduce the power of the laser beams to decrease ω_z around $4\,\mathrm{kHz}$, which corresponds to a lattice depth $U \approx k_\mathrm{B} \cdot 4.2\,\mu\mathrm{K}$. As a comparison, the potential energy due to gravity on the length scale of one fringe is $mgd = k_\mathrm{B} \cdot 0.2\,\mu\mathrm{K}$.

We found this configuration more favourable to obtain a uniform cloud than keeping a high intensity. This uniformity is the subject of the next paragraph.

2.2.3 *Creating a cloud with a uniform atomic density*

2.2.3.1 *Implementation of a box potential*

Having a cloud with a uniform density is a great advantage when investigating properties of the gas that depend on its density. In cold atoms, the use of uniform gases has developed for a few years, both for Bose and Fermi gases [59, 66–68, 103] with the development of box potentials.

We have implemented such a box potential, which also has a high tunability. We use a blue-detuned laser beam (wavelength 532 nm) and send it on a digital micro-mirror device (DMD). This device consists of an array of micro-mirrors which can individually be turned on or off by modifying their spatial orientation. We image the surface of this DMD onto the atomic plane by using our microscope objective, and we obtain light only on the position of the 'on' pixels. We have a magnification of 1/70 between the DMD and the atoms (see [65] for a precise calibration). This means that a single pixel of the DMD, which measures 13.68 µm, represents 0.2 µm on the atoms, well below the resolution of the microscope objective. The atoms are repelled by light at the wavelength we use, and they are therefore trapped in the dark regions of the beams, where the mirrors of the DMD are off. They are confined by walls of light whose maximal height is around $k_\mathrm{B} \cdot 6\,\mu\mathrm{K}$.

The beam has a waist of 45 µm on the atoms, which means that we are able to create a box potential with an edge to edge distance up to 100 µm and with a resolution of 1 µm. The DMD is easily programmable and the shape of the cloud can be modified at will. Fig. 2.8 presents a few examples of absorption images of the atomic density in this tunable box potential.

2.2.3.2 *Back to the absorption imaging*

The absorption images taken with the vertical imaging allow us to measure the 2D atomic density $n(x, y)$: in the quasi-2D regime, the wave function of the atoms along the vertical direction is given by the lowest level of the harmonic oscillator, therefore

$$n_{3\mathrm{D}}(x, y, z) = \sqrt{\frac{m\omega_z}{\pi\hbar}} \exp\left(-\frac{m\omega_z z^2}{\hbar}\right) n(x, y), \tag{2.7}$$

and the optical density obtained with the vertical imaging is, after integration of equation 2.4 along the z axis:

$$\mathrm{OD} = \sigma\, n(x, y). \tag{2.8}$$

The value of the scattering cross-section depends on the atomic transitions involved in the imaging process, on the polarisation of the imaging light, and on the magnetic field. A careful calibration of σ is necessary to extract reliable atom numbers from the absorption imaging. It has been done thanks to projection noise measurements, and the details are given in [65] (Chapter 7). We will use the result of this calibration:

$$\sigma = \frac{7}{15} \frac{3\lambda_\mathrm{L}^2}{2\pi} \mathcal{F}, \tag{2.9}$$

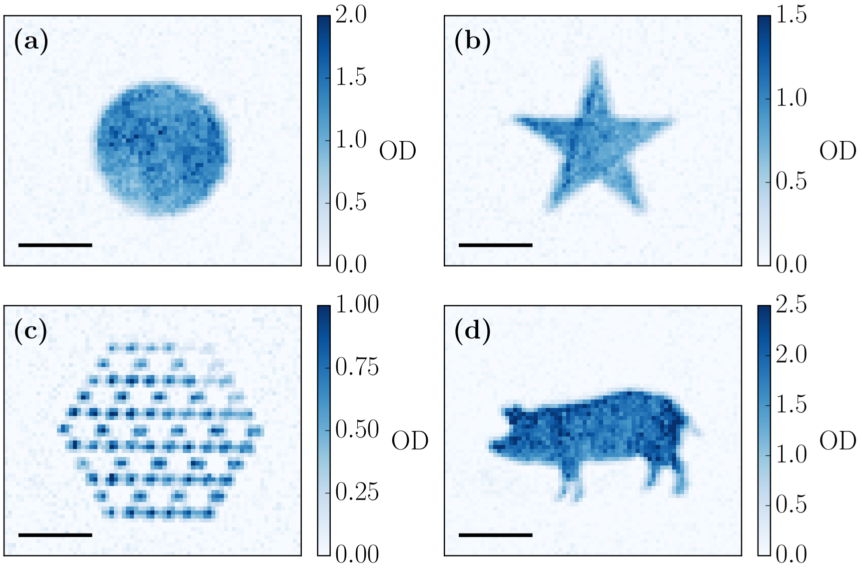

Figure 2.8: Absorption images of atoms filling different types of potentials. (a),(b): Simple shapes as a disk or a star are uniformly filled. (c): Small independent clouds can be arranged in a regular way, as a Kagome lattice. (d): More exotic and entertaining shapes can also be realised, such as a pig. The horizontal black lines represent 20 µm.

where the factor 7/15 is an average of Clebsch-Gordan coefficients for the transitions from $F = 2$ to $F = 3$, and $\mathcal{F}$ is an *ad hoc* factor to take into account the linewidth of the laser, the broadening of the resonance line by the magnetic field, etc. With our calibration, we determine $\mathcal{F} = 1.6(1)$.

The calibration of σ with projection noise turns out to be long to perform and delicate to analyse. In chapter 8 we will see a more simple and robust method to calibrate this scattering cross-section and reliably determine the number of atoms from absorption images. Both methods give compatible results for the value of $\mathcal{F}$.

2.2.3.3 *Additional features of the* DMD

The tunability of the DMD allows us to go beyond static box potentials. Here are two features that we have used in the past and can use in the future:

1. *Dynamical potentials:* The DMD can display different images at a rate up to a few kilohertz, thus modifying the potential on the atoms. The fact that the effective size of one pixel of the DMD on the atoms is smaller than the resolution of the microscope objective helps to make the dynamics of this potential smooth. We have used this feature when studying the recombination of independent condensates published in [69].

2. *Grey levels:* By locally switching on a controlled fraction of the micromirrors on the DMD, we can control the intensity we send on the atoms at each position and spatially shape the local density of the cloud at will.

This feature involves a simple algorithm to propagate errors due to the pixelisation of the DMD.

These two possibilities have not been used for the experiments presented in this thesis and I will not detail them.

2.2.3.4 *Controlling and quantifying the uniformity of the cloud*

A uniform filling of the box potential can be achieved by finely tuning the parameters of the experiment:

- The focus of the DMD on the plane of the atoms has to be adjusted to have edges as sharp as possible and as less spurious light in the dark regions as possible.
- A gradient along the x direction (transverse to the propagation direction of the accordion beams) can be compensated by slightly modifying the relative power of the two accordion beams. These beams are on purpose not perfectly overlapping in the x direction. Their centres are separated by 10 to 20 µm, so that an intensity imbalance translates into a gradient of potential in the x direction. We modify the relative power of the two beams by rotating a half-wave plate before the first polarising beam splitter of the accordion.
- A gradient along the y direction can be compensated by varying the vertical position of the two interfering beams of the accordion on the focussing lens. This is done thanks to two mirrors located between the accordion and the focussing lens. Such a vertical displacement gives a global tilt of the dark fringe in the y direction and the atoms feel a force in this direction due to gravity.

In order to quantify the uniformity of the cloud, we take M images of the cloud and average them pixel by pixel. Fig. 2.9a displays the average over 10 images of a cloud in a square box. On each pixel of the camera we get an estimation of the local density $\bar{n}(x_i, y_j)$, where the bar represents the average over the M images, and (x_i, y_j) denote the coordinates of the camera pixels. The variance of the distribution is

$$\sigma_M^2 = \left\langle \bar{n}(x_i, y_j)^2 - \langle \bar{n}(x_i, y_j) \rangle^2 \right\rangle , \tag{2.10}$$

where $\langle \cdot \rangle$ represents the average over the camera pixels that the cloud covers. It contains information about the uniformity of the cloud, but also a statistical fluctuation due to the photonic noise on the camera and the finite amount of images we take. In order to extract the information about the uniformity, we compute σ_M^2 for different numbers M of images. We expect that σ_M^2 is the sum of the variance of the cloud's density and the variance of the photonic noise, that scales as $1/M$. Fig. 2.9b shows the variance of the distribution σ_M as a function of M, along with a fit with the function $M \mapsto \sqrt{\alpha + \beta/M}$, where α and β are free parameters.

The estimator of the uniformity is

$$\varepsilon = \frac{\lim\limits_{M \to +\infty} \sigma_M}{\langle \bar{n}(x_i, y_j) \rangle}, \tag{2.11}$$

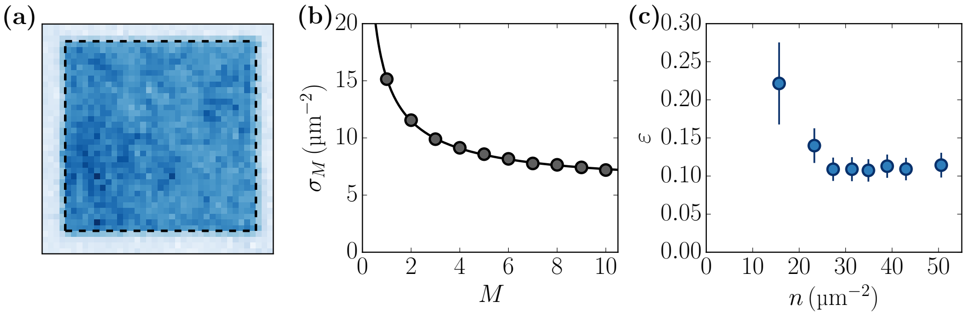

Figure 2.9: Uniformity of the cloud. (a): Average of 10 images of a square-shaped cloud. The dashed line indicates the region where we investigate the uniformity. (b): Spatial standard deviation σ_M of the atomic density as a function of the number of averaged images. The solid line is a fit with the function $M \mapsto \sqrt{\alpha + \beta/M}$. We extract from it the limit value $\sqrt{\alpha}$. On this example $\sqrt{\alpha} = 5.8\,\mu\text{m}^{-2}$. (c): Estimator of uniformity ϵ as the averaged density is varied. The two figures (a-b) correspond to the data of the largest density.

where the average $\bar{n}(x_i, y_j)$ is taken over all the images we have taken. If the density is uniform, then $\varepsilon = 0$. On the contrary, if the cloud is not uniform, then ε increases. For example, if the atomic density is evenly distributed between 0 and $n_{\max}$, then $\varepsilon = 1/\sqrt{3} \approx 0.577$.

For typical parameters of the experiment, we measure $\varepsilon \approx 0.1$. Fig. 2.9c shows how this estimator behaves as we vary the atomic density in the trap. For high densities, ε stays around 0.1, and it increases as we decrease the density enough so that the defects of the optical potential are not much smaller than the chemical potential of the gas any more, which happens around $n = 20\,\mu\text{m}^{-2}$. The measurements have been performed in the very degenerate regime, and when the atoms have a density of $20\,\mu\text{m}^{-2}$, we estimate the chemical potential to be around $h \cdot 360\,\text{Hz}$ (see section 2.3.2 for more details). Therefore the defects of the box potential have a root mean square around $h \cdot 40\,\text{Hz}$, or equivalently $k_B \cdot 2\,\text{nK}$.

We estimate that these defects are mostly due to the accordion beams. In order to improve the uniformity, one can adjust the position of the centre of the accordion beams in the x direction.

2.3 HOW TO CONTROL THE INITIAL STATE OF THE CLOUD

2.3.1 *The internal state of the atoms*

At the end of the cooling steps, the atomic cloud is polarised in the $F = 1, m_F = -1$ state, as seen in 2.2.1. We are able to control this internal state with pulses of microwave fields. I have built and installed a microwave chain inspired from the Ph.D. thesis of Kenneth Maussang from the group of Jakob Reichel [104]: a source (Nexyn NXPLOS 0680-02778, seeded by a 100 MHz generator Wenzel Associates 501-23588 A) provides a signal at 6.8 GHz and an I-Q mixer (Pulsar IMOH 03-458) mixes it with a signal with a frequency around 34 MHz provided by a generator (Rigol DG1062Z). This generator sends to the

I-Q mixer two signals in quadrature so that only one sideband is produced. The signal is then amplified (amplifier Kuhne KU PA 7000) and sent to the atoms via an antenna located near the glass cell. Fig. 2.10a presents a simplified scheme of this chain. The frequency of the generator is chosen to address the required transition between two Zeeman sub-states of the $F = 1$ and $F = 2$ manifold. We keep a vertical magnetic field around 1 G to separate the frequencies of these transitions. The transitions that can be addressed with the microwave are those coupling two states with a difference of their quantum number m_F equal to -1, 0 or 1.

We can coherently drive these transitions with microwave pulses. When sending a pulse of duration t_{MW}, detuned by δ with respect to the frequency of the transition from an initial state i to a final state f, each atom is brought to the superposition state $c_i \left|i\right\rangle + c_f \left|f\right\rangle$, where the probabilities $\mathcal{P}_i$ and $\mathcal{P}_f$ to measure an atom in i or f are

$$\begin{aligned}\mathcal{P}_i = |c_i|^2 = 1 - \frac{\Omega_0^2}{\Omega_0^2+\delta^2}\sin^2\left(\sqrt{\Omega_0^2+\delta^2}\,\frac{t_{\mathrm{MW}}}{2}\right),\\ \mathcal{P}_f = |c_f|^2 = \frac{\Omega_0^2}{\Omega_0^2+\delta^2}\sin^2\left(\sqrt{\Omega_0^2+\delta^2}\,\frac{t_{\mathrm{MW}}}{2}\right),\end{aligned} \tag{2.12}$$

where Ω_0 is the frequency describing the coupling strength between the two states and induced by the microwave pulse.

If the drive is resonant with the frequency ($\delta = 0$), we can transfer the atoms with a probability 1 by applying a pulse of duration π/Ω_0. We illustrate this on Fig. 2.10b: here, the atoms have been prepared in the state $F = 2, m_F = 0$, we couple it to the state $F = 1, m_F = 0$ during a time t_{MW} and we image the atoms in the $F = 2$ manifold. The number of atoms detected in the state $F = 2, m_F = 0$ evolves sinusoidally with a full contrast, and a Rabi frequency $\omega_0 = 2\pi \cdot 7.1(1)$ kHz. In particular, with a pulse of duration 70 µs, all the atoms are transferred in $F = 1, m_F = 0$.

In the following we will refer to the duration of the resonant pulses by the value of $\Omega_0 t_{\mathrm{MW}}$. For example a π-pulse corresponds to a full transfer from $F = 1, m_F = 0$ to $F = 2, m_F = 0$.

The frequency Ω_0 of the oscillation, called the Rabi frequency, depends on the power of the microwave field sent to the atoms and to its projection on the polarisation (here a π-polarisation) useful to drive this transition. On all transitions (σ^+, σ^- and π), we reach Rabi frequencies on the order of 5 to 10 kHz, which means that we can transfer all the atoms from one state to the other in less than 100 µs, much faster than the typical time scale on which the motional dynamics of the atoms occur (≈ 1 ms).

In order to reliably address each of the transitions, their frequencies have to be stable with a precision of a fraction of Ω_0, so that the detuning δ can always be neglected in equation 2.12. By measuring the magnetic field with a probe, we observe that the vertical component of the magnetic field fluctuates with a RMS of 2.6 mG. Since we keep a magnetic field in this direction, this fluctuation induces an important shift of the transition frequencies. For example the frequency of the transition from $F = 1, m_F = -1$ to $F = 2, m_F = 0$ fluctuates with an RMS of 1.8 kHz.

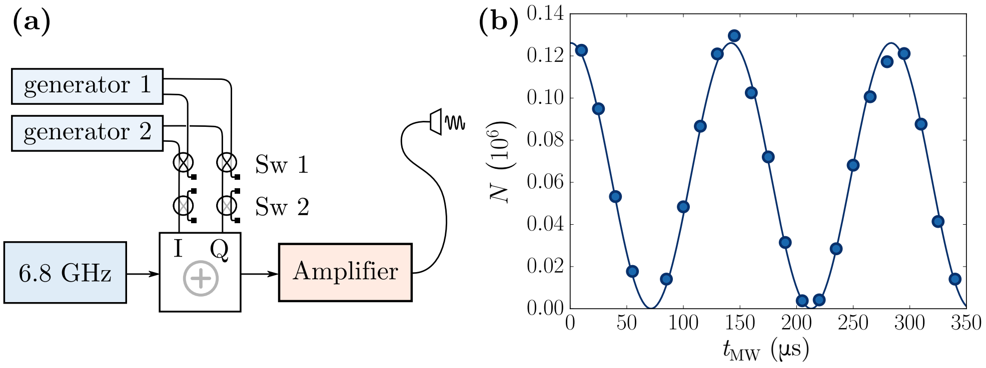

Figure 2.10: Microwave chain. (a): Simplified scheme of the microwave chain. A signal at 6.8 GHz is modulated by a signal around 34 MHz with an 'I-Q mixer'. The latter signal is produced by any of the two generators depicted, with a tunable frequency. The two sets of switches allow us to select one of the generators (Sw 1) and to turn the signal on and off (Sw 2) very rapidly. The signal is amplified and sent to the atoms with an antenna located near the glass cell. (b): Example of a Rabi oscillation between the states $F = 2$, $m_F = 0$ and $F = 1$, $m_F = 0$. The frequency of the transition is 6.834684 GHz, and the Rabi frequency induced on the atoms is $\Omega_0 = 2\pi \cdot 7.1(1)\,\mathrm{kHz}$, as extracted from the fit (solid line).

We found that this fluctuation was mostly due to the Parisian Métropolitain. In order to stabilize this magnetic field, we measure its vertical component in another room, and subtract the fluctuations of this signal to the magnetic field we ask for on the experiment. On Fig. 2.11 are shown measurements of the magnetic field near the atoms without and with this compensation system. With it, we are able to reduce the fluctuation of the magnetic field down to 0.27 mG during several hours, which is slightly bigger that the noise attributed to the power supply. It is however sufficient to address the transitions with the microwave in a reliable way.

2.3.2 *The phase-space density of the cloud and its temperature*

2.3.2.1 *The equation of state of the interacting 2D Bose gas*

The last parameter that we can vary is the temperature of the gas. For a cloud with atomic density n in a vertical confinement of strength ω_z, an important point is the critical temperature of the BKT transition [38, 105], below which the system gets superfluid:

$$T_\mathrm{c} \approx \frac{2\pi\hbar^2}{mk_\mathrm{B}} \frac{n}{\ln(C/\tilde{g})}, \tag{2.13}$$

where $C = 380 \pm 3$ [106], and $\tilde{g}$ is the effective 2D interaction strength between the atoms:

$$\tilde{g} = \sqrt{\frac{8\pi m\omega_z}{\hbar}}\, a_\mathrm{s}, \tag{2.14}$$

with a_s the 3D s-wave scattering length of the atoms. The relation 2.13 is only valid in the regime $\tilde{g} \ll 1$, in which we always are.

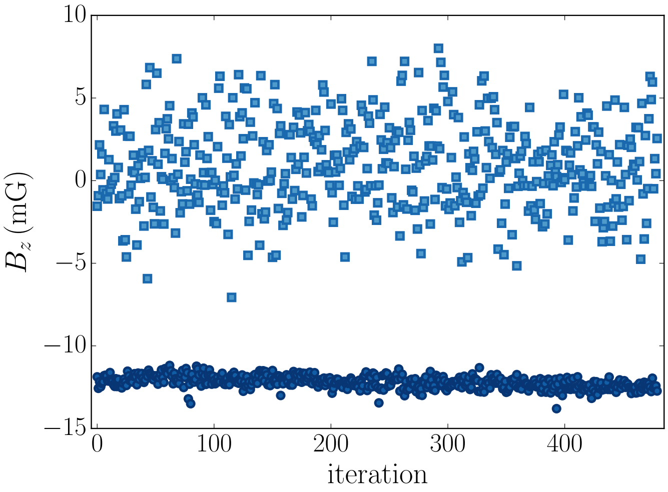

Figure 2.11: Stabilisation of the vertical magnetic field. We measure the vertical component of the magnetic field with a probe located near the atoms at a given time during the sequence. We measure it for many sequences, each lasting 30 s. Two sets of data are taken during four hours each: one without the magnetic field stabilization (light-blue squares) and one with the stabilization (dark-blue circles). The standard deviation of the latter is seven times smaller than the one of the former. The stabilization induces a small offset of 15 mG which is very small and easy to compensate.

For a given confinement ω_z, the thermodynamics of the gas depends only on the ratio n/T via its phase-space density (PSD) $\mathcal{D}$:

$$\mathcal{D} = n\frac{2\pi\hbar^2}{mk_\mathrm{B}T}. \tag{2.15}$$

Equivalently, the thermodynamics of the gas can be described with the single parameter $\mu/(k_\mathrm{B}T)$. This peculiar feature stems from the scale-invariance of the system, that will be developed in Chapter 7.

Notably, the equation of state $\mathcal{D}(\mu, T)$ that links the density n to the chemical potential μ of the gas does not depend on μ and T independently, but on the ratio $\mu/(k_\mathrm{B}T)$. This equation of state has been studied previously in the group [107, 108], and in other groups [109]. Interestingly, this equation of state is also universal around the critical point $\mathcal{D}_\mathrm{c} = \ln(C/\tilde{g})$ [109, 110]: a single function can describe the behaviour of the cloud for any interaction strength $\tilde{g} \ll 1$.

In the following we will use this equation of state to measure the PSD of the gas, and its temperature. The most important quantity to understand the physics is the ratio $\mathcal{D}_\mathrm{c}/\mathcal{D}$, or equivalently T/T_c, which gets lower than 1 when the BKT transition is crossed.

There is no analytical expression for the equation of state that links $\mu/(k_\mathrm{B}T)$ to $\mathcal{D}$, but there are two limits where it can be approximated:

1. *The Hartree-Fock regime*, where the cloud is far from degeneracy: $\mathcal{D} \ll 1$. In this case, the equation of state of a non-interacting 2D gas is

$$\mathcal{D} = -\ln\left[1 - \exp\left(\frac{\mu}{k_{\mathrm{B}}T}\right)\right]. \tag{2.16}$$

   For a weakly-interacting gas, the Hartree-Fock approximation consists in adding to the chemical potential μ the mean-field correction $-2\hbar^2\tilde{g}n/m$, where the minus sign accounts for the repulsive character of the interactions [111]. We then get:

$$\mathcal{D} = -\ln\left[1 - \exp\left(\frac{\mu}{k_{\mathrm{B}}T}\right)\exp\left(-\frac{\tilde{g}\mathcal{D}}{\pi}\right)\right], \tag{2.17}$$

   that we can re-write as

$$\frac{\mu}{k_{\mathrm{B}}T} = \frac{\tilde{g}\mathcal{D}}{\pi} - \ln\left[1 - \exp\left(-\mathcal{D}\right)\right], \tag{2.18}$$

2. *The Thomas-Fermi regime*, where the cloud is deeply in the degenerate regime: $\mathcal{D} \gg 1$. In this regime the kinetic energy is much smaller than the chemical potential. In that case, the gas is described by a classical field that obeys hydrodynamic-like equations, as it will be seen in Chapter 7. One can derive the equation of state when neglecting the kinetic energy term of this equation:

$$\frac{\mu}{k_{\mathrm{B}}T} = \frac{\tilde{g}\mathcal{D}}{2\pi}. \tag{2.19}$$

   These hydrodynamic equations supports Bogoliubov excitations. When considering that these excitations are thermally occupied, one can determine the next term of the equation of state [105], and we get

$$\frac{\mu}{k_{\mathrm{B}}T} = \frac{\tilde{g}\mathcal{D}}{2\pi} - \frac{\tilde{g}}{2\pi}\ln\left(\frac{\tilde{g}\mathcal{D}}{\pi}\right). \tag{2.20}$$

These two regimes are connected by the full equation of state. Monte-Carlo simulations have been realised by Prokof'ev and Svistunov [110] to compute this equation of state near the critical point. We will use the results of these simulations to fit our data.

The full equation of state is shown on Fig. 2.12. The left panel presents the two limits detailed above (dashed lines), and the result of the Monte-Carlo simulations taken from [110]. The right panel presents the function we use to fit our experimental data: we take the result from the Monte-Carlo simulation and add a few points in the Hartree-Fock regime. We then interpolate all these points with an analytical function (solid line).

2.3.2.2 *Controlling the PSD of the cloud*

After having loaded the gas in the 2D trap, its PSD is already above $\mathcal{D}_{\mathrm{c}}$. We can increase it by lowering the height of the box potential and further evaporating the cloud. Both the temperature T and the atom number N decrease, but in a way that makes the ratio N/T increase.

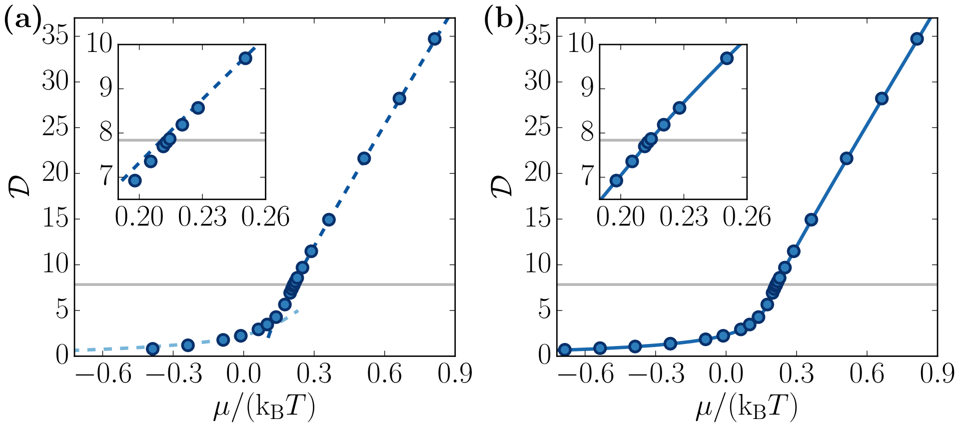

Figure 2.12: Equation of state. (a): The Hartree-Fock and the Thomas-Fermi regime are shown as dashed lines (light and dark blue respectively). The results of the Monte-Carlo simulations are shown as points. The horizontal grey line indicates the critical point $\mathcal{D}_\mathrm{c}$. (b): Determination of an interpolating function. We interpolate the results of the Monte-Carlo simulations that we extend with points in the Hartree-Fock regime. The solid line is the interpolating function that we use in the following to fit the experimental data. For both graphs, the inset is a zoom around the critical point. All the curves here are plotted for $\tilde{g} = 0.15$.

On the contrary, we can decrease the PSD of the gas by removing some atoms from the gas. We proceed in the following way: a microwave pulse is sent to transfer a fraction of the atoms in the $F = 2, m_F = 0$ state. A short (40 µs) pulse of light from the imaging beam is sent on the atoms. It is resonant only with the transferred atoms, which absorb photons. The momentum kick they experience is energetic enough to remove them from the trap. The remaining atoms are the atoms in $F = 1, m_F = 0$, which rethermalize during a few seconds. Their final PSD is lower at the end of the process.

2.3.2.3 *Measuring the PSD and the temperature of the cloud*

We have developed a method to extract the PSD of a gas, inspired from [67, 112]. We use a repulsive laser beam (wavelength 532 nm) whose intensity landscape can be shaped with another DMD, in the same way as the box potential is created. This new beam and the beam for the box potential have orthogonal polarisations, they are mixed on a polarising beam splitter, and the surface of both DMDs are focussed on the atoms with the top microscope objective. With the second light beam we create on the centre of the cloud a local potential (a disk of radius 5 µm) whose height V can be set independently from the height of the box potential. At this position, the atomic density is depleted due to the additional potential (see Fig. 2.13a).

The whole gas is at thermodynamic equilibrium, and the local density approximation ensures that, at the position of the local potential, the chemical potential of the cloud is $\mu_0 - V$, where μ_0 is the chemical potential of the rest of the gas. By varying V and measuring the atomic density in the depleted region n, we can get the relationship between n and μ. We can then search

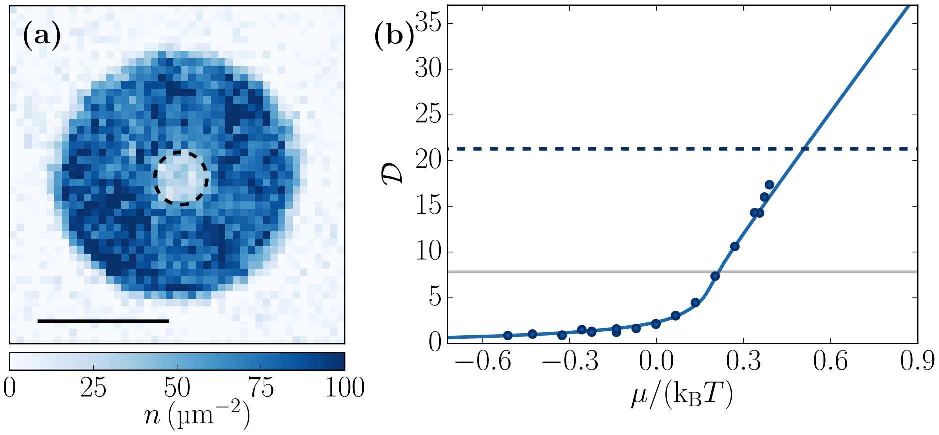

Figure 2.13: Measurement of the cloud's PSD. (a): Example of image used for the measurement of the PSD. An additional repulsive potential is sent on the area delimited by the dashed line. The atomic density is measured in and outside this region. The horizontal black line represents 20 µm. (b): The atomic density is plotted as a function of the height of the applied potential. Both axes for the data points are rescaled to match with the equation of state (solid blue). The dashed blue line shows the density outside of the small region, which gives the PSD of the cloud after rescaling. The parameter used to fit the data contain the information about the temperature. For the data shown here, $\mathcal{D} = 22(1)$, and $T = 124(10)\,\text{nK}$.

for the best parameter T so that the data points $2\pi\hbar^2 n/(mk_{\text{B}}T)$ as a function of $\mu/(k_{\text{B}}T)$ match with the equation of state. On Fig. 2.13b is presented an example of these measurements, where both axes are rescaled to fall on the equation of state. The particular elbow shape of the equation of state makes the fitting procedure very robust and allows to determine the PSD of the gas on a large range from 4 to 40, and with a 10% relative error. There might be systematic errors inherent to the method, but we would need another type of experiment to perform quantitative comparisons and estimate these errors. As far as we can judge, this method gives values of the PSD which are compatible with the physical phenomena that we observe, such as the dependence of the speed of sound with the phase-space density [94, 113].

2.4 CONCLUSION

In this chapter I have described the main features of the experimental set-up that allows us to create, manipulate and probe ultracold atomic samples.

With this set-up we are able to create 2D slabs of rubidium atoms with an optical accordion. In the plane, the cloud has a uniform density and its shape is controlled with a high resolution thanks to a DMD. The internal state of the atoms can be controlled with a high precision thanks to a microwave set-up. The thermodynamic state of the atoms can be controlled, and the cloud can be brought from above to below the critical point of the BKT transition. The degeneracy of the cloud is extracted by measuring the equation of state of the gas.

3

IMPLEMENTATION OF SPATIALLY-RESOLVED SPIN TRANSFERS

In addition to the experimental tools presented in the previous chapter, I have developed during my thesis a Raman beams set-up that allows to manipulate coherently the internal state of the atoms in a spatially-resolved way. We have seen in Chapter 2, section 2.3.1, that we are able to perform coherent oscillations between two hyperfine ground states by applying microwave pulses. The wavelength of these microwaves are on the order of a few centimetres, and we address the whole cloud at once. The goal of the Raman beams that I describe here is to perform the same kind of spin rotations but by spatially selecting the atoms that undergo these rotations. Moreover, the Raman process that we induce on the atoms is accompanied by a momentum transfer that we can choose on a large range of momenta, including a zero momentum transfer.

This experimental tool is very versatile and it allows us to perform complex manipulations of our atomic samples. It is for example at the heart of the experimental sequence described in Chapter 6 with which we are able to directly measure the first correlation function of the gas by interferometric means.

In this chapter I first describe the theoretical background of Raman transitions before explaining how they are implemented on our experiment. I then present a characterisation of our set-up: how we perform the spatial shaping of the Raman beams with a DMD and the two configurations in which we can operate, with co-propagating beams to transfer zero momentum to the atoms and with non co-propagating beams to have a finite momentum transfer to the atoms.

3.1 HOW TO INDUCE RAMAN PROCESSES ON COLD ATOMS

3.1.1 *Elements of theory about two-photon transitions*

Raman scattering describes the inelastic scattering of light by a system. Such Raman processes are fundamental in many fields of natural science such as chemistry and biology [114–116], due to the precision of the spectroscopic measurements that allow to address specific chemical bounds in molecules, and the spatial resolution they allow. In physics, stimulated Raman scattering is widely used to probe the energy spectrum of systems, but also their structure [117, 118].

In the community of atomic and molecular physics, Raman processes are used to manipulate and probe the various systems of interest. They are used to cool atoms or ions in tight traps thanks to the resolution of the different vibration modes [119], and also to perform spectroscopy of these vibrational modes [120]. Thanks to the possibility of exchanging momentum with the

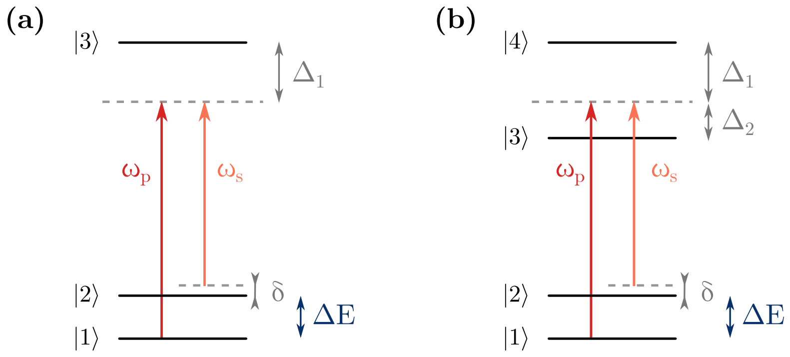

Figure 3.1: Level schemes for Raman transitions. (a): Simple scheme with a Λ-configuration. The states $|1\rangle$ and $|2\rangle$ are coupled via a two-photon transition, far-detuned from an excited state $|3\rangle$. (b): More accurate situation: the states $|1\rangle$ and $|2\rangle$ correspond respectively to Zeeman states of the $F = 1$ and $F = 2$ levels of the ground state of rubidium, and the states $|3\rangle$ and $|4\rangle$ correspond respectively to the levels ${}^2P_{1/2}$ and ${}^2P_{3/2}$.

studied system, it is possible to manipulate it and to implement sophisticated experimental procedures [121], and to perform spectroscopy of the momentum distribution of a cold gas [122, 123]. Raman processes also open rich possibilities by coupling the momentum and the spin state of particles – also known as spin-orbit coupling [124–126]. Finally, Raman beams can be used to prepare a well-controlled phase profile of an atomic sample with a single component or with a spinor condensate [127–129].

3.1.1.1 *A simple model*

The basic principle of Raman transfers is the following: two states $|1\rangle$ and $|2\rangle$ are separated by an energy ΔE and have respective momenta $\hbar\boldsymbol{q}_1$ and $\hbar\boldsymbol{q}_2$. They are effectively coupled by two laser beams of respective frequency ω_p and ω_s and wave vectors $\boldsymbol{k}_\mathrm{p}$ and $\boldsymbol{k}_\mathrm{s}$, far-detuned from the resonance with a third state $|3\rangle$ (detuning Δ_1), as depicted on Fig. 3.1a. The indices p and s correspond to the historical notations referring to 'Pump' and 'Stokes'. Intuitively, the states $|1\rangle$ and $|2\rangle$ are coupled when the conservation of energy and the conservation of momentum are fulfilled:

$$\omega_\mathrm{p} - \omega_\mathrm{s} = \Delta E, \tag{3.1}$$

$$\hbar(\boldsymbol{q}_2 - \boldsymbol{q}_1) = \hbar(\boldsymbol{k}_\mathrm{p} - \boldsymbol{k}_\mathrm{s}). \tag{3.2}$$

In the rotating-wave approximation where $\omega_\mathrm{p,s} \gg \Delta_1$, and assuming that level $|1\rangle$ is not affected by the laser labelled s nor level $|2\rangle$ by the laser labelled p, such a three-level system evolves under the following Hamiltonian, expressed in the basis $\{|1\rangle, |2\rangle, |3\rangle\}$:

$$H = \frac{\hbar}{2}\begin{bmatrix} 0 & 0 & \Omega_\mathrm{p} \\ 0 & 2\delta & \Omega_\mathrm{s} \\ \Omega_\mathrm{p}^* & \Omega_\mathrm{s}^* & 2\Delta_1 \end{bmatrix}, \tag{3.3}$$

where $\delta = \omega_{\mathrm{p}} - \omega_{\mathrm{s}} - \Delta E$, and $\Omega_{\mathrm{p,s}}$ are the Rabi frequencies associated with each of the laser beams.

When the detuning Δ_1 is much larger than the Rabi frequencies $\Omega_{\mathrm{p,s}}$ and the linewidth Γ of the state $|3\rangle$, this excited state is weakly populated, and one can adiabatically eliminate the population in this state. We are left with an effective 2-level system $\{|1\rangle, |2\rangle\}$ that evolves under the effective Hamiltonian:

$$H_{\mathrm{eff}} = \frac{\hbar}{2} \begin{bmatrix} 0 & \Omega_{\mathrm{p}}\Omega_{\mathrm{s}}^*/(2\Delta_1) \\ \Omega_{\mathrm{p}}^*\Omega_{\mathrm{s}}/(2\Delta_1) & 2\delta + (|\Omega_{\mathrm{p}}|^2 - |\Omega_{\mathrm{s}}|^2)/(2\Delta) \end{bmatrix}. \tag{3.4}$$

This corresponds to having the two states coupled with a two-photon Rabi frequency $\Omega_{\mathrm{p}}\Omega_{\mathrm{s}}^*/(2\Delta_1)$, and with an effective detuning that has an additional term corresponding to light shifts created by the two laser beams on the levels $|1\rangle$ and $|2\rangle$.

3.1.1.2 *A more realistic picture*

When applying this formalism with the states $|1\rangle$ and $|2\rangle$ being two Zeeman states of the hyperfine states of ${}^2S_{1/2}$, one needs to take into account the multi-level structure of the excited states of rubidium and the polarisation degree of freedom of light. There are indeed two main transition lines: D1 and D2, as represented on Fig. 3.1b. The energy levels corresponding to each of these lines are both degenerate. One has then to consider the interference between the contributions of all the virtual transitions to these excited states.

The polarisation of the light beams constrains the number of virtual transitions that we have to consider. In our case the two beams have orthogonal polarisation and they propagate along the quantization axis. In other words their polarisation is respectively $(\sigma^+ + \sigma^-)/\sqrt{2}$ and $(\sigma^+ - \sigma^-)/\sqrt{2}$.

The derivation of the effective coupling that these two Raman beams induce between the hyperfine states of ${}^2S_{1/2}$ in the limit where $\Delta_{1,2}$ is much larger than the hyperfine splitting of the excited states is presented in Appendix A. The results are the following. If we start with atoms in the state $F = 1, m_F = 0$, these atoms are coherently coupled to the state $F = 2, m_F = 0$ with an effective Rabi frequency

$$\Omega_{\mathrm{R}} = \frac{\Omega_{\mathrm{p}}\Omega_{\mathrm{s}}^*}{4} \left(\frac{1}{3\Delta_2} - \frac{1}{3\Delta_1} \right), \tag{3.5}$$

where the Rabi frequency of each beam is defined from the amplitude of the electric field $\mathcal{E}_{\mathrm{p,s}}$ of the laser and the reduced dipole matrix element $\langle P_{1/2} || \boldsymbol{d} || S_{1/2} \rangle$ by

$$\Omega_{\mathrm{p,s}} = \frac{\mathcal{E}_{\mathrm{p,s}} |\langle P_{1/2} || \boldsymbol{d} || S_{1/2} \rangle|}{\hbar}, \tag{3.6}$$

and the process has an effective detuning $\delta_{\mathrm{eff}} = \delta$. Each of the states also experiences a light shift V_{shift}:

$$V_{\mathrm{shift}} = \frac{\hbar(|\Omega_{\mathrm{p}}|^2 + |\Omega_{\mathrm{s}}|^2)}{4} \left(\frac{1}{3\Delta_2} + \frac{2}{3\Delta_1} \right). \tag{3.7}$$

No other Zeeman state is populated, either because their m_F number is odd and cannot be coupled via two $\sigma^{\pm}$-polarised photons, or because the contribution of all the couplings via the excited states interfere destructively in the limit $\Delta \gg \Delta E$ (states $F = 2, m_F = \pm 2$). Moreover, the choice of non-parallel polarisations for the two Raman beams is crucial to couple the two desired states. One can show that two beams with the same polarisation would not couple them.

The resonance condition is still $\hbar(\omega_\mathrm{p} - \omega_\mathrm{s}) = \Delta E$, where ΔE has two contributions: the hyperfine splitting $\hbar\omega_\mathrm{h}$ with $\omega_\mathrm{h} = 2\pi \cdot 6.834682\,\mathrm{GHz}$ and the difference of kinetic energy ΔE_c between the two states:

$$\Delta E_\mathrm{c} = \frac{\hbar^2}{2m}\left(\boldsymbol{q}_2^2 - \boldsymbol{q}_1^2\right). \tag{3.8}$$

The difference $\omega_\mathrm{p} - \omega_\mathrm{s}$ and the difference $\boldsymbol{k}_\mathrm{r} = \boldsymbol{k}_2 - \boldsymbol{k}_1$ are fixed by the laser beams, therefore, with equation 3.2, the resonance condition on the energy reads

$$\hbar(\omega_\mathrm{p} - \omega_\mathrm{s}) = \hbar\omega_\mathrm{h} + \frac{\hbar^2}{2m}\boldsymbol{k}_\mathrm{r} \cdot (2\boldsymbol{q}_1 + \boldsymbol{k}_\mathrm{r}). \tag{3.9}$$

This equation has to be fulfilled with a precision given by the Fourier broadening of the pulse we apply on the atoms with the Raman beams. If the duration of this pulse corresponds to a π-pulse, then the resonance condition 3.9 has to be fulfilled with a precision $\hbar\Omega_\mathrm{R}$. This means that the Raman beams address a velocity class that has a width

$$\Delta v = \frac{\Omega_\mathrm{R}}{k_\mathrm{r}}. \tag{3.10}$$

3.1.1.3 *Avoiding any light shift and photon scattering*

Since we want to perform local transfers, any light shift due to the Raman beams could induce spurious dephasing between the region of the gas where the beams are shone and where they are not. In order to limit this effect, we choose the frequency of the Raman laser beams to cancel the light shift V_shift:

$$\frac{1}{\Delta_2} + \frac{2}{\Delta_1} = 0, \tag{3.11}$$

which translates into an equation for the wavelength $\lambda_\mathrm{R} = 2\pi c/\omega_\mathrm{R}$ of the Raman laser (with $\omega_h \ll \Delta_{1,2}$):

$$\frac{1}{\lambda_\mathrm{R}} = \frac{1}{3}\left(\frac{1}{\lambda_{D2}} + \frac{2}{\lambda_{D1}}\right), \tag{3.12}$$

and we obtain $\lambda_\mathrm{R} = 789.9\,\mathrm{nm}$. With such a wavelength, we have a non-zero effective Rabi frequency with equation 3.5. In practice we will have Rabi frequencies $\Omega_\mathrm{R}/(2\pi)$ on the order of a several tens of kilohertz so that the duration of a full oscillation is larger than the resolution of our time sequence (1 µs) and smaller than the time scale of the spatial dynamics of the atoms ($\approx$ 1 ms). Obtaining such a frequency requires a laser intensity of several hundreds of $\mathrm{kW/m^2}$, which is possible with a reasonable power (a few milliwatts) focussed on a small region ($40 \times 40\,\mathrm{\mu m^2}$).

Due to the precision with which we are able to choose the wavelength of the laser, this wavelength is not exactly at λ_{R}, and there is a small light shift. With an imprecision of 0.1 nm on λ_{R} and a Rabi frequency of $2\pi \cdot 50\,\mathrm{kHz}$, the light shift is around $h \cdot 1\,\mathrm{kHz}$, which is on the order of the chemical potential of the clouds we are creating. We estimate that our precision on λ_{R} is better than 0.1 nm, but not much below. This means that a Raman transfer may be accompanied with a non-negligible dephasing between the transferred and non-transferred atoms. This will however not be an issue for the experiments described in this thesis.

Finally, we have to estimate the rate Γ_{sc} at which the atoms scatter photons from the Raman beams. It is given by

$$\Gamma_{\mathrm{sc}} = \frac{3\pi c^2 \Gamma^2}{2\hbar\omega_{\mathrm{R}}^3}\left(\frac{1}{\Delta_1^2} + \frac{1}{\Delta_2^2}\right) I_{\mathrm{tot}}, \tag{3.13}$$

where I_{tot} is the total intensity that the atoms receive. With the previous values and $I_{\mathrm{tot}} = 2 \cdot 10^6$, which is one order of magnitude above the required intensity to have a Rabi frequency of 50 kHz, we get $\Gamma_{\mathrm{sc}} \approx 5\,\mathrm{s}^{-1}$, which means that during a pulse of light lasting 20 µs, approximately one atom out of 10^4 will scatter a photon. With this order of magnitude we can safely manipulate the spin of the atoms without heating significantly the sample.

3.1.2 *Our experimental set-up*

3.1.2.1 *Generation of two laser beams with a proper detuning*

A naive approach to create Raman beams consists in using a laser source (wavelength λ_{R}, frequency ω_{R}) and modulating it with an electro-optic modulator (EOM) at a frequency $\omega_{\mathrm{E}} \approx 2\pi \cdot 6.83468\,\mathrm{GHz}$. It creates a sideband at frequency $\omega_{\mathrm{R}} + \omega_{\mathrm{E}}$ that can be used with the carrier at ω_{R} to induce Raman transitions between the two hyperfine states.

However, there are two sidebands created by the EOM, and the second one is at frequency $\omega_{\mathrm{R}} - \omega_{\mathrm{E}}$. It can also induce Raman transitions with the carrier at ω_{R}. The total Rabi frequency is the sum of the Rabi frequency of each pair of beams. Given the fact that the two sidebands have a difference of phase of π due to the EOM, they interfere destructively, and the total Rabi frequency is much lower than the individual ones [120].

A solution is proposed in [120]: the laser source is first separated into two beams. The first one is modulated with a frequency $\omega_{\mathrm{E}} = 2\pi \cdot 6.8\,\mathrm{GHz}$ slightly different from $\Delta E/\hbar$ by a few tens of megahertz. We compensate it by shifting the frequency of the two beams with an acousto-optic modulator (AOM) on each of them. More precisely, the first beam has a carrier at ω_{E} and sidebands at $\omega_{\mathrm{R}} \pm \omega_{\mathrm{E}}$, and we shift their frequency by $\omega_{\mathrm{A},1} = 2\pi \cdot 115\,\mathrm{MHz}$ with an AOM. The frequency of the second beam is shifted with a second AOM by $\omega_{\mathrm{A},2} = 2\pi \cdot 80.32\,\mathrm{MHz}$. The set-up to produce these beams is drawn on Fig. 3.2a, and Fig. 3.2b summarizes the frequencies we have, and illustrates the resonance conditions between these frequencies.

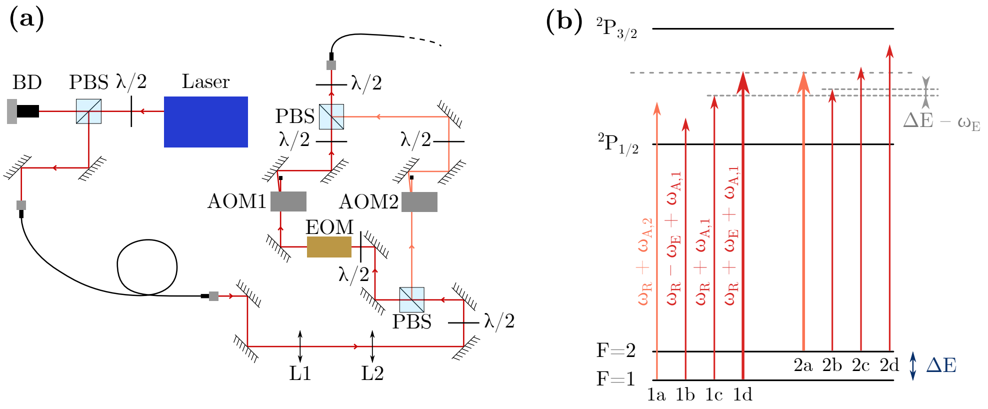

Figure 3.2: Generation of a pair of resonant beams. (a) Optical set-up that allows us to produce two beams with frequencies that can resonate to induce Raman transfers. The first path is modulated with an EOM and an AOM (path on the left, in red) and the second one is modulated with an AOM only (path on the right, in orange). The two beams are mixed with a polarising beam splitter and coupled in a fibre to be brought to the main experimental table. (b) Scheme of the four frequencies present in the two beams and that could resonate two by two with the atoms. The choice of the frequency modulations of the EOM and the two AOMs is such that only one pair of frequencies can resonate with the atoms, indicated with the thicker arrows.

There are sixteen pairs of frequencies that could lead to a resonance with the atoms. The pair that is important here is the one composed of the first sideband of the first beam and the second beam (arrows labelled 1d and 2a on Fig. 3.2b). The resonance condition between these two frequencies is

$$\hbar(\omega_\mathrm{E} + \omega_\mathrm{A,1} - \omega_\mathrm{A,2}) = \Delta E, \tag{3.14}$$

which is met in our case.

There are fifteen other pairs of frequencies. One frequency cannot resonate with itself (e.g. arrows labelled 1a and 2a on the figure) because of the hyperfine splitting of $2\pi \cdot 6.8\,\mathrm{GHz}$. Among the eleven other ones, there are eight whose resonance condition is not met by more than this hyperfine splitting. The three other ones are:

- The second sideband and the carrier of the first beam (arrows labelled 1d and 2c). They are detuned from resonance by $\Delta E - \hbar\omega_\mathrm{E} \approx h \cdot 35\,\mathrm{MHz}$. This quantity is much larger than the Rabi frequency of the Raman beams, and these two frequencies will not affect the atoms.

- The first sideband and the carrier of the first beam (arrows labelled 1c and 2b). They are also detuned from resonance by $\Delta E - \hbar\omega_\mathrm{E}$, and these two frequencies will not affect the atoms.

- The second sideband and the second beam (arrows labelled 1a and 2b). They are detuned from resonance by $\Delta E - \hbar\omega_\mathrm{E} + \hbar\omega_\mathrm{A,1} - \hbar\omega_\mathrm{A,2} \approx h \cdot 69\,\mathrm{MHz}$. For the same reason, these two frequencies will not affect the atoms.

The two beams are then mixed on a polarising beam splitter with orthogonal polarisations and they are coupled into a polarisation-maintaining optical fibre.

The set-up having been built on a table separated from the main experimental one, the two beams are transported to the main experiment with this fibre.

The power of the laser beams is not the limiting factor here since our source provides more than 1 W of light whereas we need a few tens of milliwatts on the atoms. However it has to be noted that the EOM has an efficiency around 15%, each AOM has an efficiency around $70-80\%$, and the coupling of the fibre allowes to transport 70% of the light to the main table.

3.1.2.2 *Spatial shaping and choice of the momentum transfer*

The two resonant frequencies can now be sent on the atoms. There are two important features:

- The direction in which each of them are sent. The difference between their wave vectors gives rise to a momentum transfer to the atoms.
- The spatial shaping of the intensity of the beams, which allows us to select the region where the Raman transfers will occur.

Concerning the direction of propagation of the two Raman beams, we can choose between two configurations:

1. The two beams are co-propagating: the vectors $\boldsymbol{k}_{\mathrm{p,s}}$ are positively co-linear and oriented along the vertical direction. The velocity transfer is
$$\frac{\hbar}{m}\boldsymbol{k}_{\mathrm{r}} = \frac{\hbar\omega_{\mathrm{h}}}{mc}\hat{\boldsymbol{z}}, \tag{3.15}$$
which is on the order of 0.1 µm/s, which is smaller than all the velocity scales involved in the system. The Raman processes are therefore considered to be done without the atoms experiencing any momentum transfer.
2. The two Raman beams are separated and sent on the atoms with an angle with respect to the vertical direction. In this case the atoms experience a non negligible momentum transfer, that we characterize in the following.

In the first case, the scheme is simple (see Fig. 3.3a): the two polarisations of the light transported with the fibre are sent on a DMD to spatially shape the intensity of the beam. In order to take advantage of a large surface of the DMD, the size of the beam is increased with a telescope (lenses of focal lengths −50 mm and 200 mm) to get a waist of 1.4 mm, which represents the size of 100 pixels of the DMD. Due to multi-order diffraction, the power that we get out of the DMD is half of the power we send on it. Again, this is not a limiting factor for us.

The surface of the DMD is then imaged on the atoms with a magnification around 1/37.5 through our microscope objective of high numerical aperture. The beam thus has a measured waist of 40 µm on the atoms, and each pixel has an effective size of approximately 0.4 µm (see 3.2.2). The regions where the Raman transfer will happen are selected thanks to the DMD. Its precise focus on the atoms is done with lens L4 of Fig. 3.3a which is mounted on a motorized translation stage. The method to determine the focus is described in 3.2.2.

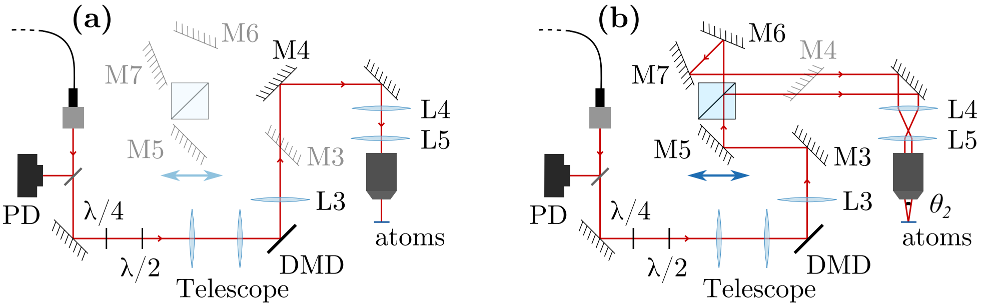

Figure 3.3: Scheme of the two configurations. (a) Configuration to induce no momentum transfer with the Raman beams. The beam is shone on a DMD to shape the intensity distribution and focused on the atomic plane with the microscope objective. The elements in grey are not used. (b) Configuration to induce a momentum transfer. We switch from one configuration to the other by flipping mirrors M3 and M4. In this configuration, the two orthogonal polarisations are separated in an optical accordion that allows us to vary their relative angle on the atomic plane. The focal lengths of the lenses of the telescope are −50 and 200 mm. The focal lengths of L3, L4, L5 are respectively 750, 400 and 200 mm.

It has to be noted that there are several light beams sent on the atoms through the microscope objective: the imaging beam at 780 nm (see 2.1.2), the two independent DMD beams at 532 nm that have orthogonal polarisations (see 2.2.3.1 and 2.3.2.3), and now the Raman beams at 790 nm.

The Raman beams are mixed with the imaging beam with an interference filter (Semrock LL01-780-12.5). Light at 780 nm has a transmission coefficient above 98%, and light at 790 nm has a transmission coefficient below $2 \cdot 10^{-5}$. The filter is oriented so that the imaging beam passes through it and the Raman beams are reflected and exit in the same direction as the imaging beam. Both beams are then mixed with the two DMD beams at 532 nm with a dichroic filter that transmit the former and reflects the latter.

From equation 3.10, the width of the velocity class in the z direction addressed with a π-pulse of the Raman beams is $\Delta v = \Omega_\mathrm{R}/k_\mathrm{r}$. In this case, it is approximately equal to $2 \cdot 10^3$ m/s. As a comparison, the width of the velocity distribution in the vertical direction is $\sqrt{\hbar\omega_z/(2m)} < 5$ mm/s, which is much smaller than Δv. The Raman beams therefore address all the cloud at once.

If we choose to have the Raman process accompanied with a momentum transfer, we have implemented another path with an optical accordion, similar to the one presented in 2.2.2.1. We manually flip mirror M3 on and mirror M4 off (see Fig. 3.3a), and we get the configuration of Fig. 3.3b. The Raman beams are sent on a polarising beam splitter that separate the two orthogonal polarisations corresponding to the two paths of Fig. 3.2a. In order to make sure that this separation is done properly, we have a $\lambda/2$ and a $\lambda/4$ plate before the beam splitter to correct for any rotation of the polarisation or ellipticity that could happen in the fibre. To check this experimentally, we block one path before the fibre and check that the remaining light goes out only on one output of the beam splitter.

The two beams are made parallel with the two mirrors labelled M6 and M7 on Fig. 3.3, and they are then sent to the atoms following the same path as described previously. They reach the atoms with a relative angle θ_2 that depends on the initial spacing of the two beams. This angle can be varied at will with the mirror labelled M5 that is mounted on a motorized translation stage, symbolized on Fig. 3.3 by the blue arrow. We can vary θ_2 between approximately 1.4° and 30°. The biggest angle we can have is limited by the diameter of lens L4 and of the interference filter.

The momentum transfer is expected to be

$$\hbar k_{\mathrm{r}} = 2\hbar k_{\mathrm{R}} \sin\left(\frac{\theta_2}{2}\right), \tag{3.16}$$

where $k_{\mathrm{R}} = 2\pi/\lambda_{\mathrm{R}}$ is the wave vector of the laser.

This momentum corresponds to an energy of $\hbar^2 k_{\mathrm{r}}^2/2m$. It is at most $\hbar \cdot 1\,\mathrm{kHz}$, which is smaller than the Rabi frequency. This means that we will not need to change the frequency of the AOMs to fulfil the resonance condition when varying the angle θ_2.

Moreover, the width of the velocity class in the xy-plane addressed by the beams is given by equation 3.10. In our case it is always larger than $80\,\mathrm{mm/s}$. We now compare this value to the width of the velocity distribution of the gas in the xy-plane.

- For a degenerate gas in a box potential of size L, a lower bound of the width of the velocity distribution is given by the Heisenberg limit [123]: $h/(mL)$. For a small box of size $10\,\mu\mathrm{m}$ this width is on the order of $0.5\,\mathrm{mm/s}$.
- For a thermal gas at a temperature T, the width of the velocity distribution can be estimated from the thermal energy: $\sqrt{k_{\mathrm{B}}T/m}$. For a temperature as high as $200\,\mathrm{nK}$, it is around $4\,\mathrm{mm/s}$.

Both of these estimated widths are smaller than the width of the velocity class that the Raman process addresses, therefore the entire momentum distribution of the cloud will be affected by these processes. If one wishes to resolve this velocity width, one needs to reduce the effective Rabi frequency so that $\hbar\Omega_{\mathrm{R}}/k_{\mathrm{r}}$ is below the width of the velocity distribution.

It is to be noted that the optical accordion described here is slightly different from the one providing the 2D confinement because we need here to have two beams with orthogonal polarisations. We tried to find the minimal modifications to add to the scheme of 2.2.2.1 in order to meet this requisite. For example, the two mirrors M6 and M7 are necessary in order to vary the angle θ_2 when displacing mirror M5.

Moreover, the optical paths of the two independent set-ups have been built on the experiment so that their length is approximately the same, with a few centimeters precision. This is to keep the DMD approximately on focus on the atoms when switching from one to the other configuration. A finer adjustment has then to be made, as later explained in 3.2.2.

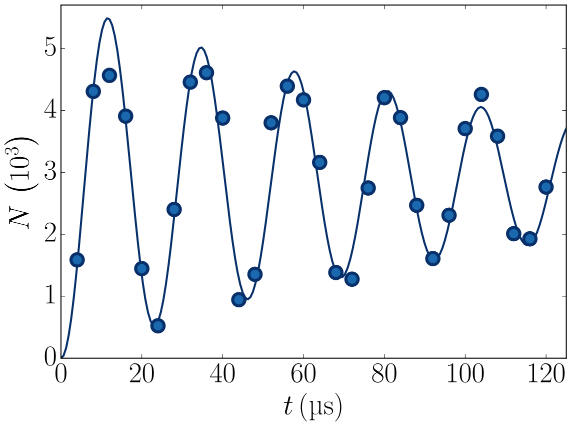

Figure 3.4: A Rabi oscillation with the Raman beams. A small cloud of radius 5 µm in the $F = 1, m_F = 0$ state is illuminated during a time t with the Raman beams. The number of atoms transferred in $F = 2, m_F = 0$ is measured. The results are fitted with an exponentially attenuated squared sine function. The fitted Rabi frequency is $\Omega_{\mathrm{R}} = 2\pi \cdot 21.7(2)\,\mathrm{kHz}$, and the decay time of the amplitude is $\gamma^{-1} = 110(10)\,\mu\mathrm{s}$.

The values of the focal lengths of the different lenses have been chosen so that the illuminated region is slightly larger than the atomic clouds we work with, and so that the Rayleigh length of the beams at the level of the accordion is the largest possible. Indeed, the two beams follow paths with a different length in the accordion (several centimetres of difference). In order to have the pattern of the DMD on the two beams overlapping properly on the atoms, we need the Rayleigh length z_{R} to be large compared to the difference of optical path. We managed to have $z_R \approx 7\,\mathrm{cm}$, which is on the same order as the difference of path lengths. It is sufficient to have a very good overlap between the DMD patterns of the two beams.

A last detail worth to be noted is that the accordion reverses one beam with respect to the other. The region on the atoms that will be illuminated by both beams will be the intersection of the DMD pattern with its mirror reflection along a given axis.[1] For simplicity we will restrict to patterns that are symmetric with respect to this axis.

3.2 RAMAN TRANSITIONS WITHOUT MOMENTUM TRANSFER

We characterize here the possibilities of our set-up in the configuration of co-propagating beams.

3.2.1 *Measuring Rabi oscillations*

We prepare a small atomic sample in a disk of radius 5 µm and in the state $F = 1, m_F = 0$. During a time t we shine the Raman beams on the

---

[1] The symmetry axis is the vertical axis on the absorption images that are shown in this thesis.

entire sample by having all the pixels of the DMD on. We image and count the atoms in $F = 2$ while varying the illumination time, as shown on Fig. 3.4. The data is fitted with a sine function whose amplitude decays exponentially: $x \mapsto a + a\left[2\sin^2(\Omega t/2) - 1\right]\exp(-\gamma t)$. We can discuss the value of the fitted parameters:

- The frequency of this oscillation is, on this particular example, $\Omega_{\mathrm{R}} = 2\pi \cdot 21.7(2)\,\mathrm{kHz}$. We estimate the powers of the two Raman beams to be 15 and 20 mW. For the latter, only 15% of the light has the proper frequency due to the EOM. With these values, equation 3.5 gives a Rabi frequency on the order of $2\pi \cdot 25\,\mathrm{kHz}$, which is on the same order of magnitude as the measured frequency.

- At short times, the amplitude of the oscillation coincides with the total atom number, demonstrating that we are able to perform a full rotation of the collective atomic spin. We can check this by performing a π-pulse with the Raman beams and subsequently performing a π-pulse with the microwave. In that case, we always measure a number of atoms compatible with zero, within the noise of our imaging system.

- The decay of the oscillation is fitted to be $\gamma^{-1} = 110(10)\,\mu\mathrm{s}$. We attribute this decay to inhomogeneous broadening due to the non-uniformity of the Raman beams. On top of the Gaussian shape of the beams, which has little influence on a cloud of 5 µm of size, there are spatial intensity fluctuations that induce slightly different Rabi frequencies on different parts of the cloud. The Rabi oscillations of the whole cloud thus has an inhomogeneous dephasing that leads to a damping. With $\gamma^{-1} = 110(10)\,\mu\mathrm{s}$, this means that the statistical distribution of the Rabi frequency over the whole cloud would have a standard deviation on the order of $10 - 20\%$ of its average value. This is compatible with the intensity profile of the Raman beams that we measure. We also measured γ^{-1} when increasing the power of the Raman beams, and we found that it increases proportionally to the Rabi frequency Ω_{R}, which is consistent with this interpretation.

Since we want to use the Raman beams to perform pulses of less than 2π, these measurements show that this tool is sufficient to accomplish this task in a reliable manner – at least on a small region of space.

For completeness we have checked that the Raman beams do not transfer the atoms to another state than $F = 2, m_F = 0$. In order to do that, we performed a Stern-Gerlach experiment with an expansion of the cloud during a few milliseconds in the presence of a vertical magnetic field gradient around 30 G/cm. The Zeeman states separate according to the value of the product $g_F m_F$ and we image them with an auxiliary horizontal imaging. No atoms have been detected in the states other than $F = 2, m_F = 0$, as far as the sensitivity of this imaging system allow us – several tens of atoms over 10^4.

Finally, it is important to mention that the two set-ups that perform spin manipulations between the hyperfine states of ${}^2S_{1/2}$ – the microwave and the Raman beams – are not locked in phase. This means that performing

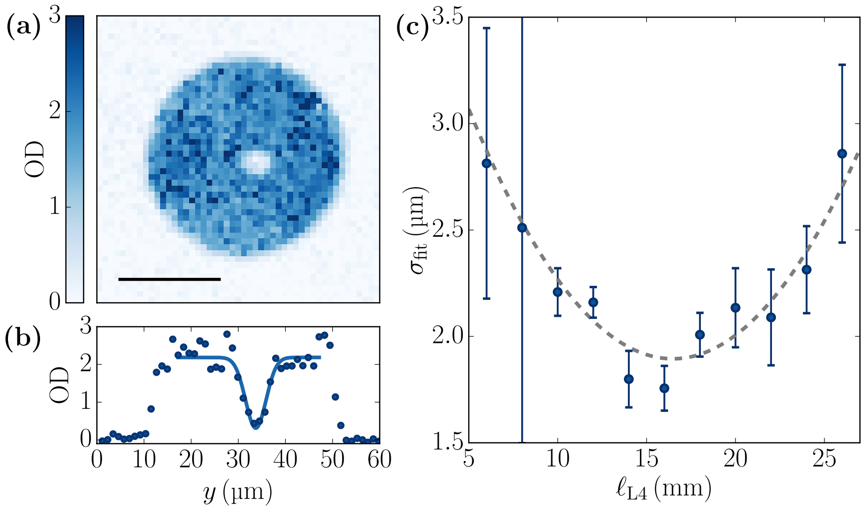

Figure 3.5: Focusing the DMD of the Raman beams on the atoms. (a): We transfer the atoms with the Raman beams to the $F = 2, m_F = 0$ state uniformly, except on a small region selected with the DMD. The image is the average of two experimental realisations. The horizontal black line represents 20 µm. (b): The density profile of this region is fitted with a 1D inverted Gaussian shape and the size along the y-direction $\sigma_{\rm fit}$ is extracted. On this example, $\sigma_{\rm fit} = 1.8(1)$ µm. (c): We plot $\sigma_{\rm fit}$ as a function of the position $\ell_{\rm L4}$ of lens L4. The position where a minimum is reached is where the DMD is on focus. With a parabolic fit of the data points we determine that this focus is at $\ell_{\rm L4} = 16.5(5)$ mm. The origin of this axis is arbitrary, and the important quantity to extract from the fit is the ratio between the error bar of this minimum and the focal length of the lens, here 400 mm.

consecutive rotations with one and the other in the same sequence does not produce accurately the same spin state, except if at least one of the rotations corresponds to a multiple of a π-pulse.

3.2.2 *Focus and size of the DMD*

The surface of the DMD has to be focused on the atomic plane with precision so that the patterns we imprint are as sharp as possible. The resolution of the microscope objective is around 1 µm, and the associated depth of field is on the order of several micrometers. We focus the DMD by displacing one of the lenses that affects only this element – displacing the microscope objective itself would put the two other DMDs out of focus. The lens labelled L4 on Fig. 3.3 is mounted on a motorized translation stage[2] and we search for its optimal position.

We prepare a cloud in the shape of a disk of radius 20 µm and in the $F = 1, m_F = 0$ state. On the DMD for the Raman beams we have all the pixels on, except a small region that corresponds to a disk of radius around 2 µm on the atoms. We apply a Raman pulse of 10 µs to transfer the atoms to the $F = 2, m_F = 0$ state and image these atoms for various positions $\ell_{\rm L4}$ of the

---

[2] Newport, CONEX-AG-LS25-27P

lens. If the DMD is on focus, the density distribution we get is a full disk with a sharp hole corresponding to the 'off' pixels. If the DMD is slightly out of focus, this dark region will be more blurry and the hole in the density distribution will be at the same time less deep and broader.

On Fig. 3.5a is displayed one of the density distribution that we obtain, averaged over two experimental realisations. We cut this density distribution along one axis or the other and get a profile such as the one presented on Fig. 3.5b. We fit the central region of this profile with a Gaussian function $x \mapsto c_{\text{fit}} - a_{\text{fit}} \cdot \exp\left[-(x - x_0)^2/(2\sigma_{\text{fit}}^2)\right]$, where c_{fit}, a_{fit}, x_0 and σ_{fit} are free parameters, with $a_{\text{fit}} > 0$ to account for the central depletion of atoms.

The values of σ_{fit} as a function of ℓ_{L4} are shown on Fig. 3.5c, and they are fitted with a parabola. The size of the density hole has a clear minimum around 16 mm, which indicates the position of the focus of the DMD. We also note that the values of the amplitudes a_{fit} present a maximum at this position.

With this analysis, we are able to determine the position of the lens L4 to focus the DMD with a precision better than 0.5% of the focal length of this lens. This also represents a displacement below 2 µm of the focus of the pattern of the atoms, which is lower than the Rayleigh length of the beam.

In order to imprint patterns with the proper size on the atoms we calibrate the effective size of the pixels of the DMD. We display on the DMD a striped pattern where alternatively $N_{\text{pix}}/2$ pixels are on and $N_{\text{pix}}/2$ pixels are off. The whole pattern has a periodicity of N_{pix} pixels. We perform a short Raman pulse of 4 µs with such a pattern, we measure the density distribution of the transferred atoms, and we obtain a picture such as presented on Fig. 3.6a. Note that the stripes appear at 45° because the axes of the DMD array are oriented with this angle compared to the axes of the camera. When averaging this density distribution along the $x + y$ direction, we can fit the profile we get with a sinusoidal function, as displayed on Fig. 3.6b. The period d_{cam} of the sine function indicates the effective size of the pixels on the atoms. For more precision we do the same measurement by varying the periodicity N_{pix}. The results are shown on Fig. 3.6c, and they are fitted with a linear function, whose slope indicates that the effective pixel size of one pixel of the DMD represents 0.36(1) µm. The real size of a DMD pixel is 13.68 µm, which means that we have a magnification of 1/38(1), compatible with the expected value of 1/37.5.

3.2.3 *Local spin transfers*

According to the previous calibration measurements, we know that we are able to create a very rich and precise spin landscape in our atomic sample:

- We control the regions where we manipulate the spin with a spatial precision around 1 µm.
- In the selected regions we can bring the atomic spin in a superposition $c_1 |1\rangle + c_2 |2\rangle$ of the two hyperfine states $|1\rangle \equiv |F = 1, m_F = 0\rangle$, and $|2\rangle \equiv |F = 2, m_F = 0\rangle$ with any relative weights $|c_1|^2$ and $|c_2|^2$ between the two components.

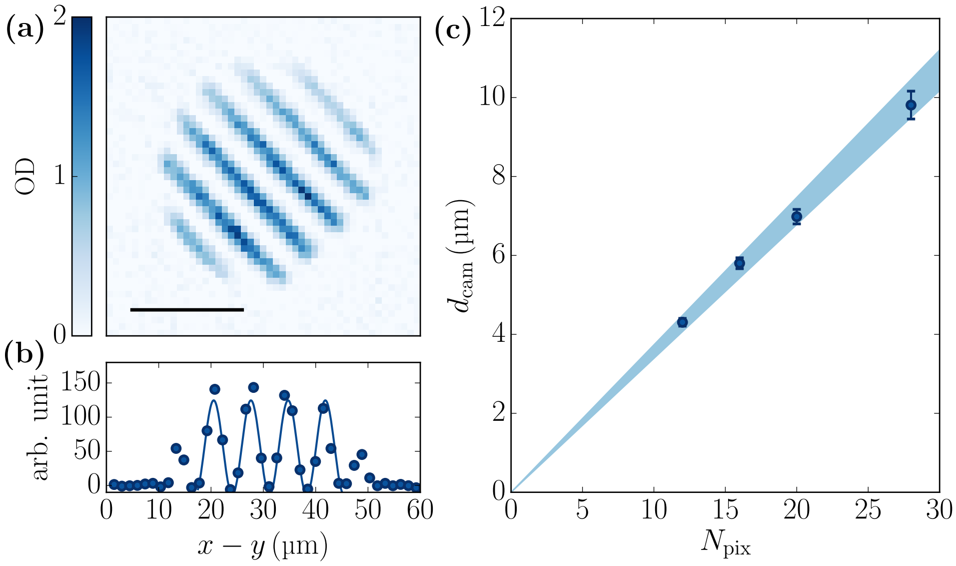

Figure 3.6: Calibration of the effective size of the DMD. (a): A striped pattern with an integer number of DMD pixels is shone on the atoms. We measure the density distribution of transferred atoms by averaging five experimental realisations. On the image shown here, the periodicity of the pattern is $N_{\mathrm{pix}} = 20$. The horizontal black line represents 20 µm. (b): This distribution is summed along the axis of the stripes, and the obtained signal is fitted with a sine function. The fitted periodicity is here $d_{\mathrm{cam}} = 7.0(2)$ µm. (c): The periodicity d_{cam} as a function of N_{pix} is plotted and fitted with a linear function. The slope is 0.36(1) µm.

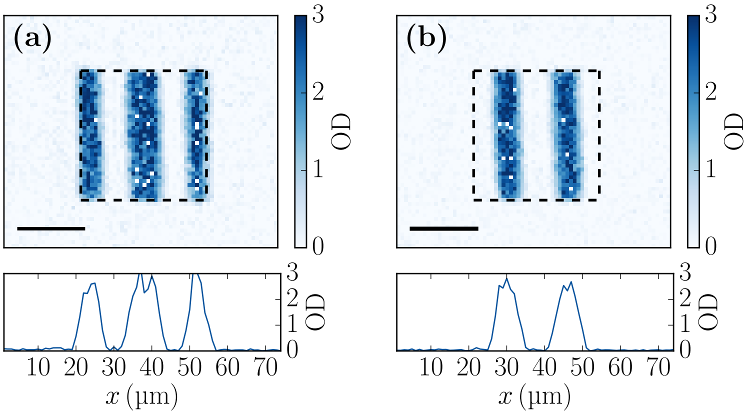

Figure 3.7: Spatially-selected π-pulse with the Raman beams. The atoms are initially in a square box represented with the dashed lines, and in the $F = 1, m_F = 0$ state. We select with the DMD a region in the shape of two stripes of width 8 µm and with a distance of 18 µm between their centres. The Raman beams are shown to induce a π-pulse on this region. (a) Average of two images of the atoms in the $F = 1, m_F = 0$ state. (b) Average of two images of the atoms in the $F = 2, m_F = 0$ state. On both pictures, the horizontal black line represents 20 µm.

- We can even spatially vary the weight of this superposition by displaying on the DMD an image where the local fraction of mirrors turned on is not simply 0 or 1. This is possible because the effective size of a pixel is below the resolution of our imaging system. The spin state of the cloud is then $c_1(\boldsymbol{r}) |1\rangle + c_2(\boldsymbol{r}) |2\rangle$, where $c_{1,2}(\boldsymbol{r})$ vary over the cloud. The relative phase between c_1 and c_2 is the same over the whole atomic cloud since it is fixed by the relative phase between the Raman beams. I will not use this feature in this thesis, but it may be very useful in the future.

We illustrate the high flexibility and precision of our spatially-resolved Raman beams on Fig. 3.7. On the DMD, an image with two stripes of width of 8 µm on the atoms and whose central axes are distant from 18 µm. We perform a π-pulse with the Raman beams, and we can either directly image the atoms in $F = 2$ (see panel b), or add a π-pulse with the microwave to image the atoms in $F = 1$ (see panel a).

We observe that the spatial selectivity of the Raman beams is very precise and the π-pulse is well controlled on the whole selected region: on Fig. 3.7a, the atomic density in the region of the two stripes is zero within the accuracy of the absorption imaging, and on Fig. 3.7b, we see that we transfer atoms only on the region of the two stripes.[3]

---

[3] The imaging is performed here with a very high atomic density, and the absorption images are saturating. The measured optical depths are therefore not reliable and can even diverge, which we see on the pixels displayed in white on the figure.

3.3 RAMAN TRANSITIONS WITH MOMENTUM TRANSFER

We now turn to the second configuration: the two polarisations of the Raman beams are separated with the optical accordion and they reach the atoms with a non-zero angle. The Raman transfer is thus accompanied with a momentum transfer.

3.3.1 *Calibrating the momentum transfer*

We start by optically calibrating the momentum transfer that we expect to occur on the atoms. In order to do that, we wish to measure the size of the lattice created by the two beams. However, the polarisation of the two beams are orthogonal and they do not interfere. And even if their polarisation were not perfectly orthogonal, the interference pattern would be a running one because of the frequency difference of the beams, so it would not be easy to image it.

We therefore block one of the polarisations before the fibre that mixes them (see Fig. 3.2) and we rotate the half wave plate right after the output of this fibre (see Fig. 3.3) so that light passes in both paths of the accordion. We then image the interference pattern with the camera. This camera is on focus with the atoms for the imaging light at 780 nm, but the chromatic shift due to the microscope objective, which is the largest shift we expect on this optical path, is estimated around 2 µm, which is much smaller than the Rayleigh length of the Raman beams on the atoms ($\approx 6\,\mathrm{mm}$).

Such an image is shown on Fig. 3.8a. We take its Fourier transform, as shown on Fig. 3.8b, and we determine the wave vector k_r of the peak corresponding to the periodic modulation. We vary the position of the translational stage on which the mirror of the accordion (labelled M5) is mounted and extract the velocity $\hbar k_\mathrm{r}/m$ associated with the momentum transfer that we expect on the atoms. We also measure with a ruler the distance d_b between the two beams right after the accordion for all the positions of the stage. Fig. 3.8c presents the measurements of the velocity $\hbar k_\mathrm{r}/m$ as a function of the distance d_b. Following equation 2.6, we expect the velocity transfer to be

$$\frac{\hbar k_\mathrm{r}}{m} = \frac{2\hbar k_\mathrm{R}}{m}\left(1+\frac{4f_\mathrm{eff}^2}{d_\mathrm{b}^2}\right)^{-1/2}, \tag{3.17}$$

where f_eff is the effective focal length of the optical system composed of the two last lenses (L4 and L5) and the microscope objective. Numerically we have $f_\mathrm{eff} = 20\,\mathrm{mm}$. This equation is plotted on the figure and the agreement with the optical measurements is very good. The two last points may deviate because of the aberrations of the microscope objective since the two beams are hitting the microscope very near its edges. The first one also deviates because the theoretical size of the interference fringes $\lambda_\mathrm{R}/[2\sin(\theta_2/2)]$ becomes on the same order as the size of the beams, and the Gouy phase of these beams also has to be taken into account, which modifies the interference pattern and increases its average wave vector k_r.

The velocity kick that we can give to the transferred atoms therefore ranges from 1 to 3.5 mm/s. An important quantity to compare these values with is the

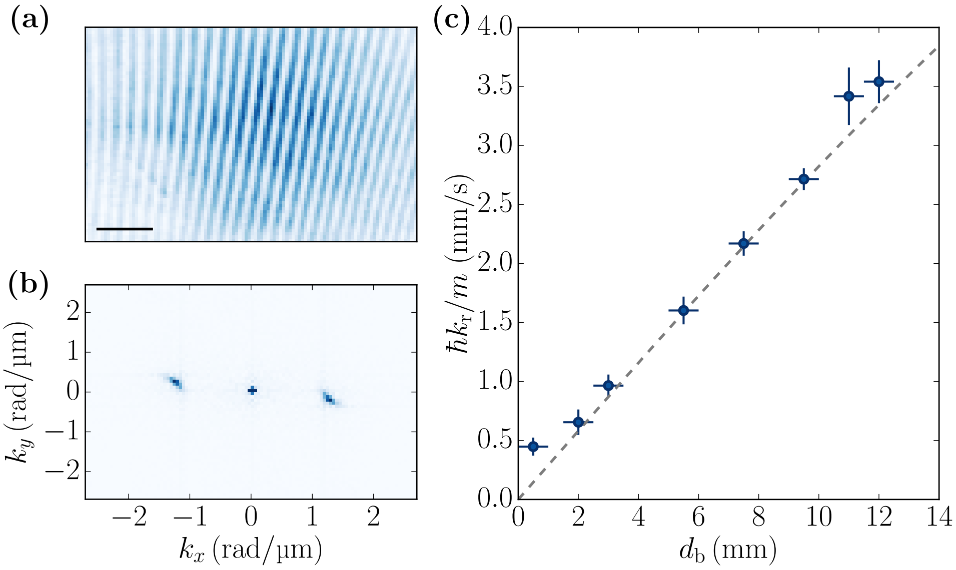

Figure 3.8: Calibration of the momentum transfer. (a): The interference pattern formed by one laser frequency passing through the two paths of the accordion is imaged on the camera. (b): We compute its Fourier transform where the two peaks on both side of the central one indicate the wave vector of the lattice. (c): We infer the velocity transfer that the atoms should experience as a function of the distance between the two beams after the accordion. The grey dashed line is what we expect following equation 3.17, in good agreement with the measurements.

speed of sound, which is in our case on the order of $1 - 2\,\mathrm{mm/s}$ [113]. With our set-up, we can therefore go from the regime where the transferred atoms get a subsonic velocity kick to the regime where this kick is supersonic. This provides a precise tool for probing the superfluid behaviour of a cloud of atoms [130].

3.3.2 *Local spin transfers with a momentum kick*

We can also test the action of the Raman beams on the atoms in this configuration with a momentum transfer. I describe here a first experiment and extract the relevant quantities that describe it. These are preliminary tests for a future project. I only give here a few elements to understand the phenomena at play.

We prepare a cloud of atoms in a disk-shaped box potential (radius $20\,\mu\mathrm{m}$) in the state $F = 1, m_F = 0$ and illuminate a small disk of radius $3\,\mu\mathrm{m}$ with the Raman beams in the centre of the cloud. We induce a pulse shorter than a π-pulse and approximately 300 atoms are transferred to the state $F = 2, m_F = 0$. We vary the duration t of the subsequent evolution and image the atoms in $F = 2$. A few pictures of this evolution are shown on Fig. 3.9a. These atoms move in the x direction, reach the edge of the box potential and bounce on it to go back in the opposite direction. We observe three of these bounces until the radial expansion of the transferred atoms is too large and the optical density is too low to detect them properly. This bouncing behaviour is expected because the kinetic energy transferred to the atoms $2\hbar^2 k_\mathrm{r}^2/m$ is lower than $k_\mathrm{B} \cdot 50\,\mathrm{nK}$ and the height of the box potential is on the order of several times $k_\mathrm{B}T$, where T is the temperature of the gas. This temperature is typically between 50 and $100\,\mathrm{nK}$. The transferred atoms thus do not have enough energy to cross the potential barrier of the box.

For each duration t we find the position of the centre of mass x_c of the transferred atoms as well as the spread σ_x of these atoms in the x direction. These quantities are presented on Fig. 3.9b and c. The evolution of the position x_c is fitted with a triangular function:

$$t \mapsto a_x \left[\frac{1}{2} - \left| 2 \left\{ \frac{t - t_0}{b_x} \right\} \right| \right], \tag{3.18}$$

where $\{x\}$ represents the fractional part of the real number x and a_x, b_x and t_0 are free parameters. The fitted amplitude is $a_x = 38(2)\,\mu\mathrm{m}$, compatible with the diameter of the full box. The velocity that we extract is $a_x/b_x = 0.94(10)\,\mathrm{mm/s}$.

Unfortunately, these data have been taken before calibrating the momentum transfer, therefore we cannot compare the value of the velocity a_x/b_x with the expected velocity. We will take these measurements again very soon in order to perform this comparison.

The radial expansion of the cloud can be fitted with a branch of hyperbola: $t \mapsto \sqrt{a_\sigma^2 t^2 + \sigma_0^2}$, where a_σ and σ_0 are free parameters. We exclude from the fit the points corresponding to the bounces. We find $a_\sigma = 0.13(2)\,\mathrm{mm/s}$ and $\sigma_0 = 2.9(5)\,\mu\mathrm{m}$.

The measured value of a_σ is well below the value that would be expected for the expansion of an isolated ensemble of atoms. Indeed, the total energy E_tot

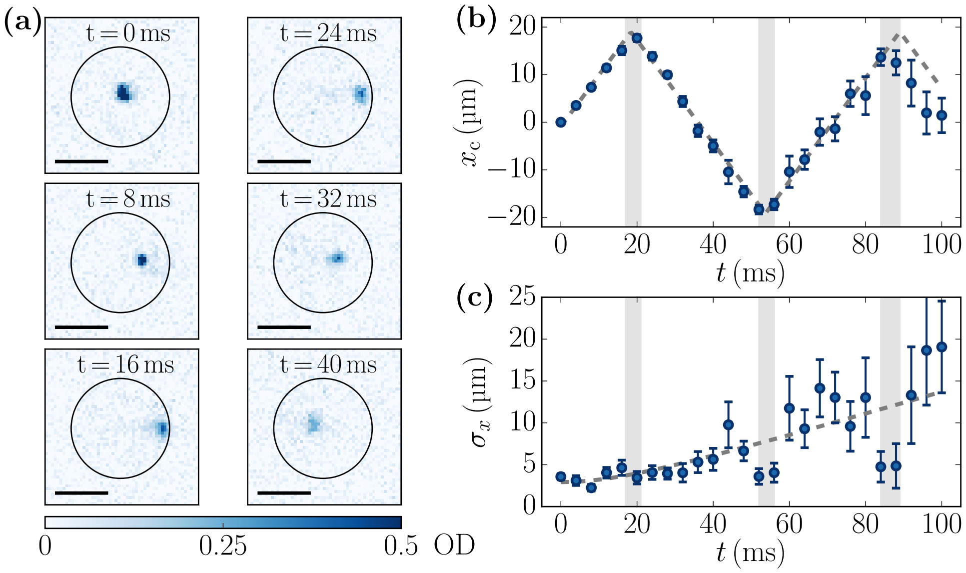

Figure 3.9: Evolution of the atoms transferred from $F = 1$ to $F = 2$ with a momentum transfer. (a) From top to bottom and from left to right: Average of a few images after a variable evolution duration t from 0 to 40 ms. The atoms move to the right of the picture and bounce on the box potential (represented by the black circle). This box is filled with atoms in $F = 1$ which are not resonant with the imaging beam. For each duration t we extract the position of the centre of mass x_c and the spread σ_x along the x direction. (b): Evolution of x_c with the evolution duration. The data points are fitted with a triangular function (dashed grey line) whose slope gives the velocity of the cloud. We get a velocity of 0.94(10) mm/s. The shaded areas mark the moments when the atoms bounce on the edge of the box. (c): Evolution of the spread σ_x. This spread is increasing with time, except during the bounces (shaded areas) where the spread is reduced. It is fitted with a branch of hyperbola (dashed grey line).

of an isolated gas would be converted into kinetic energy after the expansion, leading to an expansion

$$\sigma_x^2(t) \approx \sigma_x^2(t=0) + \frac{2E_{\mathrm{tot}}t^2}{m}. \tag{3.19}$$

An estimate of a lower bound of $\sqrt{2E_{\mathrm{tot}}/m}$ is obtained by taking into account only the interaction energy. It gives 0.1 m/s, which is much higher than the measured a_σ.

Here indeed, the atoms interact with the atoms in $F = 1$ that fill the box potential. These interactions are described by the inter-species scattering length a_{12}, while the interactions between atoms in the same hyperfine state are described by the scattering lengths a_{11} and a_{22}. These parameters are estimated to be $a_{11} = 100.9(1)a_0$ [131], $a_{22} = 94.6(0.2)a_0$ [132], and $a_{12} \approx 98.9a_0$ [133]. In this particular case, $a_{11}a_{22} < a_{12}^2$, which means it is energetically favourable to have the two species spatially separated rather than overlapping. These two species are said to be immiscible. The presence of atoms in $F = 1$ all around the transferred atoms in $F = 2$ intuitively reduces the expansion rate of these atoms.

The study of this phenomenon with a more quantitative approach still has to be made and it is a project of the team for the near future.

3.4 CONCLUSION

In this chapter I have described and characterised the Raman set-up that I have developed during my thesis. Two Raman beams with proper frequencies and polarisation are produced to perform transitions between the two hyperfine states of the ground level of the atoms with a very good precision. The intensity of the two beams is shaped thanks to a DMD to select with a high resolution (≈ 1 µm) the atoms that will undergo these transitions. The direction of propagation of the two beams can be chosen:

1. Either they propagate in the same direction and the atoms experience no momentum transfer.
2. Or they reach the atoms with a relative angle than can be varied continuously thanks to an optical accordion. In that case they induce a momentum transfer on the atoms. This transfer corresponds to a velocity kick that can be chosen below or above the speed of sound.

This new experimental tool opens many possibilities in the way we manipulate the atoms. For example it is used in Chapter 6 to measure the first correlation function of the 2D Bose gas. It is also an excellent tool to create binary mixtures of two hyperfine states with a versatile spatial distribution. This may allow us to study interesting properties of these mixtures, as developed in the conclusion of this thesis.

Part II

MEASURING THE FIRST CORRELATION FUNCTION OF THE 2D BOSE GAS

4

THEORETICAL CONSIDERATIONS ON THE FIRST CORRELATION FUNCTION

Phase transitions are at the heart of many physical systems such as the transition of matter from gaseous to liquid to solid phases. This framework also describes magnetic systems, superconducting materials, or the percolation of disordered systems [134, 135]. All these examples answer in a different manner the following question: How does a spatially extended system go from a disordered to an ordered state when an external parameter (e.g. magnetic field, temperature) is changed? Interestingly, in spite of the rich variety of systems undergoing phase transitions, all of them can be grouped into a few universality classes [136, 137]. For second-order transitions, these classes are characterized by critical exponents that describe their behaviour at the vicinity of their critical point [138]. One important aspect is that the physics of phase transitions does not depend on the details of their description, but rather on the general features of the models they rely on.

In this respect, the dimensionality of a physical system plays an important role in the way this system can be ordered [139]. While models in three and higher dimensions can display infinitely long-range phase ordering at non-zero temperatures (for cold atom systems see [48, 140]), the physics of low-dimensional systems is different. For example, infinite systems with local interactions cannot have long-range ordering at non-zero temperatures if their order parameter is continuous. This statement is called the Mermin-Wagner-Hohenberg theorem [141, 142].

However, in two dimensions there are phase transitions that lead to a quasi-long range ordering, such as the Berezinskii–Kosterlitz–Thouless (BKT) phase transition [25, 26]. Such a phase transition, contrary to many other ones, is a topological phase transition, for reasons that I detail in this chapter. It is also an infinite order phase transition, meaning that all the derivatives of the thermodynamic quantities are continuous at the critical point. This phase transition describes 2D systems such as the XY-model [26], the Coulomb gas [143] or the two-dimensional Bose gas at low temperatures [111].

Many aspects of this BKT transition have been explored with 2D atomic Bose gases, such as the appearance of a quasi-condensate phase where the density fluctuations are suppressed and a pre-superfluid state is observed [144–146]. The proliferation of vortices around the critical temperature has also been observed, confirming the nature of this phase transition [37, 147].

An important feature of the BKT transition that still needs to be observed is the behaviour of the first-order correlation function, $g_1(\boldsymbol{r})$. This function is central in the understanding of the transition, as we will see.

This chapter aims at presenting the main properties of this correlation function of several 2D systems across the BKT transition. We first consider the case of infinite systems and focus on three important models: the XY- model for magnetic systems, the ideal Bose gas and the weakly interacting Bose gas. Then we turn to the various effects that one needs to take into account when studying 2D systems produced in a laboratory that depart from ideal theoretical systems: their out-of-equilibrium character, their spatial inhomogeneity and their finite size.

4.1 THE FIRST-ORDER CORRELATION FUNCTION OF INFINITE 2D SYSTEMS

In order to understand the important features of the first-order correlation function of a two dimensional Bose gas I separate the theoretical analysis in three steps. First I present briefly the XY-model that grasps the physics of the BKT transition. Then I explain the case of non-interacting bosons in two dimensions to introduce with this simple example the notations and concepts that are useful for such a system. Finally I develop the case of interacting bosons on an infinite plane.

4.1.1 *The XY-model and the BKT transition*

4.1.1.1 *Definition of the model*

The XY-model consists in a two-dimensional array of classical arrows whose orientation stays in this plane. We consider a system of size $L \times L$ covered with a square array of arrows separated by the distance a, with $a \ll L$. The orientation of an arrow at site i located in (x_i, y_i) is given by an angle $\varphi_i = \varphi(x_i, y_i)$. Each arrow interacts with its nearest neighbours only and wants to align with them. The Hamiltonian of the system is therefore

$$H_{\mathrm{XY}} = J \sum_{\langle i,j \rangle} \left[1 - \cos(\varphi_i - \varphi_j)\right] \tag{4.1}$$

$$= 2J \sum_{\langle i,j \rangle} \sin^2\left(\frac{\varphi_i - \varphi_j}{2}\right), \tag{4.2}$$

where $J > 0$ is the strength of the interactions and the notation $\langle i, j \rangle$ designates the pairs of nearest neighbour sites. We consider periodic boundary conditions here for simplicity. The ground state of this Hamiltonian is obtained when all the arrows have the same orientation, and its energy is null. This ground state is infinitely degenerate, as the common orientation of the arrows can be arbitrarily chosen between 0 and 2π.

There are two types of excitations that we will consider in the following: phonons, which are the excitations with the lowest energy, and vortices, whose contribution matters at higher temperatures.

4.1.1.2 *High-temperature behaviour and lack of ordering*

I summarise here the high-temperature development of the model. More detailed calculations can be found for example in [148, 149].

In the high temperature limit, the interaction energy is not strong enough to keep neighbouring arrows aligning one with another. Therefore we expect to have no long-range ordering. More precisely, the correlation between two spins at sites i and j is $g_1(i,j) = \langle \exp\left[\mathrm{i}(\varphi_i - \varphi_j)\right]\rangle$, where $\langle \cdot \rangle$ denotes the statistical average in the canonical ensemble. We then have

$$g_1(i,j) = \frac{1}{\mathcal{Z}} \int_0^{2\pi} \prod_k \mathrm{d}\varphi_k \exp\left[\mathrm{i}(\varphi_i - \varphi_j)\right] \prod_{\langle i',j'\rangle} \exp\left[-\frac{2J}{k_\mathrm{B}T} \sin^2\left(\frac{\varphi_{i'} - \varphi_{j'}}{2}\right)\right], \tag{4.3}$$

where $\mathcal{Z}$ is the partition function of the system.

At high temperature, $J \ll k_\mathrm{B}T$ and one can expand the exponentials in the product at first order in $J/(k_\mathrm{B}T)$:

$$\exp\left[-\frac{2J}{k_\mathrm{B}T} \sin^2\left(\frac{\varphi_{i'} - \varphi_{j'}}{2}\right)\right] \approx 1 - \frac{2J}{k_\mathrm{B}T} \sin^2\left(\frac{\varphi_{i'} - \varphi_{j'}}{2}\right). \tag{4.4}$$

When developing the product over the links $\langle i', j'\rangle$, we get a sum over all subsets S of links of the system:

$$\prod_{\langle i',j'\rangle} \exp\left[-\frac{2J}{k_\mathrm{B}T} \sin^2\left(\frac{\varphi_{i'} - \varphi_{j'}}{2}\right)\right] = \sum_{\{S\}} \prod_{\{i',j'\} \in S} \left[-\frac{2J}{k_\mathrm{B}T} \sin^2\left(\frac{\varphi_{i'} - \varphi_{j'}}{2}\right)\right], \tag{4.5}$$

where $\{S\}$ denotes the set of all the subsets S of links in the system.

Many of these terms average to zero when integrated over the angles φ_k. The terms that do not average to zero are terms from the subsets S that involve links connecting sites i and j. Since $J/(k_\mathrm{B}T) \ll 1$, the main contributions come from the subsets S with the least amount of links. The leading term then has r/a links, where r is the distance between sites i and j.

Finally, we have the scaling

$$g_1(i,j) \propto \left(\frac{2J}{k_\mathrm{B}T}\right)^{r/a} \tag{4.6}$$

$$\propto \exp\left[-\frac{r}{a} \ln\left(\frac{k_\mathrm{B}T}{2J}\right)\right]. \tag{4.7}$$

The correlation between two arrows separated by a distance r thus decays exponentially with a correlation length ℓ given by

$$\ell = \frac{a}{\ln\left(\frac{k_\mathrm{B}T}{2J}\right)}, \tag{4.8}$$

which is smaller than the distance between two arrows as soon as the condition $k_\mathrm{B}T > 2J\mathrm{e}$ is met, where $\mathrm{e} \approx 2.718\cdots$.

4.1.1.3 *Low-temperature behaviour and quasi-long range order*

I summarise here the low-temperature limit of the model. More detailed calculations can be found in [149, 150]. In this limit, only phononic modes are considered and their thermodynamics is derived to obtain the correlation function.

Let us consider the system in the low-temperature limit: $k_{\mathrm{B}}T \ll J$ so that two neighbouring arrows have almost the same orientation. The Hamiltonian can be written as

$$H_{\mathrm{XY}} = \frac{J}{2} \sum_{\langle i,j \rangle} (\varphi_i - \varphi_j)^2. \tag{4.9}$$

The two-dimensional sequence of angles $\{\varphi(x_i, y_i)\}$ can be decomposed in a cosine and sine Fourier series of respective amplitudes $\tilde{\varphi}_{c;k_x,k_y}$ and $\tilde{\varphi}_{s;k_x,k_y}$, where k_x, k_y are integers between 0 and L/a. However the quantities $\varphi(x_i, y_y)$ are real, therefore we can restrict k_x to the positive integers.

The Hamiltonian given by equation 4.9 is diagonal in the Fourier basis:

$$H_{\mathrm{XY}} = \frac{J}{2} \sum_{\substack{k_x=0,\\ k_y=-L/2a}}^{L/2a} \boldsymbol{k}^2 \left(|\tilde{\varphi}_{c;k_x,k_y}|^2 + |\tilde{\varphi}_{s;k_x,k_y}|^2 \right), \tag{4.10}$$

where we have defined the vector $\boldsymbol{k} = (k_x, k_y)$. Each mode (k_x, k_y) with $k_x > 0$ is independent from the others. The value of their amplitude is sampled according to a Boltzmann distribution:

$$\mathcal{P}(\tilde{\varphi}_{c,s;k_x,k_y}) \propto \exp\left(-\frac{J\boldsymbol{k}^2}{k_{\mathrm{B}}T} |\tilde{\varphi}_{c,s;k_x,k_y}|^2 \right), \tag{4.11}$$

where $\tilde{\varphi}_{c,s;k_x,k_y}$ is a short notation that can refer to $\tilde{\varphi}_{c;k_x,k_y}$ or $\tilde{\varphi}_{s;k_x,k_y}$. The amplitudes are therefore independent Gaussian variables. It is then easy to compute interesting quantities of the model.

For example one can obtain the average value of the mismatch between two arrows $\varphi(\boldsymbol{0})$ and $\varphi(\boldsymbol{r})$. The sum over the modes (k_x, k_y) is replaced by an integral, which is valid when $L/a \gg 1$:

$$\left\langle [\varphi(\boldsymbol{0}) - \varphi(\boldsymbol{r})]^2 \right\rangle = \frac{k_{\mathrm{B}}T}{2\pi^2 J} \int_0^{1/a} \mathrm{d}^2\boldsymbol{k} \frac{1 - \cos(\boldsymbol{k}\cdot\boldsymbol{r})}{\boldsymbol{k}^2}. \tag{4.12}$$

One can also determine the first-order correlation function $g_1(\boldsymbol{r})$, defined as

$$g_1(\boldsymbol{r}) = \langle \exp\left[\mathrm{i}(\varphi(\boldsymbol{0}) - \varphi(\boldsymbol{r}))\right] \rangle. \tag{4.13}$$

Because the amplitudes of the Fourier modes are independent Gaussian variables, we get:

$$\begin{aligned} g_1(\boldsymbol{r}) &= \exp\left(-\frac{1}{2} \left\langle |\varphi(\boldsymbol{0}) - \varphi(\boldsymbol{r})|^2 \right\rangle \right) & (4.14)\\ &= \exp\left(-\frac{k_{\mathrm{B}}T}{4\pi^2 J} \int \mathrm{d}^2\boldsymbol{k} \frac{1 - \cos(\boldsymbol{k}\cdot\boldsymbol{r})}{\boldsymbol{k}^2} \right). & (4.15) \end{aligned}$$

Until this point, the method would be the same for systems of spins in a space of any dimensionality. The following would differ depending on this dimension, because the integral that appears in equation 4.12 behaves differently in different dimensions.

In two dimensions, the computation of this integral gives

$$\int_0^{1/a} \mathrm{d}^2\boldsymbol{k} \frac{1 - \cos(\boldsymbol{k}\cdot\boldsymbol{r})}{\boldsymbol{k}^2} = 2\pi \ln\left(\frac{\boldsymbol{r}}{a} \right), \tag{4.16}$$

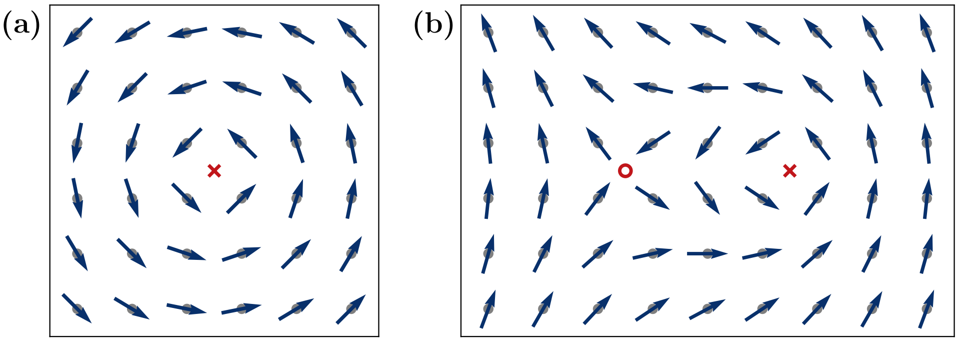

Figure 4.1: Representation of two important configurations of an array of arrows. (a): A vortex configuration. The centre of the vortex is indicated with the red cross. Here the arrows whirl counter-clockwise around this centre, and the vortex has a charge +1 (b): A pair vortex anti-vortex configuration. A vortex of charge +1 is centred around the red cross, and a vortex of opposite charge −1 is centred around the red circle.

which means that

$$g_1(\boldsymbol{r}) = \left(\frac{a}{\boldsymbol{r}}\right)^{\eta}, \tag{4.17}$$

with the exponent

$$\eta = \frac{k_{\mathrm{B}}T}{2\pi J}. \tag{4.18}$$

The correlation function goes to 0 as the distance $\boldsymbol{r}$ increases, but this decay is not as fast as an exponential decay as we had in the high temperature limit. This slow decay is called a quasi-long range order.

4.1.1.4 *Contribution of vortices*

In order to understand the connection between the high temperature limit where g_1 decays exponentially and the low temperature limit where g_1 decays as a power law, we need to take into account the role of vortices, which are topological defects. I present here the broad lines of their important role which give to the BKT transition its qualifying adjective 'topological'. More detailed discussions can be found in [26, 149, 150].

A vortex centred at the centre of the system is described by the orientation of the arrows:

$$\varphi(x_i, y_i) = \theta(x_i, y_i) + q\frac{\pi}{2}, \tag{4.19}$$

where $\theta(x_i, y_i)$ is the azimuthal angle of point (x_i, y_i) with respect to the centre of the system, and $q = \pm 1$ defines the sign of the charge of the vortex. An illustration of a vortex with charge $q = +1$ is presented on Fig. 4.1a.

The energy E_{v} of this configuration is

$$E_{\mathrm{v}} = \pi J \ln\left(\frac{L}{a}\right), \tag{4.20}$$

which depends on the size L of the whole system. Qualitatively, if this energy is larger than the thermal energy $k_\mathrm{B}T$, then it will not be favourable to form such a vortex and the system will only have phonons, as described in the low temperature limit. In the opposite case, vortices may form in the system, which will break the phase correlation between arrows located on opposite sides of the centre of the vortex.

More quantitatively, the proper thermodynamic quantity to consider is the free energy $F = E_\mathrm{v} - TS$ associated with a vortex. The centre of the vortex can be located at each site of the dual lattice of the system, which contains $(L/a)^2$ sites. The entropy associated with this random positioning is $S = 2k_\mathrm{B}\ln(L/a)$. We thus have

$$F = (\pi J - 2k_\mathrm{B}T)\ln\left(\frac{L}{a}\right). \tag{4.21}$$

The free energy changes sign at the temperature $T_\mathrm{c} = \pi J/(2k_\mathrm{B})$. There are then two different behaviours:

- $T < T_\mathrm{c}$: The free energy of one vortex is positive. It is then not favourable to create such a vortex, and the system keeps a quasi-long range order.
- $T > T_\mathrm{c}$: The free energy of one vortex is negative, and it is favourable to create at least one vortex. The quasi-long range order is destroyed.

This reasoning cannot grasp all the physics of the system, since it does not consider the interaction between vortices, nor between a vortex and a phonon. Moreover, only pairs of vortices with opposite charges can be created [148] to conserve the total angular momentum of the system. The physics associated to these pairs therefore needs to be described: whether two vortices of a pair stay close to one another or if they separate and act as two single vortices.

4.1.1.5 *Renormalization group*

A more complete approach relies on the renormalization group. I will not enter the details of the derivation, which can be found in various references [148, 149, 151, 152].

The idea is to separate the contribution of the phonons and the contribution of the pairs of vortices. The phononic part is described by the energy J as before, and the energy of the vortices is described by the energy of a pair of vortices $E_\mathrm{2v} = \pi^2 J/2$ and an interaction energy that depends on the position of all the vortices.

The renormalization group describes how this problem on a lattice of size a can be described by an equivalent problem on a lattice of larger scale a'. When performing this operation, the contribution of pairs of vortices whose distance is smaller than a' is inserted in the contribution of the phonons, and the energy J is modified to become J', which is smaller than J. The rest of the vortices has a contribution that is also modified, in particular the energy of a pair E_2v becomes E'_2v.

The process is summarized by the renormalization functions $f_{a,a'}$ and $g_{a,a'}$:

$$J' = f_{a,a'}(J, E_\mathrm{2v}) \tag{4.22}$$

$$E'_\mathrm{2v} = g_{a,a'}(J, E_\mathrm{2v}), \tag{4.23}$$

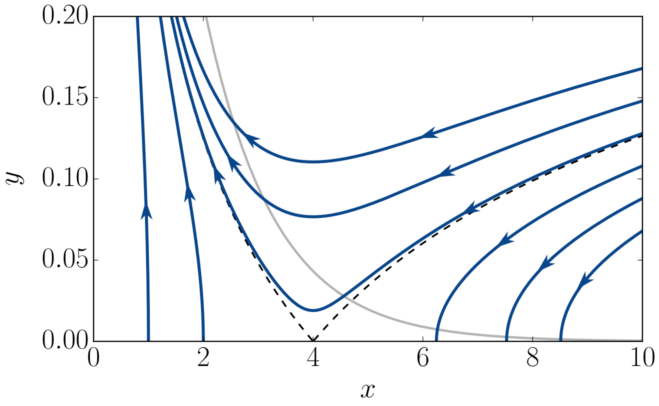

Figure 4.2: Renormalization flow of the equations 4.26 and 4.27. The solid blue lines indicate the trajectory of several initial points (x_0, y_0). The dashed black lines are the separatrices of the different regimes. The solid grey line indicates the set of physical starting points determined by equations 4.24 and 4.25, where J/T is the free parameter that determines the position of the starting point on the grey line.

and many features of the model can be derived from these equations. In the limit where $a'/a = 1 + \varepsilon$ with $\varepsilon \ll 1$, these equations may be expressed via the two variables

$$x = \frac{2\pi J}{k_\mathrm{B}T}, \tag{4.24}$$

$$y = \exp\left(-\frac{E_\mathrm{2v}}{k_\mathrm{B}T}\right). \tag{4.25}$$

The variable x is the nearest neighbour interaction energy normalized by temperature, and the variable y is the fugacity of a pair of vortices. The two renormalization functions on x and y are given by

$$\frac{\mathrm{d}x}{\mathrm{d}\varepsilon} = -2\pi^2 x^2 y^2 \tag{4.26}$$

$$\frac{\mathrm{d}y}{\mathrm{d}\varepsilon} = \frac{1}{2}\left(4 - x\right) y. \tag{4.27}$$

A graph presenting a few solutions of these equations is shown on Fig. 4.2. There are many interesting features on this graph:

- If we start with $J \gg k_\mathrm{B}T$, which means $x \gg 1$ and $y \ll 1$, we start on the bottom right of the graph and the renormalization process shows us that, when changing the scale of the system, we end up with an equivalent system with a null fugacity of the vortices and a finite interaction energy. This is the low temperature limit that we detailed above.

- On the contrary, if we start with $J \ll k_\mathrm{B}T$ on the left of the graph, we end up with an equivalent system with an infinite fugacity of the vortices and a null interaction between neighbours. In this high temperature limit, it is favourable to create pairs of vortices, and there is no coherence between spatially distant arrows.

- In the regime where spatial coherence subsists, the effective interaction energy $2\pi J_{\text{eff}}/(k_{\text{B}}T)$ is never lower than 4. This value coincides with the critical temperature that we found when crudely describing the role of the vortices. This has important consequences, notably for the power law exponent of the first-order correlation function expressed in equation 4.18. This exponent is always between 0 and 1/4.

- A more careful analysis shows [151] that the critical temperature T_{c} is given by the implicit equation

  $$\frac{2k_{\text{B}}T_{\text{c}}}{\pi J} = \frac{1}{1+\pi\exp\left(\frac{-\pi^2 J}{2k_{\text{B}}T_{\text{c}}}\right)}, \tag{4.28}$$

  which is close to the estimate we found in 4.1.1.4.

- The phase transition is reflected on the correlation function $g_1(\boldsymbol{r})$: below the critical temperature it has a power law decay with an exponent η below 1/4. Above the critical temperature, the first-order correlation function decays exponentially with a characteristic length ℓ given by equation 4.8.

4.1.2 *An ideal gas of bosons in 2D*

We now turn to the case of bosonic particles in two dimensions. I give the main results of this simple case so that the important notions that will be used in the case of interacting particles are introduced. Details of the calculations are given in Appendix B. The whole discussion is largely inspired from [150].

4.1.2.1 *General relations*

We consider a square box of size $L \times L$ with periodic boundary conditions. The Hamiltonian of one particle is

$$\hat{H} = \frac{\hat{\boldsymbol{p}}^2}{2m}, \tag{4.29}$$

whose eigenstates are the plane waves with quantized momenta $\boldsymbol{p}$: $\boldsymbol{p} = 2\pi\hbar\boldsymbol{j}/L$, with $\boldsymbol{j} = (j_x, j_y)$ a vector with integer coordinates. The energy of this state is $E_{\boldsymbol{p}} = \boldsymbol{p}^2/(2m)$.

A system of non-interacting bosons at temperature T and fugacity $z = \exp(\mu/k_{\text{B}}T)$ occupies each momentum state with an occupation number following the Bose-Einstein statistics:

$$N_{\boldsymbol{p}} = \frac{1}{z^{-1}\exp\left(\frac{\boldsymbol{p}^2}{2mk_{\text{B}}T}\right) - 1}, \tag{4.30}$$

which can be written as

$$N_{\boldsymbol{p}} = \sum_{l=1}^{+\infty} z^l \exp\left(-\frac{l\boldsymbol{p}^2}{2mk_{\text{B}}T}\right). \tag{4.31}$$

The correlation function G_1 of the gas is defined following [153]:

$$G_1(\boldsymbol{r}, \boldsymbol{r}') = \langle \boldsymbol{r}' | \, \hat{\rho}_1 \, | \boldsymbol{r} \rangle \,, \tag{4.32}$$

where $\hat{\rho}_1$ is the one-particle density matrix of the system.

We first remark that the population of the momentum state $\boldsymbol{p}$ can be written as

$$\begin{aligned} N_{\boldsymbol{p}} &= \langle \boldsymbol{p} | \, \hat{\rho}_1 \, | \boldsymbol{p} \rangle & (4.33) \\ &= \iint \mathrm{d}^2\boldsymbol{r} \; \mathrm{d}^2\boldsymbol{r}' \, \langle \boldsymbol{p} | \boldsymbol{r}' \rangle \, \langle \boldsymbol{r}' | \, \hat{\rho}_1 \, | \boldsymbol{r} \rangle \, \langle \boldsymbol{r} | \boldsymbol{p} \rangle & (4.34) \\ &= \frac{1}{L^2} \iint \mathrm{d}^2\boldsymbol{r} \; \mathrm{d}^2\boldsymbol{r}' \exp\left(\frac{\mathrm{i}\boldsymbol{p} \cdot (\boldsymbol{r} - \boldsymbol{r}')}{\hbar} \right) \langle \boldsymbol{r}' | \, \hat{\rho}_1 \, | \boldsymbol{r} \rangle \,. & (4.35) \end{aligned}$$

Since the system has a translational invariance, the quantity $\langle \boldsymbol{r}' | \, \hat{\rho}_1 \, | \boldsymbol{r} \rangle$ depends only on the relative distance $\boldsymbol{u} = \boldsymbol{r} - \boldsymbol{r}'$. The integral over $\boldsymbol{r}$ is then straightforward:

$$N_{\boldsymbol{p}} = \int \mathrm{d}^2\boldsymbol{u} \exp\left(\frac{\mathrm{i}\,\boldsymbol{p} \cdot \boldsymbol{u}}{\hbar} \right) G_1(\boldsymbol{0}, \boldsymbol{u}). \tag{4.36}$$

The momentum distribution $N_{\boldsymbol{p}}$ is therefore the Fourier transform of the correlation function $G_1(\boldsymbol{0}, \boldsymbol{r})$. An inverse Fourier transform thus provides the correlation function from the knowledge of the momentum distribution:

$$G_1(\boldsymbol{0}, \boldsymbol{r}) = \frac{1}{(2\pi\hbar)^2} \int \mathrm{d}^2\boldsymbol{p} \exp\left(-\frac{\mathrm{i}\,\boldsymbol{p} \cdot \boldsymbol{r}}{\hbar} \right) N_{\boldsymbol{p}}. \tag{4.37}$$

This general relation does not depend on the momentum distribution, it only relies on the translational invariance of the problem. When we use it for the case of the ideal gas of bosons in two dimensions with the momentum distribution found in equation 4.31, we get:

$$G_1(\boldsymbol{0}, \boldsymbol{r}) = \frac{1}{\lambda_T^2} \sum_{l=1}^{+\infty} \frac{z^l}{l} \exp\left(-\frac{\pi \boldsymbol{r}^2}{l \lambda_T^2} \right), \tag{4.38}$$

where λ_T is the thermal wavelength of the gas, defined by

$$\lambda_T = \sqrt{\frac{2\pi\hbar^2}{m k_{\mathrm{B}} T}}. \tag{4.39}$$

We can define a normalized version of this correlation function:

$$\begin{aligned} g_1(\boldsymbol{r}) &\equiv \frac{G_1(\boldsymbol{0}, \boldsymbol{r})}{\sqrt{G_1(\boldsymbol{0}, \boldsymbol{0})} \sqrt{G_1(\boldsymbol{r}, \boldsymbol{r})}} & (4.40) \\ &= \sum_{l=1}^{+\infty} \frac{z^l}{l} \exp\left(-\frac{\pi \boldsymbol{r}^2}{l \lambda_T^2} \right). & (4.41) \end{aligned}$$

In particular, this first-order correlation function $g_1(\boldsymbol{r})$ is always smaller than 1.

We can now examine this relation in the two limits of low and high degree of degeneracy for the gas.

4.1.2.2 *Limits of the first-order correlation function*

In the limit where the gas is far from quantum degeneracy, we have $z \ll 1$, or equivalently $|\mu| \ll k_\mathrm{B}T$, and the first-order correlation function in given by

$$g_1(\boldsymbol{r}) \approx \exp\left(-\frac{\pi \boldsymbol{r}^2}{\lambda_T^2}\right). \tag{4.42}$$

The spatial extension of this Gaussian-shaped first-order correlation function is given by the thermal wavelength λ_T of the gas.

In the limit where the gas is degenerate, we have $z \approx 1$ the first-order correlation function in given by

$$G_1(\boldsymbol{0}, \boldsymbol{r}) \approx \frac{1}{(2\pi\lambda_T)^2} K_0\left(\frac{|\boldsymbol{r}|}{\ell}\right), \tag{4.43}$$

where $K_0(x)$ is the Bessel function of the second kind and order zero, and the length ℓ is

$$\ell = \frac{\hbar}{\sqrt{2m|\mu|}}. \tag{4.44}$$

The derivation of this expression is given in Appendix B.

When the argument of the Bessel function is large compared to 1, we have

$$G_1(\boldsymbol{0}, \boldsymbol{r}) \approx \frac{1}{(2\pi\lambda_T)^2} \sqrt{\frac{\pi\ell}{2|\boldsymbol{r}|}} \exp\left(-\frac{|\boldsymbol{r}|}{\ell}\right). \tag{4.45}$$

The correlation function decays slightly faster than an exponential, with a characteristic length scale ℓ that is much larger compared to the thermal wavelength λ_T, since $|\mu| \ll k_\mathrm{B}T$.

The two limits of low and high degree of degeneracy are therefore very different one from the other, but in all cases, there is no long range order for an infinite system with no interactions at non-zero temperatures.

4.1.3 *Interacting bosons in 2D*

We now turn to the case of an interacting Bose gas. I first briefly present the mathematical description of this problem before examining the correlation function in this case.

4.1.3.1 *Description with a classical field*

We consider a system of N interacting particles in two dimensions. The full wave function of N particles is $\Psi(\boldsymbol{r}_1, \boldsymbol{r}_2, \cdots, \boldsymbol{r}_N)$. It is fully symmetric with respect to the positions of the particles $\boldsymbol{r}_1, \cdots, \boldsymbol{r}_N$, and we choose its normalisation to be the number of particles N:

$$\int \cdots \int \mathrm{d}^2\boldsymbol{r}_1 \cdots \mathrm{d}^2\boldsymbol{r}_N |\Psi(\boldsymbol{r}_1, \boldsymbol{r}_2, \cdots, \boldsymbol{r}_N)|^2 = N. \tag{4.46}$$

The Lagrangian density of the system is

$$\mathcal{L}[\Psi] = \Psi^* \left[-\mathrm{i}\hbar\frac{\partial}{\partial t} + \sum_{i=1}^{N} \left(-\frac{\hbar^2}{2m}\boldsymbol{\nabla}_i^2 + V_{\text{ext}}(\boldsymbol{r}_i) + \frac{1}{2}\sum_{j\neq i} V(\boldsymbol{r}_j - \boldsymbol{r}_i) \right) \right] \Psi, \tag{4.47}$$

where V_{ext} is an external potential and V is the interaction potential between the particles.

We use the Hartree *ansatz*, which consists in restraining the wave function Ψ to be a product of the same wave function ψ:

$$\Psi(\boldsymbol{r}_1, \cdots, \boldsymbol{r}_N) = \sqrt{N}\prod_{i=1}^{N}\psi(\boldsymbol{r}_i), \tag{4.48}$$

where $\psi(\boldsymbol{r})$ is a classical field normalised at 1:

$$\int \mathrm{d}^2\boldsymbol{r}|\psi(\boldsymbol{r})|^2 = 1. \tag{4.49}$$

The system is now described by the Lagrangian density

$$\mathcal{L}[\psi] = \psi^*(\boldsymbol{r})N\left[-\mathrm{i}\hbar\frac{\partial}{\partial t} - \frac{\hbar^2\boldsymbol{\nabla}^2}{2m} + V_{\text{ext}}(\boldsymbol{r}) + \frac{N}{2}\int \mathrm{d}^2\boldsymbol{r}'\, V(\boldsymbol{r}'-\boldsymbol{r})|\psi(\boldsymbol{r}')|^2 \right]\psi(\boldsymbol{r}), \tag{4.50}$$

where the atom number is large compared to 1, therefore $N-1, N-2 \approx N$.

In the case of weakly interacting bosons, the interaction between these particles can be described by a contact interaction, which leads to the following Euler-Lagrange equation:

$$\mathrm{i}\hbar\frac{\partial\psi}{\partial t} + \frac{\hbar^2}{2m}\boldsymbol{\nabla}^2\psi - V_{\text{ext}}(\boldsymbol{r})\psi - \frac{\hbar^2}{m}\tilde{g}N|\psi|^2\psi = 0. \tag{4.51}$$

This equation is called the Gross-Pitaevskii equation, and in the following we will consider it with a null external potential: $V_{\text{ext}} = 0$.

The description with a classical field is valid only if the parameter $\tilde{g}$ is small compared to 1. We will stay in this regime, since experimentally we always have $\tilde{g} \leq 0.15$.

4.1.3.2 *Mapping on the XY-model*

The density of interaction energy is $\hbar^2\tilde{g}n^2/2m$, where $n = |\psi|^2$ is the atomic density. It is proportional to the square of this atomic density, which means that the minimal interaction energy is reached when the gas has a uniform density. At $T = 0$, the gas is uniform and only on the edge of the box its density goes to zero, on a length scale given by the healing length ξ, with

$$\xi = \frac{1}{\sqrt{2\tilde{g}n}}. \tag{4.52}$$

At finite temperature, departing from a uniform density costs energy, which can come from the thermal energy of the gas. One can estimate the fluctuation of density with a Bogoliubov approach, that is detailed for example in [38]. The relative density fluctuation is given by

$$\frac{\delta n}{n} \approx \sqrt{\frac{2}{n\lambda_T^2} \ln\left(\frac{2\pi}{\tilde{g} n \lambda_T^2}\right)}. \tag{4.53}$$

The right-hand side is on the order of 1 when the phase-space density $n\lambda_T^2 \approx 4$. The regime where these density fluctuations are suppressed is called the quasi-condensate regime, or pre-superfluid regime. This regime arises for lower phase-space densities than the ones predicted by equation 4.53 [110, 144, 154]. Already when $\mathcal{D} \lesssim 1$, the density fluctuations are reduced.

In these conditions, the only degree of freedom that is left for the classical field $\psi(\boldsymbol{r})$ is its phase $\phi(\boldsymbol{r})$. We are then left with a continuous version of the XY-model presented above, and the physics of both versions is exactly the same. In particular, the system displays a BKT transition. More generally we can translate all of the results of section 4.1.1 with the vocabulary adapted for a quantum fluid.

Importantly, the interaction energy J between the arrows in the XY-model is replaced here by a quantity proportional to the superfluid density n_s. This superfluid density describes how easily the phase profile $\phi(\boldsymbol{r})$ can be deformed. It can also be linked to the correlations of the velocity field [155, 156].

More precisely, the results of the XY-model is transposed by replacing the effective interaction J_eff by $\hbar^2 n_\mathrm{s}/m$. The critical temperature is given by

$$\frac{2\pi\hbar^2 n_\mathrm{s}}{m k_\mathrm{B} T_\mathrm{c}} = 4, \tag{4.54}$$

and this relation can also be translated in terms of superfluid phase-space density $\mathcal{D}_\mathrm{s} = \lambda_T^2 n_\mathrm{s}$:

$$\mathcal{D}_{\mathrm{s,(c)}} = 4. \tag{4.55}$$

There are two regimes separated by this critical temperature, as shown by the renormalization group:

1. At temperatures lower than this critical temperature, the system has a non zero effective superfluid density n_s, and its first-order correlation function decays as a power law:

   $$g_1(\boldsymbol{r}) = \left(\frac{\lambda_T}{r}\right)^\eta, \quad \eta = \frac{1}{\lambda_T^2 n_\mathrm{s}}. \tag{4.56}$$

   The exponent η is therefore always smaller than $1/4$.

2. At temperatures higher than the critical temperature, the system has a null superfluid density: $n_\mathrm{s} = 0$ and the correlation function decays exponentially fast. The correlation length ℓ of this decay diverges as the temperature comes closer to T_c [149].

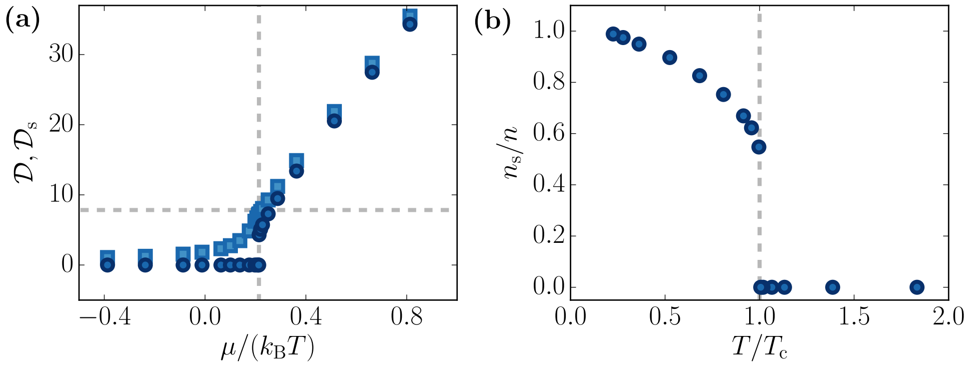

Figure 4.3: Results of the Monte-Carlo simulations from [110], plotted for $\tilde{g} = 0.15$. (a): Phase-space density $\mathcal{D}$ (light squares) and superfluid phase-space density $\mathcal{D}_s$ (dark circles) as a function of the dimensionless parameter $\mu/k_\mathrm{B}T$. The horizontal grey dashed line indicates the critical phase-space density, and the vertical grey dashed line indicates the critical point of the transition. (b): Superfluid fraction n_s/n as a function of the reduced temperature T/T_c, which is proportional to the inverse of the x-axis of the graph in (a).

We can now turn to the Monte-Carlo numerical simulations performed by Prokof'ev and Svistunov [110]. The relation between n and the ratio $\mu/k_\mathrm{B}T$ has already been presented on Fig. 2.13a. These simulations also provide the dependence of the superfluid density n_s on $\mu/k_\mathrm{B}T$. This is shown on Fig. 4.3a. On Fig. 4.3b is shown how the superfluid fraction n_s/n depends on T/T_c.

It is to note that the superfluid fraction is null for temperatures above T_c, and that it jumps to approximately 1/2 at the critical temperature. When the temperature decreases to zero, the superfluid fraction continuously increases to 1. The amplitude of this jump depends on the value of $\tilde{g}$. On the contrary, the jump of $\mathcal{D}_s$ from 0 to 4 is universal.

While all thermodynamic quantities are continuous at T_c, the superfluid fraction displays a discontinuity which stems from the disappearance of the quasi-long range ordering of the system, as described by the BKT phase transition. It is therefore an important quantity to measure experimentally. It has for example been the case with superfluid helium confined in 2D [157], where the measurement has been performed in a dynamical way. In other systems, the access to this superfluid density is much more difficult, and the measurement of the first-order correlation function may provide a way to access it. This was for example a motivation that we had to measure the second sound, as proposed in [158]. The measurements we have performed and reported in [113] could not reveal the behaviour of the superfluid fraction near the critical temperature due to the emergence of a collisionless sound, as explained in [94].

The observation of a quasi-long range order and its disappearance by the measurement of the first-order correlation function is a challenge that has been undertaken with various physical systems. The rest of the chapter is dedicated to these measurements and how the theory of infinite 2D systems translates in the laboratories.

4.2 DEVELOPMENTS FOR REALISTIC EXPERIMENTAL MEASUREMENTS

There have been several recent measurements of observables linked to the first-order correlation function of interacting 2D systems, with various experimental realizations. Some important issues are raised when comparing these measurements to the ideal theory.

- Several experiments with polaritons have been performed to measure spatial, but also temporal correlation functions. Some experiments are reported in [159–161]. Polaritons are open quantum systems and their study is interesting to understand the physics of driven and out-of equilibrium systems. The particularities of these systems and their link with equilibrium physics are discussed in 4.2.1.
- Some experiments have been performed with 2D systems of atoms in an external harmonic potential, reported in [144, 162, 163]. The presence of a harmonic in-plane confinement also changes the behaviour compared to an infinite uniform system. This point is discussed in 4.2.2.

Finally, the effects of finite size for uniform systems are briefly discussed in 4.2.3.

4.2.1 *Exciton-polaritons and out-of-equilibrium effects*

Polaritons are bosonic particles that arise from the coupling between electron-hole excitons of a semiconductor and photons of a light field in a cavity [164]. These hybrid particles are produced in two-dimensional quantum wells and their effective mass is low enough so that the temperature to reach quantum degeneracy can be above room temperature. The lifetime of polaritons is typically on the same order of magnitude as their thermalisation time [165], which means that, in order to reach a steady-state, one needs to drive the system to counterbalance the losses. This is referred to as a driven-dissipative system.

Such systems are therefore different from closed systems at equilibrium, and the properties of both systems can be very different. For example their universality class is not the same: for isotropic systems, an isolated system at equilibrium is described by the XY-model, as we have seen above, while a driven-dissipative system falls in the Kardar-Parisi-Zhang (KPZ) class [166]. It has also been shown that a strongly anisotropic system can recover a description with the XY-model [166, 167], but this regime is not the one in which the experiments are operating.

However, experiments show that the decay of the first-order correlation function is compatible with a power law [159–161]. From a theoretical point of view, this behaviour is expected only for a finite range of distances. If measured with large enough systems the first-order correlation function is not expected to follow such a power-law decay [167].

The exponent of the power law that are measured in the three cited experiments do not agree with one another, due to the different excitation procedures.

The exponents reported in [159, 161] are higher than what the BKT theory predicts, but this difference is well-explained by numerical simulations [168], and may be due to spatial inhomogeneities of the samples. The exponents reported in [160] agree with the BKT prediction.

The measurement of the first-order correlation function is not the only experimental observation that one can perform in order to clarify the link between gases of polaritons and the BKT transition. Another interesting direction would be the observation of vortex pairing below the BKT transition and the proliferation of isolated vortices above it. While theoretical findings and numerical simulation support this scenario [166, 168], such a mechanism has not yet been observed experimentally [169].

4.2.2 *Cold atoms and trapping effects*

We now turn to atomic systems, which are more reliably linked to the BKT physics: their thermalisation timescale is on the order of several milliseconds, whereas their lifetime is on the order of a few seconds. They do not need any pumping and they are hence much closer to a system at thermal equilibrium.

At least three experiments have measured quantities linked to the first-order correlation function in a 2D Bose gas, and all of them were using a harmonic potential to confine the atoms in the xy plane. In the first one [162], the authors measure the interference pattern between two identically prepared 2D clouds, as initially proposed in [170]. These interference patterns have a local contrast $c(x)$ and a local phase $\theta(x)$. The images they have are taken in the xz plane, and the quantities $c(x)$ and $\theta(x)$ are an average over the y direction. They compute a spatially-averaged contrast $C(x)$ defined as

$$C(x) = \frac{1}{x}\left|\int_{-x/2}^{x/2} \mathrm{d}u\ c(x)\exp[\mathrm{i}\theta(x)]\right|, \tag{4.57}$$

and they average its square over several experimental realizations. One expects to have

$$\left\langle C^2(x)\right\rangle = \frac{1}{x}\int_{-x/2}^{x/2} \mathrm{d}u[g_1(0,u)]^2, \tag{4.58}$$

where $\langle\cdot\rangle$ denotes this average. If g_1 decays algebraically with an exponent η, one gets

$$\left\langle C^2(x)\right\rangle \propto x^{-2\eta}. \tag{4.59}$$

The authors measure the exponent of the decay of $\left\langle C^2(x)\right\rangle$ around the critical temperature and report the coincidence between a jump of this exponent from 0.5 and 1 and the appearance of dislocations in their interference patterns indicating the presence of vortices. This indicates that right below the critical temperature, $g_1(\boldsymbol{r})$ has a decay compatible with an algebraic decay of exponent 1/4, and that right above the critical temperature, $g_1(\boldsymbol{r})$ has a different behaviour, due to the vortices that appear and break the quasi long-range order.

In the second study (reference [144]), the authors measure the contrast of the interference between two copies of the same initial cloud. These copies are produced thanks to Raman beams with a momentum transfer. The measured contrast is directly linked to the first-order correlation function, as I will develop in more details in Chapter 6. The authors observe qualitatively the increase of the range of the coherence of phase when the phase-space density of the gas is increased. This is a very interesting complement to the study of the multi-modal shape of the cloud after a short time-of-flight developed in the first pages of their article. However the cloud is not very deep in the degenerate regime, as they work with atomic densities lower than $20\,\mu\mathrm{m}^{-2}$, a temperature around $100\,\mathrm{nK}$ and an interaction parameter with a low value: $\tilde{g} \approx 0.02$. While the effects of the in-plane trapping ($\omega_r = 2\pi \cdot 20\,\mathrm{Hz}$) are visible in the first part of the study, their importance in the second part is not clear.

In the third study, reported in [163], the authors measure the momentum distribution of a cloud, which is the Fourier transform of the first-order correlation function for translational invariant systems. They compute the inverse Fourier transform of this momentum distribution to determine the g_1 function, and perform this procedure for different temperatures.

They observe that below the critical temperature, $g_1(\boldsymbol{r})$ decays algebraically, and above the critical temperature it decays exponentially. However, the exponents of the power laws they measure are always above 0.5 and can go up to 1.5, which is not compatible with the theoretical prediction.

This discrepancy has been explained in [171], and it is based on the non-uniform character of the cloud: while measuring the momentum distribution of the cloud, all the regions of the cloud interfere and contribute to the quantity $N_{\boldsymbol{p}}$. Over the whole cloud, the product $\lambda_T^2 n_s$ spans a large interval between 0 and $\lambda_T^2 n_{s,\mathrm{max}}$, which then blurs the measurement of $N_{\boldsymbol{p}}$ and then the determination of $g_1(\boldsymbol{r})$.

By taking into account the non-uniformity of the cloud, the authors of [171] are able to reproduce numerically the exponents measured in [163]. It is to note that these considerations also apply to the previous experiment [162], but there, the quantity measured was more directly linked to $g_1(\boldsymbol{r})$, and the effect of the non-uniformity of the cloud has a much smaller effect.

These three experiments provide important information about the 2D Bose gas and its BKT phase transition, but they do not provide a proper measurement of $g_1(\boldsymbol{r})$ from which one could extract exponents that are directly linked to an infinite and uniform system. Our experimental system provides uniform samples, which is a major improvement compared to the experimental conditions of [163].

We now need to understand whether our finite-sized sample allows us to measure quantities that are related to the physics of infinite systems. This is the object of the next paragraph.

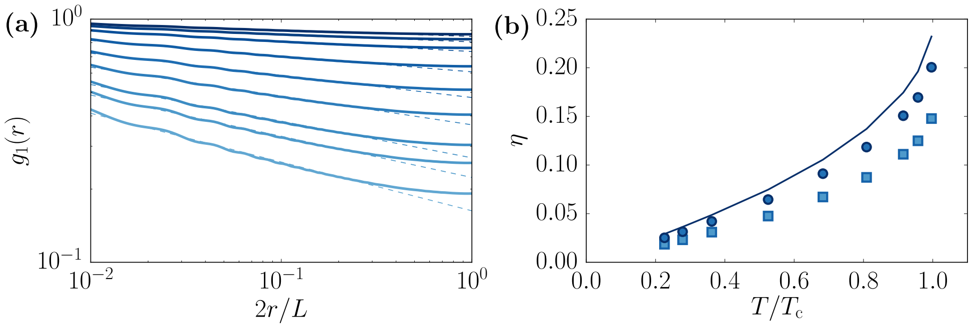

Figure 4.4: Effect of the finite size of the system. (a): The first-order correlation function between the centre of the gas and a point at distance r is plotted for different values of T/T_c. From dark blue to light blue, the value of this ratio is 0.22, 0.28, 0.36, 0.52, 0.68, 0.81, 0.91, 0.96 and 0.996. Each of these curves are fitted with a straight line, corresponding with a power law. (b): The exponent of the fitted power laws is plotted as a function of T/T_c for two values of L/ξ: 100 (dark circles) and 10 (light squares). The black solid line indicates the theoretical prediction given by equation 4.56.

4.2.3 *Finite-size effects*

One can evaluate numerically the effect of the finite-size of the cloud by computing the phase fluctuations due to phonons. The expression of these phase fluctuations is given by equation 4.15 that, in the context of a 2D Bose gas in a square box of size L with periodic boundary conditions, can be written as

$$g_1(\boldsymbol{r}, \boldsymbol{0}) = n_s \exp\left[-\frac{2}{\pi \mathcal{D}_s} \sum_{j_x, j_y} \frac{1 - \cos(2\pi/L\, \boldsymbol{j} \cdot \boldsymbol{r})}{j_x^2 + j_y^2}\right], \tag{4.60}$$

where $\mathcal{D}_s$ is the superfluid phase-space density, n_s is the superfluid fraction and $\boldsymbol{j} = (j_x, j_y)$ is a vector of integers.

The sum in equation 4.60 diverges if the indices $j_{x,y}$ are allowed to be arbitrarily large. We therefore introduce a cut-off for the momenta $k_{x,y}$ at $1/\xi$, where ξ is the healing length of the gas [38]. This restricts the sum on $j_{x,y}$ to the integers between 1 and L/ξ. The first-order correlation $g_1(\boldsymbol{r}, \boldsymbol{0})$ thus depends only on this ratio between the size L of the system and the healing length of the gas.

The results of this computation are presented on Fig. 4.4. On Fig. 4.4a are shown the phase correlation $g_1(r)$ between the centre of the square and the point on the x-axis at distance r from this centre, for different values of T/T_c. The data are computed here for $L/\xi = 100$.

At very low temperatures ($T = 0.22\ T_c$ for the top curve), the phase correlation decreases very slowly with the distance r, much slower than at higher temperatures ($T = T_c$ for the bottom curve). Both axes of the graph have a logarithmic scale, and the function $g_1(r)$ follows a straight line when $r \ll L/2$, indicated on the graph with dashed lines. This behaviour is the same as for the infinite system. However, when r is close to $L/2$, the phase correlation deviates from this power law.

These lines are fitted on the range $2r/L = [0.01, 0.4]$, and their slopes $-\eta$ are extracted. The value of η as a function of T/T_c is shown on Fig. 4.4b. Two values of L/ξ are tested: 100 (dark circles) and 10 (light squares). The solid line is the prediction for the infinite system: $\eta = 1/\mathcal{D}_s$. The exponents corresponding to $L/\xi = 10$ are smaller than the ones for $L/\xi = 100$ because the finite-size effects appear on smaller distances r for smaller values of L/ξ and affect the slope of the fit.

This analysis shows that a system with a finite size reproduces well the physics of an infinite 2D plane, as long as the ratio L/ξ is much larger than 1, and as long as the probed regions are not distant by a length close to the full size of the system. Typically, the ratio L/ξ is on the order of 100 on our experiment.

4.2.4 *Conclusion*

In this chapter I have presented the main features of the BKT transition with the XY-model before showing how it adapts to the case of weakly interacting bosons in two dimensions. This transition is well illustrated by the behaviour of the first-order correlation function g_1, which decays exponentially above the critical temperature, and as a power law below it with an exponent depending on the superfluid density of the system.

I have also discussed several recent experiments that were linked to this first-order correlation function across the BKT transition. There are some experiments with polaritons, whose out-of-equilibrium character makes the link with the BKT physics difficult to draw unambiguously. There are also experiments with atomic gases in harmonic potentials. In a first one, the coincidence between the appearance of vortices and a change of behaviour in the g_1 function has been demonstrated without measuring this correlation function. In a second one, the range of the phase ordering is qualitatively shown to be increased when the degeneracy of the gas is increased, but the in-plane trapping may have played an important role in these measurements. In the third one, the measured momentum distribution shows the two different behaviours of g_1 across the transition. However, the fitted exponents of the power law decays cannot be linked to a superfluid fraction due to the inhomogeneities of the system.

Finally I have shown that, with a uniform system, working with a finite-size system did not mask the effects of the BKT physics below the critical temperature, when working with reasonable parameters.

This analysis seems very promising for the perspective of performing experiments with our experimental set-up, since it can produce large uniform Bose gases in two dimensions. The goal of such experiments would be to properly measure the correlation function $g_1(\boldsymbol{r})$ and, below the critical temperature, to link the exponent of their power law decay to the exponents predicted by the BKT theory.

The experiments that we have performed are presented and discussed in the next two chapters.

5

PROBING PHASE COHERENCE BY MEASURING A MOMENTUM DISTRIBUTION

As we have seen in the previous Chapter, uniform Bose gases constitute a very promising platform to measure the first-order correlation function of a system described by the BKT physics, and extract proper exponents of a power-law decay below the critical temperature. We have performed a set of experiments inspired by reference [163] and based on the measurement of the momentum distribution of the gas. I detail these experiments in this chapter. However, due to several reasons that I will develop, these measurements did not allow us to determine the first-order correlation function with a satisfying reliability.

In a first part I explain our experimental scheme to measure the momentum distribution of a cloud of atoms, and I present the results that we have obtained. In a second part I detail the reasons why these measurements are not able to provide us with a proper estimate of the first-order correlation function.

5.1 MEASURING THE MOMENTUM DISTRIBUTION OF OUR ATOMIC CLOUDS

The method that we use to measure the momentum distribution of a cloud is similar to the one used in [163]. It is explained in detail in [172], and it is a technique that has been used in many previous cold atom experiments [145, 173–176].

It consists in letting a cloud evolve without interactions in an isotropic harmonic potential of frequency ω and measuring its density distribution after a duration of evolution of $\pi/2\omega$, which corresponds to a quarter of period in the harmonic potential. At this time in the evolution, the spatial distribution of the cloud reflects exactly the initial momentum distribution, similarly to a classical system.

More precisely, we have

$$\psi\left(\boldsymbol{r}, t=\frac{\pi}{2\omega}\right) = \psi_{\boldsymbol{p}}\left(\boldsymbol{p}=m\omega\boldsymbol{r}, t=0\right), \tag{5.1}$$

where ψ and $\psi_{\boldsymbol{p}}$ are the wave function expressed respectively in the position and momentum basis. Measuring the density distribution of the atoms at $t=\pi/2\omega$ and at position $\boldsymbol{r}$ thus provides a direct measurement of the initial momentum distribution of the cloud at momentum $m\omega\boldsymbol{r}$.

5.1.1 *Creating an harmonic potential with a magnetic field*

We create a harmonic potential with a magnetic field thanks to the coils that are used for the quadrupole trap (see Chapter 2, section 2.1.1.4). These coils are in an anti-Helmholtz configuration and the magnetic field they create is a quadrupolar field:

$$\boldsymbol{B}(x,y,z) = b' \begin{pmatrix} -x/2 \\ -y/2 \\ z \end{pmatrix}, \tag{5.2}$$

where the origin of the reference frame is chosen here at the zero of the quadrupole and $b' > 0$ is the vertical gradient on the axis of the coils.

The atoms are in the plane $z = -d_{\mathrm{Q}}$ with $d_{\mathrm{Q}} \approx 450\,\mu\mathrm{m}$. In this plane, atoms in the state $F = 1, m_F = -1$ feel a potential energy

$$V(x,y) = -g_F \mu_{\mathrm{B}} |\boldsymbol{B}(x,y)|, \tag{5.3}$$

where the Landé factor is here $g_F = -1/2$.

The cloud is located near the axis, with $|x|, |y| \ll d_{\mathrm{Q}}$, so that this potential is

$$V(x,y) = \frac{\mu_{\mathrm{B}} b' d_{\mathrm{Q}}}{2} \left(1 + \frac{x^2+y^2}{4d_{\mathrm{Q}}^2}\right)^{1/2} \tag{5.4}$$

$$\approx \frac{\mu_{\mathrm{B}} b' d_{\mathrm{Q}}}{2} + \frac{\mu_{\mathrm{B}} b'}{16 d_{\mathrm{Q}}}(x^2+y^2). \tag{5.5}$$

The gradient b' is chosen so that the vertical force compensates gravity: $b' = 2mg/\mu_{\mathrm{B}}$, with $g = 9.81\,\mathrm{m/s^2}$. The potential in the plane is then, up to a constant term:

$$V(x,y) = \frac{1}{2} m\omega^2 r^2, \tag{5.6}$$

with

$$\omega = \sqrt{\frac{g}{4d_{\mathrm{Q}}}}. \tag{5.7}$$

With our value of d_{Q}, we get $\omega \approx 2\pi \cdot 11.7\,\mathrm{Hz}$.

Due to experimental imperfections, the harmonic potential that we obtain with the quadrupole coils is not perfectly isotropic. By observing the evolution of the atoms in this potential, we will be able to correct this anisotropy with suitable compensation coils, as explained in the next paragraphs.

5.1.2 *Evolution of atoms in the harmonic potential*

The experimental sequence is illustrated on Fig. 5.1 and goes as follows.

- The cloud of atoms is prepared in the optical box potential, in the state $F = 1, m_F = 0$ whose energy does not depend on the magnetic field for low fields (Fig 5.1a).
- At $t = 0$ we apply two consecutive microwave pulses to transfer a controlled fraction of atoms first to the state $F = 2, m_F = 0$ and then to the state $F = 1, m_F = -1$. We also remove the optical traps to keep only the magnetic potential (Fig 5.1b).

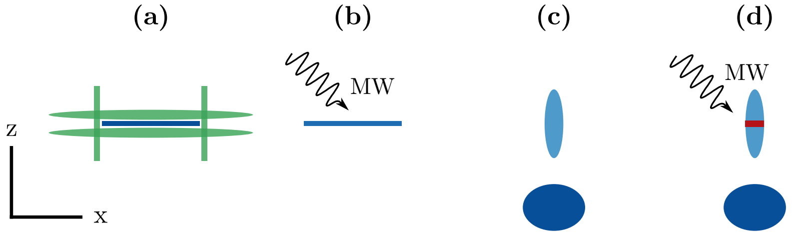

Figure 5.1: Scheme of the experimental sequence, as viewed in the xz plane. (a): Initially the gas is prepared in the 2D box potential in the $F = 1, m_F = 0$ state, and its temperature and atom number are controlled. (b): A fraction of the atoms are transferred to the $F = 1, m_F = -1$ state by two consecutive microwave pulses. The box potential is switched off. (c): The atoms expand vertically and separate due to the vertical gradient of magnetic field. The atoms in $F = 1, m_F = -1$ evolve in a magnetic harmonic potential of frequency $\omega \approx 2\pi \cdot 10\,\text{Hz}$. (d): A slice of atoms (in red) is transferred in the state $F = 2, m_F = 0$ thanks to a chirped microwave pulse. These atoms are then imaged.

- The atoms transferred to $F = 1, m_F = -1$ evolve in this magnetic potential during a chosen duration. Their centre of mass does not move vertically because the vertical magnetic gradient compensates their weight. The atoms that are left in the state $F = 1, m_F = 0$ are not sensitive to the magnetic field and fall due to gravity. In a few milliseconds they are spatially separated from the atoms in $F = 1, m_F = -1$ (Fig 5.1c). Both clouds expand vertically due to the high initial confinement. This expansion occurs with a velocity of a few micrometers per millisecond.

- After the evolution in the harmonic potential, we apply a final microwave pulse to transfer atoms in $F = 2, m_F = 0$. Due to the vertical gradient, this microwave pulse is resonant only with the atoms located in a given horizontal plane. During 1 ms, we sweep the frequency of the microwave to induce adiabatic transfers for atoms located in a slice of controllable thickness. This allows us to image only atoms that are on focus with our camera. The thickness of this slice depends on the frequency range we sweep. Typically this range is of a few tens of kilohertz, and the thickness we obtain is around ten micrometers (Fig 5.1d).

- The atoms that are transferred to the state $F = 2, m_F = 0$ are imaged with our vertical imaging system.

We choose to let the atoms expand in the vertical direction so that the atomic density decreases, and with it the strength of the interactions. The evolution in the harmonic potential indeed has to be performed without interactions in order to measure the initial momentum distribution. We do not have any Feshbach resonance at our disposal that could lower the interaction parameter [172]. As a consequence, the number of atoms that are imaged in the slice is much lower than the initial atom number. The expansion in the vertical direction is approximately linear with time, therefore the number of atoms that we image is inversely proportional to the evolution duration. We want to take

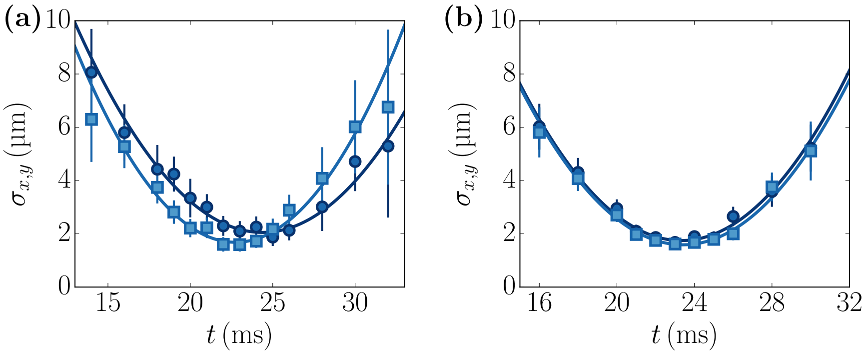

Figure 5.2: Size of the cloud along the x and y directions during the evolution in the harmonic potential. (a): The density distribution of the cloud is integrated over the two directions x and y, and both profiles are fitted with a Gaussian function. The half widths at half-maximum in the x and y directions σ_x (dark circles) and σ_y (light squares) are plotted as a function of the evolution duration. The errorbars represent the confidence interval of the Gaussian fit. The two curves display a minimum at 24.4(2) and 22.7(2) ms respectively. (b): The same measurement are performed after having adjusted the current in the horizontal coils. The minima of the two curves in x and y are respectively at 23.3(1) and 23.4(1) ms.

images of the atoms after a quarter of period in the harmonic potential, which means that the number of atoms we image is proportional to ω. We then need to have ω as large as possible to increase the signal-to-noise ratio.

Equation 5.1 indicates that the size of the cloud after an evolution during $\pi/2\omega$ is inversely proportional to ω. In order to have the best resolution in the measurement of the momentum distribution, we thus need to have the smallest value of ω possible.

We need to find a good compromise between the two last requirements. We found that a value of ω around $2\pi \cdot 10$ Hz allowed us to have a high enough atomic signal and a region covered by the atoms large enough to be captured by our imaging system. We will come back to the size of the cloud in a more quantitative way in the following.

We measure the size of the slice in the x and y directions as a function of the evolution time in the harmonic potential. An example of this measurement is given on Fig. 5.2a, where the initial cloud is a uniform disk of radius 20 µm. We find that the size in both directions reach a minimum, but not at the same time. This reflects the anisotropy of the harmonic potential, which is here

$$\frac{\omega_x}{\omega_y} - 1 \approx 7\%. \tag{5.8}$$

We found that we could reduce this anisotropy by using the pair of coils in the y direction that creates a quadrupole field for the MOT in the early stages of the experimental sequence. We adjust the current in these coils so that the harmonic potential becomes isotropic. On Fig. 5.2b are shown the measurements we obtain after this optimisation. In the end, we bring the anisotropy under 1%.

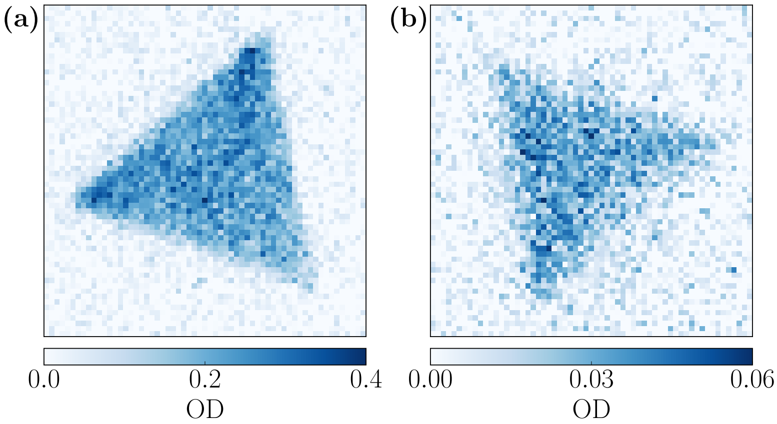

Figure 5.3: Investigating the role of the interactions. (a): A cloud in a box potential with the shape of an equilateral triangle is prepared. Its temperature is as low as possible, and its atom number is chosen so that the atomic signal after a quarter of oscillation in the harmonic potential is well above our detection noise. (b): Density distribution of this cloud after an evolution of half a period in the harmonic potential. This distribution has the shape of an inverted triangle, which is what one expects when the atoms evolve with negligible interactions.

We finally need to have an indication whether the evolution in the harmonic potential is affected by interactions or not. The density of the cloud is the largest at $t = \pi/(2\omega)$, and we need to evaluate for which densities these interactions are negligible at this time of the evolution and always work with densities on this order of magnitude or below.

We let the atoms evolve during half a period, corresponding to a duration π/ω, and we measure the density distribution of the atoms. If the interactions do not have any effect on the evolution, we expect the density distribution of the cloud to be exactly the initial one, but with an inversion symmetry with respect to the centre of the potential. In a classical picture, every atom has performed half a period in the potential and its position is the symmetric of the initial one with respect to this centre.

On Fig. 5.3a is shown the initial density distribution, and on Fig. 5.3b is shown the density distribution after an evolution during π/ω. The initial distribution is chosen to be a equilateral triangle so that the inversion symmetry appears more clearly. An evolution with interactions playing an important role would not give such a density distribution[1].

We measure the optical density of this cloud after an evolution of duration $\pi/2\omega$, when the density is the highest. This provides us with an indication of the density for which the interactions are not relevant. In the following, we make sure that the maximal density of the cloud is always on this order of magnitude or below.

---

[1] The last part of this thesis (chapters 7, 8 and 9) is entirely devoted to the properties of an evolution with interactions. In particular, section 9.1.1 shows how different the density distribution of the cloud would be if the interactions played a role in the evolution.

5.2 INVESTIGATING THE WIDTH OF THE MOMENTUM DISTRIBUTION

The size and shape of the momentum distribution we measure is influenced by several factors. Some are technical, such as the finite optical resolution ($\approx 1\,\mu\text{m}$) and the thickness of the atomic slice that we image. More interestingly, this momentum distribution depends on the initial size of the cloud and on its temperature. In this section I detail both factors, and I explain why these measurements do not provide reliable estimates of the first-order correlation, but only give general trends concerning the range of the spatial correlations.

5.2.1 *Influence of the initial size of the cloud*

We start with a cloud filling uniformly a disk of variable radius R. At zero temperature, the wave function of the cloud has a uniform phase:

$$\psi(\boldsymbol{r}) = \frac{1}{\sqrt{\pi R^2}}\,\mathbb{1}_{\mathcal{D}}(\boldsymbol{r}), \tag{5.9}$$

where $\mathbb{1}_{\mathcal{D}}(\boldsymbol{r})$ is the indicator function of the disk. The wave function in the momentum basis of this cloud is easily computed via the Fourier transform of this spatial wave function:

$$\psi_p(\boldsymbol{p}) = \frac{1}{\sqrt{\pi}|\boldsymbol{p}|}\,J_1\left(\frac{R|\boldsymbol{p}|}{\hbar}\right), \tag{5.10}$$

where J_1 is the Bessel function of the first kind and first order.

The half width at half-maximum (HWHM) of this momentum distribution $|\psi_p|^2$ is thus:

$$\sigma_p = \frac{1.62\hbar}{R}, \tag{5.11}$$

where the factor 1.62 is the HWHM of the function $x \mapsto (J_1(x)/x)^2$. When measuring this momentum distribution with our method, we expect the spatial HWHM σ_r of the density distribution to be

$$\sigma_r = \frac{1.62\hbar}{m\omega R}. \tag{5.12}$$

We test this on the experiment: we vary the radius R from 4 to $30\,\mu\text{m}$, and fix the temperature of the cloud as low as possible, corresponding to $T/T_\text{c} < 0.2$. We measure the HWHM of its momentum distribution with a Gaussian fit. The results are presented on Fig. 5.4, along with the zero temperature prediction. The width of the momentum distribution increases when the radius of the initial disk decreases, accordingly to the Heisenberg limit set by equation 5.12. The data points are always above this zero temperature prediction, which may be attributed to the resolution of our imaging system and to the non-zero temperature of the cloud.

Under the assumption that the correlation function between two points of the gas is not affected by the finite size of the system, one can decouple

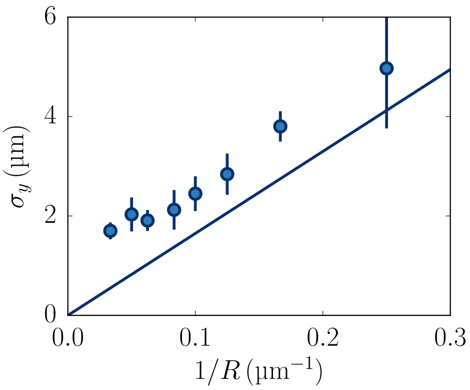

Figure 5.4: Half width at half-maximum of a cloud as a function of its initial radius R. The cloud is initially at $T/T_\mathrm{c} < 0.2$ to minimize the thermal effects as much as possible. The errorbars represent the confidence interval of the fit. The solid line is the zero temperature prediction given by the Heisenberg limit (equation 5.12). The data points are consistently above this line, which may be due to residual temperature effects, and/or to the finite resolution of our imaging system. The rightmost point has a large errorbar because the signal is much lower than for the other points.

the contribution of the size of the initial cloud from the contribution of this correlation function: We assume that

$$\langle \boldsymbol{r}' |\, \hat{\rho}_1 \,| \boldsymbol{r} \rangle = \frac{1}{\pi R^2}\, g_1^\infty(\boldsymbol{r}-\boldsymbol{r}')\; \mathbb{1}_\mathcal{D}(\boldsymbol{r})\; \mathbb{1}_\mathcal{D}(\boldsymbol{r}'), \tag{5.13}$$

where $g_1^\infty(\boldsymbol{r})$ is the correlation function of an infinite system, in which case the correlations between two points depend only on their relative position. The expression of the momentum distribution is then adapted from equation 4.35:

$$N_{\boldsymbol{p}} = \frac{1}{\pi R^2} \iint \mathrm{d}^2\boldsymbol{r}\; \mathrm{d}^2\boldsymbol{r}'\; \exp\left(\frac{\mathrm{i}\boldsymbol{p}\cdot(\boldsymbol{r}-\boldsymbol{r}')}{\hbar}\right) g_1^\infty(\boldsymbol{r}-\boldsymbol{r}')\; \mathbb{1}_\mathcal{D}(\boldsymbol{r})\; \mathbb{1}_\mathcal{D}(\boldsymbol{r}'), \tag{5.14}$$

which can be written under the form:

$$N_{\boldsymbol{p}} = \int \mathrm{d}^2\boldsymbol{r}\; \exp\left(\frac{\mathrm{i}\boldsymbol{p}\cdot\boldsymbol{r}}{\hbar}\right) g_1^\infty(\boldsymbol{r}) F(\boldsymbol{r}), \tag{5.15}$$

where the function F is the convolution of the indicator function of the disk with itself:

$$F(\boldsymbol{r}) = \frac{1}{\pi R^2} \int \mathrm{d}^2\boldsymbol{u}\; \mathbb{1}_\mathcal{D}(\boldsymbol{u})\; \mathbb{1}_\mathcal{D}(\boldsymbol{u}+\boldsymbol{r}) \tag{5.16}$$

$$= \frac{2}{\pi}\left[\arccos\left(\frac{\boldsymbol{r}}{2R}\right) - \frac{\boldsymbol{r}}{2R}\sqrt{1-\frac{\boldsymbol{r}^2}{4R^2}}\right] \mathbb{1}_\mathcal{D}\left(\frac{\boldsymbol{r}}{2}\right). \tag{5.17}$$

The Fourier transform of the momentum distribution $N_{\boldsymbol{p}}$ is then simply the product between g_1^∞ and F.[2]

---

[2] At $T = 0$, $g_1^\infty = 1$, and the equations 5.10 and 5.15 allow one to demonstrate the identity:

$$\forall \alpha \in \mathbb{R}, \quad \int_0^{+\infty} \mathrm{d}u\, \frac{J_1^2(u) J_0(\alpha u)}{u} = \frac{1}{\pi}\left[\arccos\left(\frac{|\alpha|}{2}\right) - \frac{|\alpha|}{2}\sqrt{1-\frac{\alpha^2}{4}}\right] \mathbb{1}_{[-2,2]}(\alpha),$$

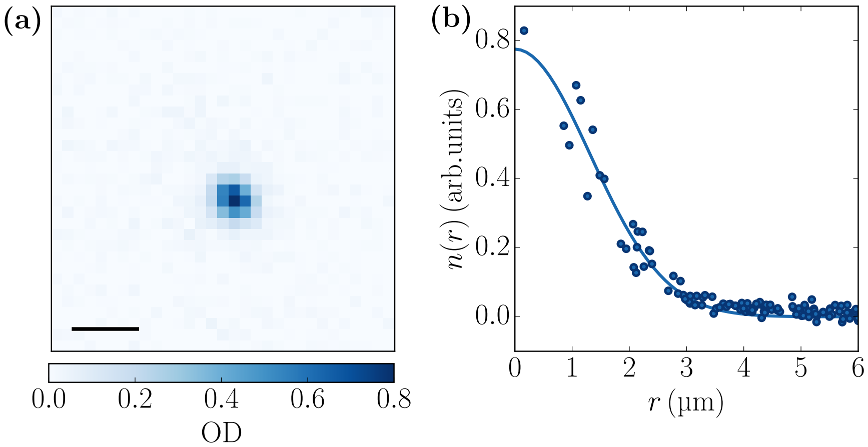

Figure 5.5: Measurement of a momentum distribution. The data presented here are taken at $T/T_\mathrm{c} = 1.3(1)$. (a): Average of 100 experimental realisations in the same conditions. The black line indicates the scale of 5 µm. (b): We determine the centre of this momentum distribution and we display the density as a function of the distance r to this center. The data are fitted with a Gaussian function (solid line) to determine the HWHM of this distribution. On this particular example we obtain a width of 1.55(12) µm.

5.2.2 *Influence of the temperature of the cloud*

We now fix the radius of the initial disk at $R = 20\,\mu\mathrm{m}$ to investigate the effect of temperature on the momentum distribution. The initial cloud is prepared in this disk, and its temperature is adjusted by varying the height of the box potential. In these conditions, we always end up with a temperature below the critical temperature T_c. Indeed, we always load a Bose-Einstein condensate in the 2D potential, which does not allow us to prepare a cloud with a high enough temperature. In order to have samples with $T/T_\mathrm{c} > 1$, we remove a controlled fraction of the atoms to reduce the value of T_c, as explained in Chapter 2, paragraph 2.3.2.2. The gas we prepare then has a ratio T/T_c from 0.2 to 1.8.

For each of these initial clouds we measure the ratio T/T_c and we measure the HWHM of their momentum distribution by averaging the images of 100 experimental realisations. An example of the obtained density distributions with the determination of this width is presented on Fig. 5.5. All the results are summarized on Fig. 5.6, that shows the width σ_H of the momentum distribution as a function of T/T_c. Below the critical temperature, the width of the momentum distribution does not significantly vary. It increases when T gets above T_c, which indicates that the range of the correlation function g_1^∞ gets smaller, which is in agreement with what we expect.

Due to the small amount of pixels that the atoms cover and due to the experimental imperfections, such as the finite optical resolution, it is difficult

---

where $\mathbb{1}_{[-2,2]}(x)$ is the indicator function of the interval $[-2, 2]$. This identity will not be useful in the work presented in this thesis.

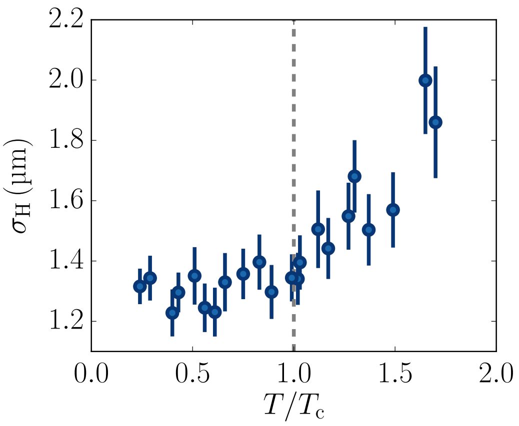

Figure 5.6: Half width at half-maximum σ_{H} of the momentum distribution of the cloud as a function of the ratio T/T_{c}. This width stays around 1.3 µm when $T < T_{\mathrm{c}}$. When the temperature is increased above T_{c}, the momentum distribution gets wider, with a HWHM as high as 2 µm.

to determine the exact shape of these momentum distributions. Their width is essentially the only reliable quantity that we can extract from them.

5.2.3 *Determining the first-order correlation function?*

The method we use to measure the momentum distribution has two main limitations due to the presence of interactions between the atoms during their evolution in the harmonic potential: the small spatial extent of the cloud when we image it, and the low atom number that we image. Since the level of the experimental noise cannot be reduced below a few percent if we want to keep the required number of experimental realisations at a reasonable value, both of these limitations do not allow us to have signal on a large range of momenta. One can therefore wonder whether it is possible to reliably determine the correlation function by measuring this momentum distribution.

The momentum distribution that we measure is the Fourier transform of the product between g_1^{∞} and F, as expressed in equation 5.15. Since the initial cloud is a disk, all the functions involved have a rotational invariance, and we have

$$N_{\boldsymbol{p}} \propto \int_0^{+\infty} \mathrm{d}u \; u \; J_0\left(\frac{\mathrm{i}up}{\hbar}\right) g_1^{\infty}(u) F(u). \tag{5.18}$$

We can also include a contribution due to the resolution of the imaging system by introducing the Fourier transform of a point-spread function (PSF) in the integral of 5.18:

$$N_{\boldsymbol{p}} \propto \int_0^{+\infty} \mathrm{d}u \; u \; J_0\left(\frac{\mathrm{i}up}{\hbar}\right) g_1^{\infty}(u) F(u) \; \mathcal{FT}[PSF](u), \tag{5.19}$$

where PSF is chosen to be a Gaussian with a width that is adapted to reproduce the smallest widths that we measure on Fig. 5.6. This width is on the order of 1.2 µm, which is compatible with the numerical aperture of our imaging system.

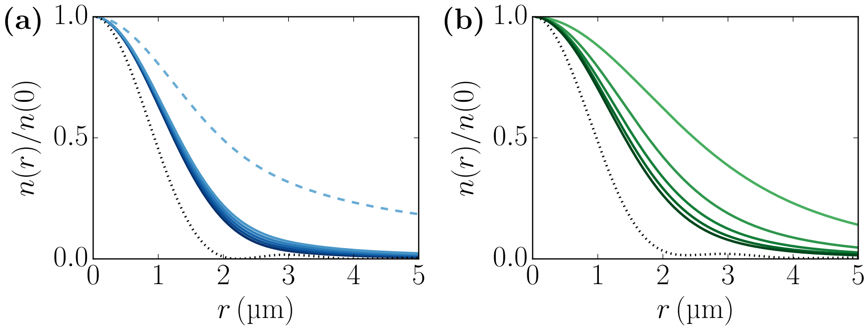

Figure 5.7: Numerical computations of the momentum distribution measurement using our experimental method from equation 5.19 and for a disk of radius 20 µm. (a): The correlation function is a power law $\boldsymbol{r}^{-\eta}$ for $\eta = 0.05$, 0.1, 0.15, 0.2 and 0.25 from dark blue to light blue, solid lines. The five curves are very close to one another. The dashed line is the result we obtain with $\eta = 1$, which is not in the range theoretically allowed. The dotted black line is the momentum distribution we would measure when $\eta = 0$ and a perfect optical resolution. (b): The correlation function is an exponential decay $\exp(-r/\ell)$ with $\ell = 5$, 10, 15, 20, 25 µm from light green to dark green. A correlation function with a short range gives a broad momentum distribution. The dotted black line is the momentum distribution we would measure when $\ell = 100$ and a perfect optical resolution.

The density distribution $n(\boldsymbol{r})$ that we measure on the images is then linked to this momentum distribution via

$$n(\boldsymbol{r}) = N_{\boldsymbol{p}=m\omega\boldsymbol{r}}. \tag{5.20}$$

One can numerically evaluate the expected density distribution $n(\boldsymbol{r})$ with two different shapes for the correlation function $g_1^\infty(r)$: either a power law $r^{-\eta}$, or an exponential decay $\exp(-r/\ell)$, as suggested by the theoretical analysis of the BKT transition. These computations are shown respectively on Fig. 5.7a and 5.7b, and they have been performed with parameters close to the experimental ones: $\omega = 2\pi \cdot 10\,\text{Hz}$ and $R = 20\,\mu\text{m}$.

The curves of Fig. 5.7a indicate that the difference between power laws with exponents η between 0 and 0.25 are very difficult to determine with a spatial resolution on the order of 1 µm. This difference is below the experimental noise, as the typical experimental curve shown on Fig. 5.5 illustrates. It is also difficult to distinguish a power law behaviour from an exponential decay with a large ℓ by looking at the shape of the momentum distribution: the narrowest of Fig. 5.7a and 5.7b have very similar shapes, that are mostly determined by the Fourier transform of F.

For each of the computed momentum distributions, we can determine their HWHM σ_H. These quantities are reported on Fig.5.8. The exponent η for the power law is chosen between 0 and 1.5, and the characteristic length ℓ of the exponential decay is chosen between 1 and 50 µm.

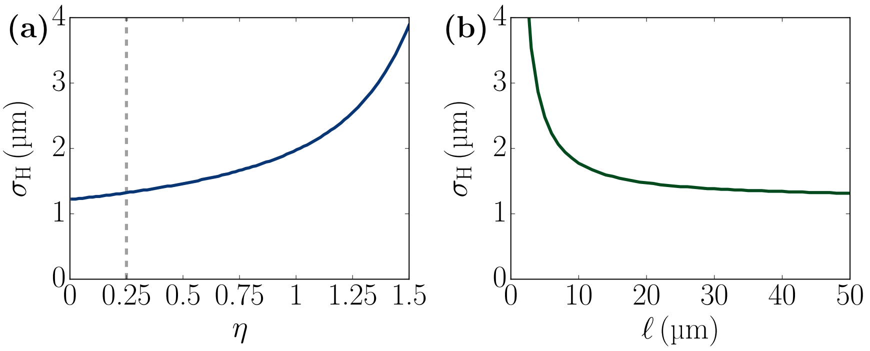

Figure 5.8: Half width at half-maximum σ_H of the computed momentum distributions for a disk of radius 20 µm. (a): The function g_1^∞ is modelled by a power law of exponent η. The graph shows the width of the obtained momentum distribution as a function of η. The interesting region for the BKT transition is for $0 \leq \eta \leq 0.25$, delimited by the dashed grey line. (b): The function g_1^∞ is modelled by an exponential with characteristic length ℓ. The graph shows the width of the obtained momentum distribution as a function of ℓ.

One can now try to compare the experimental data with these numerical computations. For each experimental point of Fig. 5.6, we determine on one hand the values of the exponents η that are compatible with the measured value of the width of the momentum distribution if it is modelled with a power law. We take as a criterion for compatibility the error bar on the measured width, which is the confidence interval at one standard deviation of the fit. On the other hand we determine the values of the length ℓ compatible with this measurement if it is modelled with an exponential law. The results are presented respectively on Fig. 5.9a and Fig. 5.9b. Each vertical bar represents the range of parameters that are compatible with the experimental data.

One can first observe that the results do not provide an accurate determination of the parameters η or ℓ. For example, at very low temperature, the width of the momentum distribution is compatible with a power law with exponent η going from 0 to 0.3 or 0.4, and with an exponential decay with a correlation length larger than 30 µm. This shows however that the correlation of the gas extends from one side to the other of the full system.

When the temperature is increased above T_c, the width of the momentum distribution increases and it becomes incompatible with low values of η, and with high values of ℓ. We cannot say whether the correlation function g_1^∞ is a power low or an exponential, but in the first case, its exponent would be larger than 0.25, and in the second case, the coherence length would become smaller than the full size of the system.

It is to note that the ratio T/T_c is determined independently from the measurements of the momentum distribution. The width of the momentum distribution changes of behaviour when this ratio is around 1, which is a direct hint that this effect is due to the change of behaviour of the phase coherence across the gas.

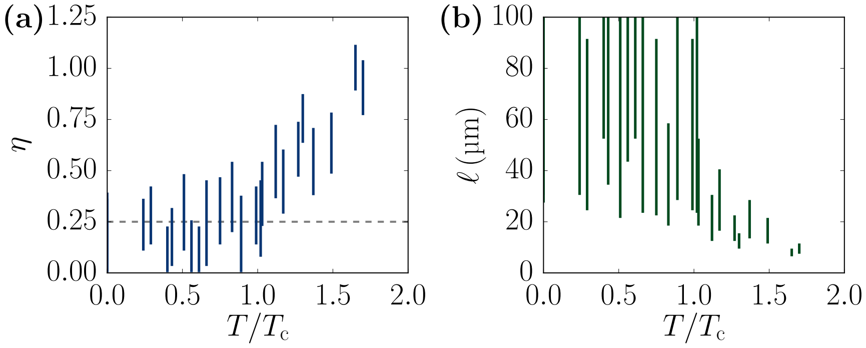

Figure 5.9: Comparison between the experimental data presented on Fig. 5.6 and the computations summarized on Figs. 5.7 and 5.8. (a): For each experimental point, assuming that the correlation function is a power law, the range of exponents η that are compatible with the measurement is indicated as a vertical bar. (b): For each experimental point, assuming that the correlation function is an exponential, the range of characteristic lengths ℓ that are compatible with the measurement is indicated as a vertical bar.

When performing the same numerical simulations with different parameters, for example with a disk of larger radius, one finds that the ability to distinguish a power law from an exponential decay, or to determine the parameter of any of these functions is not improved. The shape of the momentum distribution is mostly given by the function F describing the finite size of the system, and our experiment is limited by the small size of the momentum distribution and the low number of atoms that we allow ourselves to image.

This picture is slightly different if one uses a different atomic species. The ability to tune the interactions with a Feshbach resonance could allow one to work with a higher number of atoms, and using a lighter atom such as Lithium increases the size of the region that the cloud occupies after the evolution in the harmonic potential. The data reported in [163] indeed show that for a frequency similar to the one we have, the atomic signal has a much larger range than ours, with a factor given by the mass ratio $m_{\mathrm{Rb}}/m_{\mathrm{Li}} = 87/6 \approx 15$.

5.3 CONCLUSION

In this chapter, I have presented a method to measure the momentum distribution of a uniform 2D Bose gas and I have explained how the measurement of such distributions can be linked to the size of the initial gas and to its first-order correlation function. Due to the limitations of the experimental scheme, which come from the interactions between the atoms that we need to avoid, this method does not allow us to determine the exact shape of the first-order correlation function - power law or exponential decay, nor to extract precise parameters of any of these two laws if one assumes which describes the best the system.

However, some trends can be extracted by measuring the width of the momentum distribution. This width indeed increases when increasing the temperature T of the gas, which indicates that the range of the first-order correlation function decreases. If one assumes that this correlation function is a power law, its exponent is below 0.3 when T is below the critical temperature T_c, as expected from the BKT theory. This exponent increases notably above 0.25 when T gets larger than T_c. If one assumes that the correlation function is a decaying exponential, its characteristic length ℓ is larger than the size of the system when $T < T_\mathrm{c}$, which means that the system has a full coherence, and it decreases to values smaller than the system size when $T > T_\mathrm{c}$. This is compatible with the BKT theory for which g_1 is a power law with an exponent smaller than 0.25 when $T < T_\mathrm{c}$, and an exponential with a coherence length diverging at the critical temperature when $T > T_\mathrm{c}$.

These measurements are not accurate enough to assert stronger statements, and this particular experimental method does not seem to be precise enough, at least not with our experimental constraints. Alternative methods need to be used in order to determine more precisely the first-order correlation function, methods that are more direct and not relying on the measurement of $n_{\boldsymbol{p}}$. This is the subject of the next chapter.

6

MEASURING g_1 VIA ATOMIC INTERFEROMETRY

To measure the first-order correlation function with a precision better than what has been presented in the previous chapter, one can turn to the direct measurement of the phase correlation between points of the gas separated by a variable distance. The correlation G_1 for a classical field ψ is defined as

$$G_1(\mathbf{0}, \boldsymbol{r}) = \langle \psi(\mathbf{0}) | \psi(\boldsymbol{r}) \rangle \,, \tag{6.1}$$

and such a measurement of phase correlations can be achieved by interferometric methods.

A possible scheme, illustrated for example in [177, 178], consists in creating a copy of the gas with a pulse of Bragg beams. This copy is given a momentum kick and moves with respect to the original cloud. A second pulse recombines the two copies, and varying the relative phase between the two pulses allows one to determine the contrast of the local interference between the two clouds. The time interval Δt between the two pulses controls the relative distance that is probed, and one can reconstruct the phase coherence of the cloud.

This scheme could be implemented on our experimental set-up with the Bragg beams that I presented in Chapter 3. We tried to perform such a scheme, but we were limited by the fact that the two copies of the cloud interact while one moves with respect to the other. Their relative phase gets a large spurious term due to this interaction and masks the initial relative phase that we wish to probe. This is the case as soon as the phase

$$\phi_{\mathrm{d}} = \frac{E_{\mathrm{int}} \Delta t}{\hbar} \tag{6.2}$$

is not small compared to 1. In our case, the time interval Δt has to be on the order of several milliseconds if we want to probe distances on the order of the system size, and E_{int}/h is on the order of a few hundreds of hertz. We have ϕ_{d} on the order of unity, which is detrimental to measure the initial relative phase of the two copies of the cloud. In reference [178], the atomic density, and thus the interaction energy, is much lower than ours, which explains why this method is well-suited in one case and not in the other.

We have nevertheless determined an experimental scheme that could allow us to measure the phase correlation between different points of the gas. This scheme relies on an interferometric measurement, similarly to experiments with polaritons [159–161], and to the experiments in three-dimensional gases reported in [48, 140]. We select two regions of the gas with the Raman beams, we remove the atoms in the other regions and we let the atoms in the two selected regions interfere, very similarly to Young's slits experiment. With this scheme, we have recently performed a set of experiments to measure the first-order correlation function across the BKT transition.

I first develop a few elements of theory to describe how two initially separated wave functions expand and interfere. I then describe the experimental sequence that we use to extract the first-order correlation function. Finally, I present a preliminary method of analysis of the obtained data, I show the results that we get with this method, and I discuss the various effects that we need to take into account to increase the confidence we have in these results.

6.1 INTERFERENCE BETWEEN TWO SEPARATED WAVE PACKETS

I describe here how two separate wave packets freely expand and interfere, and how we can extract information from such an interference. In the first paragraph I present a simple one-dimensional model, and in the following one I include a second dimension to be closer to the experimental situation.

6.1.1 *Free expansion of two wave packets in one dimension*

Let us consider two wave packets in a one-dimensional space, that have an initial Gaussian shape of waist σ_l, and separated by a distance $d_l > \sigma_l$. The initial wave functions of the two wave packets, labelled as ψ_1 and ψ_2 are

$$\psi_1(x, t = 0) = \sqrt{\frac{2}{\pi\sigma_l^2}} \exp\left[-\frac{2(x - d_l/2)^2}{\sigma_l^2} + \mathrm{i}\phi_1\right], \tag{6.3}$$

$$\psi_2(x, t = 0) = \sqrt{\frac{2}{\pi\sigma_l^2}} \exp\left[-\frac{2(x + d_l/2)^2}{\sigma_l^2} + \mathrm{i}\phi_2\right]. \tag{6.4}$$

The two lines are centred on $\pm d_l/2$ and $\phi_{1,2}$ are the initial phases of the two wave packets.

In the absence of interactions one can compute the evolution of the wave function of each packet thanks to the propagator K of a free particle in a one-dimensional space [179]. For example for the first packet:

$$\psi_1(x, t) = \int_{-\infty}^{+\infty} \mathrm{d}x' K(x, x', t)\ \psi_1(x', t = 0), \tag{6.5}$$

with

$$K(x, x', t) = \sqrt{\frac{m}{2\pi\mathrm{i}\hbar t}} \exp\left[-\frac{m(x - x')^2}{2\mathrm{i}\hbar t}\right]. \tag{6.6}$$

We find that the wave function of the initial line at time t is

$$\psi_1(x, t) = A(x, t) \exp\left[-\frac{\left(\frac{\mathrm{i}mx}{\hbar t} - \frac{2d_l}{\sigma_l^2}\right)^2}{\frac{2\mathrm{i}m}{\hbar t} - \frac{8}{\sigma_l^2}} + \mathrm{i}\phi_1\right], \tag{6.7}$$

with the amplitude

$$A(x, t) = \frac{-\mathrm{i}}{\sqrt{\pi}\sqrt{\frac{\sigma_l^2}{2} + \frac{2\mathrm{i}\hbar t}{m}}} \exp\left(\frac{\mathrm{i}mx^2}{2\hbar t} - \frac{4d_l^2}{\sigma_l^2}\right) \tag{6.8}$$

that is common to ψ_1 and ψ_2. The width $\sigma_l(t)$ of this wave function is

$$\sigma_l^2(t) = \sigma_l^2 + \frac{16\hbar^2 t^2}{m^2\sigma_l^2}. \tag{6.9}$$

The evolution of the full initial wave function $\psi_{1\mathrm{D}} = (\psi_1 + \psi_2)/\sqrt{2}$ is given by the superposition of their individual evolutions:

$$\psi_{1\mathrm{D}}(x,t) = \frac{A(x,t)}{\sqrt{2}} \left\{ \exp\left[-\frac{\left(\frac{\mathrm{i}mx}{\hbar t} - \frac{2d_l}{\sigma_l^2}\right)^2}{\frac{\mathrm{i}m}{2\hbar t} - \frac{2}{\sigma_l^2}} + \mathrm{i}\phi_1 \right] + \exp\left[-\frac{\left(\frac{\mathrm{i}mx}{\hbar t} + \frac{2d_l}{\sigma_l^2}\right)^2}{\frac{\mathrm{i}m}{2\hbar t} - \frac{2}{\sigma_l^2}} + \mathrm{i}\phi_2 \right] \right\}. \tag{6.10}$$

The two parts will interfere when their width $\sigma_l(t)$ is on the order of d_l. When this time is reached, and in the limit where $x \ll d_l$, the wave function can be written as

$$\psi_{1\mathrm{D}}(x,t) = A'(x,t) \cos\left(\frac{x}{\frac{2\hbar t}{m d_l} + \frac{m\sigma_l^4}{8\hbar t d_l}} + \frac{\phi_1 - \phi_2}{2} \right), \tag{6.11}$$

where

$$A'(x,t) = \frac{A(x,t)}{\sqrt{2}} \exp\left(-\frac{\frac{m^2 x^2 \sigma_l^4}{\hbar^2 t^2} + 4d_l^2}{2\sigma_l^2 - \frac{\mathrm{i}m\sigma_l^4}{2\hbar t}} + \mathrm{i}\frac{\phi_1 + \phi_2}{2} \right). \tag{6.12}$$

The modulus square of this wave function gives the interference between the two initial packets:

$$|\psi_{1\mathrm{D}}(x,t)|^2 \propto \exp\left(-\frac{2x^2}{\frac{\sigma_l^2}{8} + \frac{2\hbar^2 t^2}{m^2 \sigma_l^2}} \right) \cos^2\left(k_l x + \frac{\phi_1 - \phi_2}{2} \right), \tag{6.13}$$

where

$$k_l = \frac{1}{\frac{2\hbar t}{m d_l} + \frac{m\sigma_l^4}{8\hbar t d_l}} \tag{6.14}$$

is the wave vector of the cosine function involved here. Around $x = 0$, the interference pattern is therefore well approximated by a Gaussian envelope modulated by a squared cosine function whose phase depends on the initial phase difference $\phi_1 - \phi_2$ between the two initial packets.

If the evolution time is large enough, the second term of the denominator in equation 6.14 can be neglected. The wave vector k_l is thus inversely proportional to t and does not depend on the width σ_l of the initial wave functions:

$$k_l \approx \frac{m d_l}{2\hbar t}. \tag{6.15}$$

If the phase difference $\phi_1 - \phi_2$ fluctuates from one experimental realisation to the other due to the non-perfect phase correlation between the two initial lines, then the interference pattern will change from one realisation to the other. This fluctuation is directly linked to the first-order correlation function g_1 that we want to measure. Equivalently, one can average the interference pattern over several experimental realisations and the contrast of this averaged pattern will reflect the fluctuation of relative phase. This is the approach that we have in the following, and a more accurate description of the experimental situation is developed in the next paragraph.

6.1.2 *Free expansion of two wave packets in two dimensions*

Let us now consider a two-dimensional geometry. We denote as $\psi(x,y)$ the classical field describing a two-dimensional Bose gas on an infinite plane. We suppose that we are able to isolate two parts from this classical field, and we choose to isolate two lines with a Gaussian shape in the x direction with a width σ_l, separated by a distance d, and infinite in the y direction. The initial wave function of the two isolated lines is then

$$\psi_1(x,y) = \psi(x,y) \cdot \sqrt{\frac{2}{\pi\sigma_l^2}} \exp\left(-\frac{2(x-d_l/2)^2}{\sigma_l^2}\right), \tag{6.16}$$

$$\psi_2(x,y) = \psi(x,y) \cdot \sqrt{\frac{2}{\pi\sigma_l^2}} \exp\left(-\frac{2(x+d_l/2)^2}{\sigma_l^2}\right). \tag{6.17}$$

We derive the subsequent evolution of these two lines thanks to the two-dimensional propagator $K(x,y,x',y',t)$, given by:

$$K(x,y,x',y',t) = \frac{m}{2\pi \mathrm{i}\hbar t} \exp\left[-\frac{(x-x')^2+(y-y')^2}{2\mathrm{i}\hbar t/m}\right]. \tag{6.18}$$

We perform the calculation in the limit where the width σ_l is smaller than the length on which the wave function ψ fluctuates. We obtain for ψ_1 and ψ_2 considered separately:

$$\psi_1(x,y,t) = B_1(x,t)\, I_1(y,t), \tag{6.19}$$

$$\psi_2(x,y,t) = B_2(x,t)\, I_2(y,t), \tag{6.20}$$

where

$$B_1(x,t) = \frac{-\mathrm{i}}{\sqrt{\pi}\sqrt{\frac{\sigma_l^2}{2}+\frac{2\mathrm{i}\hbar t}{m}}} \exp\left[-\frac{(x-d_l/2)^2}{\frac{\sigma_l^2}{2}+\frac{2\mathrm{i}\hbar t}{m}}\right], \tag{6.21}$$

$$B_2(x,t) = \frac{-\mathrm{i}}{\sqrt{\pi}\sqrt{\frac{\sigma_l^2}{2}+\frac{2\mathrm{i}\hbar t}{m}}} \exp\left[-\frac{(x+d_l/2)^2}{\frac{\sigma_l^2}{2}+\frac{2\mathrm{i}\hbar t}{m}}\right], \tag{6.22}$$

$$I_1(y,t) = \int \mathrm{d}y'\ \psi\left(\frac{d_l}{2}, y'\right) \exp\left[\frac{im}{2\hbar t}(y-y')^2\right], \tag{6.23}$$

$$I_2(y,t) = \int \mathrm{d}y'\ \psi\left(-\frac{d_l}{2}, y'\right) \exp\left[\frac{im}{2\hbar t}(y-y')^2\right]. \tag{6.24}$$

The interference pattern is the modulus square of the sum of the two wave functions ψ_1 and ψ_2:

$$|\psi_{2\mathrm{D}}(x,y,t)|^2 = \frac{1}{2}|\psi_1(x,y,t)+\psi_2(x,y,t)|^2. \tag{6.25}$$

Since the lines are infinite in the y direction we choose to evaluate this interference pattern when $y=0$:

$$|\psi_{2\mathrm{D}}(x,0,t)|^2 = |\psi_1(x,0,t)|^2 + |\psi_2(x,0,t)|^2 + 2\mathrm{Re}\left[\psi_1^*(x,0,t)\psi_2(x,0,t)\right]. \tag{6.26}$$

More precisely we will be interested in this interference pattern averaged over many experimental realisations: $\left\langle|\psi_{2\mathrm{D}}(x,0,t)|^2\right\rangle$. In this expression there are terms involving products of $B_1(x,t)$ and $B_2(x,t)$, which will give terms similar to the ones obtained in the previous paragraph. There are also averaged values of products of $I_{1,2}(0,t)$. We evaluate one of them separately:

$$\langle I_1^*(0,t)I_2(0,t)\rangle = \iint \mathrm{d}y'\mathrm{d}y'' \left\langle \psi^*\left(\frac{d_l}{2},y'\right)\psi\left(-\frac{d_l}{2},y''\right)\right\rangle \exp\left[\frac{\mathrm{i}m}{2\hbar t}(y'^2-y''^2)\right], \tag{6.27}$$

and we perform the change of variable $y' = Y - y_r/2$, $y'' = Y + y_r/2$ of unit Jacobian:

$$\begin{aligned}\langle I_1^*(0,t)I_2(0,t)\rangle = \iint \mathrm{d}Y\mathrm{d}y_r \left\langle \psi^*\left(\frac{d_l}{2},Y-\frac{y_r}{2}\right)\psi\left(-\frac{d_l}{2},Y+\frac{y_r}{2}\right)\right\rangle \\ \times \exp\left[\frac{\mathrm{i}m}{\hbar t}Yy_r\right].\end{aligned} \tag{6.28}$$

The averaged value does not depend on Y because the problem has a translational invariance in the y direction. The integration over Y is then straightforward:

$$\langle I_1^*(0,t)I_2(0,t)\rangle = \frac{2\pi\hbar t}{m}\int \mathrm{d}y_r \left\langle \psi^*\left(\frac{d_l}{2},-\frac{y_r}{2}\right)\psi\left(-\frac{d_l}{2},\frac{y_r}{2}\right)\right\rangle \delta(y_r), \tag{6.29}$$

which in turn gives

$$\begin{aligned}\langle I_1^*(0,t)I_2(0,t)\rangle &= \frac{2\pi\hbar t}{m}\left\langle \psi^*\left(\frac{d_l}{2},0\right)\psi\left(-\frac{d_l}{2},0\right)\right\rangle &(6.30)\\ &= \frac{2\pi\hbar t}{m}G_1(d_l), &(6.31)\end{aligned}$$

where $G_1(d_l)$ is the correlation function of the classical field ψ at distance d_l.

The other terms in the expression of $\left\langle|\psi_{2\mathrm{D}}(x,0,t)|^2\right\rangle$ are obtained similarly. We use the same assumptions as in 6.1.1: the expansion duration t is large enough so that the two initial lines overlap and we stay in the limit $x \ll d_l$. In the end we get:

$$\left\langle|\psi_{2\mathrm{D}}(x,0,t)|^2\right\rangle \propto \exp\left(-\frac{2x^2}{\frac{\sigma_l^2}{8}+\frac{2\hbar^2t^2}{m^2\sigma_l^2}}\right)\left[G_1(0)+G_1(d_l)\cos(2k_lx)\right]. \tag{6.32}$$

The centre of the interference pattern is thus a Gaussian envelope with a cosine modulation whose contrast C is

$$C = \frac{G_1(d_l)}{G_1(0)} = g_1(d_l). \tag{6.33}$$

Measuring the average value of the interference pattern between two lines isolated from a 2D Bose gas and extracting the contrast of this pattern thus provide an estimate of the first-order correlation function. This is what we want to achieve with the experimental scheme that I present in the next section.

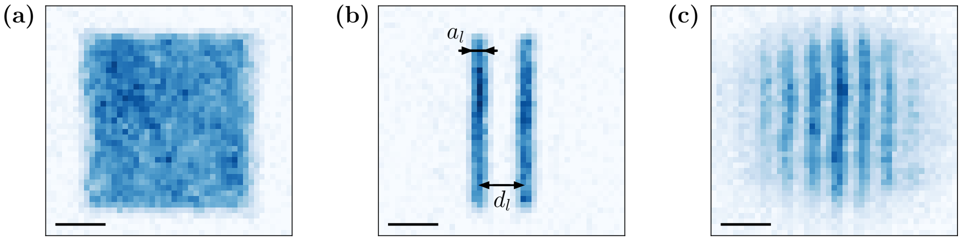

Figure 6.1: Experimental procedure. (a) The gas is prepared in a square of side 40 µm and its ratio T/T_c is controlled and can be measured independently. (b): All the atoms are transferred to the state $F = 2, m_F = 0$ with a microwave pulse. A controlled fraction of the atoms contained in the region of two lines is transferred back to the state $F = 1, m_F = 0$ with the Raman beams. We send a beam resonant with the transition $F = 2 \rightarrow F' = 3$ on the sample, and the atoms that have stayed in the state $F = 2$ are expelled from the trap. The picture shows the two lines that we isolate with this method. Their expected full-width is a_l and the distance between their centre is d_l. (c): The two lines expand and interfere. On all the images, the solid black line corresponds to 10 µm.

6.2 SETTING UP AND CHARACTERISING THE EXPERIMENTAL SCHEME

I explain here how we experimentally implement the interferometric scheme described above: isolating two lines from an initial gas, and letting them interfere. I characterise the expansion of these two lines and compare it to the previous calculations.

6.2.1 *The experimental sequence*

The main steps of the experimental sequence are illustrated on Fig. 6.1, and they happen as follows:

1. We start with a uniform cloud in a square-shaped optical box potential of side $L = 40$ µm (Fig. 6.1a). We control the number of atoms and the height of the box potential to fix the ratio T/T_c. We measure this ratio independently.

2. We transfer all the atoms to the state $F = 2, m_F = 0$ with a microwave pulse. We then spatially transfer a controlled fraction of atoms in a chosen region of space back to the state $F = 1, m_F = 0$ thanks to the Raman beams presented in Chapter 3. This region where we want the atoms to be transferred has the shape of two uniform lines of full-width a_l and their centre is separated by a distance d_l that can vary from 3 to 22 µm, as shown on Fig. 6.1b. When $d_l > 4$ µm, we choose $a_l \approx 4$ µm, and if $d_l = 4$ µm (resp. 3 µm) we reduce it to 2 µm (resp. 1 µm). An example of the density distribution of the atoms transferred back in $F = 1, m_F = 0$ is presented on Fig. 6.1b. The profile of the two lines in the x direction is not exactly flat due to the optical resolution of the microscope objectives: the edges of the two lines are smoothed on a range on the order of 1 µm. On the picture, this profile is well fitted with a Gaussian with a full-width

at $1/\mathrm{e}^2$ of $\approx 5\,\mu\mathrm{m}$, but this picture is taken after almost 1 ms of free expansion, and therefore does not represent well the initial profile of the two lines.

3. At $t = 0$ we send a pulse of light resonant with the closed transition $F = 2 \rightarrow F' = 3$ during $40\,\mu\mathrm{s}$ in the vertical direction. The atoms that are in $F = 2$ absorb several photons and receive a momentum kick in the z direction. Each photon gives a kinetic energy E_{kin} to the atoms:

$$\frac{E_{\mathrm{kin}}}{k_{\mathrm{B}}} \approx 200\,\mathrm{nK}. \tag{6.34}$$

The vertical confinement is lowered to a height U that is on the order of

$$\frac{U}{k_{\mathrm{B}}} \approx 100\,\mathrm{nK}. \tag{6.35}$$

This height is not strong enough to keep the atoms that have absorbed photons. These atoms then leave the trap. If we image the atoms in $F = 2$ that have stayed in the trap after a few milliseconds, the signal is below the noise of our imaging system. Shortly after $t = 0$, the atoms in the two lines that have been transferred to $F = 1$ are thus left without any neighbours.

4. At $t = 0$, we also remove the confining walls of the box potential and we let the atoms in $F = 1$ expand in the vertical confinement during a few milliseconds. The interaction parameter $\tilde{g}$ during this expansion is 0.08. These two lines interfere, as shown on Fig. 6.1c.

6.2.2 *Measuring the expansion of one line*

The expansion of the two lines does not exactly match the description of the previous section, mostly because of interactions. We experimentally quantify this by preparing a single line with a full-width $a_l = 4\,\mu\mathrm{m}$ and measuring its full-width at $1/\mathrm{e}^2$ σ_x as a function of the evolution time. This experiment is performed for several numbers of atoms transferred to the state $F = 1, m_F = 0$ by the Raman beams. This is achieved by changing the duration of the Raman pulse. These measurements are presented on Fig. 6.2a. The expansion of the lines is fairly linear with time and a velocity of expansion can be extracted from these curves.

This velocity is larger when the initial density is larger, as shown on Fig. 6.2b. When extrapolating this velocity to zero density, we get $v_x \approx 1\,\mathrm{mm/s}$, which would be the expansion velocity of an initial Gaussian with a full-width at $1/\mathrm{e}^2$ of $4\,\mu\mathrm{m}$.

Qualitatively, the extra energy due to the initial interactions is converted into kinetic energy during the expansion, which explains why the asymptotic velocity increases when increasing the initial atom number. One can try to quantitatively take into account this initial interaction energy, and naively estimate the asymptotic expansion velocity that we can expect:

$$v_{\mathrm{int}} = \sqrt{\frac{16\hbar^2}{m^2\sigma_l^2} + \frac{\hbar^2\tilde{g}n}{m^2}}, \tag{6.36}$$

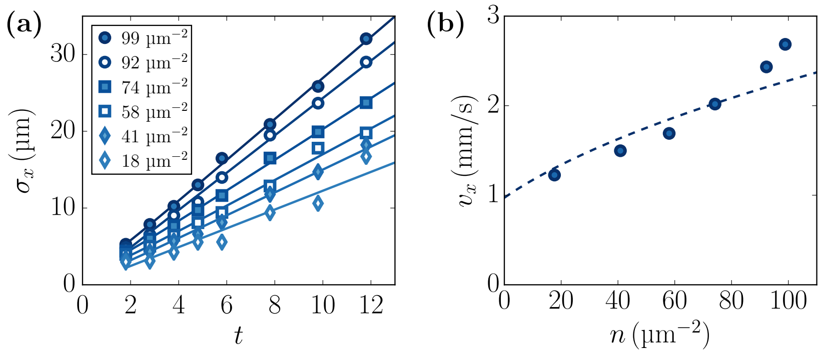

Figure 6.2: Expansion of a single line of initial full-width $a_l = 4$ µm. (a): A single line is isolated with the method presented above, with a variable number of atoms. The width of this line is measured as a function of the time of expansion. The expansion is faster when the initial density is larger. The value of the initial densities span from 20 to 100 µm^{-2}, as reported in the legend. (b): The velocity of expansion is extracted from the graph on the left, as a function of the initial density. The dashed line represents the simple model 6.36 that takes into account the initial interactions.

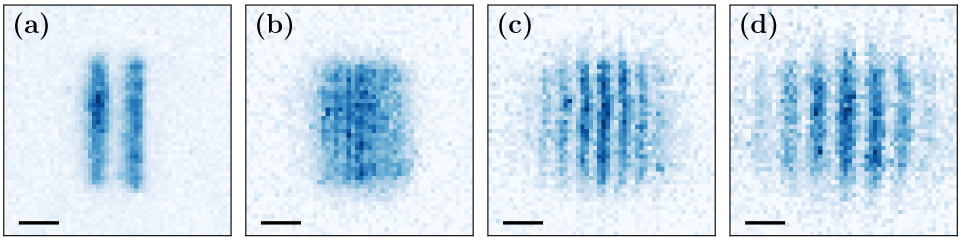

Figure 6.3: Interference of two lines. The two initial lines are separated by 10 µm and have an initial full-width of 4 µm. The four images correspond respectively to an expansion time of 1.9, 5.8, 9.8 and 13.8 ms from left to right. The solid black line corresponds to 10 µm.

where the first term is the asymptotic velocity without interactions obtained from equation 6.9 and the second term is the contribution of the initial interactions. This simple estimate is shown on Fig. 6.2b as a dashed line. It does not describe very accurately the data points, but it provides the good order of magnitude of the increase of velocity that we have on the experiment.

Interactions between atoms play a role only at the beginning of the expansion: after a few milliseconds, the atomic density drops, and the expansion is a single-particle expansion, which justifies that we will use the form of the wave function given by the expansion presented above. The fact that the initial wave function is not exactly a Gaussian should not be very important, and the width of the whole cloud after a few milliseconds of expansions is well described by a Gaussian envelope.

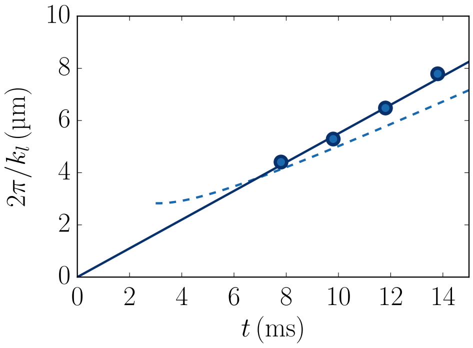

Figure 6.4: The period $2\pi/k_l$ of the interference fringes shown on Fig. 6.3 is measured and plotted as a function of the duration of expansion. This period is linear with time, as shown by the fit represented as a solid dark line. It slightly differs from the theoretical prediction given by equation 6.14 represented as a dashed light line.

6.2.3 *Measuring the expansion of two lines*

We now perform experiments with two lines isolated from the initial square. On Fig. 6.3 are shown a few images of the expansion of two lines separated by 10 µm. The two lines overlap after 5 ms approximately (see Fig. 6.4b), and interference fringes appear [180] with a fringe spacing that increases with time, as shown on Fig. 6.4c and d.

We can measure the periodicity of the interference pattern as a function of the time of evolution. These measurements can only be done when the two lines overlap and when this periodicity can be resolved by our imaging system. The results for the two lines separated by $d_l = 10\,\mu\text{m}$ are shown on Fig. 6.4. The period of the pattern is fairly linear with the duration t of the evolution, as the limit of equation 6.14 predicts. However, the fitted slope (indicated as a solid dark blue line) does not match the predicted one. The dashed light blue line represents the non-interacting model given by equation 6.14. At present, we do not have a quantitative explanation for this $\approx 25\%$ difference.

For the following experiments, we fix the fraction of atoms transferred in the state $F = 1, m_F = 0$. We adjust the time of expansion to have the periodicity of the interference pattern around 5 µm. This value of the periodicity is chosen so that the duration of expansion is not too large, and so that it is well resolved by our optical system.

6.3 MEASURING THE PHASE ORDERING ACROSS THE BKT TRANSITION

I detail here a still preliminary method to estimate the first-order correlation function from the average of a finite number of experimental realisations. I then present the results of our measurements of the phase correlation when varying the temperature from below to above the critical temperature. Finally, I discuss the effects that could affect these measurements.

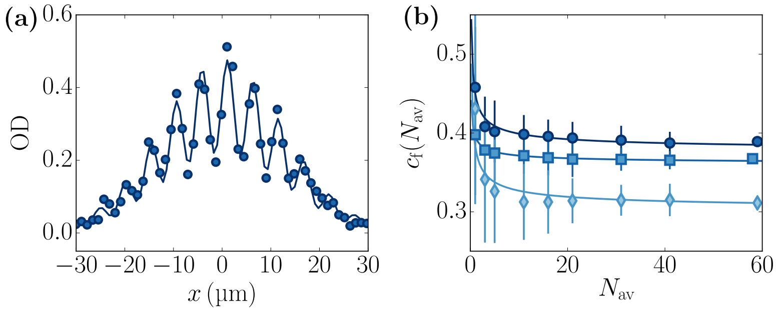

Figure 6.5: Determining the average contrast of the interference fringes. (a): The interference pattern between the two lines is averaged over N_{av} images. The graph shows the profile along x of the density distribution averaged over five pixels in the y direction. On this particular example, the initial distance between the two lines is $d_l = 10\,\mu m$, and $N_{av} = 59$. (b): The contrast c_f of the interference pattern is measured as a function of N_{av}, for three values of d_l: 4, 12 and 18 µm, respectively represented by disks, squares and diamonds. The asymptote of each curve is determined and is our estimate of the value of $g_1(d_l)$. On these examples we already see that the phase coherence decreases when increasing the distance d_l.

6.3.1 *Extracting the contrast of the averaged interference pattern*

When averaging several experimental realisations of the interference between the same two lines, we saw that the pattern we obtain along the x direction is

$$n(x) = \frac{n_0}{2} \exp\left(-\frac{x^2}{\sigma_e^2}\right) [1 + g_1(d_l) \cos(2k_e x)] , \tag{6.37}$$

where n_0 is the average density in the centre of the pattern, σ_e is the experimental width of the Gaussian envelope and k_e is the experimental wave vector of the interference pattern.

An example is given on Fig. 6.5a, where is shown the profile integrated along five pixels of the camera in the y direction. This profile is fitted with the function

$$x \mapsto A_f \exp\left(-\frac{x^2}{\sigma_e^2}\right) \; [1 + c_f \cos(2k_e x + \phi)] , \tag{6.38}$$

where ϕ is an adjustable phase.

Due to the finite number of experimental realisations that we can perform, the contrast c_f we measure is not exactly $g_1(d_l)$. In order to better estimate $g_1(d_l)$, we vary the number of images N_{av} that we average, and we extract the contrast $c_f(N_{av})$ of the averaged interference pattern. This contrast is plotted as a function of N_{av} on Fig. 6.5b, for the same initial gas and different values of d. The contrast of the fringes decreases when averaging more and more images, and we expect it to converge to $g_1(d_l)$ when averaging a larger and larger number of images.

The data points are then fitted with the function $x \mapsto C + A/\sqrt{N_{av}}$, where A and C are free parameters of the fit. The value of C that we obtain is the limit of the contrast when N_{av} goes to infinity, and it is our estimate of $g_1(d_l)$.

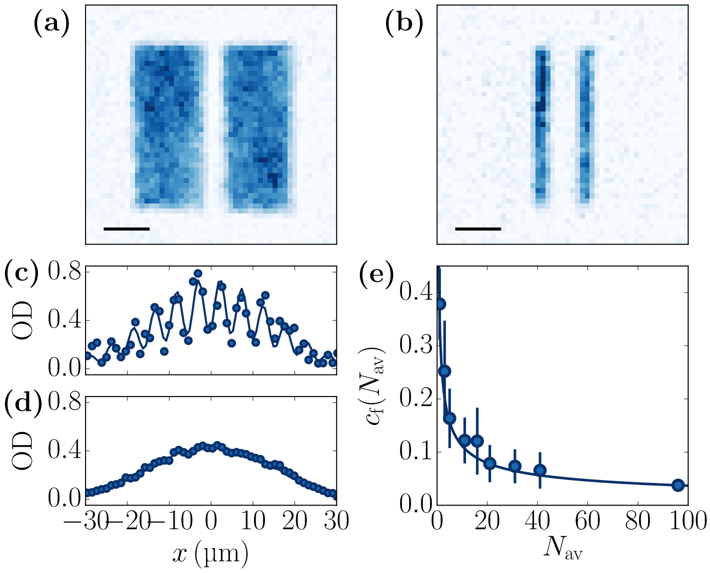

Figure 6.6: Correlation between two independent boxes. (a): Two independent clouds are prepared. Their relative phase is expected to uniformly sample the interval from 0 to 2π. (b): Two lines of full-width 4 µm are isolated, one from each cloud. (c): The two lines interfere. The density distribution obtained with a single experimental realisation is integrated over a few pixels in the y direction. The contrast of the interference pattern is large, on the order of 0.4. (d): The profiles obtained from 100 experimental realisations are averaged. The contrast of the fringes is much lower, around 0.05. (e): The measured contrast is plotted as a function of the number of averaged images N_{av} (blue circles). It is fitted to obtain the correlation between the two initial lines. The limit of contrast when $N_{av} \to \infty$ is 0.002(5), which is compatible with an absence of correlations between the two initial clouds.

We check our method, with the interference between two independent clouds that have no phase correlation. These clouds are shown on Fig. 6.6a. The two box potentials are first filled by a thermal cloud, and then we proceed to the evaporation step. In these conditions, we expect that the relative phase between the two clouds is uniformly sampled between 0 and 2π. Then, we isolate two lines of full-width $a_l = 4\,\mu\text{m}$, one from each cloud and let them interfere.

On Fig. 6.6b and 6.6c are shown respectively the profile of this interference pattern along the x direction of a single image and of the average of 100 images taken in the same conditions. The limit C of the average contrast is extracted. It is estimated to be $C = 0.002(5)$, which is compatible with the absence of correlations between the two clouds.

We note that the contrast of a single image is not equal to 1, which could be due to several effects, which are discussed in paragraph 6.3.3.

6.3.2 *Results of the measurements across the critical temperature*

We now come back to the interference between two lines from an initial single square-shaped cloud of side 40 µm. We vary the ratio T/T_c of the system

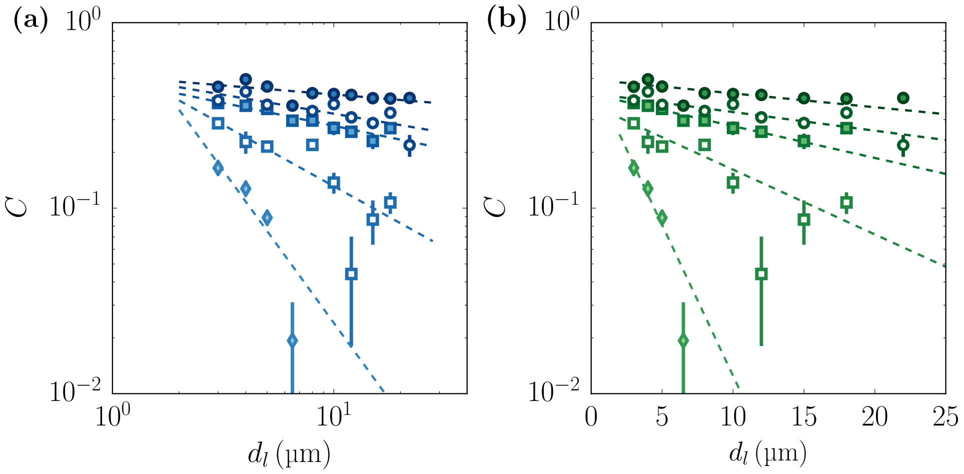

Figure 6.7: Variation of the contrast C with the distance d_l between the two lines. Five curves are presented, with $T/T_\mathrm{c} = 0.49(5)$ (filled circles), 0.93(3) (empty circles), 1.01(5) (filled squares), 1.29(4) (empty squares) and 1.63(7) (filled diamonds). The curves with low values of T/T_c are the flattest. (a): The data points are represented in a graph with axes that have a logarithmic scale. The dashed lines are the fits of the curves with power laws. (b): The same data points are represented in a graph where only the y axis has a logarithmic scale. The dashed lines are the fits of the curves with exponential decays.

between 0.3 and 1.6. For each value of this ratio, we measure the averaged contrast C of the interference pattern for different distances d_l between the lines. Typically, d_l varies from 3 to 22 µm. The results of a few curves are shown on Fig. 6.7.

The contrast C decreases when the distance d_l between the two lines increases, and this decrease is much faster when the ratio T/T_c is large, which shows that the phase coherence between distant points decreases when the temperature increases. On Fig. 6.7a, these data are presented in log-log graph, and they are fitted with a straight line. The slope $-\eta$ of this line corresponds to the exponent of the algebraic law that fits the best the measurements.

The same data points are plotted on Fig. 6.7b in a semi-log graph, and fitted with a straight line. This corresponds to the exponential $A\exp(-d_l/\ell)$ that best fits the measurements. We can extract a characteristic length ℓ from the slope of this line.

The data points are too scattered for us to be able to determine whether a power law or an exponential decay describe better any of the curves. For example, computing the χ^2 of the fits does not provide interesting information. With such a quality of data, a larger range of probed distances d_l would be necessary to distinguish between the two behaviours. We are limited here to $d_l \geq 3$ µm because of the resolution of the Raman beams that create the slits, and to $d_l \leq 22$ µm to keep a good signal-to-noise ratio and to prevent edge effects – we recall that the box has a side of 40 µm.

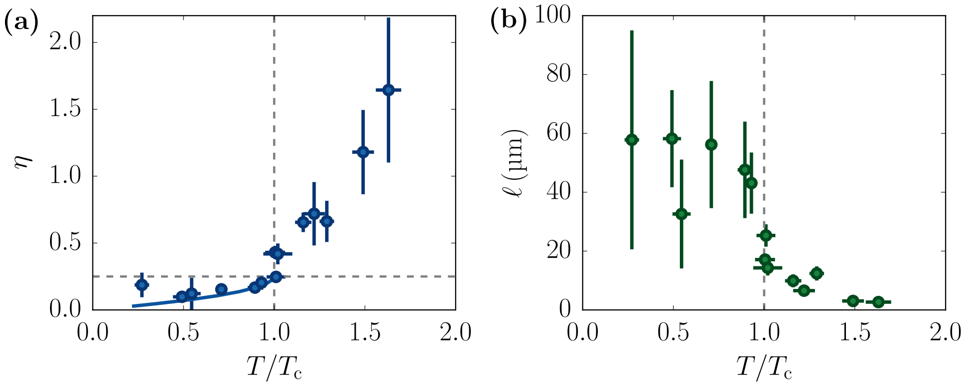

Figure 6.8: Parameters of the fits presented on Fig. 6.7. (a): The exponent η of the power-law fits shown on Fig. 6.7a are plotted as a function of T/T_c. The prediction below the critical temperature given by equation 6.39, is shown as a solid line. The vertical dashed represents $T = T_c$, and the horizontal line indicates the value $\eta = 0.25$. (b): The characteristic length ℓ of the exponential fit shown on Fig. 6.7b is plotted as a function of T/T_c. The vertical dashed line represents $T = T_c$.

The parameters that we extract from the two types of fits are presented on Fig. 6.8. The slope η of the power-law fits is plotted as a function of T/T_c on Fig. 6.8a. When the temperature is lower than the critical temperature, the fitted exponents are lower than 0.25, as predicted by the theory of the BKT transition. The theoretical prediction is

$$\eta = 1/\mathcal{D}_s, \tag{6.39}$$

where $\mathcal{D}_s$ is the superfluid phase-space density, which decreases from $+\infty$ to 4 when T increases from 0 to T_c. The exponent η thus goes from 0 to 0.25. This prediction is shown as a solid line on the graph, and is in good agreement with the data points. The leftmost point corresponds to data spanning a smaller range of distances, which goes against a proper determination of a slope in a logarithmic graph, and is reflected on its larger errorbar. When the temperature is higher than T_c, a fit with a power law gives an exponent which is significantly larger than 0.25, and increases with T/T_c. This is in good agreement with recent numerical simulations reported in [156, 181].

These results are compatible with the ones found in the previous chapter with the measurement of the momentum distribution, but here the measurements are more precise when determining the best exponent η that can describe the data. Moreover, around the critical temperature, while the width of the momentum distribution was not varying a lot, we found that the contrast of the interference fringes was very sensitive to the experimental fluctuations of T/T_c. This critical temperature is determined independently by measuring the equation of state of the gas, and the coincidence between $T \approx T_c$ and a high sensitivity of the experiment with respect to small fluctuations of temperature is a good qualitative sign that we are probing the physics of the BKT transition around its critical point.

The agreement between the data and the theory might however be only fortuitous, since we did not take into account several effects, as discussed in the next paragraph.

If we try to model the data with an exponential decay as on Fig. 6.7b, we can extract the parameter ℓ corresponding to the characteristic length of the decay. The dependence of this length with T/T_c is shown on Fig. 6.8b. For temperatures below the critical temperature, the contrast C decreases very slowly with the distance between the lines, and an exponential fit returns a large value of ℓ. The large error bars are due to the small range of distances probed (less than a decade) and to the scattering of the data. The characteristic lengths that we obtain are compatible with values larger than the full size of the system, which shows that there is phase ordering across the whole cloud.

As soon as the temperature is above the critical temperature, the contrast of the interference fringes decays faster with d_l, therefore an exponential fit gives a lower characteristic length ℓ. The values of these lengths get smaller than the size of the system, and go down to a few micrometers for T/T_c above 1.5, which shows that there is no phase ordering across the system any more.

6.3.3 *Discussion and effects that may affect the measurements*

The preliminary analysis that I have presented above does not take into account several effects that may change the result of the measurements. These effects are the following ones:

1. *Finite resolution of the imaging system*: This resolution has two contributions. First, the resolution of the microscope objective with which we image the atoms. It may blur the interference pattern that we image, and artificially decrease the contrast of the interference patterns. Second, the pixellisation of the camera. The period of the interference pattern covers a bit more than 4 pixels of the camera, which can reduce the measured contrast of the pattern. These two effects are the same for all the data points, since we chose the evolution time of the expansion of the lines so that this period is always the same. With an effective point-spread function of 1.2 µm, and a pixel size of 1.15 µm, the contrast is reduced by approximately 20%, which can account for a part of the reduction of contrast that we measure.

2. *Relative fluctuation of the atom number in the lines*: A possible effect that could prevent us to measure very accurately the relative phase between the two initial lines is the phase shift induced by interactions. A single line with an atomic density n indeed has a dynamical phase ϕ_d that evolves as
$$\phi_\mathrm{d} = \frac{\hbar \tilde{g} n t}{m}. \tag{6.40}$$
During the expansion of the lines, the density decreases in the first milliseconds and the interaction energy gets much smaller than the kinetic energy, therefore this dynamical phase is important only during the time

scale $t_{\mathrm{int}} \lesssim 1\,\mathrm{ms}$. The interference pattern has a position that depends on the total relative phase ϕ_{tot} between the two lines:

$$\phi_{\mathrm{tot}} = \Delta\phi + \Delta\phi_{\mathrm{d}}, \tag{6.41}$$

where $\Delta\phi$ is the initial phase difference between the two lines, and $\Delta\phi_{\mathrm{d}} = \hbar\tilde{g}t_{\mathrm{int}}(n_2 - n_1)/m$ and $n_{1,2}$ is the density of each of the lines.

If the relative atom number fluctuates from one experimental realisation to the other, then the fluctuation of the position of the bright fringes will not only depend on $\Delta\phi$, but also on $\Delta\phi_{\mathrm{d}}$. We have measured the atom number N_1 and N_2 in each of the two lines for 100 experimental realisations in the same conditions. While the relative fluctuation of the atom number in each of the lines is

$$\frac{\langle N_1\rangle}{N_1} = \frac{\langle N_2\rangle}{N_2} \approx 10\%, \tag{6.42}$$

the relative fluctuation of the difference in atom numbers in the two lines is on the order of

$$\frac{\langle N_2 - N_1\rangle}{N_1 + N_2} \approx 4\%. \tag{6.43}$$

This means that the number of the atoms that we transfer with the Raman beams can fluctuate, but this fluctuation partly affects the two lines in the same way. For a density below $50\,\mu\mathrm{m}^{-2}$, we estimate that the induced phase fluctuation is

$$\langle\Delta\phi_{\mathrm{d}}\rangle < 10\%, \tag{6.44}$$

and if one assumes that the statistical distribution of $\Delta\phi_{\mathrm{d}}$ is Gaussian, then one gets

$$\langle\cos(\Delta\phi_{\mathrm{d}})\rangle > 0.995. \tag{6.45}$$

The estimation of $\langle\Delta\phi_{\mathrm{d}}\rangle$ is sufficiently low to have a signal dominated by the fluctuation of $\Delta\phi$. Note that this effect is important only for the samples with the largest density. Moreover, it does not depend on the distance between the two lines.

3. *Finite width of the lines*: The lines that interfere have a width a_l of a few micrometers, and the phase of the initial wave function may fluctuate on this range. The interference pattern thus may have an averaged contrast that does not reflect only the phase ordering at distance d, but also the lack of phase ordering at distances lower than a_l. This effect should be small when $T/T_{\mathrm{c}} < 1$ and we indeed measure a large correlation between the phase of distant regions. However, for the point with the largest T/T_{c} for which we measure a correlation length on the order of a few micrometers, the low values of the contrast may be reduced due to the width of the lines, and it may even reduce the measured value of such a correlation length. This question could be settled by performing numerical simulations to estimate this effect.

4. *Phase fluctuation along the lines:* Since the length of the two lines in the y direction is 40 µm, the phase can fluctuate in the y direction, especially when $T > T_\mathrm{c}$. However, the expansion of the lines happens mostly in the x direction during the probed times of evolution. The position of the dark fringe may vary with y, and indeed there are images for which it is the case and where the fringes look curvy. However, the contrast that we extract is averaged over only a few pixels of the camera in the y direction. When T/T_c is lower than 1.5, the phase fluctuation is not too important over this distance.

5. *Other effects of the interactions*: As shown in the beginning of this chapter, the way the two lines expand in the presence of initial interactions is not completely understood. We have assumed that the contrast of the interference pattern is not affected by these interactions for a single experimental realisation. Numerical simulations could also give an answer to the questions whether the contrast is decreased by the initial interactions, and if this decrease depends on the distance between the two lines once the periodicity of the pattern is fixed, as we do experimentally.

In order to check whether the physics that we are probing here depends on the finite size of our experimental sample, we have performed the same procedure on a square of side 28 µm, and for a ratio T/T_c around 1. For distances d_l lower than ≈ 17 µm, the contrast of the interference fringes is very similar to the one in a square of side 40 µm. When $d_l \gtrsim 18$ µm, the contrast is much lower than the one measured in the large square, which is probably due to the proximity of the edges of the cloud.

6.4 CONCLUSION

In this chapter, I have presented an experimental method to measure the first-order correlation function of a uniform 2D Bose gas across the Berezinskii-Kosterlitz-Thouless transition. This method relies on the interference between distant regions of the gas that are isolated from the rest of the gas thanks to the spatially resolved Raman beams that we have developed. The statistically-averaged contrast of the interference pattern gives a direct estimate of the phase correlation between these two regions.

The recent measurements that we have performed give very encouraging preliminary results. Below the critical temperature, the phase correlation does not decrease much with the distance, and it is compatible with a power-law decay with an exponent below 0.25, as predicted by the theory of the BKT transition. Around the critical temperature, this behaviour changes significantly, and above T_c, the phase correlation decreases faster with the distance than at low temperatures. This decay may be described by an exponential decay with a characteristic length ℓ. When T decreases from a high value down to T_c, ℓ grows to a value on the order of the size of the system.

These measurements are compatible with the results obtained with the first method presented in the previous chapter, and they provide a direct access to $g_1(d_l)$ and give a more reliable picture of the phase ordering across the phase transition. However, because of the relatively small range of distances that could be probed, we cannot determine the exact form of this first-order correlation function, in particular to favour either a power-law decay or an exponential one.

The analysis is still preliminary and there are still several effects that we need to understand in order to confirm and publish these results. Among them, the finite resolution of the imaging system and the pixellisation of the camera, the finite width of the lines that interfere and the spurious phase fluctuation due to atom number imbalance, and finally the role of the interactions during the first milliseconds of the expansion of the lines.

Part III

DYNAMICAL SYMMETRY OF THE 2D BOSE GAS

Most of the results presented in this part have been published in Saint-Jalm et al., *Physical Review X* 9, 021035 (2019) [182]. I develop in slightly more details the content of this article in the next three chapters.

7

ELEMENTS OF THEORY ON DYNAMICAL SYMMETRIES

Symmetries are ubiquitous in physics and their study is of great help in order to understand various physical phenomena. The most famous example is Noether's first theorem [1]: if a system is described by an action that is invariant under a continuous symmetry, then this system exhibits invariant quantities.

One can apply this theorem to an action that is invariant under the transformation of the special Euclidean group, composed of the translations and rotations of space. One then deduces that the linear momentum and the angular momentum of the system of interest are conserved. The transformations of this group are purely geometric: they only act on the spatial coordinates of the system.

Other invariant quantities can be found when considering more subtle symmetry groups with transformations that involve the time coordinate. They are thus called *dynamical* symmetries. An important example is the Kepler problem that describes a single particle of mass m in a central force field proportional to $1/r^2$:

$$\boldsymbol{F} = -\frac{mk}{r^2}\hat{\boldsymbol{r}}, \tag{7.1}$$

where $\hat{\boldsymbol{r}}$ is the unitary radial vector of the particle. In that case, the action in invariant under a rotation group acting on space and time, and the Laplace-Runge-Lenz vector $\boldsymbol{A}$, defined as

$$\boldsymbol{A} = \boldsymbol{p} \times \boldsymbol{L} - mk\hat{\boldsymbol{r}}, \tag{7.2}$$

is found to be invariant, where $\boldsymbol{p}$ is the momentum of the particle and $\boldsymbol{L} = \boldsymbol{r} \times \boldsymbol{p}$ is its (constant) angular momentum.

In this chapter I present the theoretical tools that are useful to study the symmetries of a physical system. These tools are also extended to map two similar physical systems and their solutions. The dynamical symmetries of weakly interacting bosons in 2D are then determined: first the symmetries of N bosons without any external potential, and then in the presence of an external harmonic trap. I also show that these two different systems can be mapped one onto the other. Finally, I show that, in a certain regime, systems with different atom numbers and different interaction parameters can be linked one with another, leading to a universal dynamics of a large class of systems.

7.1 SYMMETRIES OF A PHYSICAL SYSTEM

7.1.1 *The symmetry group as a Lie group*

A physical system is characterised by its action S. In the case of particles described by their coordinates $\boldsymbol{q}, \dot{\boldsymbol{q}}$, this action is

$$S = \int \mathrm{d}t \, \mathcal{L}(\boldsymbol{q}, \dot{\boldsymbol{q}}, t), \tag{7.3}$$

where $\mathcal{L}$ is the Lagrangian of the system. In the case of a field $\psi(\boldsymbol{r})$, the action reads

$$S = \iint \mathrm{d}t \, \mathrm{d}^D\boldsymbol{r} \, \mathcal{L}\left(\psi, \boldsymbol{\nabla}\psi, \frac{\partial \psi}{\partial t}, \boldsymbol{r}, t\right), \tag{7.4}$$

where $\mathcal{L}$ is the Lagrangian density of the system and D is the dimension of space.

The symmetries of the system are the transformations on the coordinates (space, time, etc.) and on the variables describing the state of the system (for example the field ψ) that leave the action invariant. Mathematically, these transformations g are such that

$$gS = Sg. \tag{7.5}$$

With such a definition, it is clear that these transformations form a group G. In many cases, this group is continuous. There may be discrete symmetries in it, such as the inversion symmetry. The properties in which we are interested here are due to the fact that the group is continuous, and we therefore will omit these discrete symmetries in the following.

In general, the group G is also differentiable. Such groups are called Lie groups.

It is important to note that the transformations of G are not necessarily restricted to geometrical transformations (also called Lie point-symmetries), but they may include more general ones that involves time and the derivatives of the coordinates of the system. These general transformations are called Lie-Bäcklund transformations [183]. In that respect, this framework is an extension of the one initially considered at the time of Lie and Noether.

The properties of this type of groups are gathered in the structure of their underlying Lie algebra: one can determine the infinitesimal transformations $\{L_i\}$. [1] For example, in the case of the rotation symmetry in three dimensions, the infinitesimal transformations are proportional to the components of the angular momentum L_x, L_y, L_z.

The structure of the algebra generated by the elements $\{L_i\}$ is fully characterised by the commutation relations $[L_i, L_j]$, and interesting properties of the system can be inferred from this structure. In the case of the rotation symmetry, we have the commutation relations

$$[L_\alpha, L_\beta] = \mathrm{i}\hbar \sum_\gamma \varepsilon_{\alpha\beta\gamma} L_\gamma, \tag{7.6}$$

---

[1] It is a minimal set that generate the tangent space of G around the identity. This set can be finite or infinite.

for $\alpha, \beta, \gamma \in \{1, 2, 3\}$, and where $\varepsilon_{\alpha\beta\gamma}$ is the Levi-Civita symbol. This algebra is called SO(3) and it represents the rotations in three dimensions.

The Zassenhaus formula illustrates the importance of these commutation relations. This formula is closely linked to the Campbell-Baker-Hausdorff formula. The exponentiation of infinitesimal generators $\exp(\mathrm{i}L_j)$ provide explicit elements of the group G, and the Zassenhaus formula allows to determine the exponential of the sum of two generators:

$$\begin{aligned}\exp(\mathrm{i}L_1 + \mathrm{i}L_2) = \quad & \exp(\mathrm{i}L_1) * \exp(\mathrm{i}L_2) * \exp\left(\frac{[L_1, L_2]}{2}\right) \\ & * \exp\left(-\frac{\mathrm{i}}{6}(2[L_2,[L_1,L_2]] + [L_1,[L_1,L_2]])\right) * \cdots\end{aligned} \tag{7.7}$$

where $*$ denotes the composition of elements of G.

Another example of symmetry is found in the Kepler problem. It has a dynamical symmetry group with a Lie algebra that has the structure of the rotation group in four dimensions SO(4) when it is restricted to the orbits with the same negative energy [6].

This symmetry group can be used to derive invariant quantities of the system [5] by applying Noether's first theorem. Again, this statement is broader than the original theorem by Noether because the class of transformations that can be used is larger. For example, the dynamical symmetry group of the Kepler problem provides the invariance of the Laplace-Runge-Lenz vector, even if it was for a long time considered as not being grasped by Noether's theorem [184, 185].

Note that Noether's theorem does not always provide interesting conserved quantities and can sometimes lead to trivial ones. For example it is the case for the symmetries that will be presented in this chapter.

7.1.2 *Linking different solutions of a differential equation*

The dynamics of a system can be derived from its action to obtain an Euler-Lagrange equation:

$$\frac{\partial \mathcal{L}}{\partial \boldsymbol{q}} - \frac{\mathrm{d}}{\mathrm{d}t}\frac{\partial \mathcal{L}}{\partial \dot{\boldsymbol{q}}} = 0, \tag{7.8}$$

or in the case of a field ψ:

$$\frac{\partial \mathcal{L}}{\partial \psi} - \sum_{\mu} \frac{\partial}{\partial x_\mu} \frac{\partial \mathcal{L}}{\partial \left(\dfrac{\partial \psi}{\partial x_\mu}\right)} = 0, \tag{7.9}$$

where the coordinates $\{x_\mu\}$ include the spatial and temporal coordinates. In the following, I will refer to the field version of the Euler-Lagrange equation 7.9 since it is the one which is developed in section 7.2 and investigated experimentally in Chapter 8.

The elements of the symmetry group G also leave this equation invariant since it is directly obtained from the action of the system. We can now slightly change the point of view that we have on the transformations of the group G and let them act on a solution of the Euler-Lagrange equation.

If the field $\psi(\boldsymbol{r}, t)$ is a solution of the Euler-Lagrange equation 7.9 and g is a transformation that leaves the action invariant, then $g\psi$ is also a solution of the Euler-Lagrange equation.

This property explains the denomination of the Lie-Bäcklund transformations. In the field of non-linear differential equations, a Bäcklund transformation is a transformation that allows one to construct from the solution of a differential equation another solution of the same equation [186]. Here the Bäcklund transformations have the structure of the Lie group G, hence the use of Lie's name.

A step further can be made to get closer to the experimental situations that are discussed in Chapter 8. Let us consider two wave functions at $t = 0$: $\psi_1(\boldsymbol{r}, 0)$ and $\psi_2(\boldsymbol{r}, 0)$, along with their derivatives $\left.\frac{\partial \psi_{1,2}}{\partial t}\right|_{t=0}$ and $\boldsymbol{\nabla}\psi_{1,2}(t = 0)$. These two situations correspond to two initial conditions of the Euler-Lagrange equation 7.9. Suppose that there exists a Lie-Bäcklund transformation g of this equation that maps the first situation to the second one at $t = 0$:

$$\left\{\begin{array}{l} \boldsymbol{r} \\ t \\ \psi_1(\boldsymbol{r}, 0) \\ \left.\dfrac{\partial \psi_1}{\partial t}\right|_{t=0} \\ \boldsymbol{\nabla}\psi_1(t = 0) \end{array}\right. \xrightarrow{g} \left\{\begin{array}{l} \boldsymbol{r}' \\ t' \\ \psi_2(\boldsymbol{r}', 0) \\ \left.\dfrac{\partial \psi_2}{\partial t'}\right|_{t'=0} \\ \boldsymbol{\nabla}'\psi_2(t' = 0) \end{array}\right. \tag{7.10}$$

where the notation $\boldsymbol{\nabla}'$ denotes the gradient with respect to the coordinate $\boldsymbol{r}'$.

Then the subsequent evolutions of ψ_1 and ψ_2, which are fully determined by these initial conditions and the Euler-Lagrange equation, will be linked by the Lie-Bäcklund transformation g for all times: $\psi_1(\boldsymbol{r}, t) \xrightarrow{g} \psi_2(\boldsymbol{r}', t')$

7.1.3 *Linking solutions of two differential equations*

The previous paragraph can be generalized to the solutions of two differential equations [4]:

$$\mathcal{P}\left[\psi, \frac{\partial \psi}{\partial t}, \boldsymbol{\nabla}\psi, \boldsymbol{r}, t\right] = 0, \tag{7.11}$$

$$\mathcal{Q}\left[\psi, \frac{\partial \psi}{\partial t}, \boldsymbol{\nabla}\psi, \boldsymbol{r}, t\right] = 0. \tag{7.12}$$

There can exist a transformation on the coordinates $\boldsymbol{r}, t$ and the variables ψ, $\frac{\partial \psi}{\partial t}$, $\boldsymbol{\nabla}\psi$ such that any solution $\psi_1(\boldsymbol{r}, t)$ of equation 7.11 is transformed into $\psi_2(\boldsymbol{r}', t')$, a solution of equation 7.12.

In that case, the solution spaces of the two differential equations have the same algebraic structure (e.g. the same Lie group and the same Lie algebra).

Such a relationship between two differential equations is stronger than if they only have the same Lie algebra, for example. Indeed, two equations with the same Lie algebra are only locally similar, whereas two equations whose solutions are linked by a transformation are globally similar.

The transformations that link the solutions of equations 7.11 and 7.12 are also called Bäcklund transformations. When the transformations link a differential equation with itself, such as in equation 7.10, they are called auto-Bäcklund or invariant Bäcklund transformations.

7.2 DYNAMICAL SYMMETRY OF WEAKLY INTERACTING BOSONS IN 2D

In this section I present the dynamical symmetry group of the Gross-Pitaevskii equation for bosons in two dimensions, first without a trap and then with a harmonic trap. The solutions in the two cases are then linked by Bäcklund transformations. Finally, when a gas is in the hydrodynamic regime, the solutions of equations with different atoms numbers are also linked.

7.2.1 *Symmetry group of the free Gross-Pitaevskii equation*

7.2.1.1 *The Gross-Pitaevskii equation and its associated action*

We have seen in Chapter 4 that a ensemble of N weakly interacting bosons in two dimensions can be described by a classical field $\psi(\boldsymbol{r},t)$ whose evolution is given by the Gross-Pitaevskii equation:

$$\mathrm{i}\hbar\frac{\partial\psi}{\partial t}+\frac{\hbar^2}{2m}\boldsymbol{\nabla}^2\psi-V_{\mathrm{ext}}(\boldsymbol{r})\psi-\frac{\hbar^2}{m}\tilde{g}N|\psi|^2\psi=0, \tag{7.13}$$

where V_{ext} is an external potential, and $\tilde{g}$ is the dimensionless interaction parameter.

This equation is associated with the following action:

$$S=\iint \mathrm{d}t\,\mathrm{d}^2\boldsymbol{r}\;N\left[-\mathrm{i}\hbar\psi^*\frac{\partial\psi}{\partial t}+\frac{\hbar^2}{2m}|\boldsymbol{\nabla}\psi|^2+V_{\mathrm{ext}}(\boldsymbol{r})|\psi|^2+\frac{\hbar^2}{2m}\tilde{g}N|\psi|^4\right], \tag{7.14}$$

which is the time integral of a Lagrangian density.

Note that this description with a classical field is valid in two dimensions only if the interaction parameter $\tilde{g}$ is small compared to 1 [187]. If it is not the case, a quantum anomaly may appear [188, 189] and the system will not have the same symmetry group.

7.2.1.2 *Lie-Bäcklund transformations of the free* GPE

In this section we are interested in the symmetry group of a system with no external potential, which means that we consider the Gross-Pitaevskii equation:

$$\mathrm{i}\hbar\frac{\partial\psi}{\partial t}+\frac{\hbar^2}{2m}\boldsymbol{\nabla}^2\psi-\frac{\hbar^2}{m}\tilde{g}N|\psi|^2\psi=0, \tag{7.15}$$

which is associated with the action

$$S = \iint \mathrm{d}t\,\mathrm{d}^2\boldsymbol{r}\ N\left[-\mathrm{i}\hbar\psi^*\frac{\partial\psi}{\partial t} + \frac{\hbar^2}{2m}|\boldsymbol{\nabla}\psi|^2 + \frac{\hbar^2}{2m}\tilde{g}N|\psi|^4\right]. \tag{7.16}$$

The case with an external potential will be discussed in section 7.2.2, in the particular case where this external potential is harmonic.

We now determine the transformations that keep the action of free particles 7.16, and therefore the free GPE given by equation 7.15, invariant, in other words the Lie-Bäcklund transformations of the system. A full derivation can be found in [190] for non interacting particles, and the reasoning can be adapted easily to our case. I present here the most important lines and some tedious justifications are done in Appendix D.

Transformations that trivially leave the action invariant are all the transformations of the Galilean group: the translations and rotations of space, the uniform motions ($\boldsymbol{r} \longrightarrow \boldsymbol{r} - \boldsymbol{v}t$ for any constant velocity $\boldsymbol{v}$), and all the compositions of these transformations. It is not very surprising, as S is a non-relativistic action that describe a physical system which has to respect Galilean invariance. These transformations are not the ones in which we are interested here.

The first transformation that we consider is simply a time translation without changing the space coordinates nor the wave function:

$$\begin{cases} \boldsymbol{r} \\ t \\ \psi(\boldsymbol{r}) \end{cases} \longrightarrow \begin{cases} \boldsymbol{r}' = \boldsymbol{r} \\ t' = t + \beta \\ \psi'(\boldsymbol{r}') = \psi(\boldsymbol{r}). \end{cases} \tag{7.17}$$

The action is obviously invariant under this transformation, and Noether's first theorem applied to it guarantees the conservation of the total energy E_{tot} of the system:

$$E_{\mathrm{tot}} = \iint \mathrm{d}^2\boldsymbol{r}\ N\left[\frac{\hbar^2}{2m}|\boldsymbol{\nabla}\psi|^2 + \frac{\hbar^2}{2m}\tilde{g}N|\psi|^4\right]. \tag{7.18}$$

More interestingly, the action is kept invariant by any dilation defined for any parameter $\lambda > 0$ as

$$\begin{cases} \boldsymbol{r} \\ t \\ \psi(\boldsymbol{r}) \end{cases} \longrightarrow \begin{cases} \boldsymbol{r}' = \boldsymbol{r}/\lambda \\ t' = t/\lambda^2 \\ \psi'(\boldsymbol{r}') = \lambda\,\psi(\boldsymbol{r}). \end{cases} \tag{7.19}$$

The verification of this statement is straightforward. This property is true because the interaction parameter $\tilde{g}$ is dimensionless, and therefore there is no characteristic length associated with the interaction between the particles.

The system is invariant under any dilation, it is therefore scale invariant. This is not the case for interacting bosons described by the GPE in one or three dimensions where the interaction parameter has a dimension and leads to the definition of a characteristic length scale.

Finally, another transformation that keeps the action invariant is the so-called *expansion*, defined for any parameter $\gamma > 0$ as

$$\begin{cases} \boldsymbol{r} \\ t \\ \psi(\boldsymbol{r}) \end{cases} \longrightarrow \begin{cases} \boldsymbol{r}' = \dfrac{\boldsymbol{r}}{\gamma t + 1} \\ t' = \dfrac{t}{\gamma t + 1} \\ \psi'(\boldsymbol{r}') = f_{\gamma,1}(\boldsymbol{r},t)\,\psi(\boldsymbol{r}), \end{cases} \tag{7.20}$$

with

$$f_{\gamma,1}(\boldsymbol{r},t) = (\gamma t + 1)\,\exp\left(-\frac{im}{2\hbar}\frac{\gamma \boldsymbol{r}^2}{\gamma t + 1}\right). \tag{7.21}$$

A proof of this statement is given in Appendix D section D.1.

Unlike the previous transformation, this one mixes space and time in the transformation of space, which makes it a non-purely geometric dynamical symmetry.

It can be shown (e.g. [190]) that all the transformations that leave the action and the GPE invariant are a composition of these three transformations and of the Galilean transformations.

The three above transformations can be composed one with another, which gives the following general transformation, denoted as $\mathcal{T}_{\alpha,\beta,\gamma,\delta}$:

$$\mathcal{T}_{\alpha,\beta,\gamma,\delta} : \begin{cases} \boldsymbol{r} \\ t \\ \psi(\boldsymbol{r}) \end{cases} \longrightarrow \begin{cases} \boldsymbol{r}' = \dfrac{\boldsymbol{r}}{\gamma t + \delta} \\ t' = \dfrac{\alpha t + \beta}{\gamma t + \delta} \\ \psi'(\boldsymbol{r}') = f_{\gamma,\delta}(\boldsymbol{r},t)\,\psi(\boldsymbol{r}), \end{cases} \tag{7.22}$$

where

$$f_{\gamma,\delta}(\boldsymbol{r},t) = (\gamma t + \delta)\,\exp\left(-\frac{im}{2\hbar}\frac{\gamma \boldsymbol{r}^2}{\gamma t + \delta}\right), \tag{7.23}$$

and the four parameters α, β, γ and δ are not independent and fulfil the constraint $\alpha\delta - \beta\gamma = 1$.

When applying the transformation $\mathcal{T}_{\alpha,\beta,\gamma,\delta}$ right after the transformation $\mathcal{T}_{\alpha',\beta',\gamma',\delta'}$, one can show that it amounts to the transformation $\mathcal{T}_{\alpha'',\beta'',\gamma'',\delta''}$, where the parameters $\alpha'', \beta'', \gamma'', \delta''$ are defined by the matrix equation

$$\begin{pmatrix} \alpha'' & \beta'' \\ \gamma'' & \delta'' \end{pmatrix} = \begin{pmatrix} \alpha & \beta \\ \gamma & \delta \end{pmatrix} \times \begin{pmatrix} \alpha' & \beta' \\ \gamma' & \delta' \end{pmatrix}. \tag{7.24}$$

The set of transformations that one can apply on time is therefore homomorphic to the matrix group

$$\mathrm{SL}(2,\mathbb{R}) = \left\{ \begin{pmatrix} \alpha & \beta \\ \gamma & \delta \end{pmatrix} \in \mathcal{M}_2(\mathbb{R}) \,\middle|\, \alpha\delta - \beta\gamma = 1 \right\}, \tag{7.25}$$

and the dynamical symmetry group of the system is also homomorphic to this group.

7.2.1.3 *Lie algebra of the free GPE*

We can now determine the Lie algebra of this dynamical symmetry group. One can either look up the mathematical literature to find the Lie algebra of $\mathrm{SL}(2,\mathbb{R})$, for example [191], or fully perform the calculations from the expression of the Lie-Bäcklund transformations. For the reader to get an better insight of the structure of the dynamical symmetry group, I present here the full calculations.

We first determine the infinitesimal transformations associated with the three transformations 7.19, 7.20 and 7.17. When applying an infinitesimal transformation of small parameter $\varepsilon \ll 1$, the wave function ψ is transformed into $\psi - \mathrm{i}\varepsilon L\psi$, where L is the generator of the transformation.

(a) We apply transformation 7.17 to the wave function $\psi(\boldsymbol{r},t)$ with $\beta = \varepsilon t_0$, where $\varepsilon \ll 1$ and t_0 is an arbitrary time scale that can be chosen as a typical time scale of the evolution of the wave function. The wave function $\psi(\boldsymbol{r},t)$ is transformed into

$$\psi(\boldsymbol{r},t) + \varepsilon t_0 \frac{\partial\psi}{\partial t}, \tag{7.26}$$

and the associated generator is simply

$$L_a = \mathrm{i}t_0 \frac{\partial}{\partial t}. \tag{7.27}$$

(b) We apply transformation 7.19 to the wave function $\psi(\boldsymbol{r},t)$ with $\lambda = 1+\varepsilon$ and $\varepsilon \ll 1$. It is transformed into

$$\psi(\boldsymbol{r},t) + \varepsilon\left(1 + \boldsymbol{r}\cdot\boldsymbol{\nabla} + 2t\frac{\partial}{\partial t}\right)\psi(\boldsymbol{r},t), \tag{7.28}$$

therefore the associated generator is

$$L_b = \mathrm{i}\left(1 + \boldsymbol{r}\cdot\boldsymbol{\nabla} + 2t\frac{\partial}{\partial t}\right). \tag{7.29}$$

(c) We apply transformation 7.20 to the wave function $\psi(\boldsymbol{r},t)$ with $\gamma = \varepsilon/t_0$, where t_0 is an arbitrary time scale and $\varepsilon \ll 1$. It is transformed into

$$\psi(\boldsymbol{r},t) + \varepsilon\left(\frac{t}{t_0} + \frac{t}{t_0}\boldsymbol{r}\cdot\boldsymbol{\nabla} + \frac{t^2}{t_0}\frac{\partial}{\partial t} - \mathrm{i}\frac{m\boldsymbol{r}^2}{2\hbar t_0}\right)\psi(\boldsymbol{r},t), \tag{7.30}$$

and the associated generator is

$$L_c = \mathrm{i}\frac{t}{t_0}\left(1 + \boldsymbol{r}\cdot\boldsymbol{\nabla} + t\frac{\partial}{\partial t}\right) + \frac{m\boldsymbol{r}^2}{2\hbar t_0}. \tag{7.31}$$

The three generators that we obtained are not the most convenient ones to recognise the structure of the Lie algebra. We define the three new generators:

$$\begin{aligned} L_1 &= L_b/2, \\ L_2 &= (L_c - L_a)/2, \\ L_3 &= (L_c + L_a)/2. \end{aligned} \tag{7.32}$$

The commutation relations between these three generators are then straightforwardly calculated, and we obtain:

$$[L_1, L_2] = \mathrm{i}L_3, \tag{7.33}$$
$$[L_2, L_3] = -\mathrm{i}L_1, \tag{7.34}$$
$$[L_3, L_1] = -\mathrm{i}L_2. \tag{7.35}$$

This algebra has the structure of $\mathrm{SO}(2,1)$. The commutation relations are close to the ones of the rotation group $\mathrm{SO}(3)$, except that there are two minus signs and one plus sign, hence the indication $(2,1)$ in the name of the group.

7.2.2 *Symmetry group with a harmonic trap*

Let us now turn to the case of a gas trapped in a harmonic potential. The action of the system is now

$$S = \iint \mathrm{d}t\,\mathrm{d}^2\boldsymbol{r}\; N\left[-\mathrm{i}\hbar\psi^*\frac{\partial\psi}{\partial t} + \frac{\hbar^2}{2m}|\boldsymbol{\nabla}\psi|^2 + \frac{\hbar^2}{2m}\tilde{g}N|\psi|^4 + \frac{m\omega^2\boldsymbol{r}^2}{2}|\psi|^2\right], \tag{7.36}$$

where ω is the frequency of the harmonic potential. The GPE also gets an additional term:

$$\mathrm{i}\hbar\frac{\partial\psi}{\partial t} + \frac{\hbar^2}{2m}\boldsymbol{\nabla}^2\psi - \frac{\hbar^2}{m}\tilde{g}N|\psi|^2\psi - \frac{1}{2}m\omega^2\boldsymbol{r}^2\psi = 0. \tag{7.37}$$

7.2.2.1 *Lie-Bäcklund transformations*

The transformations 7.19 and 7.20 do not conserve this action, in particular the system is not scale invariant any more. However, the system still has Lie-Bäcklund transformations outside the Galilean group [192]. The most general transformation is given by

$$\begin{cases} \boldsymbol{r} \\ t \\ \psi(\boldsymbol{r}) \end{cases} \longrightarrow \begin{cases} \boldsymbol{r}' = \boldsymbol{r}/\lambda(t) \\ t' = \tau(t) \\ \psi'(\boldsymbol{r}') = f(\boldsymbol{r},t)\,\psi(\boldsymbol{r}), \end{cases} \tag{7.38}$$

where

$$\lambda(t) = \left[(\alpha\sin(\omega t) + \beta\cos(\omega t))^2 + (\gamma\sin(\omega t) + \delta\cos(\omega t))^2\right]^{1/2}, \tag{7.39}$$

$$\omega\tau(t) = \arctan\left(\frac{\alpha\tan(\omega t) + \beta}{\gamma\tan(\omega t) + \delta}\right) + \pi\left\lfloor\frac{\omega t}{\pi} - \frac{1}{\pi}\arctan\left(-\frac{\delta}{\gamma}\right)\right\rfloor, \tag{7.40}$$

$$f(\boldsymbol{r},t) = \lambda(t)\exp\left(-\frac{\mathrm{i}m\dot{\lambda}\boldsymbol{r}^2}{2\hbar\lambda}\right). \tag{7.41}$$

In 7.40, the second term makes sure that the function is continuous, and $\lfloor x\rfloor$ is the largest integer that is smaller than x. In the expression of $f(\boldsymbol{r},t)$, the notation $\dot{\lambda}$ represents $\frac{\mathrm{d}\lambda}{\mathrm{d}t}$. The four real parameters α, β, γ, δ are not independent and fulfil the condition $\alpha\delta - \beta\gamma = 1$. A proof of this general transformation is given in Appendix D.2.

It is to note that equation 7.40 can be written in the form

$$\eta' = \frac{\alpha\eta + \beta}{\gamma\eta + \delta} \tag{7.42}$$

with $\eta = \tan(\omega t)$ and $\eta' = \tan(\omega\tau(t))$. This form is reminiscent of the one of the time transformation in equation 7.22. It hints at the fact that the structure of the Lie group of the harmonically trapped gas is the same as the one of the free gas.

7.2.2.2 *Lie algebra*

We follow the method used in 7.2.1.3. In total, the symmetry group of the equation has eight independent generators [192], but we are interested here in three of them. They stem from the transformations defined by the following parameters:

(a) $\alpha = 1/\delta = \exp(-s_1/2)$, $\beta = \gamma = 0$,

(b) $\alpha = \delta = \cosh(s_2/2)$, $\beta = \gamma = -\sinh(s_2/2)$,

(c) $\alpha = \delta = \cos(s_3/2)$, $\beta = -\gamma = \sin(s_3/2)$.

The three generators associated with these transformations are

$$L_1 = \frac{\mathrm{i}}{2}\cos(2\omega t)(1 + \boldsymbol{r}\cdot\nabla) - \frac{1}{2\omega}\sin(2\omega t)\left(\frac{m\omega^2\boldsymbol{r}^2}{\hbar} - \mathrm{i}\frac{\partial}{\partial t}\right), \tag{7.43}$$

$$L_2 = -\frac{1}{2\omega}\cos(2\omega t)\left(\frac{m\omega^2\boldsymbol{r}^2}{\hbar} - \mathrm{i}\frac{\partial}{\partial t}\right) - \frac{\mathrm{i}}{2}\sin(2\omega t)(1 + \boldsymbol{r}\cdot\nabla), \tag{7.44}$$

$$L_3 = -\frac{\mathrm{i}}{2\omega}\frac{\partial}{\partial t}. \tag{7.45}$$

The commutation relations between these three generators are tedious but easy to determine, and one gets

$$[L_1, L_2] = \mathrm{i}L_3, \tag{7.46}$$

$$[L_2, L_3] = -\mathrm{i}L_1, \tag{7.47}$$

$$[L_3, L_1] = -\mathrm{i}L_2, \tag{7.48}$$

which are the exact same ones as the commutation relations found in 7.2.1.3.

These commutation relations have an important consequence here, as stated in [193]. Consider the operator $m\omega^2\boldsymbol{r}^2/2$ associated with the potential energy per particle of the system:

$$\frac{1}{2}m\omega^2\boldsymbol{r}^2 = -\hbar\omega\left(L_3 + \cos(2\omega t)L_2 + \sin(2\omega t)L_1\right). \tag{7.49}$$

The potential energy per particle is

$$\frac{E_{\text{pot}}}{N} = \left\langle \frac{1}{2}m\omega^2\boldsymbol{r}^2 \right\rangle, \tag{7.50}$$

where the notation $\langle A \rangle$ applied to an operator A represents $\int \mathrm{d}^2\boldsymbol{r}\ \psi^* A \psi$. In a Heisenberg-like picture, the derivative of the potential energy per particle of the system is obtained via

$$\frac{\partial}{\partial t}\left\langle \frac{1}{2} m\omega^2 \boldsymbol{r}^2 \right\rangle = \left\langle \left[\frac{\partial}{\partial t}, \frac{1}{2} m\omega^2 \boldsymbol{r}^2 \right] \right\rangle . \tag{7.51}$$

Therefore we get

$$\begin{aligned} \frac{\partial}{\partial t}\left\langle \frac{1}{2} m\omega^2 \boldsymbol{r}^2 \right\rangle &= -2\hbar\omega^2 \mathrm{i} \left\langle [L_3, L_3 + \cos(2\omega t) L_2 + \sin(2\omega t) L_1] \right\rangle & (7.52) \\ &= 2\hbar\omega^2 \left\langle \cos(2\omega t) L_1 - \sin(2\omega t) L_2 \right\rangle & (7.53) \\ &= \mathrm{i}\hbar\omega^2 \left\langle 1 + \boldsymbol{\nabla} \cdot \boldsymbol{r} \right\rangle . & (7.54) \end{aligned}$$

The second derivative of the potential energy per particle is then

$$\begin{aligned} \frac{\partial^2}{\partial t^2}\left\langle \frac{1}{2} m\omega^2 \boldsymbol{r}^2 \right\rangle &= 4\hbar\omega^3 \mathrm{i} \left\langle [L_3, \cos(2\omega t) L_1 - \sin(2\omega t) L_2] \right\rangle & (7.55) \\ &= -4\omega^2 \left\langle \frac{1}{2} m\omega^2 \boldsymbol{r}^2 \right\rangle + 2\omega^2 \left\langle \mathrm{i}\hbar \frac{\partial}{\partial t} \right\rangle , & (7.56) \end{aligned}$$

and the last term is equal to the total energy per particle of the system E_{tot}/N, which is conserved, therefore

$$\frac{\partial^2 E_{\mathrm{pot}}}{\partial t^2} + (2\omega)^2 E_{\mathrm{pot}} = 2\omega^2 E_{\mathrm{tot}} . \tag{7.57}$$

This solution of this equation is

$$E_{\mathrm{pot}}(t) = \frac{1}{2} E_{\mathrm{tot}} + \frac{1}{2} \Delta E \cos(2\omega t) + \frac{1}{2\omega} \dot{E}_{\mathrm{pot}}(0) \sin(2\omega t), \tag{7.58}$$

where $\Delta E = 2E_{\mathrm{pot}}(0) - E_{\mathrm{tot}}$.

The potential energy thus oscillates sinusoidally at twice the frequency ω of the harmonic potential. This behaviour is a direct consequence of the algebraic structure of the differential operators involved in the problem, as the demonstration shows. Such a property also holds for other scale invariant systems, since it depends only on the algebraic structure of the operators and not on the detail of their expression. It has thus already been observed in [194] for an elongated cloud of bosons effectively described by a two-dimensional scale invariant equation, and in [195] for a two-dimensional Fermi gas at unitarity.

7.2.3 *Link between different trap frequencies*

The Gross-Pitaevskii equations of a free cloud (equation 7.15) and of a harmonically trapped one (equation 7.37) can be linked via a Bäcklund transformation. It is therefore not a surprise if we find that their respective Lie groups have the same algebraic structure.

The Bäcklund transformation, denoted as $\mathcal{T}_{0,\omega}$, is defined by the following expressions: if $\psi_0(\boldsymbol{r}, t)$ is a solution of the free GPE, then the function

$$\psi_\omega(\boldsymbol{r}', t') = f_{0,\omega}(\boldsymbol{r}, t)\, \psi_0(\boldsymbol{r}, t), \tag{7.59}$$

is a solution of the GPE with a harmonic trap of frequency ω, with

$$\boldsymbol{r}' = \boldsymbol{r}/\lambda_{0,\omega}(t), \tag{7.60}$$

$$\tan\bigl(\omega t'\bigr) = \omega t, \tag{7.61}$$

$$\lambda_{0,\omega}(t) = \bigl(1 + \omega^2 t^2\bigr)^{1/2}, \tag{7.62}$$

$$f_{0,\omega}(\boldsymbol{r}, t) = \lambda_{0,\omega}(t) \exp\left(-\frac{\mathrm{i} m \dot{\lambda}_{0,\omega} \boldsymbol{r}^2}{2\hbar \lambda_{0,\omega}}\right), \tag{7.63}$$

where in the last expression, $\dot{\lambda}_{0,\omega} = \mathrm{d}\lambda_{0,\omega}/\mathrm{d}t$. A proof of this statement is given in the Appendix D.2.

One can also extend these relations to link the solution ψ_{ω_1} of the GPE with a harmonic trap of frequency ω_1 to a solution ψ_{ω_2} of the GPE with a harmonic trap of frequency ω_2. It is easily done by using twice the formulas 7.59 to 7.63 and using an intermediate function ψ_0 that is solution of the free GPE. It amounts to applying the transformation $\mathcal{T}_{0,\omega_2} \circ \mathcal{T}_{0,\omega_1}^{-1}$:

$$\psi_{\omega_2}(\boldsymbol{r}', t') = f_{\omega_1,\omega_2}(\boldsymbol{r}, t) \psi_{\omega_1}(\boldsymbol{r}, t), \tag{7.64}$$

with

$$\boldsymbol{r}' = \boldsymbol{r}/\lambda_{\omega_1,\omega_2}(t), \tag{7.65}$$

$$\tan\bigl(\omega_2 t'\bigr) = \frac{\omega_2}{\omega_1} \tan(\omega_1 t), \tag{7.66}$$

$$\lambda_{\omega_1,\omega_2}(t) = \left[\left(\frac{\omega_2}{\omega_1}\right)^2 \sin^2(\omega_1 t) + \cos^2(\omega_1 t)\right]^{1/2}, \tag{7.67}$$

$$f_{\omega_1,\omega_2}(\boldsymbol{r}, t) = \lambda_{\omega_1,\omega_2}(t) \exp\left(-\frac{\mathrm{i} m \dot{\lambda}_{\omega_1,\omega_2} \boldsymbol{r}^2}{2\hbar \lambda_{\omega_1,\omega_2}}\right). \tag{7.68}$$

It is not surprising either that two GPEs with different trap frequencies have the same Lie group, but it is much more surprising that their solutions can be mapped one onto the other in this way.

This analysis is valid only in two dimensions, however there are similar results for three dimensional gases [196].

The properties of these families of equations can be extended to Gross-Pitaevskii equations where the frequency of the harmonic trap can vary with time, similarly to what is derived in [196–200].

Let $\psi(\boldsymbol{r}, t)$ be a solution of the Gross-Pitaevskii equation with a harmonic trap of frequency ω (equation 7.37). Then we can construct a solution $\psi_{\tilde{\omega}}$ of the equation

$$\mathrm{i}\hbar \frac{\partial \psi}{\partial t} + \frac{\hbar^2}{2m} \boldsymbol{\nabla}^2 \psi - \frac{\hbar^2}{m} \tilde{g} N |\psi|^2 \psi - \frac{1}{2} m \tilde{\omega}(t)^2 \boldsymbol{r}^2 \psi = 0, \tag{7.69}$$

where $\tilde{\omega}(t)$ is a smooth function of time. We set

$$\psi_{\tilde{\omega}}(\boldsymbol{r}', t') = f_{\tilde{\omega}}(\boldsymbol{r}, t)\psi(\boldsymbol{r}, t), \tag{7.70}$$

where the new coordinates are

$$\boldsymbol{r}' = \frac{\boldsymbol{r}}{\lambda_{\tilde{\omega}}(t)}, \tag{7.71}$$

$$t' = \int_0^t \frac{\mathrm{d}u}{\lambda_{\tilde{\omega}}^2(u)}, \tag{7.72}$$

with

$$f_{\tilde{\omega}}(\boldsymbol{r}, t) = \lambda_{\tilde{\omega}} \exp\left(-\frac{\mathrm{i}m\dot{\lambda}_{\tilde{\omega}}\boldsymbol{r}^2}{2\hbar\lambda_{\tilde{\omega}}}\right), \tag{7.73}$$

and $\lambda_{\tilde{\omega}}$ is a solution of the differential equation

$$\ddot{\lambda} = \frac{\tilde{\omega}^2(t)}{\lambda^3} - \omega^2\lambda \tag{7.74}$$

with any initial conditions. A proof of this statement is given in Appendix D.2.

Note that the case where $\tilde{\omega}(t)$ is constant has been treated above, where we had chosen the initial conditions $\lambda_{\tilde{\omega}}(0) = 1$ and $\dot{\lambda}_{\tilde{\omega}}(0) = 0$.

The differential equation 7.74 is called a Ermakov equation and it is at the origin of many developments about the dynamical symmetries of physical systems [201–204].

We will not investigate further this last property of the Gross-Pitaevskii equations, in particular it will not be tested experimentally in the next Chapter.

7.3 MORE SYMMETRIES IN THE HYDRODYNAMIC REGIME

In the previous section we could link the solutions of Gross-Pitaevskii equations with different trap frequencies, while keeping the same atom number and the same interaction parameter. We focus here on these two other parameters of the GPE that can experimentally be varied: N and $\tilde{g}$. It is possible to link the solutions of equations with different values of these parameters, but only in a particular regime, as discussed in the following.

First we note that the two parameters N and $\tilde{g}$ appear in the GPE only as their product. Changing one is therefore equivalent to changing the other.

We then translate the Gross-Pitaevskii equation in terms of density field $n(\boldsymbol{r}, t)$ and velocity field $\boldsymbol{v}(\boldsymbol{r}, t)$, with

$$n(\boldsymbol{r}, t) = N|\psi(\boldsymbol{r}, t)|^2, \tag{7.75}$$

$$\boldsymbol{v}(\boldsymbol{r}, t) = \frac{\hbar}{m}\frac{\mathrm{Im}(\psi^*\boldsymbol{\nabla}\psi)}{|\psi(\boldsymbol{r}, t)|^2}. \tag{7.76}$$

We get two equations, one for the density field and one for the velocity field. These two equations on real fields are equivalent to the GPE that acts on a complex field:

$$\frac{\partial n}{\partial t} + \boldsymbol{\nabla} \cdot (n\boldsymbol{v}) = 0, \tag{7.77}$$

$$\frac{\partial \boldsymbol{v}}{\partial t} + \boldsymbol{\nabla}\left(\frac{1}{2}m\boldsymbol{v}^2 + \frac{\hbar^2}{m}\tilde{g}n + \frac{1}{2}m\omega^2\boldsymbol{r}^2 + P(n)\right) = 0, \tag{7.78}$$

where

$$P(n) = \frac{\hbar^2}{2m}\frac{\boldsymbol{\nabla}^2\sqrt{n}}{\sqrt{n}} \tag{7.79}$$

is the quantum pressure term. This term describes a pressure that arises from the curvature of the density field. In the case of uniform gases, this pressure is non zero only near the edges of the gas, where the density goes from zero to the density of the bulk. The order of magnitude of this quantum pressure term is then $\hbar^2/2m\xi^2$ where ξ is the typical size on which the density varies near the edge. The length ξ is called the healing length of the gas and it is defined as

$$\xi = \sqrt{\frac{\hbar^2 N}{2mE_{\text{int}}}}, \tag{7.80}$$

where E_{int} is the interaction energy of the gas, given by

$$E_{\text{int}} = \frac{\hbar^2 N^2}{2m}\tilde{g}\int \mathrm{d}^2\boldsymbol{r}\,|\psi(\boldsymbol{r})|^4. \tag{7.81}$$

In the case where the density of the cloud varies on length scales given by the typical size L of the gas, $|\psi| \approx 1/L$, the interaction energy and the healing length have the following orders of magnitude

$$E_{\text{int}} \approx \frac{\hbar^2\tilde{g}N^2}{2mL^2}, \tag{7.82}$$

$$\xi \approx \frac{L}{\sqrt{\tilde{g}N}}. \tag{7.83}$$

In the hydrodynamic regime (or Thomas-Fermi regime), the healing length is much smaller than the typical size L of the gas, which means that $\tilde{g}N \gg 1$. The density and velocity fields vary on length scales comparable with L. Then the ratio between the interaction term and the quantum pressure term in equation 7.78 is

$$\frac{\left|\boldsymbol{\nabla}\left(\frac{\hbar^2\tilde{g}n}{m}\right)\right|}{|\boldsymbol{\nabla}P(n)|} \approx \tilde{g}nL^2 \approx \tilde{g}N. \tag{7.84}$$

The quantum pressure term can therefore be neglected compared to the interaction term.

The equations 7.77 and 7.78 then simplify into

$$\frac{\partial n}{\partial t} + \boldsymbol{\nabla} \cdot (n\boldsymbol{v}) = 0, \tag{7.85}$$

$$\frac{\partial \boldsymbol{v}}{\partial t} + \boldsymbol{\nabla}\left(\frac{1}{2}m\boldsymbol{v}^2 + \frac{\hbar^2}{m}\tilde{g}n + \frac{1}{2}m\omega^2\boldsymbol{r}^2\right) = 0. \tag{7.86}$$

These two equations are invariant under the transformations presented in 7.2.2.1 when they are translated to act on n and $\boldsymbol{v}$, and solutions of this equation can also be mapped onto the solutions of an equation with a different trap frequency as explained in 7.2.3. Thanks to the simplification of the quantum pressure term, it is now possible to map a solution of this equation onto a solution of an equation with a different product $\tilde{g}N$.

Let $n_1(\boldsymbol{r}, t)$, $\boldsymbol{v}_1(\boldsymbol{r}, t)$ be a solution of equations 7.85 and 7.86, where the interaction parameter and the atom number have the values $\tilde{g}_1$ and N_1. Then we can define a solution of equations 7.85 and 7.86 with parameters $\tilde{g}_2$ and N_2 by setting

$$n_2(\boldsymbol{r}', t') = \frac{N_2}{N_1} n_1(\boldsymbol{r}, t), \tag{7.87}$$

$$\boldsymbol{v}_2(\boldsymbol{r}', t') = \mu\lambda_\mu(t)\boldsymbol{v}_1(\boldsymbol{r}, t) - \mu\dot{\lambda}_\mu(t)\boldsymbol{r}, \tag{7.88}$$

where $\mu^2 = \tilde{g}_2 N_2 / \tilde{g}_1 N_1$, and the new coordinates are

$$\boldsymbol{r}' = \frac{\boldsymbol{r}}{\lambda_\mu(t)}, \tag{7.89}$$

$$\tan\left(\omega t'\right) = \frac{1}{\mu}\tan(\omega t), \tag{7.90}$$

and the scaling function λ_μ is

$$\lambda_\mu(t) = \left[\cos^2(\omega t) + \frac{1}{\mu^2}\sin^2(\omega t)\right]^{1/2}. \tag{7.91}$$

A proof of this statement is given in Appendix D.3.

In this particular regime, thanks to the previous scaling laws that also apply here, the solutions of the Gross-Pitaevskii equation with parameters ω, $\tilde{g}$ and N can therefore be linked to the solutions of a Gross-Pitaevskii equation with any other parameters ω', $\tilde{g}'$ and N', as long as $\tilde{g}'N' \gg 1$. More precisely, if $n_1(\boldsymbol{r}, t)$ and $\boldsymbol{v}_1(\boldsymbol{r}, t)$ are solutions of the hydrodynamic equations 7.85 and 7.86 with parameters ω_1 and $\tilde{g}_1 N_1$, then $n_2(\boldsymbol{r}', t')$ and $\boldsymbol{v}_1(\boldsymbol{r}, t)$, as defined below, are solutions of these equations with parameters $\omega_2 = \zeta\omega_1$ and $\tilde{g}_2 N_2 = \mu^2 \tilde{g}_1 N_1$:

$$n_2(\boldsymbol{r}', t') = \frac{N_2}{N_1}\lambda_{\zeta,\mu}(t)\, n_1(\boldsymbol{r}, t), \tag{7.92}$$

$$\boldsymbol{v}_2(\boldsymbol{r}', t') = \mu\lambda_{\zeta,\mu}(t)\,\boldsymbol{v}_1(\boldsymbol{r}, t) - \mu\dot{\lambda}_{\zeta,\mu}(t)\boldsymbol{r}, \tag{7.93}$$

with

$$\boldsymbol{r}' = \frac{\boldsymbol{r}}{\lambda_{\zeta,\mu}(t)}, \tag{7.94}$$

$$\tan\left(\omega_2 t'\right) = \frac{\zeta}{\mu}\frac{\alpha\tan(\omega_1 t) + \beta}{\gamma\tan(\omega_1 t) + \delta}, \tag{7.95}$$

$$\lambda_{\zeta,\mu}(t) = \left[\frac{\zeta^2}{\mu^2}\left(\alpha\sin(\omega_1 t) + \beta\cos(\omega_1 t)\right)^2 + \left(\gamma\sin(\omega_1 t) + \delta\cos(\omega_1 t)\right)^2\right]^{1/2}, \tag{7.96}$$

and $\alpha\delta - \beta\gamma = 1$.

7.4 CONCLUSION

In this chapter I have detailed some mathematical tools to study the continuous dynamical symmetries of a physical system. In particular, the algebraic structure of its Lie group is very important to infer consequences on the dynamics of this system. Moreover, if there exists a link that maps a physical system onto another, many properties of the first one can be transported to the other one, notably the Lie group.

I have then applied this formalism on two different systems: N weakly interacting, free bosons in two dimensions (interaction parameter $\tilde{g}$) and the N weakly interacting, harmonically trapped bosons in two dimensions (same interaction parameter $\tilde{g}$). The first one displays the property of scale-invariance and its Lie group has the structure of SO(2,1). The second one has a more subtle symmetry group with the same algebraic structure. It strikingly leads to a periodic evolution of the potential energy of the system at twice the frequency of the harmonic trap. These two systems are in fact linked by a map that can also be extended to systems with a time-dependent trap frequency. The existence of such a map ensures that all these systems are captured by the same physics.

Finally, I have shown that in the hydrodynamic regime, two systems with different atom numbers and interacting with different interaction parameters can also be mapped one onto the other. In this particular regime, the dynamics of the system is basically the same, regardless of the number of particles, the interaction parameter, the size of the system and the (possibly time-dependent) frequency of the external harmonic potential.

8

AN EXPERIMENTAL APPROACH OF DYNAMICAL SYMMETRIES

The goal of this chapter is to experimentally probe the dynamical symmetries presented in the previous Chapter. We are indeed able to produce a cloud of weakly interacting bosons in two dimensions with various initial conditions, such as its initial size and atom number. When the temperature of this cloud is much lower than the critical temperature of the BKT transition, its dynamics is well-captured by a Gross-Pitaevskii equation [111]. Moreover, we can put the atoms either in a flat potential, or in an isotropic harmonic potential, thus realizing the two types of evolutions described in Chapter 7.

I first describe the experimental sequence by detailing its different steps and by introducing the observables that are accessible and that we use in this study. I also present the main calibrations of the parameters of the experiment.

Then I detail the experimental investigation of the symmetries of the system in the case where the atom number and the interaction parameter are fixed, corresponding to the sections 7.2.1, 7.2.2 and 7.2.3.

Finally I present the experimental study corresponding to the scaling laws explained in section 7.3, where the atom number and the interaction parameter of the system may vary.

8.1 EXPERIMENTAL SEQUENCE

8.1.1 *The course of events*

We use two different experimental sequences, according to the potential in which we want the atoms to evolve: a flat potential or a harmonic potential. I start by describing the former, which is simpler.

8.1.1.1 *Evolution in a flat potential*

As in Chapters 5 and 6, we start with a cloud of atoms at equilibrium in a box-like potential of arbitrary shape. There are typically several tens of thousands of atoms and we choose their temperature T much lower than the critical temperature T_c. We extract the ratio T/T_c with the method presented in 2.3.2.3 and we estimate it to be below 0.3, which correspond to a PSD $\gtrsim 30$. We cannot have a better estimate because our method is not reliable any more for such high PSDs.

The atoms are initially in the ground state $S_{1/2}$, in the hyperfine state $F = 1, m_F = 0$. At $t = 0$ the confining walls of the box potential are removed and the cloud evolves during a variable duration in the potential given by the vertical confinement. The spatial expansion of the cloud is small compared to the size of the light beams creating this vertical confinement. The corrugations of this potential are small enough compared to the chemical potential so that we can safely consider that the atoms evolve in a flat potential in two dimensions.

At time t we take an absorption image of the cloud: a controlled fraction of the atoms is transferred to the state $F = 2, m_F = 0$ and imaged.

The atom number is fixed by the loading process in the initial box-potential. We do not try to control this value. On the contrary, the interaction parameter $\tilde{g}$ can be chosen in a large range of values (from 0.07 to 0.16 approximately) by changing the intensity of the beams creating the vertical potential. Indeed, equations 2.14 and 2.5 indicate respectively how the parameter $\tilde{g}$ depends on the vertical frequency ω_z and how this frequency depends on the height of the potential of the vertical optical lattice. We find that $\tilde{g}$ is proportional to the fourth root of the power of the light beams. To span the range indicated above we have to vary this power by a factor ≈ 30. We note that the lattice depths we use remain always large enough to hold the atoms against gravity.

The determination of the value of $\tilde{g}$ is detailed in 8.1.3. It is based on the measurement of the vertical frequency ω_z.

8.1.1.2 *Evolution in a harmonic potential*

If we wish to have the atoms evolve in a harmonic potential, the experimental sequence is slightly more complex. It is however very similar to the one detailed in Chapter 5.

We start with a cloud in the same conditions as in the previous case. We additionally create a static magnetic field with the vertical anti-Helmholtz coils. As in Chapter 5, the vertical gradient b' is chosen so that it compensates gravity for atoms in the state $F = 1, m_F = -1$:

$$b' = \frac{2mg}{\mu_{\mathrm{B}}}, \tag{8.1}$$

which gives $b' \approx 30\,\mathrm{G/cm}$. The zero of the field is located around $160\,\mu\mathrm{m}$ above the plane of atoms, which gives in the xy-plane a residual harmonic potential of frequency $\omega \approx 2\pi \cdot 20\,\mathrm{Hz}$.

Initially, the atoms are not sensitive to this harmonic potential since they are in the state $F = 1, m_F = 0$ whose energy does not appreciably depend on the magnetic field for such low values. At time $t = 0$, we apply successively two microwave pulses with two different frequencies. The first one transfers all the atoms to the state $F = 2, m_F = 0$ and the second one brings them to the state $F = 1, m_F = -1$. We also remove the walls of the box potential. The atoms can then evolve in the combination of the vertical confinement and the harmonic potential. After a given duration of evolution we take an absorption image after having transferred a controlled fraction of the atoms in the state $F = 2, m_F = 0$ with a final microwave pulse.

8.1.2 *The measured observables*

With the absorption images we take, we have a direct access to the density distribution $n(\boldsymbol{r}, t)$. There are several interesting quantities that we can extract from it:

1. We determine the atom number N:
$$N = \iint \mathrm{d}^2\boldsymbol{r}\; n(\boldsymbol{r}, t). \tag{8.2}$$

2. We determine the position of the centre of mass $(x_\mathrm{c}, y_\mathrm{c})$:
$$x_\mathrm{c} = \frac{1}{N} \iint \mathrm{d}^2\boldsymbol{r}\; x\; n(\boldsymbol{r}, t) \tag{8.3}$$
$$y_\mathrm{c} = \frac{1}{N} \iint \mathrm{d}^2\boldsymbol{r}\; y\; n(\boldsymbol{r}, t). \tag{8.4}$$
One can separate the motion of this centre of mass from the dynamics of the rest of the degrees of freedom [192]. In the following we will thus work in the reference frame of this centre of mass. Experimentally, we make sure that the motion of the centre of mass has a small amplitude (less than 2 µm) to reduce the effect of the anharmonicity of the potential as much as possible.

3. We then determine the mean square radius of this distribution $\langle \boldsymbol{r}^2 \rangle$:
$$\langle \boldsymbol{r}^2 \rangle = \frac{1}{N} \iint \mathrm{d}^2\boldsymbol{r}\; \left[(x - x_\mathrm{c})^2 + (y - y_\mathrm{c})^2\right]\; n(\boldsymbol{r}, t). \tag{8.5}$$
This quantity allows us to determine the potential energy per particle
$$\frac{E_\mathrm{pot}}{N} = \frac{1}{2} m\omega^2 \langle \boldsymbol{r}^2 \rangle. \tag{8.6}$$

4. We finally extract the interaction energy per particle:
$$\frac{E_\mathrm{int}}{N} = \frac{\hbar^2 \tilde{g}}{2mN} \iint \mathrm{d}^2\boldsymbol{r}\; n^2(\boldsymbol{r}, t). \tag{8.7}$$

We do not attempt to extract the kinetic energy from the evolution of the density distribution. It is in principle possible to do so: we have
$$E_\mathrm{kin} = \frac{\hbar^2}{2m} \iint \mathrm{d}^2\boldsymbol{r}\, |\boldsymbol{\nabla}\psi|^2 \tag{8.8}$$
$$= \iint \mathrm{d}^2\boldsymbol{r} \left(\frac{1}{2} m\boldsymbol{v}^2 + P(n)\right) n(\boldsymbol{r}, t). \tag{8.9}$$

The second term can be determined from the density distribution at a given time t by computing the spatial derivative of the square root of this density distribution. The first term is accessible from the hydrodynamic equation 7.77:
$$\boldsymbol{\nabla}(n\boldsymbol{v}) = -\frac{\partial n}{\partial t}. \tag{8.10}$$

One could measure the right hand side from the evolution of the density distribution, and integrate it over space to extract the velocity $\boldsymbol{v}$. However the precision of our measurements both in terms of spatial resolution, of signal to noise ratio and of time resolution is not sufficient to reliably determine any of the two terms of the kinetic energy.

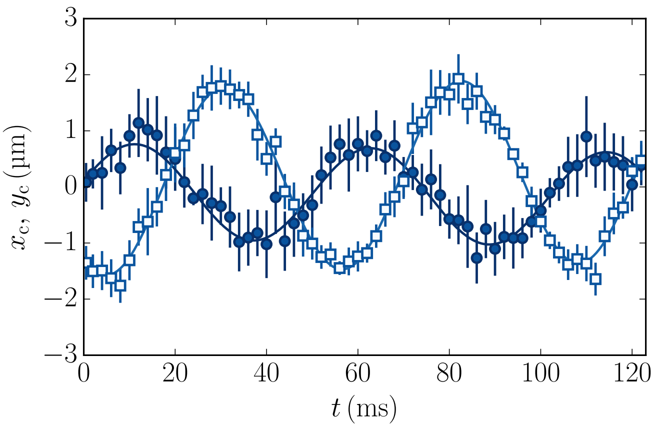

Figure 8.1: Frequency of the harmonic potential. The position of the centre of mass x_c (filled disks) and y_c (empty squares) in the two directions of space are calculated from the density distribution. The error bars represent the statistical error on the ten experimental realisations. The evolution of x_c and y_c is fitted with a sinusoidal function. We get the frequencies in the two directions, here $\omega_x = 2\pi \cdot 19.4(2)$ Hz and $\omega_x = 2\pi \cdot 19.3(1)$ Hz. The anisotropy of the potential is in this case around 1%.

8.1.3 *Some calibrations*

8.1.3.1 *Frequency and anisotropy of the harmonic trap*

We measure the two frequencies $\omega_{x,y}$ by measuring the position of the centre of mass as a function of time. We compensate the experimental anisotropy of the harmonic potential with the MOT coils, as we did in Chapter 5. On Fig. 8.1 is presented the oscillation of the two components of the centre of mass of an initially square-shaped cloud. The oscillations are each fitted with a sinusoidal function whose respective frequency are $\omega_x = 2\pi \cdot 19.4(2)$ Hz and $\omega_y = 2\pi \cdot 19.3(1)$ Hz. The anisotropy $\omega_x/\omega_y - 1$ is in this case around 1%, and it is below 2% for all the data presented here.

For practical reasons we do not change the value of the in-plane frequency ω. In particular we do not test the scaling laws associated with a time-dependent trap frequency (see the end of section 7.2.3) because this would require to compensate at each time for the anisotropy of the harmonic trap, which is technically difficult.

8.1.3.2 *Value of the vertical confinement*

We determine the value of the vertical frequency ω_z similarly to the measurements presented in section 2.2.2.4. We prepare the sample with a high vertical confinement. This is achieved by having a high laser intensity. At $t = 0$ we decrease in 1 ms this intensity to a chosen value. The minimum of the potential energy in the vertical direction is displaced due to gravity, the atoms get a vertical kick due to this displacement and they oscillate in the vertical harmonic potential. After a variable duration of oscillation we remove the vertical confinement and let the atoms expand freely during 12 ms.

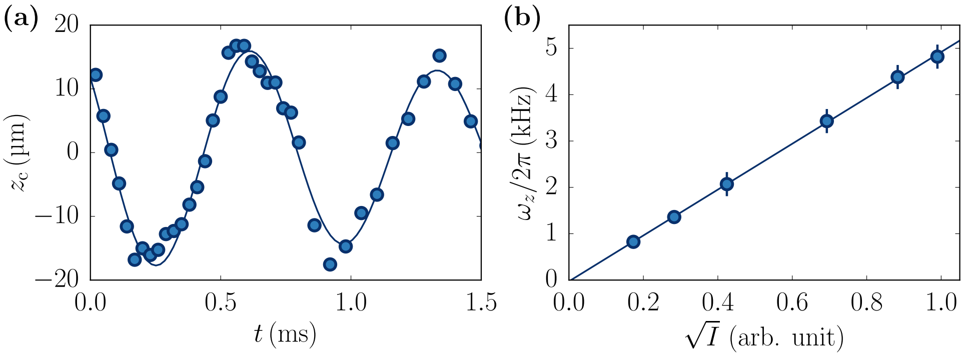

Figure 8.2: Frequency of the vertical confinement. (a): We give a vertical kick to the atoms and let them evolve in the vertical harmonic trap during a variable duration t. Their vertical position z_c is measured after a time of flight of 12 ms as a function of time, and it is fitted with a sine function. On the example shown here the fitted vertical frequency is $\omega_z = 1.39(26)$ kHz. (b): The vertical frequency of the harmonic confinement is measured for different values of the intensity of the laser beams, and plotted as a function of the square root of this intensity. The data points are fitted with a linear function. We can thus operate with any intensity in this range and infer the value of the vertical confinement with an accuracy of a few percent.

We then measure the vertical position of the centre of mass as a function of the oscillation duration. An example of the evolution of this vertical position is shown on Fig. 8.2a. The oscillations are fitted with a sine function, and we extract its frequency. On Fig 8.2b are shown the fitted frequencies as a function of the square root of the intensity of the laser. The data points form a line, which confirms the relation 2.5:

$$\omega_z = \sqrt{\frac{2\pi^2 U}{md^2}}, \tag{8.11}$$

where the potential height U is proportional to the intensity I. From these measurements we are able to determine the value of $\tilde{g}$.

8.2 VERIFICATION OF THE SO(2,1) SYMMETRY

In this section I describe two experiments to test predictions of the dynamical symmetries of the system: the oscillation of the potential energy and one of the scaling laws presented in Chapter 7.

8.2.1 *Evolution of the potential energy*

We prepare a cloud of $N = 4.1(2) \cdot 10^4$ atoms initially in a square-shaped box potential of side $L = 27.6(5)$ µm. After switching off the box potential, we let it evolve in the xy-plane in the presence of the harmonic potential, as described above. We probe the first 120 ms of this evolution. For each duration we perform several realisations (typically 10) that we average to measure the density distribution. We then extract the potential energy per particle E_{pot}/N and the interaction energy E_{int}/N.

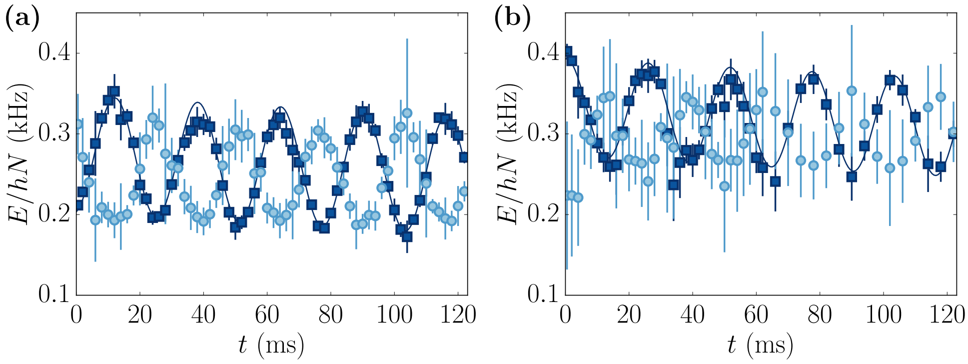

Figure 8.3: Potential and interaction energy per particle of a cloud evolving in a harmonic potential. An initial uniform cloud is prepared in a box potential, and released in a harmonic potential. The potential energy (dark squares) and interaction energy (light circles) per particle are extracted from the density distribution. The error bars represent the statistical error on the ten experimental realisations. (a): The initial cloud has $N = 4.1(2) \cdot 10^4$ atoms and has the shape of a square of side 27.6(5) µm. (b): The initial cloud has $N = 6.3(4) \cdot 10^4$ and has the shape of a disk of radius 23.6(5) µm. In both cases, the potential energy is fitted with a sinusoidal function. The fitted frequencies are respectively $2\pi \cdot 38.4(1)$ Hz and $2\pi \cdot 38.8(2)$ Hz, which is compatible with twice the frequency of their centre of mass.

The results are shown on Fig. 8.3a. The potential energy per particle (dark squares) is oscillating periodically. We fit the data points with a sine function and an additional negative slope. The frequency of the oscillation is $\omega_{\text{fit}} = 2\pi \cdot 38.4(2)$ Hz, which is compatible with twice the frequency of the harmonic oscillator $\omega = 2\pi \cdot 19.3(1)$ Hz. The additional slope accounts for the small loss of atoms that leave the plane. The fit gives a slope of $-0.25(4)$ Hz/s, which is compatible with the atom loss rate that we measure.

The interaction energy per particle (light circles) varies in opposition with the potential energy, and the higher and lower values correspond approximatively to the higher and lower values of the potential energy per particle.

We perform the same experiment with $N = 6.3(4) \cdot 10^4$ atoms initially in a disk-shaped box potential of radius 23.6(5) µm. The potential and interaction energies as a function of the evolution time are shown on Fig. 8.3b. The oscillation frequency of the potential energy is very similar to the one of the previous experiment: we get here $2\pi \cdot 38.8(2)$ Hz, and the frequency of the centre of mass is $2\pi \cdot 19.4(2)$ Hz. The interaction energy per particle varies in opposition with the potential energy per particle, as for the previous example.

What is more interesting here is that for the first experiment the potential energy starts by increasing, whereas it starts by decreasing for the second one. This is because the ratio between the initial potential and interaction energies is not the same in the two experiments. This behaviour is captured in the expression of the potential energy:

$$E_{\text{pot}}(t) = \frac{1}{2} E_{\text{tot}} + \frac{1}{2} \Delta E \cos(2\omega t) + \frac{1}{2\omega} \dot{E}_{\text{pot}}(0) \sin(2\omega t), \tag{8.12}$$

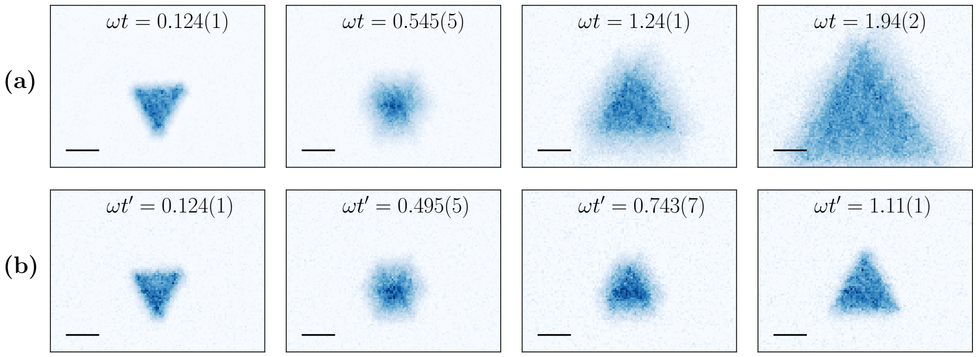

Figure 8.4: Evolution of a cloud in different potentials. A cloud with $N = 3.9(3) \cdot 10^4$ atoms is prepared in a triangular box-potential of side 40.2(3) µm. Two different experiments are performed. (a): The box potential is removed and the cloud evolves in a flat potential. The density distribution $n_1(t)$ is displayed (b): The atoms are transferred in a harmonic potential of frequency $\omega = 19.6(2)\,\mathrm{Hz}$ and they evolve in it. The density distribution $n_2(t')$ is displayed. For both experiments, the evolution time is multiplied by the frequency of the harmonic potential of the second experiment. The images that are shown are chosen so that they look similar two by two, up to a scaling of space.

where ΔE can be written as:

$$\Delta E = E_{\text{pot}}(0) - E_{\text{int}}(0) - E_{\text{kin}}(0). \tag{8.13}$$

In our case, the initial kinetic energy is negligible. In the first experiment, the initial interaction energy is larger than the initial potential energy, ΔE is negative and the cloud starts by expanding when it is released in the harmonic potential. In the second experiment, it is the contrary: the initial interaction energy is lower than the initial potential energy. We have $\Delta E > 0$, and the cloud thus starts by shrinking in the harmonic potential.

8.2.2 *Evolution in traps of different frequency*

We now turn to the experimental verification of the scaling law derived in the last Chapter and that links the evolution of a cloud in a harmonic trap to the free evolution of a cloud. This scaling law is summarized from equation 7.59 to equation 7.63:

$$\psi_\omega(\boldsymbol{r}', t') = f_{0,\omega}(\boldsymbol{r}, t)\, \psi_0(\boldsymbol{r}, t), \tag{8.14}$$

$$\boldsymbol{r}' = \boldsymbol{r}/\lambda_{0,\omega}(t), \tag{8.15}$$

$$\tan\!\big(\omega t'\big) = \omega t, \tag{8.16}$$

$$\lambda_{0,\omega}(t) = \left(1 + \omega^2 t^2\right)^{1/2}, \tag{8.17}$$

$$f_{0,\omega}(\boldsymbol{r}, t) = \lambda_{0,\omega}(t) \exp\left(-\frac{\mathrm{i} m \dot{\lambda}_{0,\omega} \boldsymbol{r}^2}{2\hbar \lambda_{0,\omega}}\right), \tag{8.18}$$

In order to probe this scaling law, we prepare a cloud of $N = 3.9(3) \cdot 10^4$ atoms initially in a box potential with the shape of an equilateral triangle of side 40.2(3) µm. In a first experiment we measure the evolution $n_1(\boldsymbol{r}, t)$ of this cloud in a flat potential during the first 20 ms. In order to have a proper estimate of this density distribution, we average the measurements of a few experimental realisations. A few images of this evolution are shown on Fig. 8.4a. We are limited to this range of evolution times because the atoms expand in a large region. This first leads to a diminution of the signal to noise ratio since the density gets lower when the cloud is expanding, but, more detrimentally, a part of the cloud gets out of the region that we are able to image.

In a second experiment, we measure the evolution $n_2(\boldsymbol{r}', t')$ of the same initial cloud in the harmonic trap. As relation 8.16 indicates, the free evolution of the cloud between $t = 0$ and $t = +\infty$ maps on its evolution in the harmonic potential during the first quarter of period, which means between $t' = 0$ and $t' = \pi/(2\omega)$. For this evolution we therefore limit its duration to the first 12 ms. A few images of this evolution are shown on Fig. 8.4b.

The two evolutions are very similar: the images of the figure have been chosen so that they approximately correspond two by two. These pairs of images only differ by a spatial scaling factor and by the duration of the evolution after which the image has been taken. This is exactly what the scaling laws predict: an initial cloud with a given wave function $\psi(\boldsymbol{r}, 0)$ will evolve as $\psi_1(\boldsymbol{r}, t)$ in a flat potential and as $\psi_2(\boldsymbol{r}', t')$ in a harmonic potential with

$$\boldsymbol{r}' = \frac{\boldsymbol{r}}{\sqrt{1 + \omega^2 t^2}}, \tag{8.19}$$

$$\tan\bigl(\omega t'\bigr) = \omega t, \tag{8.20}$$

and the same laws apply for the density distributions $n_1(\boldsymbol{r}, t)$ and $n_2(\boldsymbol{r}', t')$.

We experimentally reconstruct the scaling laws 8.19 and 8.20 in the following way. For two density distributions $n_1(\boldsymbol{r}, t_1)$ and $n_2(\boldsymbol{r}, t_2')$ taken at respective times t_1 and t_2, we need to define their overlap $\mathcal{O}\left[n_1(t_1), n_2(t_2')\right]$ to quantify how similar they are, irrespective of a scaling factor on space there might be between them.

We first define the scalar product $(n_1|n_2)$ between two density distributions n_1 and n_2:

$$(n_1|n_2) = \int \mathrm{d}^2\boldsymbol{r}\; n_1(\boldsymbol{r})\, n_2(\boldsymbol{r}). \tag{8.21}$$

For a scaling factor $\lambda > 0$, we then define the quantity

$$p\left[n_1, n_2, \lambda\right] = \frac{(n_1^{(\lambda)}|n_2)}{||n_1^{(\lambda)}||\; ||n_2||}, \tag{8.22}$$

where $||n||^2 = (n|n)$ is the norm of a density distribution, and $n^{(\lambda)}(\boldsymbol{r}) = \lambda^2 n(\lambda \boldsymbol{r})$ is the density distribution $n(\boldsymbol{r})$ rescaled by the spatial scaling factor λ. The quantity $p\left[n_1, n_2, \lambda\right]$ is between 0 and 1, and is equal to 1 if and only if the density distributions n_1 and n_2 differ only by the scaling factor λ.

We then define the overlap between $n_1(\boldsymbol{r}, t_1)$ and $n_2(\boldsymbol{r}, t_2')$ by

$$\mathcal{O}\left[n_1(t_1), n_2(t_2')\right] = \max_{\lambda} p[n_1(t_1), n_2(t_2'), \lambda]. \tag{8.23}$$

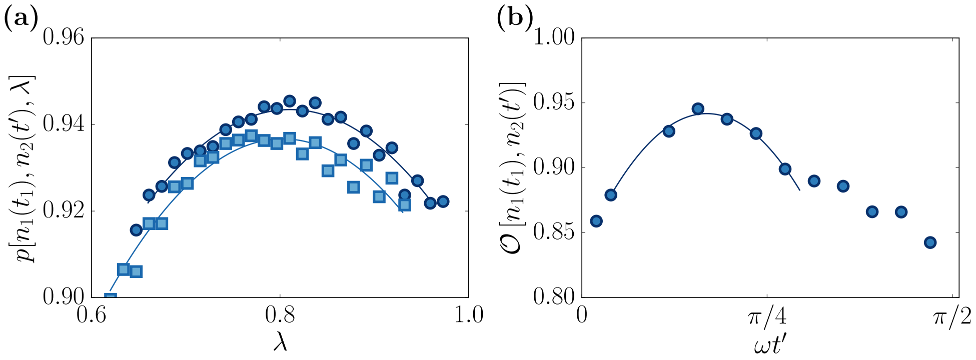

Figure 8.5: Method of analysis to reconstruct a scaling law on space and time. A specific time of the first evolution is picked to illustrate this method: $t_1 = 5.9\,\text{ms}$. (a) The quantity $p[n_1(t_1), n_2(t'), \lambda]$ is plotted as a function of λ for two values of t': 4 ms for the dark circles and 5 ms for the light squares. The maxima of each of these curves, determined by a parabolic fit, give the value of $\mathcal{O}\,[n_1(t_1), n_2(t')]$. (b): The overlap between the density distribution $n_1(t_1)$ and the density distribution $n_2(t')$ is plotted as a function of $\omega t'$. A maximum at 0.94 is found around $\omega t' = 0.53$, and is determined with a parabolic fit, shown as a solid line. It is the value we assign to $t'(t_1)$. Going back to the graph (a), we can then determine $\Lambda(t_1)$, which is the value for which $p[n_1(t_1), n_2(t'(t_1)), \lambda]$ is maximum. Here, $\Lambda(t_1) = 0.82(6)$.

With these tools we can reconstruct the scaling laws: for a given time t_1 of the free evolution, we compute $p\,[n_1(t_1), n_2(t'), \lambda]$ for all times t' and various scaling factors λ. For every time t', we can then determine the overlap $\mathcal{O}\,[n_1(t_1), n_2(t')]$ by maximising $p\,[n_1(t_1), n_2(t'), \lambda]$ over λ. This overlap is maximum for $t' = t'(t_1)$, and the scaling factor λ for which $p\,[n_1(t_1), n_2(t'(t_1)), \lambda]$ reaches $\mathcal{O}\,[n_1(t_1), n_2(t'(t_1))]$ is denoted as $\Lambda(t_1)$.

If this overlap between $n_1(t_1)$ and $n_2(t'(t_1))$ is close to 1, then these density distributions are similar, up to the scaling factor $\Lambda(t_1)$.

An example of this analysis is presented on Fig. 8.5, for the density distribution $n_1(t_1)$ at the specific time $t_1 = 5.9\,\text{ms}$. The first graph presents the values of $p\,[n_1(t_1), n_2(t'), \lambda]$ for two values of t'. The maximum of each curves is the overlap between $n_1(t_1)$ and $n_2(t')$. These overlaps are reported on the second graph as a function of t'. A maximum is reached around $\omega t' = 0.53$ with an overlap at about 0.94. The overlap is reached for $\lambda \approx 0.8$, as shown on the first graph, and it is the value we assign to $\Lambda(t_1)$.

We perform this analysis for all the density distributions of the first evolution. The results are summarized on Fig. 8.6. The first graph shows $t'(t_1)$, which represents the corresponding times between the free evolution of the cloud and its evolution in the harmonic trap. The theoretical prediction 8.20 is shown as a solid line and is in good agreement with the experimental data.

The second graph displays the behaviour of the scaling factor $\Lambda(t)$ between the first and the second evolutions. The theoretical prediction

$$\Lambda(t) = \sqrt{1 + \omega^2 t^2} \tag{8.24}$$

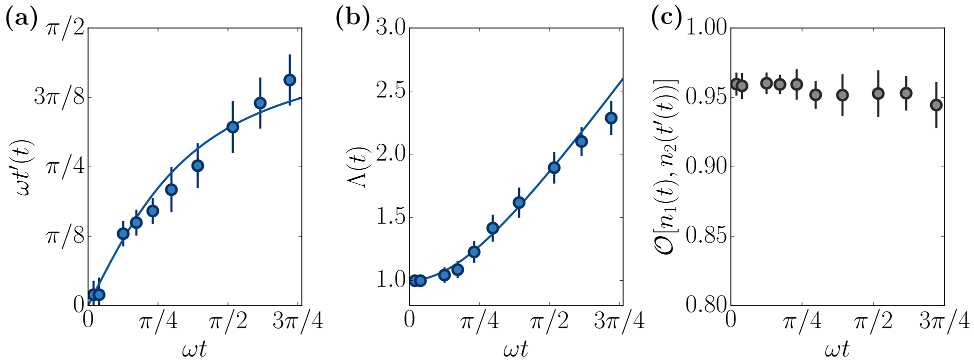

Figure 8.6: Reconstructing the scaling law between a free evolution and an evolution with a harmonic potential. (a): The time $\omega t'(t)$ of the evolution in the harmonic trap is linked to the time t of the free evolution. (b): Scaling factor $\Lambda(t)$ on space that links these two evolutions. On these two first graphs, the theoretical curves 8.20 and 8.24 are shown as solid lines and do not have any adjustable parameters. (c): The overlap between corresponding density distributions of the two evolutions is plotted. This overlap is always above 0.95, to be compared with the value of 0.98 to 0.99 between two density distributions taken in the same experimental conditions. This confirms that the two evolutions are similar up to a scaling law on space and time. On the three graphs the error bars represent the confidence interval within 2 standard deviations of the fits we use.

is shown as a solid line. Here again the agreement between theory and experiment is very good.

Finally, the overlap $\mathcal{O}[n_1(t), n_2(t'(t))]$ is plotted on the third graph. It is always around 0.95, which confirms the fact that the two evolutions are indeed similar. This value can be compared to the overlap between two density distributions measured with the same experimental conditions and each averaged over a few realisations. Such an overlap is not exactly 1, but rather on the order of 0.98 to 0.99 due to experimental imperfections.

It is experimentally challenging to verify the other scaling laws presented in 7.2.2, because it would require to initially prepare clouds with different sizes and the same atom number. Instead, we now probe the scaling laws in which the atom number and the interaction parameter can be changed.

8.3 UNIVERSAL DYNAMICS IN THE HYDRODYNAMIC REGIME

The scaling laws that allow to link the evolution of clouds with a different product $\tilde{g}N$ are valid in the hydrodynamic regime, where this product is large compared to 1. In this regime, the scaling laws that can link the evolution of different clouds contain the ones which are valid in any regime, and they are richer.

I present here two complementary experiments to test these scaling laws. On the first one only the product $\tilde{g}N$ is varied, and on the second one, both this product and the initial size of the cloud are changed.

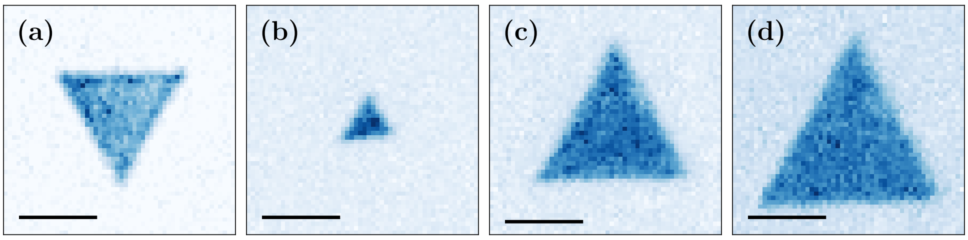

Figure 8.7: Evolution a cloud after a quarter of oscillation in a harmonic potential. (a): A cloud is prepared in a triangular-shaped box potential of side 38.2(3) µm, and the initial density distribution is displayed. The initial cloud evolves during a quarter of period in a harmonic potential with various interaction parameters. Images (b), (c), (d) display the density distribution after this evolution for $\tilde{g}N = 2.5(3) \cdot 10^2$, $2.3(2) \cdot 10^3$ and $3.5(2) \cdot 10^3$ respectively.

8.3.1 *Evolution with different interaction parameters*

We explore here the evolution in the harmonic potential of a cloud whose initial shape is an equilateral triangle of side 38.2(3) µm. Fig. 8.7a shows the average of a few absorption images to illustrate this initial density distribution. We prepare this cloud with various values of the vertical confinement frequency ω_z. The corresponding values of $\tilde{g}$ range from 0.07 to 0.16. The number of atoms that we trap in the initial box potential also varies slightly, depending on this vertical confinement, and we extract it from absorption images. In the end, the product $\tilde{g}N$ varies approximately from $2.5 \cdot 10^2$ to $4.3 \cdot 10^3$.

The scaling laws on space and time that link the evolution of two of these initial clouds are the equations 7.90 and 7.91:

$$n_2(\boldsymbol{r}', t') = \frac{N_2}{N_1} n_1(\boldsymbol{r}, t), \tag{8.25}$$

$$\boldsymbol{r}' = \frac{\boldsymbol{r}}{\lambda_\mu(t)}, \quad \lambda_\mu(t) = \left[\cos^2(\omega t) + \frac{1}{\mu^2}\sin^2(\omega t)\right]^{1/2} \tag{8.26}$$

$$\tan\big(\omega t'\big) = \frac{1}{\mu}\tan(\omega t), \tag{8.27}$$

$$\tag{8.28}$$

where $\mu^2 = \tilde{g}_2 N_2 / \tilde{g}_1 N_1$. In particular, the times $\omega t = \pi/2$ and $\omega t' = \pi/2$ verify the equation on time 8.27. We can therefore perform the evolution of two different clouds with this duration and their density distributions will be similar one with the other, up to the scaling factor

$$\lambda\left(t = \frac{\pi}{2\omega}\right) = \frac{1}{\mu}, \tag{8.29}$$

where μ^2 is the ratio between the products $\tilde{g}N$ of these clouds.

For each value of the product $\tilde{g}N$ we let the cloud evolve during $\pi/(2\omega)$ and measure its density distribution by averaging a few experimental realisations.

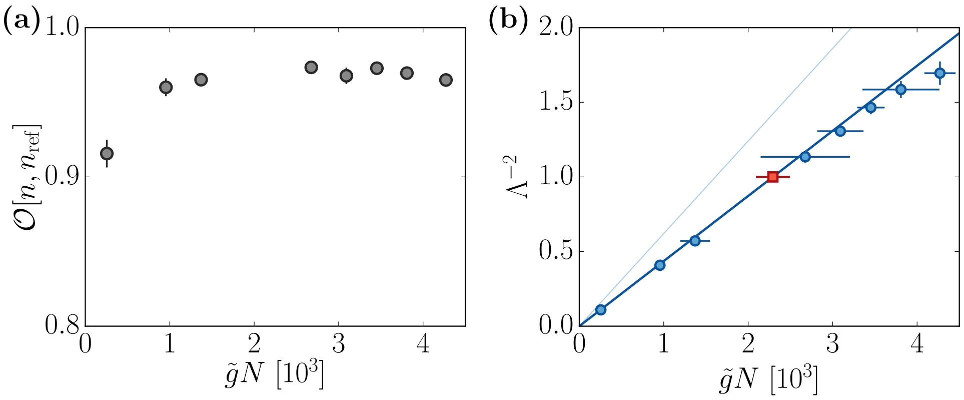

Figure 8.8: Size of an initially uniform triangle-shaped cloud after a quarter of oscillation in a harmonic potential. The density distribution shown on Fig. 8.7c is taken as a reference. All the other density distributions measured after a quarter of oscillation in the harmonic trap are compared to this reference by allowing for a scaling factor on space. (a): Overlap between the reference density distribution and the density distributions for each of the other values of $\tilde{g}N$. These overlaps are above 0.95, except for the first point, probably because of the low number of pixels of the camera that the cloud covers. (b): Scaling factor between the reference density distribution and the density distributions for the other values of $\tilde{g}N$. The red point corresponding to the reference is fixed at 1. The theoretical curve is the solid line, passing through the origin and the reference point. The shaded area represents the uncertainty on the slope of this line, due to the uncertainty we have on $\tilde{g}N$ for the reference point. On both graphs the vertical error bars represent the confidence interval within 2 standard deviations of the fits that we use.

A few examples are shown on Fig. 8.7b,c and d, and one can directly see that the density distributions are all similar. The particularity that the cloud seems to be a triangular shape with a uniform density after a quarter of oscillation is very surprising and it is discussed in Chapter 9. In the following we will only be interested in the size of these different density distributions and their similarity.

We perform the analysis as follows. We choose the density distribution corresponding to $(\tilde{g}N)_{\mathrm{ref}} \approx 2.3 \cdot 10^3$ as a reference, and we compute the overlap as defined in equation 8.23 between this distribution and each of the other density distributions. We also determine the scaling factor λ for which this overlap is reached, that we denote as $\Lambda(\tilde{g}N)$. The choice of the reference is arbitrary, and choosing another one would give similar results.

On Fig. 8.8a are shown the values of the overlap between the reference distribution and the density distributions corresponding to the other values of $\tilde{g}N$. They are all higher than 0.95, except for the first point, which may be explained because of the low number of camera pixels on which the atoms are located. On Fig. 8.8b is plotted the value of $\Lambda^{-2}(\tilde{g}N)$. The value for the reference point is fixed at 1 (red square on the graph). The theory predicts that

$$\Lambda^{-2}\left(\tilde{g}N\right) = \frac{\tilde{g}N}{(\tilde{g}N)_{\mathrm{ref}}}, \tag{8.30}$$

which is represented as the solid line, and the shaded area indicates the uncertainty on the denominator of this prediction.

The data points are in very good agreement with the theory, except maybe for the rightmost point. We attribute it to the fact that, at such a large value of $\tilde{g}$, the defects of the light potential creating the vertical confinement start to play a significant role in the evolution of the cloud.

This particular behaviour that, after a quarter of period in a harmonic potential, the area of the cloud is proportional to its number of atoms is at the same time very surprising and very interesting. We can understand it from the fact that, at this specific time, the initial potential and interaction energies have been exchanged: when the initial kinetic energy is neglected in equation 8.12[1], and with the initial condition $\dot{E}_{\mathrm{pot}}(0) = 0$ that we have on the experiment, we get

$$E_{\mathrm{pot}}\left(\frac{\pi}{2\omega}\right) = E_{\mathrm{int}}(0). \tag{8.31}$$

For a given initial shape of the cloud, the initial interaction energy per particle is proportional to the product $\tilde{g}N$ and the potential energy per particle at $t = \pi/(2\omega)$ is proportional to the mean square radius of the density distribution. This reasoning does not explain that the density distributions shown on Fig. 8.7b, c and d are similar, but it captures the expression of the scaling factor (equation 8.30).

This property can be used to perform a very reliable and robust method to calibrate the scattering cross-section of the absorption imaging (see Chapter 2, section 2.2.3.2). One can indeed prepare a cloud with a uniform density in a box potential of surface S and measure both the optical density of a controlled fraction ε of this cloud and the potential energy of the cloud after a quarter of period in the harmonic potential.

The initial interaction energy is

$$E_{\mathrm{int}}(0) = \frac{\hbar^2}{2m}\frac{\tilde{g}N^2}{S}, \tag{8.32}$$

which means that at $t = \pi/(2\omega)$, the mean radius square reads

$$\langle r^2 \rangle_{\frac{\pi}{2\omega}} = \frac{\hbar^2 \tilde{g} N}{m^2 \omega^2 S}. \tag{8.33}$$

This provides us with a very good estimate of the absolute atom number N, as long as the calibration of the magnification of the imaging system is proper, and if the measurement of the parameters $\tilde{g}$ and ω are accurate.

On the other hand, as we saw in Chapter 2 section 2.2.3.2, the measured optical density of a fraction ε of the cloud in the initial box potential is

$$\mathrm{OD} = \frac{7}{15}\frac{3\lambda_{\mathrm{L}}^2}{2\pi}\mathcal{F}\,\frac{\varepsilon N}{S}, \tag{8.34}$$

---

[1] For an initially triangular shape, the kinetic energy is null after a quarter of period of oscillation because of the particular dynamics of this shape. This dynamics is studied in the next chapter.

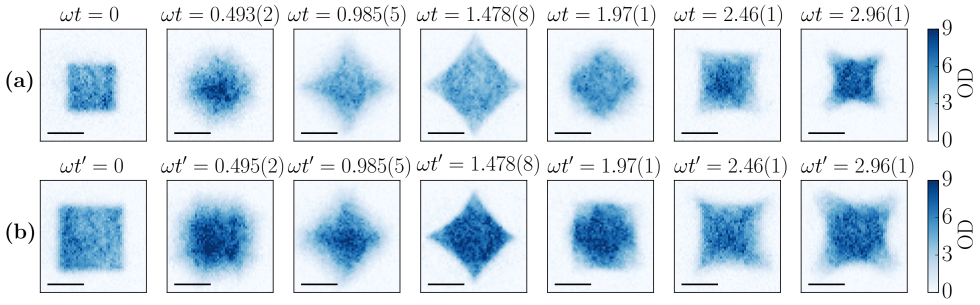

Figure 8.9: Evolution of two initially uniform square-shaped clouds with a different initial size and a different atom number. (a): Evolution in a harmonic potential during the first half period of a cloud of $N_1 = 3.7(3) \cdot 10^4$ atoms initially in a square-shaped box potential of side $L_1 = 27.0(5)\,\mu\text{m}$. (b): Evolution in the same harmonic potential during the first half period of a cloud of $N_2 = 5.4(3) \cdot 10^4$ atoms initially in a square-shaped box potential of side $L_1 = 36.8(5)\,\mu\text{m}$.

where the factor $\mathcal{F}$ depends on the experimental conditions in which the absorption imaging is performed. It is then determined by

$$\mathcal{F} = \frac{15}{7}\,\frac{2\pi}{3\lambda_{\mathrm{L}}^2}\,\frac{\hbar^2 \mathrm{OD}}{\varepsilon m^2 \omega^2}\,\frac{\tilde{g}}{\langle r^2 \rangle_{\frac{\pi}{2\omega}}}. \tag{8.35}$$

When performing these measurements on the density distributions of Fig. 8.7, we get a factor $\mathcal{F}$ of 1.6(2), which is compatible with the estimate that we did with projection noise measurements [65]. This new method is however much easier to implement and requires much less data than the previous one. Moreover it is robust with respect to parameters of the imaging system such as the point-spread function, contrary to the projection noise method.

8.3.2 *Evolution with different sizes and atom numbers*

Finally, we probe a last type of scaling law by looking at the evolution in a given harmonic trap of two clouds that have the same initial shape, but a different size, and a different atom number.

We prepare two clouds that are initially in a square-shaped box potential. The first one has a side $L_1 = 27.0(5)\,\mu\text{m}$ and contains $N_1 = 3.7(3) \cdot 10^4$, and the second one has a side $L_2 = 36.8(5)\,\mu\text{m}$ and contains $N_2 = 5.4(3) \cdot 10^4$ atoms. The interaction parameter is $\tilde{g} = 0.15$, therefore the product $\tilde{g}N$ is large compared to 1 for both clouds, which are thus in the hydrodynamic regime.

We let these two clouds evolve in the harmonic potential of frequency $\omega = 2\pi \cdot 19.6(2)\,\text{Hz}$ and measure their respective density distributions $n_1(\boldsymbol{r}, t)$ and $n_2(\boldsymbol{r'}, t')$ during more than one full period of the potential (from 0 to 60 ms). A few images of these two evolutions are displayed on Fig. 8.9.

We perform the exact same analysis as the one developed in section 8.2.2: we extract the corresponding times between the first evolution and the second one, the scaling factor between the images at these corresponding times, and the overlap between the corresponding images. These three graphs are shown on Fig. 8.10.

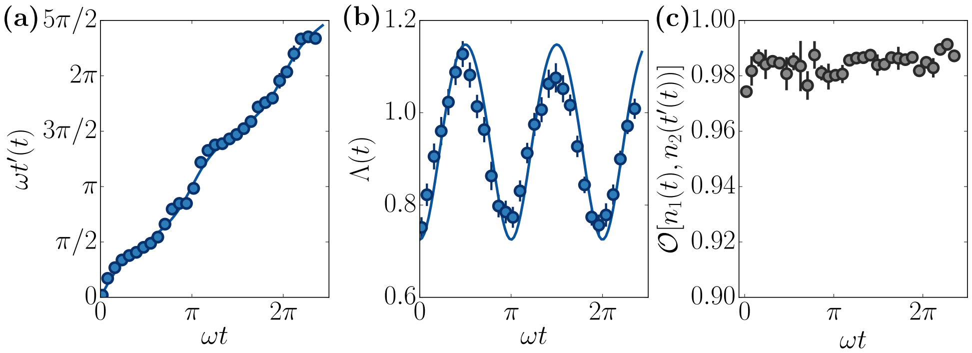

Figure 8.10: Reconstruction of the scaling law between two initially uniform square-shaped clouds with different size and atom number. (a): Correspondence between the time t of the evolution of the first cloud and the time t' of the evolution of the second cloud. (b): Scaling factor between the corresponding images of the first and second evolutions. On these two graphs, the theoretical predictions are plotted as solid lines and have no adjustable parameters. (c): Overlap between corresponding images of the two evolutions. This overlap is larger than 0.97, confirming that the two evolutions are similar up to a scaling law on space and time. On the three graphs the error bars represent the confidence interval within 2 standard deviations of the fits we use.

The overlaps between corresponding images, displayed on the last graph, are always above 0.97, which confirms that the evolutions of the two clouds are captured by the same dynamics.

The theoretical predictions are given by equations 7.92 to 7.96 with $\alpha = 1/\delta = L_2/L_1$, and $\beta = \gamma = 0$. This choice of β and γ is imposed by the facts that the wave functions at $t = 0$ and $t' = 0$ are similar up to a dilation and that their initial velocity is null. The choice of α and δ is imposed by the ratio of the sizes of the initial shapes and the constraint $\alpha\delta - \beta\gamma = 1$. We also have $\mu^2 = N_2/N_1$, because the interaction parameter of the two evolution is chosen to be the same, and $\zeta = 1$.

In the end, the relationship between n_1 and n_2 is

$$n_1(\boldsymbol{r}, t) = \mu^2 \lambda^2(t)\, n_2(\boldsymbol{r}', t'), \tag{8.36}$$

with

$$\boldsymbol{r}' = \boldsymbol{r}/\lambda(t), \tag{8.37}$$

$$\lambda(t) = \left[\frac{1}{\alpha^2}\cos^2(\omega t) + \left(\frac{\alpha}{\mu}\right)^2 \sin^2(\omega t)\right]^{1/2}, \tag{8.38}$$

$$\tan\big(\omega t'\big) = \frac{\alpha^2}{\mu}\tan(\omega t). \tag{8.39}$$

These two laws are completely determined by the values of $L_{1,2}$, $N_{1,2}$ and ω, which are measured independently from the evolution of $n_1(t)$ and $n_2(t')$. They are plotted on Fig. 8.10b, and c as solid lines. The shaded areas represent the uncertainties on the measurement of the atom numbers and the initial sizes. The theory and the experimental data are in excellent agreement.

With the three last experiments, we have experimentally explored the three parameters that the scaling laws derived in the previous chapter allow to vary in order to link the evolution of two different clouds: the size of the cloud, the frequency of the harmonic trap and the product between the interaction parameter and the total atom number.

8.4 CONCLUSION

In this chapter, I have presented the experimental investigation of the dynamical symmetries and scaling laws presented in the previous chapter.

First, the evolution of the potential energy is measured to be oscillating at a frequency twice the frequency of the harmonic trap, which is an important consequence of the algebraic structure of the dynamical symmetry group.

Then, the evolution of different clouds with the same shape are shown to be linked by simple scaling laws on space and time. Three independent experiments demonstrate that, in the hydrodynamic regime, two clouds that have the same shape, but different sizes and a different atom number, and that evolve in potentials of different frequencies and that interact with a different strength, share the same universal dynamics.

These very robust properties are the consequence of the dynamical symmetries of the 2D Bose gas, and their rich structure can be used for example to calibrate in a very efficient way the number of particles in an ultracold two-dimensional sample of atoms.

s

9

BREATHERS OF THE 2D GROSS-PITAEVSKII EQUATION

The study of non-linear equations constitutes entire fields in mathematics and physics [205–207]. The study of their properties, such as chaotic behaviour, is important in many branches of science, from biology [208] to meteorology [209], from optics [210] to hydrodynamics [211]. We will be interested here in particular solutions of such equations that do not deform, or that have periodic behaviour, in spite of the non-linearity of the equations.

One important non-linear equation that displays many of these solutions is the sine-Gordon equation [186]:

$$\frac{\partial^2 \phi}{\partial t^2} = \frac{\partial^2 \phi}{\partial x^2} - \sin(\phi). \tag{9.1}$$

This equation looks similar to the Klein-Gordon equation, except for the second term of the right-hand side that gives its name to the equation and provides its non-linearity. This one-dimensional equation supports very interesting solutions, called solitons, *i.e.* solutions of the form

$$\phi(x,t) = \phi_0(x - vt), \tag{9.2}$$

where ϕ_0 is a form function and v is a propagation velocity. In the case of the sine-Gordon equation, this soliton is given by

$$\phi_s(x,t) = 4 \arctan\left[\exp(\gamma x - \gamma v t)\right], \tag{9.3}$$

with $\gamma = (1 - v^2)^{-1}$ and $|v| < 1$. This solution is a waveform that propagates at velocity v and that does not deform. The existence of a soliton whose expression is analytic is surprising and has drawn the interest of many mathematicians and physicists.

Interestingly, this solution can be obtained thanks to an auto-Bäcklund transformation of the equation and using it on the trivial solution $\psi(x,t) = 0$ [212–214]. Contrary to the Bäcklund transformations that we have studied in Chapter 7, this transformation has no continuous parameter that could link it to a Lie group and a Lie algebra. This symmetry is a discrete symmetry, such as a mirror symmetry.

Other non-linear equations also have solutions that are referred to as solitons: the Korteweg-de Vries equation and the 1D non-linear Schrödinger equation [186]. In the case of equations on complex fields, a solution with an amplitude that does not deform and propagates is also called a soliton, even if its phase may oscillate in time. When these equations apply to an electric field (resp. to a wave function), the associated intensity (resp. the associated density of probability) propagates without being deformed, which is why such solutions are given the name of solitons.

The Korteweg-de Vries equation describes for example the propagation of waves at the surface of shallow waters, which is the system for which solitons have been first observed by John Scott Russell in the 19th century [215].

For the 1D non-linear Schrödinger equation, such a soliton is predicted [216] and it has been observed in an optical fibre [217], but also in glass waveguides [218], and with polaritons [219]. Another soliton is predicted, called a dark-soliton [216]. It has been observed for example in optical fibres [220] and cigar-shaped Bose gases [221].

Another type of spectacular solutions of non-linear equations is constituted by so-called breathers. These are solutions whose form oscillates periodically in time or in space and may propagate. For example, the sine-Gordon equation has such breathers:

$$\phi_\mathrm{b} = 4 \arctan \left[\frac{\sqrt{1-\omega^2}}{\omega} \frac{\sin\left(\omega\gamma(t - vx)\right)}{\cosh\left(\gamma\sqrt{1-\omega^2}(x-vt)\right)} \right], \tag{9.4}$$

where ω is the characteristic frequency of the breather, v is its velocity and $\gamma = (1-v^2)^{-1}$ as above. A stationary breather is obtained for $v = 0$.

The 1D non-linear Schrödinger equation has breather solutions of several types [222]:

- The Akhmediev breather which is periodic in time and localised in space. It has not been observed, but there are proposals for optical fibres [223].
- The Kuznetsov-Ma breather which is periodic in space and localised in time. It has been observed in optical fibers [224] and optomechanical systems [225].

Finally there may exist solutions of non-linear equations that are both localized in space and time, such as rogue waves that are observed in the ocean [226]. The 1D non-linear Schrödinger equation has such a solution, which is called the Peregrine soliton [222]. It has been observed in optical fibres [227], in hydrodynamics systems [228] and in plasmas [229].

Many other non-linear equations have been studied in the hope of discovering solitons and breathers and of understanding the conditions in which these solutions may exist. For example, one can add a linear and/or a harmonic potential term to the 1D non-linear Schrödinger equation [230, 231].

One can also wonder whether solitons and breathers may exist for the 2D non-linear Schrödinger equation. Few studies have been reported, but solitonic solutions have been predicted and observed [232–234]. Vortices may also be considered as dark solitons [235].

This is of direct relevance for our experiment, since the 2D non-linear Schrödinger equation describes the evolution of the wave function of our Bose gas with the name of '2D Gross-Pitaevskii equation' that we will keep in the following of the chapter.

In this chapter I present evidence that the 2D Gross-Pitaevskii equation with a harmonic potential term may sustain at least two families of yet-unsuspected

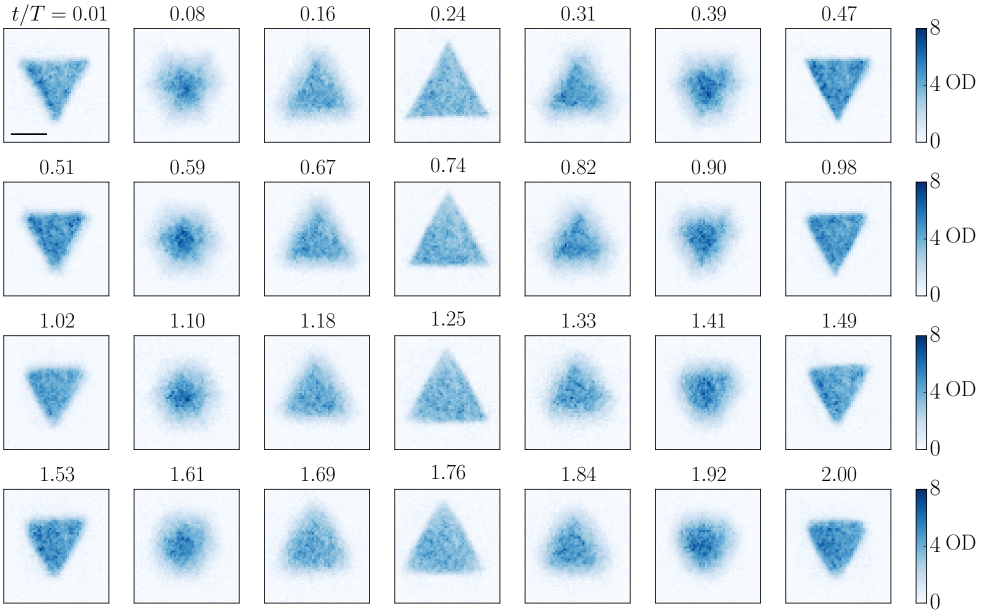

Figure 9.1: Evolution of an initially uniform triangle-shaped cloud. The initial cloud has $4.0(2) \cdot 10^4$ atoms and is prepared in a box potential with the shape of an equilateral triangle of side 41.7(5) µm. It is transferred and released in a harmonic potential at $t = 0$. The images show the density distribution for different evolution times, indicated in units of the period T of the potential. All the images have the same scale, given by the horizontal black line in the first image that represents 20 µm. Each line spans half a period of the harmonic potential, and the four lines are very similar one to the other, indicating a $T/2$ periodicity.

breathers. In a first part I present the experimental measurements indicating that two different initial wave functions evolve periodically. In a second part I show the numerical simulations that we performed to confirm these experiments. We have found no analytical proof of this periodicities, and I briefly mention in a last part some of the difficulties to provide such a proof.

9.1 EXPERIMENTAL HINTS

9.1.1 *Initial triangular shape*

As in the previous chapter, the Gross-Pitaevskii equation with a harmonic potential term is considered. A first glimpse of the periodic behaviour of a wave function evolving with this equation has been given in Chapter 8, paragraph 8.3.1: a cloud with an initial uniform density and the shape of an equilateral triangle, after an evolution of a quarter of oscillation in the harmonic potential seems to have the shape of an equilateral triangle with an inversion symmetry compared to the initial one. The size of this triangle depends on the initial interaction energy, as it was explained in 8.2.1.

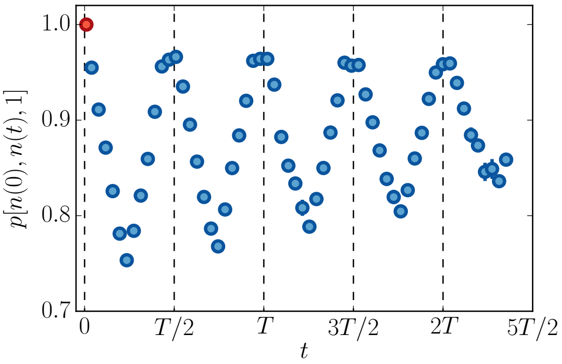

Figure 9.2: Quantifying the periodicity of the dynamics for the dataset presented on Fig. 9.1. We compute the quantity $p[n(0), n(t), \lambda = 1]$ between the initial and the subsequent density distributions, with a unity scaling factor on space. We observe that for times multiple of $T/2$ indicated by the vertical dashed lines, this quantity is close to 1.

We observe the evolution of this cloud beyond $T/4$ and we go up to $t = 2T$. We prepare a cloud of $N = 4.0(2) \cdot 10^4$ atoms in a triangular-shaped box potential of side $L = 41.7(5)$ µm and let it evolve in a harmonic potential. A few images of the density distribution at several times are shown on Fig. 9.1. After half a period in the harmonic trap, the density distribution seems to be the same as the initial one. This is compatible with the periodicity of the potential energy. Indeed, at $t = T/2$, the potential energy should be equal to the initial potential energy, which is fulfilled if the density distribution is the same as the initial one.

We recover this behaviour after a time evolution of T, $3T/2$ and $2T$. Already after one period in the harmonic potential, the density distribution seems not to recover a perfect triangular shape. This may be due to experimental imperfections, such as the anisotropy of the potential, its anharmonicity, or the finite temperature of the gas.

The initial size and atom number of the cloud do not matter because of the scaling laws presented in Chapter 8. We start here with a uniform cloud in the Thomas-Fermi regime, and we can apply all the scaling laws. If a cloud with a given size and atom number evolves periodically, then the evolution of another cloud with the same initial shape and density distribution, but with a different size and a different atom number can be mapped onto the one of the first cloud, and it is found to be also periodic.

In order to quantify better the similarity between the initial density distribution $n(\boldsymbol{r}, 0)$ and the density distributions $n(\boldsymbol{r}, t)$ obtained after the evolution, we compute the quantity $p[n(\boldsymbol{r}, 0), n(\boldsymbol{r}, t), \lambda = 1]$, as defined in equation 8.22. Fig. 9.2 shows the evolution of this quantity as a function of t. Here we do not allow for dilations of space: the computed quantity is close to 1 when the two distributions are the same, up to a translation in space.

The data points start at 1 and decrease below 0.8 at times between 0 and $T/4$. Then they increase again and reach values around 0.96 for times around

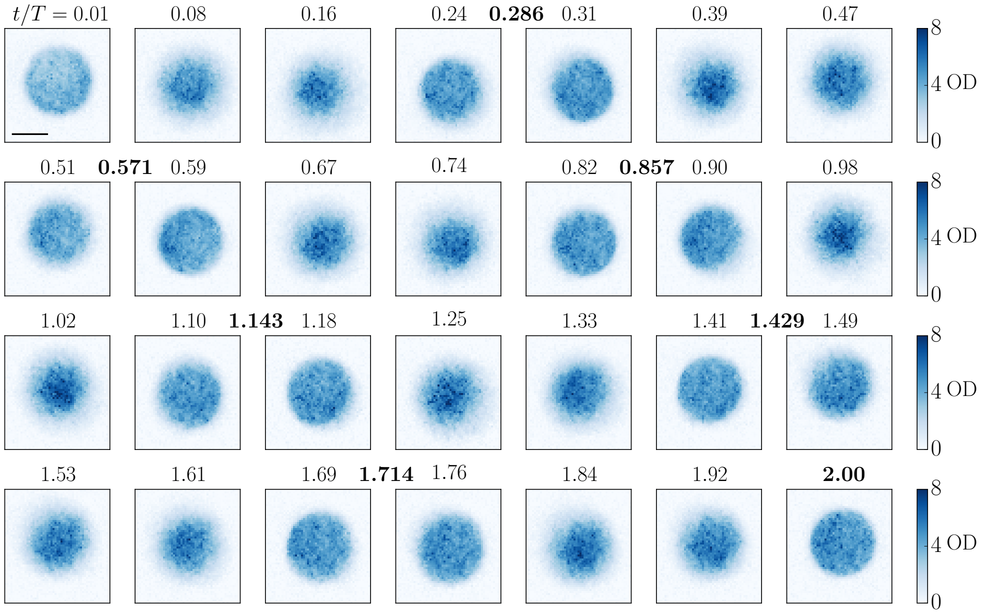

Figure 9.3: Evolution of an initially uniform disk-shaped cloud. The initial cloud has $5.7(2) \cdot 10^4$ atoms and is prepared in a box potential with the shape of a disk of radius 19.5(5) µm. The images show the density distribution for different evolution times in the harmonic potential. These times are indicated in units of the period T of the potential. All the images have the same scale, given by the horizontal black line in the first image that represents 20 µm. For each time t close to a multiple of $2T/7$, the density distribution seems to recover the initial one. These multiples are indicated in bold letters between the experimental images.

$T/2$, T, $3T/2$ and $2T$. This confirms the visual impression given by the images of Fig. 9.1, but this does not constitute a strong evidence that an initially uniform equilateral triangle is a breather of the GPE. We may indeed be limited here by experimental imperfections such as deviations from uniformity of the initial density distribution, finite temperature effects, or imprecisions in the measurement of the density distribution due to the absorption imaging.

9.1.2 *Initial disk shape*

Another shape seems to evolve in a periodic way: an initially disk-shaped cloud with a uniform density. We prepare $N = 5.7(2) \cdot 10^4$ in a disk-shaped box potential of radius $R = 19.5(5)$ µm, and let it evolve in a harmonic potential of frequency $\omega = 2\pi \cdot 19.6(2)$ Hz. A few images of the density distribution from $t = 0$ to $t = 2T$ are shown on Fig. 9.3. The overall features that can be noted are the following:

1. The size of the cloud does not vary a lot during the evolution. This is because the initial size and the atom number have been chosen so that the potential and interaction energy per particle at $t = 0$ are approximately

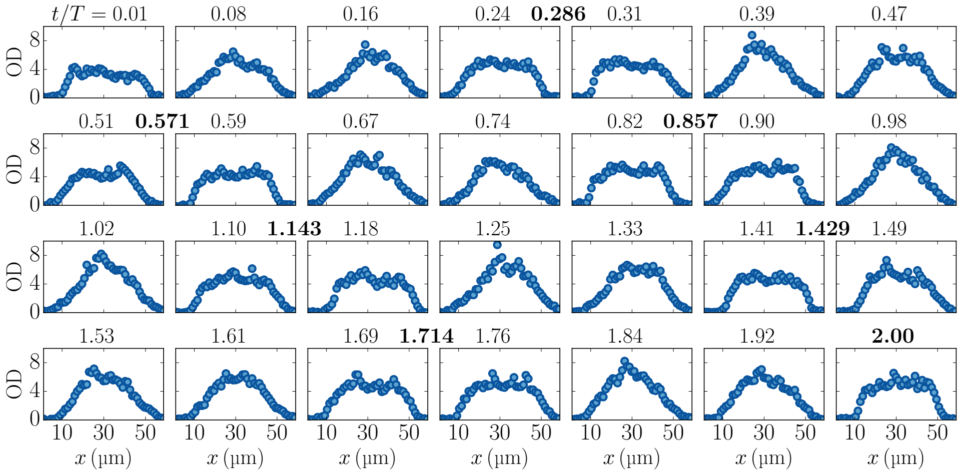

Figure 9.4: Evolution of an initially uniform disk-shaped cloud: radial density. On this figure are presented cuts in the y direction of the density distributions shown on Fig. 9.3. When t/T is close to a multiple of 2/7 (indicated in bold), the flatness of the density over the whole disk appears more clearly.

equal. Indeed the density is close to $n(\boldsymbol{r}, t = 0) = N/(2\pi R^2)$ in the disk, which gives

$$\frac{E_{\text{pot}}}{N} = \frac{1}{2} m\omega^2 \frac{R^2}{2}, \tag{9.5}$$

$$\frac{E_{\text{int}}}{N} = \frac{\hbar^2 \tilde{g}}{2m} \frac{N}{\pi R^2}, \tag{9.6}$$

which are respectively equal to $h \cdot 0.314(32)$ kHz and $h \cdot 0.275(45)$ kHz.

2. The density distribution seems to be flat for eight different times between $t = 0$ and $t = 2T$, corresponding to the times $2T/7 \times k$, with $k = 0, 1, \cdots, 7$. This is illustrated on Fig. 9.4, that displays cuts of the density distributions presented on Fig. 9.3.

We proceed to the same analysis as for the triangular shape: we evaluate the quantity $p[n(0), n(t), \lambda = 1]$ to study the similarity between the initial distribution and the subsequent ones. The results are shown on Fig. 9.5. We recover more quantitatively the features described above. The data points reach values as high as 0.96 when t/T is a multiple of 2/7, as indicated by the dashed lines.

A periodic behaviour with a period equal to $2T/7$ could not be generalized to any initially disk-shaped cloud with any atom number and any size, but only to the ones for which the potential energy stays constant. If this potential energy is not constant, then an initial cloud can recover its initial shape only if it also recovers its initial potential energy. This can happen only at a time multiple of $T/2$, which is not the case for $2T/7$. The smaller common multiple between these two numbers is $2T$, which would be the period of any initially uniform disk-shaped cloud.

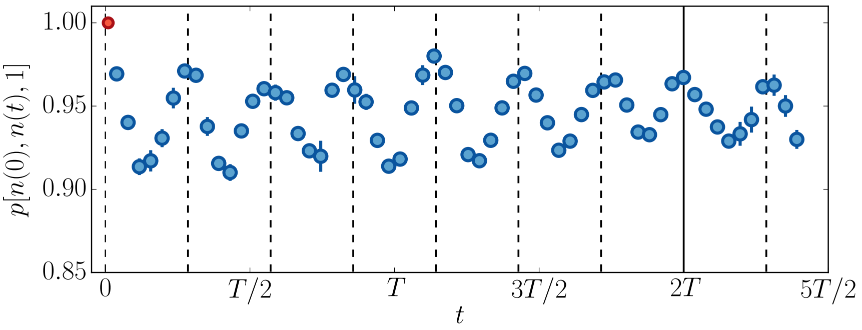

Figure 9.5: Quantifying the periodicity of the dynamics for the dataset presented on Fig. 9.3. We compute the quantity $p[n(0), n(t), \lambda = 1]$ between the initial and the subsequent density distributions, with a unity scaling factor on space. We observe that for times multiple of $2T/7$ indicated by the vertical dashed lines, this quantity is close to 1. The vertical solid line indicates $2T$, which is the time that we will consider in the next paragraph.

These two initial shapes - a uniform triangle and a uniform disk - seem to have a periodic dynamics when investigating it experimentally. We have also tried several other initial shapes filled uniformly, such as a square, a pentagon, a hexagon, and a right-angled isosceles triangle. None of these shapes seemed to evolve periodically, at least on the course of two periods in the harmonic potential.

The precision of the experiment is however not infinite, and the evolution of the density distribution that we measure does not simulate a perfect Gross-Pitaevskii equation at zero temperature. If we want to determine with more confidence whether a wave function evolves periodically, we need to turn to numerical simulations.

9.2 NUMERICAL SIMULATIONS

9.2.1 *Initially triangular-shaped cloud*

We perform numerical simulations of the full 2D GPE in order to have more evidence concerning the possible periodic evolution of the two shapes described above.

In order to simulate the evolution of a physical system, we translate the GPE in terms of dimensionless parameters. We first define a dimensionless scale coordinate $\rho = N_s \boldsymbol{r}/L$, where L is the size of the region that the grid simulates. The length L/N_s thus represents the physical size of one pixel of the simulation. We then define:

$$\tau = \frac{N_s^2 \hbar t}{mL^2}, \tag{9.7}$$

$$\Omega = \frac{m\omega L^2}{N_s^2 \hbar}, \tag{9.8}$$

$$\Psi(\boldsymbol{\rho}, \tau) = \frac{L}{N_s} \psi(\boldsymbol{r}, t). \tag{9.9}$$

The GPE then reads:

$$\mathrm{i}\frac{\partial \Psi}{\partial \tau} = -\frac{1}{2}\boldsymbol{\nabla}^2\Psi + \tilde{g}N|\Psi|^2\Psi + \frac{1}{2}\Omega^2\rho^2\Psi, \tag{9.10}$$

where the nabla operator represents the derivative with respect to the spatial coordinate $\boldsymbol{\rho}$. There are then several parameters to adjust for these numerical simulations:

1. The grid has a number of pixels $N_s \times N_s$, where N_s is an adjustable parameter of the simulation.

2. The box potential in which the wave function will be initialized is chosen with a full length approximately equal to $L/2$. For a triangular box, the side of the triangle is chosen to be half of the grid size, and for a disk box, the diameter is chosen to be half of the grid size. In both cases, the centre of mass of the box is positioned on the origin of the harmonic potential, in the centre of the grid.

3. The product $\tilde{g}N$ is chosen so that the healing length of the initial cloud $\xi = L/2\sqrt{\tilde{g}N}$ is small compared to the box size $L/2$, which corresponds to having the cloud in the Thomas-Fermi regime, but ξ should not be small compared to the size of a pixel L/N_s, so that the edge of the cloud is well sampled by the pixelisation of space. In practice we fix the value of the parameter α which is the number of pixels that cover the healing length:

   $$\alpha = \frac{N_s}{2\sqrt{\tilde{g}N}}, \tag{9.11}$$

   This parameter has to be at least on the order of 1, and it has to be small compared to N_s.

4. The frequency Ω of the harmonic potential is chosen so that the initial potential and interaction energies are equal. With such a choice, we make sure that the value of the wave function near the edge of the grid is small at all times.

5. The time step τ of the evolution is chosen so that $1/\tau$ is much smaller than all the energy scales involved.

The choice of Ω does not restrict the validity of the future conclusions to this value only, because of the scaling laws of the GPE: we can infer the properties of the evolution of a cloud in a harmonic potential of any frequency Ω' from the evolution of the same cloud in a harmonic potential with a given value of its frequency.

The simulation is performed by calculating the wave function at each time step from its value at the previous time step. We first apply the kinetic energy term in the Fourier space where it is diagonal, and then apply the interaction and the potential energy terms in the real space.

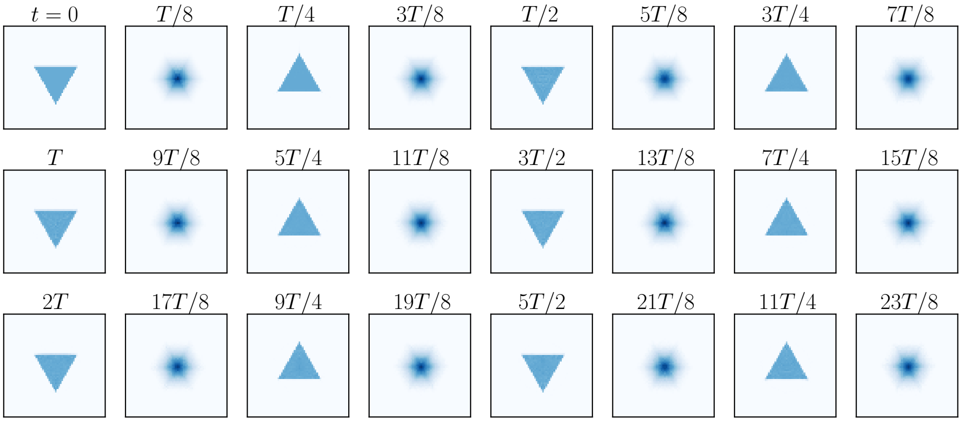

Figure 9.6: Numerical simulation with an initially uniform triangle-shaped cloud, for the parameters $N_s = 512$ and $\alpha = 2$. The initial wave function is the ground state of a triangular box-potential. The images show the density distribution of this wave function during an evolution according to the full Gross-Pitaevskii equation. The same density distribution seems to appear every $T/2$, in agreement with the experimental observation.

The initial wave function is obtained after an imaginary time evolution of a uniform wave function in the desired box potential, without the harmonic potential. The state ψ that we get is the ground state of a Hamiltonian, therefore it can be chosen real. In particular, its initial phase is flat. This wave function is normalized to unity. The evolution of this initial wave function is then performed without the box potential and with the harmonic potential, exactly as the experiment is done. We do not add any phase noise to the initial wave function, which simulates the evolution of a cloud at zero temperature.

We first perform simulations with an initially triangle-shaped cloud. An example of the evolution of the density distribution of such a cloud is shown on Fig. 9.6 over more than two periods in the harmonic potential. The parameters of this simulation are $N_s = 512$ and $\alpha = 2$.

Already we can notice that the density distribution seems to evolve periodically with a period of $T/2$. The images reproduce all the features that the experiment was showing, and here all the imperfections due to the experimental issues and the temperature effects are absent.

The question we want to answer is whether the wave function Ψ evolves periodically in the harmonic potential. Instead of comparing the density distributions to quantify their similarity as we did with the experimental data, we compare directly the wave functions: we compute the modulus of the scalar product between the initial wave function and the subsequent wave functions: $|\langle\Psi(0)|\Psi(t)\rangle|$. The evolution of this quantity is displayed on Fig. 9.7.

This scalar product starts at 1, and, since the information of the phase is also taken into account in this observable, it rapidly falls to a low value. Then at times multiple of $T/2$, it goes up to a value very close to 1 (0.994 on this

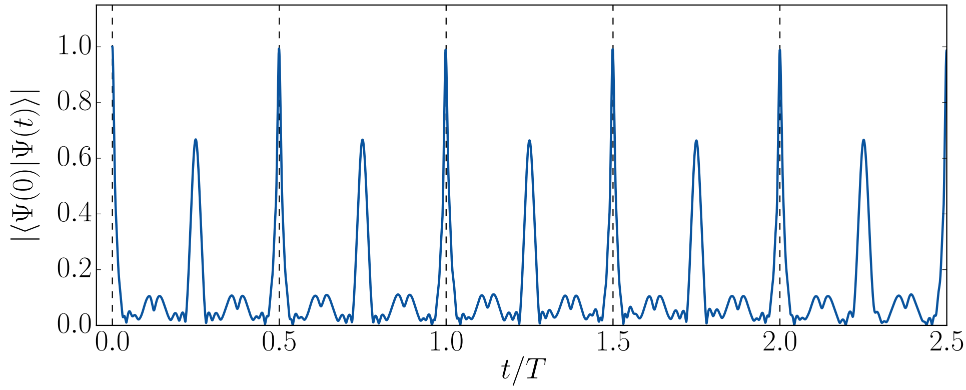

Figure 9.7: Scalar product between the initial and the subsequent wave functions for an initially triangle-shaped cloud. We quantify the similarity between the wave function $|\Psi(t)\rangle$ and the initial one $|\Psi(0)\rangle$ by computing the modulus of their scalar product. This scalar product is sensitive to the difference between the density distributions, but also to the spatial variations of the phase of the wave function. From this curve, it seems that the dynamics is periodic with a period $T/2$.

example), indicating that the wave function is the same as the initial one, up to a global phase.

We also notice that, at $t = T/4$, the plotted scalar product reaches a value around 0.66. This is the value we expect if the cloud has a wave function that is obtained from the initial one by a central symmetry around the centre of the grid. In particular, we deduce that the cloud has a uniform phase at this time.

A single numerical simulation cannot constitute a proper proof of the periodicity of a cloud, since it may be limited by the discretisation of space and of time. We verified that the duration of the time step did not limit the accuracy of the numerical simulations, and we focus here on the size of the grid N_s and the parameter α describing the healing length.

We perform several simulations with various values of N_s and α. We are interested in the value of the scalar product $|\langle\Psi(0)|\Psi(T/2)\rangle|$, and Fig. 9.8 shows this value for all the simulations.

The same physical system is simulated when two simulations have the same ratio N_s/α. The accuracy of the simulation is increasing when N_s (and therefore α) is increased. When increasing the accuracy of a simulation, the scalar product between the initial wave function and the wave function at $T/2$ gets systematically closer to 1.

There is a more efficient way for this scalar product to approach 1: by increasing N_s and increasing α while also increasing the ratio N_s/α. This corresponds to considering physical systems that are more and more in the Thomas-Fermi regime. The highest scalar product we found is slightly above 0.995.

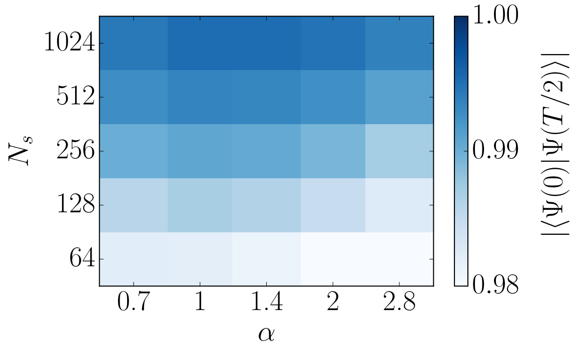

Figure 9.8: Finite-size scaling of the numerical simulations for the triangle-shaped cloud. The scalar product between $|\Psi(0)\rangle$ and $|\Psi(T/2)\rangle$ is shown for different values of the grid size N_s and the ratio α between the healing length and the physical size of a pixel.

These numerical simulations do not provide a proof that an initially uniform triangle-shaped cloud evolves periodically in a harmonic potential, but it gives a better idea of what can be expected: the motion of such a cloud may converge to a periodic motion when increasing the accuracy of the simulation for a given value of the healing length ξ, and this convergence seems to be faster when decreasing ξ.

9.2.2 *Initially disk-shaped cloud*

A similar treatment is performed for an initially disk-shaped cloud. On Fig. 9.9 are shown the evolution of the density distribution for the parameters $N_s = 512$ and $\alpha = 4$. On these images we observe the same features as on the experiment: the radial distribution oscillates between a distribution that is close to flat and a distribution with more atoms in the centre. There are seven oscillations in two periods of the harmonic potential.

The modulus of the scalar product between the initial and the subsequent wave functions $|\langle\psi(0)|\psi(t)\rangle|$ is displayed on Fig. 9.10. It illustrates better the fact that every $2T/7$, the wave function is very close to the initial one. Between these peaks, there are other peaks that almost reach 0.9. They correspond to the points where the radial density is the least flat and reaches a turning point in its evolution. The phase is also flat at these times, which is why the scalar product with the initial wave function is high.

When looking more carefully at this scalar product, one can see that it is not symmetric with respect to the time $2T/7$, nor to its first multiples. There is such a symmetry only around $t = 2T$, and around $t = T$. This indicates that, even for a cloud with a constant potential energy, $2T/7$ is not a period of the motion, but that $t = 2T$ is a much better candidate.

Finally, we turn to the finite-size scaling analysis to see if the features we conjecture from a single simulation are robust.

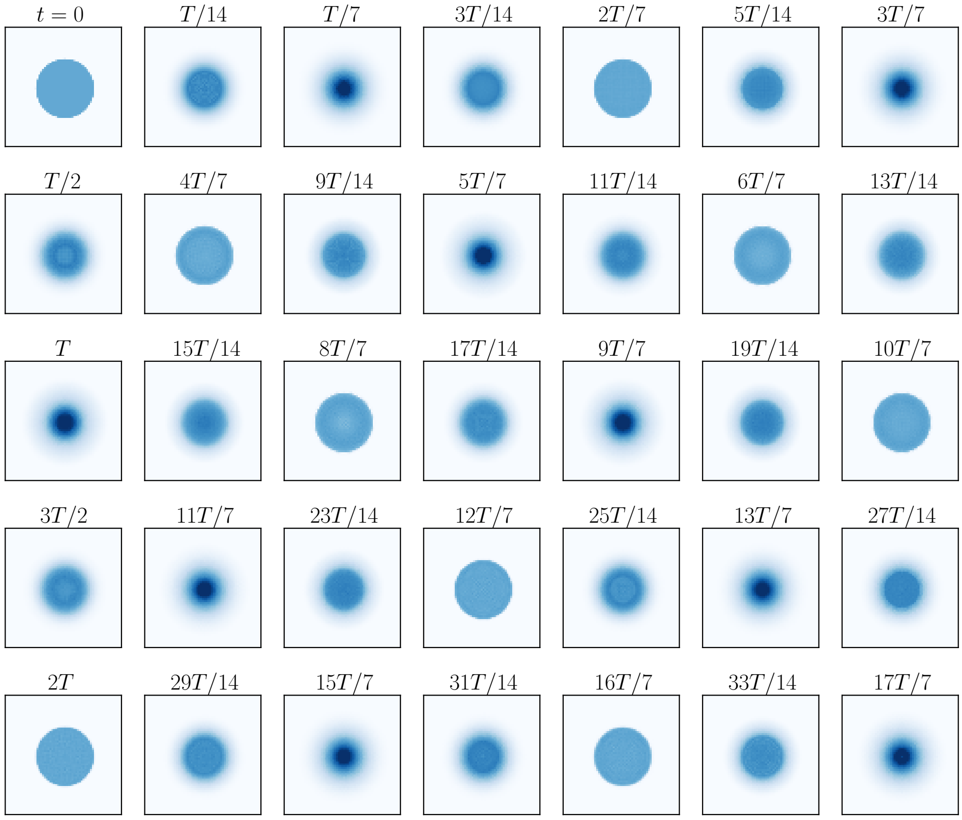

Figure 9.9: Numerical simulation with an initially uniform disk-shaped cloud, for the parameters $N_s = 512$ and $\alpha = 4$. The initial wave function is the ground state of a disk-shaped box-potential. The images show the density distribution of this wave function during an evolution according to the full Gross-Pitaevskii equation. The same density distribution seems to appear every $2T/7$.

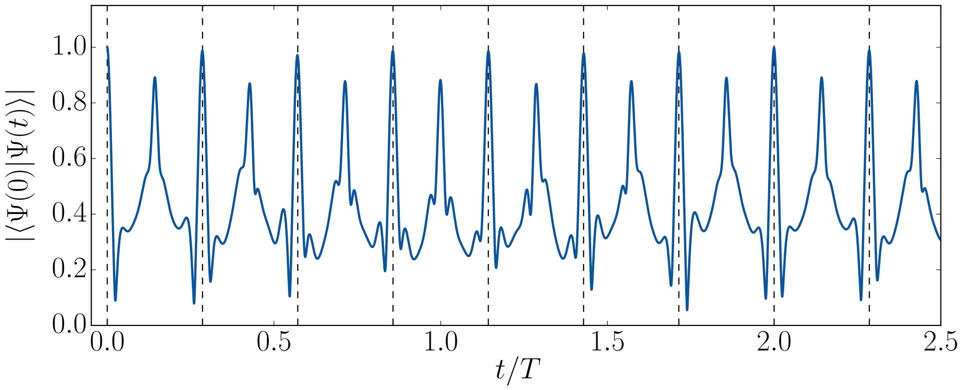

Figure 9.10: Scalar product between the initial and the subsequent wave functions for an initially disk-shaped cloud. We compute the modulus of the scalar product between the wave function $|\psi(t)\rangle$ and the initial one $|\psi(0)\rangle$. From this curve, it seems that the dynamics is periodic with a period $2T$.

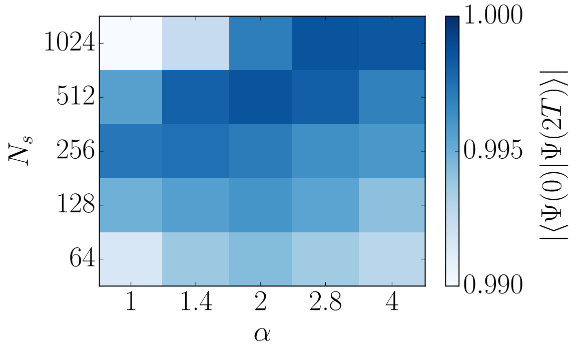

Figure 9.11: Finite-size scaling of the numerical simulations for the disk-shaped cloud. The scalar product between $|\psi(0)\rangle$ and $|\psi(2T)\rangle$ is shown for different values of the grid size N_s and the ratio α between the healing length and the pixel size.

When looking at the overlap between the initial wave function and the wave function at $t = 2T/7$, we find that it is close to 1, but does not always get closer to it when increasing the size of the grid or decreasing the healing length. We therefore have more evidence that an initially uniform disk-shaped cloud with a constant potential energy does not evolve periodically with a period $2T/7$.

We therefore concentrate on the time $t = 2T$, which is also more interesting since it applies in all cases, whether the potential energy is constant or not. On Fig. 9.11 are represented the overlap between $|\psi(0)\rangle$ and $|\psi(2T)\rangle$ for various values of the grid size N_s and the ratio α between the healing length and the pixel size.

Here, simulating the same physical system and increasing the size of the grid does not always provide an overlap closer to 1. However, when performing the simulation with a larger grid, there is always a value of α that provides a better overlap between the two wave functions. The highest value that we obtain is 0.9986, corresponding to $N_s = 1024$ and $\alpha = 2.8$.

These simulations indicate that the evolution of an initially uniform disk-shaped cloud may be periodic with a period $2T$. The same conclusion as for the triangle-shaped cloud apply here: the convergence of the dynamics to a periodic motion seems to be faster when decreasing the healing length ξ.

9.2.3 *Other initial shapes*

We have run these numerical simulations starting from wave functions with several other shapes. These simulations have been performed until an evolution time of $t = 5T$.

We have tried several uniformly-filled regular polygons: a square, a pentagon, an hexagon. We have also tried more shapes with a 3-fold rotational symmetry and a uniform initial density: a six-pointed star and a triangle with a triangular hole in its centre, similar to the first iteration of the Sierpiński triangle.

None of these shapes seemed to evolve in a periodic way. Of course this does not exclude the possibility that one of them recovers its initial wave function after a time larger than $5T$. On the evolution of the overlap with the initial wave function, we saw no symmetry point similar to the point at $t = T$ for the disk, which indicates that no periodicity is to be expected for these shapes between 0 and $10T$.

9.3 TOWARDS AN ANALYTICAL PROOF?

We found no analytical proof that either of the two investigated initial shapes (triangle and disk) should evolve periodically in a harmonic potential.

The two-dimensional Gross-Pitaevskii equation does not have a general analytical solution due to its non-linear character and its dimensionality. Any attempt to solve it based on linear algebra is vowed to fail, except in the perturbative regime. In this case, one can identify small oscillation modes, such as the breathing mode at 2ω, but it is not useful when searching for solutions where several modes have a large amplitude.

The eigenfunctions of a cloud trapped in a harmonic potential are indexed by two integer numbers, n_1 and n_2 [236, 237], and their eigenfrequency is

$$\omega_{n_1,n_2} = \omega\sqrt{2n_1^2 + 2n_1 n_2 + 2n_1 + n_2}. \tag{9.12}$$

Most of these frequencies are not commensurate with 2ω. The decomposition of a uniform shape in this basis involves many modes. When deriving the evolution of the wave function with the GPE, all these modes are coupled with the non-linear term, and the set of coupled differential equations that we obtain are as hard to solve as the original problem. However, the non-linearity could lead to the synchronisation of all these coupled modes and to a periodic behaviour.

The disk shape has a rotational symmetry, which indicates that the evolution can be described with only one dimension of space, the distance to the centre. One-dimensional systems are much easier to solve, and it could be a way to prove that this shape evolves periodically. Another possibility could be to determine differential equations on the moments $\left\langle \boldsymbol{r}^{2k} \right\rangle$ of the distribution, with $k \in \mathbb{N}^*$. Such a differential equation has been derived for $k = 1$, and it has a closed form. The equations for $k > 1$ do not have such a simple form, but they could be useful to prove that an initial disk is periodic.

The triangular shapes raises even more questions: it does not respect the rotational symmetry of the GPE, which excludes certain solving methods. For example, methods to find particular solutions via the dynamical symmetries of the equation will probably not grasp this shape.

9.4 CONCLUSION

In this chapter I have shown experiments and numerical simulations to study the evolution under the GPE with a harmonic potential term of two different Bose gases. The first one is an initially uniform triangular-shaped cloud and the second one is an initially uniform disk-shaped cloud. Both are at rest at $t = 0$. These two clouds seem, both experimentally and numerically to evolve periodically with respective periods $T/2$ and $2T$, where T is the period of the harmonic trap.

We have not proved analytically that these clouds indeed evolve periodically, but such a proof could be difficult to provide.

If these are indeed breathers, they would constitute new and interesting objects for mathematicians and physicists to consider in the study of two-dimensional non-linear equations. Applications to other fields of physics are direct, since the 2D GPE describes several different physical systems, such as the propagation of light in an optical fibre. If there exist fibres exhibiting a harmonic potential such as the one we have introduced, then the breathers could be observed and used in this system as well.

10

CONCLUSION

SUMMARY

In this thesis I have presented experiments that explore the physics of two-dimensional systems. Two main directions have motivated these experiments:

1. The measurement of the first-order correlation function in a uniform atomic sample across the Berezinskii-Kosterlitz-Thouless transition.
2. The dynamical symmetries of the two-dimensional Gross-Pitaevskii equation and their consequences on the evolution of a cloud in a harmonic potential.

In the first part of this thesis, I have described the experimental set-up that has allowed us to investigate these two rich and fundamental subjects. I have explained how we are able to create two-dimensional uniform degenerate clouds of Rubidium atoms, with a full characterisation of the ‘optical accordion’ that I have developed. I have introduced the detection methods that are used in the rest of the thesis: the determination of the density distribution and the determination of the phase-space density of the clouds of atoms (Chapter 2). I have also explained the methods that we use to control their internal and external degrees of freedom. I have notably characterised a new tool based on Raman beams with which we are now able to perform spatially-dependent coherent control between two internal states of the atoms (Chapter 3)

In the second part I have presented the particular topological phase transition that occurs for a gas in two dimensions: the Berezinskii-Kosterlitz-Thouless transition that describes several other two-dimensional systems. One important feature of this transition is the phase ordering that has a quasi-long range below the critical temperature and a short range above it. This phase ordering is described by the first-order correlation function (Chapter 4).

I have developed two methods to estimate this first-order correlation function in a uniform gas. The first one is based on the measurement of the momentum distribution of the cloud, but technical issues limit the interpretation of the results to qualitative statements (Chapter 5). The second one is a more direct measurement of the phase correlation by interferometric means. This second method provides more precise and reliable results. While further analysis is needed to support our preliminary conclusions, it seems that we are able to measure how the first-order correlation function decreases with the distance both below and above the critical temperature. These measurements are compatible with the theoretical prediction (Chapter 6).

The results of this part will be summed up in an article which is currently under preparation.

In a third part I have presented the symmetries of a weakly interacting Bose gas (Chapter 7). These symmetries constitute a continuous Lie group whose algebra is $\mathrm{SO}(2,1)$. Their existence have been known for several decades, but many of their consequences have not been tested as thoroughly as what we have been able to do. In particular, we have demonstrated the ability, when the cloud is in the Thomas-Fermi regime, to link the evolution of two clouds with the same initial shape but different lengths and atom numbers, and evolving with different external parameters (Chapter 8).

We have also found two types of initial wave functions that seem to evolve periodically in an isotropic harmonic potential when they are deep in the Thomas-Fermi regime: clouds that uniformly fill a triangle or a disk (Chapter 9). They could constitute breathers of the two-dimensional non-linear Schrödinger equation and could be relevant for several systems described by this equation, but also for theoreticians who study the properties of non-linear differential equations.

The results of this part have been gathered in an article that has been published in May 2019.

OUTLOOK

On the phase ordering of the 2D Bose gas

Our measurements constitute an important step in the understanding the specificities of two-dimensional phase transitions such as the BKT transition. They are focussed on the equilibrium properties of the gas, but further interesting experiments can be performed on a uniform 2D system to investigate its dynamical properties.

For example, a sudden quench of the ratio T/T_c from above to below 1 leads to the disappearance of vortices with time, following a power law with an exponent that depends on the dynamical exponent of the transition z [181]. The investigation of this dynamical exponent has already been started in two-dimensional Bose gases with experiments based on the Kibble-Zurek mechanism [103], and the access to the first-order correlation function could be an interesting tool to understand the dynamics of a quench [238] and thus to probe the critical properties of the transition.

The experimental methods that we have developed are readily available for such measurements, although they require a certain amount of data taking. These methods and the counting of topological defects constitute two complementary tools to probe the physics of out-of-equilibrium dynamics.

On the dynamical symmetries of 2D systems

The experiments we performed demonstrate the consistency of the dynamics of a weakly-interacting Bose gas with the dynamical symmetries of the two-dimensional Gross-Pitaevskii equation. A possible direction, in which references [239, 240] and also [241] are already heading with fermionic gases, is to observe how these dynamical symmetries are broken when increasing the interaction parameter $\tilde{g}$ to values at least on the order of unity. In this regime, a contact interaction is introduced and with it a length scale which breaks the scale invariance of the system [242, 243].

Our methods to reconstruct scaling laws could be used to determine experimentally whether such laws still exist in the strongly interacting regime and could pave the way to the understanding of quantum anomalies. In particular, the use of uniform initial clouds with simple shapes proved to be very powerful to reliably extract these scaling laws.

More questions arise concerning the possible breathers that we observed, assuming that it can be proven that their behaviour is periodic.

First comes the question whether their existence is a consequence of the dynamical symmetries of the system. Such a question could be investigated by testing different types of interactions that fulfil or not the scale invariance of the system. For example, a system of classical particles in two dimensions, interacting with a potential in $1/r^2$ is scale invariant. It could also be experimentally explored by looking at the evolution of a two-dimensional gas in the regime where the scale invariance is expected to be broken.

Another question is whether such breathers could exist in scale invariant systems in other dimensions. In three dimensions, the pseudo-spin 1/2 Fermi gas at unitarity is also scale invariant [244], with the same underlying algebra as the weakly-interacting Bose gas. One could then consider a unitary Fermi gas in three dimensions and test whether an initially uniform sphere or an initially uniform tetrahedron evolves periodically in an isotropic harmonic potential.

The question whether we observed breathers of the Gross-Pitaevskii equation is still open, and it might be a subject of interest for mathematicians and theoretical physicists involved in the study of nonlinear equations. In particular, one may wonder whether other initial clouds with more complicated shapes and/or a non-uniform density could also have such a behaviour.

On the dynamics of mixtures in two dimensions

With the recent development of versatile experimental tools, such as the spatially-resolved Raman beams described in Chapter 3, our set-up constitutes an excellent platform to investigate the physics of mixtures in two dimensions.

Let us consider the two internal states $F = 1, m_F = 0$ and $F = 2, m_F = 0$, labelled 1 and 2 here. The intraspecies scattering length $a_{11} = 100.9(1)a_0$, $a_{22} = 94.60(2)a_0$ [132] and the interspecies scattering length $a_{12} = 98.9(3)a_0$ [133], where a_0 is the Bohr radius, are such that

$$\frac{a_{11}a_{22}}{a_{12}^2} < 1.$$

The two species are thus immiscible [41]. It is then interesting to initially prepare the system in a state where the components of the two species overlap, and observe how these two components subsequently evolve to spatially separate. An example is given on Fig. 10.1, where the initial state is a uniform superposition of the two species obtained with a $\pi/2$ microwave pulse. The dynamics is very reproducible at short evolution times ($t \lesssim 40\,\text{ms}$ on the given example) and shows the formation of regular patterns, whose shape follow the geometry of

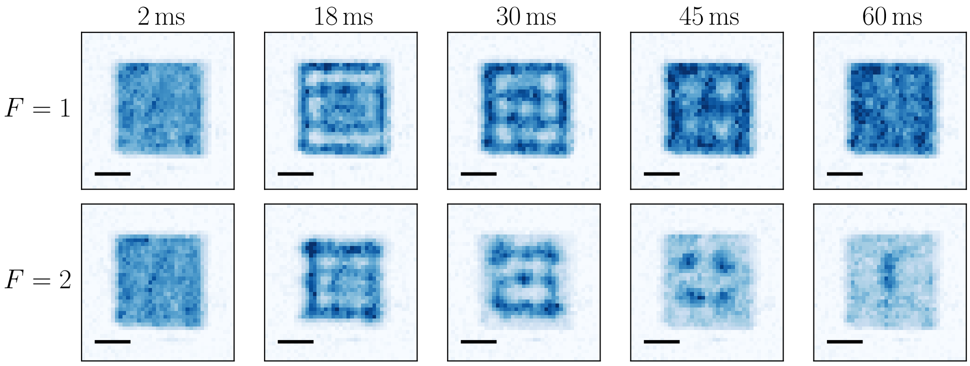

Figure 10.1: Dynamics of an initially balanced and uniform mixture of $F = 1, m_F = 0$ and $F = 2, m_F = 0$ atoms. The first row shows the density distribution of the first species and the second row shows the density distribution of the second species. The different columns refer to the following evolution durations, as indicated on top of each of them.

the box potential and whose size depends on the atomic density. The evolution of these patterns is the result of a non-linear coupling between different density modes.

We can also prepare the cloud in a superposition of both species that has a spatial modulation at a precise wave vector and look at the evolution of a single of the density modes. This may allow us to probe the Bogoliubov dispersion relation of the mixture [111].

The dynamics is grasped by coupled Gross-Pitaevskii equations that describe a gas at zero temperature. One can then include the effects of a non-zero temperature in order to better describe the experimental observations. At long times indeed, the density distribution of a single realisation fluctuates a lot probably due to the temperature, and the system reaches a disordered state as shown on the last column of Fig. 10.1. There are also losses of atoms in $F = 2$ with a typical time scale on the order of several tens of milliseconds that occur on such an experiment.

One can also wonder what kind of symmetries these coupled Gross-Pitaevskii equations have. The spin degree of freedom enriches the system and could result in a more complex symmetry group that could be investigated both experimentally and theoretically. A first partial answer can already be given: the coupled equations stay scale-invariant and in the presence of a harmonic potential of frequency ω they still have a SO(2,1) symmetry. In particular the total potential energy oscillates sinusoidally at frequency 2ω.

There is also the question of the existence of breathers. In the case $a_{11} = a_{22}$, a mixture where the two components initially share the same spatial wavefunction has the same breathers as a one-component cloud. The question is open if $a_{11} \neq a_{22}$.

Another direction that the team has already begun to follow is to study the dynamics of small impurities composed of atoms of one component immersed in a large sea of atoms of the other component. This dynamics can be studied in different regimes, from a coherent regime where the two components are well-described by a wave function and coupled Gross-Pitaevskii equations to a regime described by the physics of the Bose polaron [245], where the impurity consists in only a few or a few tens of atoms that would be dilute enough not to interact one with another, and whose dynamics could be captured by a quantum Brownian model [246].

APPENDICES

A

COUPLING TWO HYPERFINE STATES WITH RAMAN BEAMS

Consider two light fields with respective frequency ω_p and ω_s, and with respective polarisation $\boldsymbol{\varepsilon}_\mathrm{p}$ and $\boldsymbol{\varepsilon}_\mathrm{s}$. The Hamiltonian induced by the light field is therefore $H_\mathrm{p} + H_\mathrm{s}$, with

$$H_\alpha = -\frac{1}{2}(\boldsymbol{d}\cdot\boldsymbol{\varepsilon}_\alpha)\,\mathcal{E}_\alpha \exp(\mathrm{i}\omega_\alpha t) + \text{h.c.}, \tag{A.1}$$

where $\boldsymbol{d}$ is the electrical dipole moment of the atom and $\mathcal{E}_\mathrm{p,s}$ are the electric fields of each of the laser beams.

The frequencies $\omega_\mathrm{p,s}$ are chosen so that they are between the frequencies of the D1 and the D2 lines, and so that their difference $\omega_\mathrm{p} - \omega_\mathrm{s}$ is close to the ground state hyperfine splitting ω_h.

We want to couple the states $\left|S_{1/2}, F=1, m_F\right\rangle$ to the states $\left|S_{1/2}, F=2, m_F\right\rangle$, and we have to consider the following excited states:

- $\left|P_{1/2}, F, m_F\right\rangle$ with $F = 1, 2$ and $m_F = -F, \cdots, F$
- $\left|P_{3/2}, F, m_F\right\rangle$ with $F = 0, 1, 2, 3$ and $m_F = -F, \cdots, F$.

We decompose the state of the system on this basis. We denote as A_{F,m_F} its amplitude for the state $\left|S_{1/2}, F, m_F\right\rangle$, B_{F,m_F} the one for $\left|P_{1/2}, F, m_F\right\rangle$ and C_{F,m_F} the one for $\left|P_{3/2}, F, m_F\right\rangle$.

In the rotating frame associated with the frequency ω_p, we can project the Schrödinger equation on the states that we consider. The detunings $\Delta_{1,2}$ are much larger than the hyperfine splitting within each of the ${}^2P$ states, which gives:

$$\begin{aligned}2\mathrm{i}\hbar\,\dot{A}_{1,m_F} = &-\sum_{\substack{F',m'_F\\ \in P_{1/2}}} \left\langle S_{1/2}, 1, m_F\right|(\boldsymbol{d}^*\cdot\boldsymbol{\varepsilon}^*_\mathrm{p})\,\mathcal{E}^*_\mathrm{p}\left|P_{1/2}, F', m'_F\right\rangle\, B_{F',m'_F}\\ &-\sum_{\substack{F',m'_F\\ \in P_{1/2}}} \left\langle S_{1/2}, 1, m_F\right|(\boldsymbol{d}^*\cdot\boldsymbol{\varepsilon}^*_\mathrm{s})\,\mathcal{E}^*_\mathrm{s}\left|P_{1/2}, F', m'_F\right\rangle\, B_{F',m'_F}\\ &-\sum_{\substack{F',m'_F\\ \in P_{3/2}}} \left\langle S_{1/2}, 1, m_F\right|(\boldsymbol{d}^*\cdot\boldsymbol{\varepsilon}^*_\mathrm{p})\,\mathcal{E}^*_\mathrm{p}\left|P_{3/2}, F', m'_F\right\rangle\, C_{F',m'_F}\\ &-\sum_{\substack{F',m'_F\\ \in P_{3/2}}} \left\langle S_{1/2}, 1, m_F\right|(\boldsymbol{d}^*\cdot\boldsymbol{\varepsilon}^*_\mathrm{s})\,\mathcal{E}^*_\mathrm{s}\left|P_{3/2}, F', m'_F\right\rangle\, C_{F',m'_F},\end{aligned} \tag{A.2}$$

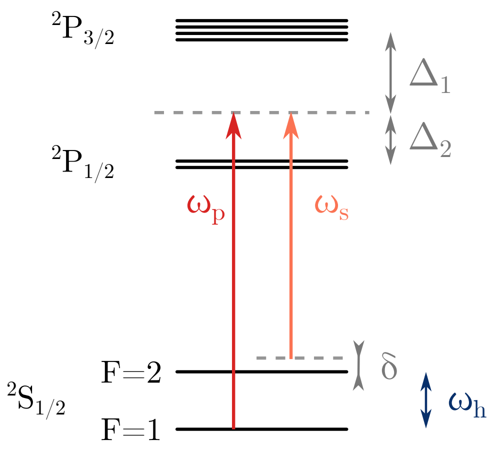

Figure A.1: Electronic structure of the lowest states of rubidium and representation of the two Raman beams.

$$\begin{aligned}
2\mathrm{i}\hbar\,\dot{A}_{2,m_F} = &- \sum_{\substack{F',m'_F\\ \in P_{1/2}}} \big\langle S_{1/2}, 2, m_F \big| (\boldsymbol{d}^* \cdot \boldsymbol{\varepsilon}_\mathrm{p}^*)\, \mathcal{E}_\mathrm{p}^* \big| P_{1/2}, F', m'_F \big\rangle\ B_{F',m'_F} \\
&- \sum_{\substack{F',m'_F\\ \in P_{1/2}}} \big\langle S_{1/2}, 2, m_F \big| (\boldsymbol{d}^* \cdot \boldsymbol{\varepsilon}_\mathrm{s}^*)\, \mathcal{E}_\mathrm{s}^* \big| P_{1/2}, F', m'_F \big\rangle\ B_{F',m'_F} \\
&- \sum_{\substack{F',m'_F\\ \in P_{3/2}}} \big\langle S_{1/2}, 2, m_F \big| (\boldsymbol{d}^* \cdot \boldsymbol{\varepsilon}_\mathrm{p}^*)\, \mathcal{E}_\mathrm{p}^* \big| P_{3/2}, F', m'_F \big\rangle\ C_{F',m'_F} \\
&- \sum_{\substack{F',m'_F\\ \in P_{3/2}}} \big\langle S_{1/2}, 2, m_F \big| (\boldsymbol{d}^* \cdot \boldsymbol{\varepsilon}_\mathrm{s}^*)\, \mathcal{E}_\mathrm{s}^* \big| P_{3/2}, F', m'_F \big\rangle\ C_{F',m'_F} \\
&+ 2\hbar\delta\, A_{2,m_F}.
\end{aligned} \tag{A.3}$$

$$\begin{aligned}
2\mathrm{i}\hbar\,\dot{B}_{F',m'_F} = &- \sum_{m_F} \big\langle P_{1/2}, F', m'_F \big| (\boldsymbol{d} \cdot \boldsymbol{\varepsilon}_\mathrm{p})\, \mathcal{E}_\mathrm{p} \big| S_{1/2}, 1, m_F \big\rangle\ A_{1,m_F} \\
&- \sum_{m_F} \big\langle P_{1/2}, F', m'_F \big| (\boldsymbol{d} \cdot \boldsymbol{\varepsilon}_\mathrm{s})\, \mathcal{E}_\mathrm{s} \big| S_{1/2}, 1, m_F \big\rangle\ A_{1,m_F} \\
&- \sum_{m_F} \big\langle P_{1/2}, F', m'_F \big| (\boldsymbol{d} \cdot \boldsymbol{\varepsilon}_\mathrm{p})\, \mathcal{E}_\mathrm{p} \big| S_{1/2}, 2, m_F \big\rangle\ A_{2,m_F} \\
&- \sum_{m_F} \big\langle P_{1/2}, F', m'_F \big| (\boldsymbol{d} \cdot \boldsymbol{\varepsilon}_\mathrm{s})\, \mathcal{E}_\mathrm{s} \big| S_{1/2}, 2, m_F \big\rangle\ A_{2,m_F} \\
&+ 2\hbar\Delta_2\, B_{F',m'_F},
\end{aligned} \tag{A.4}$$

$$\begin{aligned}2\mathrm{i}\hbar\,\dot{C}_{F',m'_F} = &-\sum_{m_F}\left\langle P_{3/2},F',m'_F\middle|(\boldsymbol{d}\cdot\boldsymbol{\varepsilon}_\mathrm{p})\,\mathcal{E}_\mathrm{p}\middle|S_{1/2},1,m_F\right\rangle\,A_{1,m_F}\\ &-\sum_{m_F}\left\langle P_{3/2},F',m'_F\middle|(\boldsymbol{d}\cdot\boldsymbol{\varepsilon}_\mathrm{s})\,\mathcal{E}_\mathrm{s}\middle|S_{1/2},1,m_F\right\rangle\,A_{1,m_F}\\ &-\sum_{m_F}\left\langle P_{3/2},F',m'_F\middle|(\boldsymbol{d}\cdot\boldsymbol{\varepsilon}_\mathrm{p})\,\mathcal{E}_\mathrm{p}\middle|S_{1/2},2,m_F\right\rangle\,A_{2,m_F}\\ &-\sum_{m_F}\left\langle P_{3/2},F',m'_F\middle|(\boldsymbol{d}\cdot\boldsymbol{\varepsilon}_\mathrm{s})\,\mathcal{E}_\mathrm{s}\middle|S_{1/2},2,m_F\right\rangle\,A_{2,m_F}\\ &+2\hbar\Delta_1\,C_{F',m'_F},\end{aligned}\tag{A.5}$$

Since the detunings $\Delta_{1,2}$ are much larger than the line widths of the excited states and than the Rabi frequencies induced by the laser beams, we can adiabatically eliminate the populations in the excited states: $\dot{B}_{F',m'_F}\approx 0$ and $\dot{C}_{F',m'_F}\approx 0$. We get from A.4 andA.5:

$$\begin{aligned}B_{F',m'_F} = \frac{1}{2\hbar\Delta_2}\Bigg(&\sum_{m_F}\left\langle P_{1/2},F',m'_F\middle|(\boldsymbol{d}\cdot\boldsymbol{\varepsilon}_\mathrm{p})\,\mathcal{E}_\mathrm{p}\middle|S_{1/2},1,m_F\right\rangle\,A_{1,m_F}\\ &\sum_{m_F}\left\langle P_{1/2},F',m'_F\middle|(\boldsymbol{d}\cdot\boldsymbol{\varepsilon}_\mathrm{s})\,\mathcal{E}_\mathrm{s}\middle|S_{1/2},1,m_F\right\rangle\,A_{1,m_F}\\ &\sum_{m_F}\left\langle P_{1/2},F',m'_F\middle|(\boldsymbol{d}\cdot\boldsymbol{\varepsilon}_\mathrm{p})\,\mathcal{E}_\mathrm{p}\middle|S_{1/2},2,m_F\right\rangle\,A_{2,m_F}\\ &\sum_{m_F}\left\langle P_{1/2},F',m'_F\middle|(\boldsymbol{d}\cdot\boldsymbol{\varepsilon}_\mathrm{s})\,\mathcal{E}_\mathrm{s}\middle|S_{1/2},2,m_F\right\rangle\,A_{2,m_F}\Bigg),\end{aligned}\tag{A.6}$$

$$\begin{aligned}C_{F',m'_F} = \frac{1}{2\hbar\Delta_1}\Bigg(&\sum_{m_F}\left\langle P_{3/2},F',m'_F\middle|(\boldsymbol{d}\cdot\boldsymbol{\varepsilon}_\mathrm{p})\,\mathcal{E}_\mathrm{p}\middle|S_{1/2},1,m_F\right\rangle\,A_{1,m_F}\\ &\sum_{m_F}\left\langle P_{3/2},F',m'_F\middle|(\boldsymbol{d}\cdot\boldsymbol{\varepsilon}_\mathrm{s})\,\mathcal{E}_\mathrm{s}\middle|S_{1/2},1,m_F\right\rangle\,A_{1,m_F}\\ &\sum_{m_F}\left\langle P_{3/2},F',m'_F\middle|(\boldsymbol{d}\cdot\boldsymbol{\varepsilon}_\mathrm{p})\,\mathcal{E}_\mathrm{p}\middle|S_{1/2},2,m_F\right\rangle\,A_{2,m_F}\\ &\sum_{m_F}\left\langle P_{3/2},F',m'_F\middle|(\boldsymbol{d}\cdot\boldsymbol{\varepsilon}_\mathrm{s})\,\mathcal{E}_\mathrm{s}\middle|S_{1/2},2,m_F\right\rangle\,A_{2,m_F}\Bigg).\end{aligned}\tag{A.7}$$

We insert these expressions in the differential equations for the states $S_{1/2}$, although it does not look friendly. We also remove all the terms that are not resonant, such as terms describing the coupling of $\left|S_{1/2},F=1,m_F\right\rangle$ and $\left|S_{1/2},F=2,m_F\right\rangle$ via two photons from the same laser beam.

$$
\begin{aligned}
&\mathrm{i}\hbar\,\dot{A}_{2,m_F} = \\
&\quad \frac{1}{4\hbar\Delta_2}\Bigg(\sum_{\substack{F',m'_F\\ \in P_{1/2}}} \sum_{m''_F} \big\langle S_{1/2},2,m_F \big| (\boldsymbol{d}^* \cdot \boldsymbol{\varepsilon}_{\mathrm{p}}^*)\, \mathcal{E}_{\mathrm{p}}^* \big| P_{1/2},F',m'_F \big\rangle \\
&\qquad\qquad \times \big\langle P_{1/2},F',m'_F \big| (\boldsymbol{d} \cdot \boldsymbol{\varepsilon}_{\mathrm{p}})\, \mathcal{E}_{\mathrm{p}} \big| S_{1/2},2,m''_F \big\rangle \; A_{2,m''_F} \\
&\qquad + \sum_{\substack{F',m'_F\\ \in P_{1/2}}} \sum_{m''_F} \big\langle S_{1/2},2,m_F \big| (\boldsymbol{d}^* \cdot \boldsymbol{\varepsilon}_{\mathrm{s}}^*)\, \mathcal{E}_{\mathrm{s}}^* \big| P_{1/2},F',m'_F \big\rangle \\
&\qquad\qquad \times \big\langle P_{1/2},F',m'_F \big| (\boldsymbol{d} \cdot \boldsymbol{\varepsilon}_{\mathrm{p}})\, \mathcal{E}_{\mathrm{p}} \big| S_{1/2},1,m''_F \big\rangle \; A_{1,m''_F} \\
&\qquad + \sum_{\substack{F',m'_F\\ \in P_{1/2}}} \sum_{m''_F} \big\langle S_{1/2},2,m_F \big| (\boldsymbol{d}^* \cdot \boldsymbol{\varepsilon}_{\mathrm{s}}^*)\, \mathcal{E}_{\mathrm{s}}^* \big| P_{1/2},F',m'_F \big\rangle \\
&\qquad\qquad \times \big\langle P_{1/2},F',m'_F \big| (\boldsymbol{d} \cdot \boldsymbol{\varepsilon}_{\mathrm{s}})\, \mathcal{E}_{\mathrm{s}} \big| S_{1/2},2,m''_F \big\rangle \; A_{2,m''_F} \Bigg) \\
&\quad + \frac{1}{4\hbar\Delta_1}\Bigg(\sum_{\substack{F',m'_F\\ \in P_{3/2}}} \sum_{m''_F} \big\langle S_{1/2},2,m_F \big| (\boldsymbol{d}^* \cdot \boldsymbol{\varepsilon}_{\mathrm{p}}^*)\, \mathcal{E}_{\mathrm{p}}^* \big| P_{3/2},F',m'_F \big\rangle \\
&\qquad\qquad \times \big\langle P_{3/2},F',m'_F \big| (\boldsymbol{d} \cdot \boldsymbol{\varepsilon}_{\mathrm{p}})\, \mathcal{E}_{\mathrm{p}} \big| S_{1/2},2,m''_F \big\rangle \; A_{2,m''_F} \\
&\qquad + \sum_{\substack{F',m'_F\\ \in P_{3/2}}} \sum_{m''_F} \big\langle S_{1/2},2,m_F \big| (\boldsymbol{d}^* \cdot \boldsymbol{\varepsilon}_{\mathrm{s}}^*)\, \mathcal{E}_{\mathrm{s}}^* \big| P_{3/2},F',m'_F \big\rangle \\
&\qquad\qquad \times \big\langle P_{3/2},F',m'_F \big| (\boldsymbol{d} \cdot \boldsymbol{\varepsilon}_{\mathrm{p}})\, \mathcal{E}_{\mathrm{p}} \big| S_{1/2},1,m''_F \big\rangle \; A_{1,m''_F} \\
&\qquad + \sum_{\substack{F',m'_F\\ \in P_{3/2}}} \sum_{m''_F} \big\langle S_{1/2},2,m_F \big| (\boldsymbol{d}^* \cdot \boldsymbol{\varepsilon}_{\mathrm{s}}^*)\, \mathcal{E}_{\mathrm{s}}^* \big| P_{3/2},F',m'_F \big\rangle \\
&\qquad\qquad \times \big\langle P_{3/2},F',m'_F \big| (\boldsymbol{d} \cdot \boldsymbol{\varepsilon}_{\mathrm{s}})\, \mathcal{E}_{\mathrm{s}} \big| S_{1/2},2,m''_F \big\rangle \; A_{2,m''_F} \Bigg) \\
&\quad + \hbar\delta\, A_{2,m_F}, \qquad\qquad \text{(A.8)}
\end{aligned}
$$

and we have a similar equation for $\dot{A}_{1,m_F}$.

For each of these terms, the sum over the indices m'_F and m''_F depends on the polarisation of the light: the matrix elements are null if the light does not contain the polarisation that links the two considered states. There are also terms that are null because the numbers F and F' they involve do not fulfill $|F' - F| \leq 1$.

In our case we chose the two following polarisations: $(\sigma^+ + \sigma^-)/\sqrt{2}$ and $(\sigma^+ - \sigma^-)/\sqrt{2}$, which means that we can only couple states of ${}^2S_{1/2}$ that have m_F numbers of the same parity.

If we initially have atoms in $\big|{}^2S_{1/2}, F = 1, m_F = 0\big\rangle$, then we can populate only the states $\big|{}^2S_{1/2}, F = 2, m_F = -2, 0, 2\big\rangle$. Let us first demonstrate that the states with $m_F = -2, 2$ cannot be populated by developing the expression of $\dot{A}_{2,2}$ at $t = 0$, when $A_{2,m_F} = 0$:

$$\begin{aligned} \mathrm{i}\hbar^2\, \dot{A}_{2,2} = -\frac{1}{4\Delta_2} \Bigg(\sum_{F'=1,2} & \big\langle S_{1/2}, 2, 2 \big| \boldsymbol{d}^{+} \mathcal{E}_{\mathrm{s}}^{*} \big| P_{1/2}, F', 1 \big\rangle \\ & \times\ \big\langle P_{1/2}, F', 1 \big| \boldsymbol{d}^{+}\, \mathcal{E}_{\mathrm{p}} \big| S_{1/2}, 1, 0 \big\rangle\ A_{1,0} \Bigg) \\ - \frac{1}{4\Delta_1} \Bigg(\sum_{F'=1,2} & \big\langle S_{1/2}, 2, 2 \big| \boldsymbol{d}^{+} \mathcal{E}_{\mathrm{s}}^{*} \big| P_{3/2}, F', 1 \big\rangle \\ & \times\ \big\langle P_{3/2}, F', 1 \big| \boldsymbol{d}^{+}\, \mathcal{E}_{\mathrm{p}} \big| S_{1/2}, 1, 0 \big\rangle\ A_{1,0} \Bigg) . \end{aligned} \tag{A.9}$$

In this last expression we have only kept the processes allowed by the selection rules: a light with polarisation σ^{+} (resp. σ^{-}) can couple states with quantum numbers $F = 1, m_F$ and $F' = 2, m'_F$ only if $m'_F = m_F + 1$ (resp. $m'_F = m_F - 1$). The operator $\boldsymbol{d}^{+}$ denotes here the component of the dipole operator associated with a σ^{+} polarisation.

Each matrix element can be decomposed into a product of two terms thanks to the Wigner-Eckhart theorem [247].

For example a matrix element $\big\langle S_{1/2}, F, m_F \big| \boldsymbol{d}^{+}\mathcal{E} \big| P_{1/2}, F', m'_F \big\rangle$ is equal to the product of a reduced matrix element $\big\langle S_{1/2}, F \big|\big| \boldsymbol{d} \big|\big| P_{1/2}, F' \big\rangle$ and of a Clebsch-Gordan coefficient $\langle F, 1, m_F, +1 | F', m'_F \rangle$ describing the composition of a spin F with a photon of spin 1 to obtain a spin F', and quantifying the transition probability between the states of respective quantum numbers m_F, m'_F with a photon of polarisation σ^{+}.

The reduced matrix element can be further decomposed:

$$\begin{aligned} \big\langle S_{1/2}, F \big|\big| \boldsymbol{d} \big|\big| P_{1/2}, F' \big\rangle = & \big\langle S_{1/2} \big|\big| \boldsymbol{d} \big|\big| P_{1/2} \big\rangle \times (-1)^{F'+J+1+I} \\ & \times \sqrt{(2F'+1)(2J+1)} \begin{Bmatrix} J & J' & 1 \\ F' & F & I \end{Bmatrix} , \end{aligned} \tag{A.10}$$

where J is the quantum number associated here with the state $S_{1/2}$, J' is the one associated here with the state $P_{1/2}$, $I = 3/2$ is the nuclear spin of the atom, and the last term is a Wigner 6-j symbol.

We regroup some of these terms by defining the coefficient

$$\begin{aligned} \big\langle S_{1/2}, 2, 2 \big| P_{1/2}, F', 1 \big\rangle = & (-1)^{F'+J+1+I} \sqrt{(2F'+1)(2J+1)} \\ & \times \begin{Bmatrix} J & J' & 1 \\ F' & F & I \end{Bmatrix} \big\langle F, 1, m_F, +1 \big| F', m'_F \big\rangle \end{aligned} \tag{A.11}$$

that are tabulated in [248].

Equation A.9 can therefore be rewritten as

$$\begin{aligned}
\mathrm{i}\hbar^2\,\dot{A}_{2,2} = &-\frac{1}{4\Delta_2}\sum_{F'=1,2}\big\langle S_{1/2}\big|\big|\boldsymbol{d}\big|\big|P_{1/2}\big\rangle\,\big\langle S_{1/2},2,2\big|P_{1/2},F',1\big\rangle \\
&\qquad\times\,\big\langle P_{1/2}\big|\big|\boldsymbol{d}\big|\big|S_{1/2}\big\rangle\,\big\langle P_{1/2},F',1\big|S_{1/2},1,0\big\rangle\;\mathcal{E}_\mathrm{s}^*\mathcal{E}_\mathrm{p}\,A_{1,0} \\
&-\frac{1}{4\Delta_1}\sum_{F'=1,2}\big\langle S_{1/2}\big|\big|\boldsymbol{d}\big|\big|P_{3/2}\big\rangle\,\big\langle S_{1/2},2,2\big|P_{3/2},F',1\big\rangle \\
&\qquad\times\,\big\langle P_{3/2}\big|\big|\boldsymbol{d}\big|\big|S_{1/2}\big\rangle\,\big\langle P_{3/2},F',1\big|S_{1/2},1,0\big\rangle\;\mathcal{E}_\mathrm{s}^*\mathcal{E}_\mathrm{p}\,A_{1,0},
\end{aligned} \tag{A.12}$$

and we can factor terms out of the sums:

$$\begin{aligned}
&\mathrm{i}\hbar^2\,\dot{A}_{2,2} = \\
&\Bigg(-\frac{1}{4\Delta_2}\big|\,\big\langle S_{1/2}\big|\big|\boldsymbol{d}\big|\big|P_{1/2}\big\rangle\,\big|^2 \\
&\qquad\times\sum_{F'=1,2}\big\langle S_{1/2},2,2\big|P_{1/2},F',1\big\rangle\,\big\langle P_{1/2},F',1\big|S_{1/2},1,0\big\rangle \\
&-\frac{1}{4\Delta_1}\big|\,\big\langle S_{1/2}\big|\big|\boldsymbol{d}\big|\big|P_{3/2}\big\rangle\,\big|^2 \\
&\qquad\times\sum_{F'=1,2}\big\langle S_{1/2},2,2\big|P_{3/2},F',1\big\rangle\,\big\langle P_{3/2},F',1\big|S_{1/2},1,0\big\rangle\Bigg)\;\mathcal{E}_\mathrm{s}^*\mathcal{E}_\mathrm{p}\,A_{1,0}.
\end{aligned} \tag{A.13}$$

The two sums can be computed with the tables of [248]:

$$\begin{aligned}
\sum_{F'=1,2}\big\langle S_{1/2},2,2\big|P_{1/2},F',1\big\rangle\,\big\langle P_{1/2},F',1\big|S_{1/2},1,0\big\rangle &= -\frac{1}{\sqrt{4}}\frac{1}{\sqrt{6}}+\frac{1}{\sqrt{12}}\frac{1}{\sqrt{2}} \\
&= 0
\end{aligned} \tag{A.14}$$

$$\begin{aligned}
\sum_{F'=1,2}\big\langle S_{1/2},2,2\big|P_{3/2},F',1\big\rangle\,\big\langle P_{3/2},F',1\big|S_{1/2},1,0\big\rangle &= -\frac{1}{\sqrt{8}}\frac{1}{\sqrt{12}}-\frac{\sqrt{5}}{\sqrt{24}}\frac{1}{\sqrt{20}} \\
&= 0
\end{aligned} \tag{A.15}$$

Therefore $\dot{A}_{2,2}(t=0)=0$ and the state $\big|S_{1/2},2,2\big\rangle$ cannot be populated. By symmetry it is the same for $\big|S_{1/2},2,-2\big\rangle$. This is true because we are in the limit where the detunings $\Delta_{1,2}$ are much larger than the hyperfine splitting of the ground and excited states and they can be factored out of the sums over the hyperfine states.

The only states that can be coupled are then $\big|S_{1/2},1,0\big\rangle$ and $\big|S_{1/2},2,0\big\rangle$. The differential equations on their amplitudes can be expressed in the same way as we did for $\dot{A}_{2,2}$:

$$
\begin{aligned}
\mathrm{i}\hbar^2\,\dot{A}_{2,0} = {} & -\frac{1}{4\Delta_2}\Bigg(\sum_{F'=1,2} \big|\big\langle S_{1/2}\big|\big|\boldsymbol{d}\big|\big|P_{1/2}\big\rangle\big|^2 \big\langle S_{1/2},2,0\big|P_{1/2},F',1\big\rangle \\
& \qquad\qquad \times \big\langle P_{1/2},F',1\big|S_{1/2},2,0\big\rangle\,\big|\mathcal{E}_\mathrm{p}\big|^2 A_{2,0} \\
& + \sum_{F'=1,2} \big|\big\langle S_{1/2}\big|\big|\boldsymbol{d}\big|\big|P_{1/2}\big\rangle\big|^2 \big\langle S_{1/2},2,0\big|P_{1/2},F',1\big\rangle \\
& \qquad\qquad \times \big\langle P_{1/2},F',1\big|S_{1/2},1,0\big\rangle\,\mathcal{E}_\mathrm{s}^*\mathcal{E}_\mathrm{p}\,A_{1,0} \\
& + \sum_{F'=1,2} \big|\big\langle S_{1/2}\big|\big|\boldsymbol{d}\big|\big|P_{1/2}\big\rangle\big|^2 \big\langle S_{1/2},2,0\big|P_{1/2},F',1\big\rangle \\
& \qquad\qquad \times \big\langle P_{1/2},F',1\big|S_{1/2},2,0\big\rangle\,\big|\mathcal{E}_\mathrm{s}\big|^2 A_{2,0}\Bigg) \\
& -\frac{1}{4\Delta_1}\Bigg(\sum_{F'=1,2} \big|\big\langle S_{1/2}\big|\big|\boldsymbol{d}\big|\big|P_{3/2}\big\rangle\big|^2 \big\langle S_{1/2},2,0\big|P_{3/2},F',1\big\rangle \\
& \qquad\qquad \times \big\langle P_{3/2},F',1\big|S_{1/2},2,0\big\rangle\,\big|\mathcal{E}_\mathrm{p}\big|^2 A_{2,0} \\
& + \sum_{F'=1,2} \big|\big\langle S_{1/2}\big|\big|\boldsymbol{d}\big|\big|P_{3/2}\big\rangle\big|^2 \big\langle S_{1/2},2,0\big|P_{3/2},F',1\big\rangle \\
& \qquad\qquad \times \big\langle P_{3/2},F',1\big|S_{1/2},1,0\big\rangle\,\mathcal{E}_\mathrm{s}^*\mathcal{E}_\mathrm{p}\,A_{1,0} \\
& + \sum_{F'=1,2} \big|\big\langle S_{1/2}\big|\big|\boldsymbol{d}\big|\big|P_{3/2}\big\rangle\big|^2 \big\langle S_{1/2},2,0\big|P_{3/2},F',1\big\rangle \\
& \qquad\qquad \times \big\langle P_{3/2},F',1\big|S_{1/2},2,0\big\rangle\,\big|\mathcal{E}_\mathrm{s}\big|^2 A_{2,0}\Bigg) \\
& + \hbar^2\delta A_{2,0},
\end{aligned}
\tag{A.16}
$$

where the contributions of the σ^+ and σ^- of each beams interfere constructively. If we had chosen the same polarisations for the two beams, they would have interfered destructively and there would be no coupling between the two hyperfine states. We can perform the sums over the coefficients separately:

$$
\begin{aligned}
\sum_{F'=1,2} \big|\big\langle S_{1/2},2,0\big|P_{1/2},F',1\big\rangle\big|^2 &= \frac{1}{4}+\frac{1}{12} \\
&= \frac{1}{3},
\end{aligned}
\tag{A.17}
$$

$$
\begin{aligned}
\sum_{F'=1,2} \big|\big\langle S_{1/2},2,0\big|P_{3/2},F',1\big\rangle\big|^2 &= \frac{1}{5}+\frac{1}{8}+\frac{1}{120} \\
&= \frac{1}{3},
\end{aligned}
\tag{A.18}
$$

$$\sum_{F'=1,2} \langle S_{1/2},2,0|P_{1/2},F',1\rangle \langle P_{1/2},F',1|S_{1/2},1,0\rangle = -\frac{1}{\sqrt{4}}\frac{1}{\sqrt{4}} - \frac{1}{\sqrt{12}}\frac{1}{\sqrt{12}} = -\frac{1}{3}, \tag{A.19}$$

$$\sum_{F'=1,2} \langle S_{1/2},2,0|P_{3/2},F',1\rangle \langle P_{3/2},F',1|S_{1/2},1,0\rangle = \frac{1}{\sqrt{8}}\frac{1}{\sqrt{8}} + \frac{1}{\sqrt{120}}\frac{\sqrt{5}}{\sqrt{24}} = \frac{1}{6}. \tag{A.20}$$

And finally we get

$$\begin{aligned} \mathrm{i}\hbar^2 \dot{A}_{2,0} = &-\frac{1}{4\Delta_2}\left|\langle S_{1/2}||\boldsymbol{d}||P_{1/2}\rangle\right|^2 \left(\frac{|\mathcal{E}_\mathrm{p}|^2+|\mathcal{E}_\mathrm{s}|^2}{3}A_{2,0} - \frac{\mathcal{E}_\mathrm{s}^*\mathcal{E}_\mathrm{p}}{3}A_{1,0}\right) \\ &- \frac{1}{4\Delta_1}\left|\langle S_{1/2}||\boldsymbol{d}||P_{3/2}\rangle\right|^2 \left(\frac{|\mathcal{E}_\mathrm{p}|^2+|\mathcal{E}_\mathrm{s}|^2}{3}A_{2,0} + \frac{\mathcal{E}_\mathrm{s}^*\mathcal{E}_\mathrm{p}}{6}A_{1,0}\right) \\ &+ \hbar^2\delta A_{2,0}, \end{aligned} \tag{A.21}$$

We also have $\left|\langle S_{1/2}||\boldsymbol{d}||P_{3/2}\rangle\right|^2 = 2\left|\langle S_{1/2}||\boldsymbol{d}||P_{1/2}\rangle\right|^2$ due to the degeneracy of the excited states, therefore we obtain

$$\begin{aligned} \mathrm{i}\,\dot{A}_{2,0} = &\left[\delta - \left(\frac{1}{3\Delta_2}+\frac{2}{3\Delta_1}\right)\frac{|\Omega_\mathrm{p}|^2+|\Omega_\mathrm{s}|^2}{4}\right]A_{2,0} \\ &- \left(\frac{1}{3\Delta_1}-\frac{1}{3\Delta_2}\right)\frac{\Omega_\mathrm{s}^*\Omega_\mathrm{p}}{4}A_{1,0}, \end{aligned} \tag{A.22}$$

where $\Omega_{\mathrm{p,s}}$ are the Rabi frequencies associated with each of the laser beams. Similarly we have

$$\begin{aligned} \mathrm{i}\,\dot{A}_{1,0} = &-\left(\frac{1}{3\Delta_2}+\frac{2}{3\Delta_1}\right)\frac{|\Omega_\mathrm{p}|^2+|\Omega_\mathrm{s}|^2}{4}A_{1,0} \\ &- \left(\frac{1}{3\Delta_1}-\frac{1}{3\Delta_2}\right)\frac{\Omega_\mathrm{p}^*\Omega_\mathrm{s}}{4}A_{2,0}. \end{aligned} \tag{A.23}$$

We therefore obtain from the two light beams an effective coupling between the states $|S_{1/2},F=1,m_F=0\rangle$ and $|S_{1/2},F=2,m_F=0\rangle$ with an effective Rabi frequency

$$\Omega_\mathrm{R} = \left(\frac{1}{3\Delta_2}-\frac{1}{3\Delta_1}\right)\frac{\Omega_\mathrm{p}^*\Omega_\mathrm{s}}{4}, \tag{A.24}$$

and with an effective detuning $\delta_\mathrm{eff} = \delta$. Moreover, each of the states experiences a light shift V_shift:

$$V_\mathrm{shift} = -\left(\frac{1}{3\Delta_2}+\frac{2}{3\Delta_1}\right)\frac{|\Omega_\mathrm{p}|^2+|\Omega_\mathrm{s}|^2}{4}. \tag{A.25}$$

B

CORRELATION FUNCTION OF AN IDEAL 2D BOSE GAS

I detail here the calculations that provide the results discussed in Chapter 4, section 4.1.2.

The eigenfunctions of a square box of size L are the plane waves

$$\psi_{\boldsymbol{p}}(\boldsymbol{r}) = \frac{1}{L}\exp\left(\frac{\mathrm{i}\,\boldsymbol{p}\cdot\boldsymbol{r}}{\hbar}\right), \tag{B.1}$$

where the momentum $\boldsymbol{p}$ is quantized:

$$\boldsymbol{p} = 2\pi\hbar\boldsymbol{k}/L, \tag{B.2}$$

$$\boldsymbol{k} = (k_x, k_y), \quad k_{x,y} \in \mathbb{Z}. \tag{B.3}$$

The energy of a state with momentum $\boldsymbol{p}$ is

$$E_{\boldsymbol{p}} = \boldsymbol{p}^2/(2m). \tag{B.4}$$

In the grand-canonical ensemble, the Bose-Einstein distribution provides the occupation number $N_{\boldsymbol{p}}$ of the state labelled by the momentum $\boldsymbol{p}$ for a system characterized by its temperature T and its chemical temperature μ:

$$N_{\boldsymbol{p}} = \frac{1}{\exp\left(\frac{E_{\boldsymbol{p}}-\mu}{k_{\mathrm{B}}T}\right) - 1}. \tag{B.5}$$

In this expression, the chemical potential μ has to stay negative. We introduce the fugacity z of the system: $z = \exp\left(\mu/(k_{\mathrm{B}}T)\right)$, and we can write the last equation as

$$N_{\boldsymbol{p}} = \sum_{l=1}^{+\infty} z^l \exp\left(-\frac{l\boldsymbol{p}^2}{2mk_{\mathrm{B}}T}\right). \tag{B.6}$$

To get the total atom number N, we sum this quantity over all the momentum states:

$$N = \sum_{k_x,k_y}\sum_{l=1}^{+\infty} z^l \exp\left(-\frac{2\pi^2 l\hbar^2\boldsymbol{k}^2}{mL^2k_{\mathrm{B}}T}\right). \tag{B.7}$$

In the regime where the thermal wave length $\lambda_T = \sqrt{2\pi\hbar^2/(mk_{\mathrm{B}}T)}$ is smaller than the size L of the box, one can replace the sum over the discrete modes $\boldsymbol{k}$ by an integral over $\mathbb{R}^2$:

$$N = \sum_{l=1}^{+\infty} z^l \int \mathrm{d}^2\boldsymbol{k}\,\exp\left(-\frac{2\pi^2 l\hbar^2\boldsymbol{k}^2}{mL^2k_{\mathrm{B}}T}\right) \tag{B.8}$$

$$= \frac{mL^2k_{\mathrm{B}}T}{2\pi^2\hbar^2}\sum_{l=1}^{+\infty}\frac{z^l}{l}\int \mathrm{d}^2\boldsymbol{u}\,\exp(-\boldsymbol{u}^2). \tag{B.9}$$

We finally replace the integral by its value π, and we use the identity $\ln(1-z) = -\sum_{l=1}^{+\infty} z^l/l$ to express the 2D density $n = N/L^2$:

$$n = -\frac{1}{\lambda_T^2}\ln(1-z). \tag{B.10}$$

We also express the PSD $\mathcal{D} = n\lambda_T^2$ of the gas:

$$\mathcal{D} = -\ln(1-z). \tag{B.11}$$

The total number of atoms is not bounded, such as in three dimensions, which means that there is no Bose-Einstein condensation at the thermodynamic limit in two dimensions.

We have shown in Chapter 4 that the correlation function G_1 of a translational invariant system can be obtained via the Fourier transform of the momentum distribution $N_{\boldsymbol{p}}$. In the case of the ideal 2D Bose gas, $N_{\boldsymbol{p}}$ is a sum of Gaussian functions, therefore G_1 is also the sum of Gaussian functions:

$$G_1(\boldsymbol{0},\boldsymbol{r}) = \frac{1}{\lambda_T^2}\sum_{l=1}^{+\infty}\frac{z^l}{l}\exp\left(-\frac{\pi\boldsymbol{r}^2}{l\lambda_T^2}\right). \tag{B.12}$$

In the limit where the gas is far from quantum degeneracy, we have $|\mu| \gg 1$ and $\mu < 0$, which means a fugacity $z \ll 1$, and all the sums over the index l can be evaluated with their first term only. The momentum distribution in equation $B.6$ is then a simple Gaussian, and so is the first-order correlation function in equation $B.12$:

$$g_1(\boldsymbol{r}) = \exp\left(-\frac{\pi\boldsymbol{r}^2}{\lambda_T^2}\right). \tag{B.13}$$

In the limit where the gas is degenerate, we have $z \approx 1$, and $1-z \approx |\mu|/(k_{\mathrm{B}}T)$. The expression B.12 is not easy to interpret. However, we can develop the expression of the momentum distribution from equation B.5:

$$N_{\boldsymbol{p}} = \frac{z}{1 - z\sum_{l=1}^{+\infty}\frac{1}{l!}\left(\frac{\boldsymbol{p}^2}{2mk_{\mathrm{B}}T}\right)^l}. \tag{B.14}$$

For the momenta $\boldsymbol{p}$ verifying $\boldsymbol{p}^2 < 2mk_{\mathrm{B}}T$, we can approximate $N_{\boldsymbol{p}}$ by keeping only the first term in the sum:

$$N_{\boldsymbol{p}} = \frac{2mk_{\mathrm{B}}T}{2m|\mu| + \boldsymbol{p}^2}. \tag{B.15}$$

When counting the number of atoms N_1 that have a momentum verifying $\boldsymbol{p}^2 < 2mk_{\mathrm{B}}T$, we obtain:

$$\begin{aligned}
N_1 &= \frac{L^2}{(2\pi\hbar)^2}\int_{p=0}^{\sqrt{2mk_{\mathrm{B}}T}} 2\pi p\,\mathrm{d}p\,\frac{2mk_{\mathrm{B}}T}{2m|\mu| + p^2} && \text{(B.16)}\\
&= \frac{L^2}{\lambda_T^2}\ln\left(1 + \frac{k_{\mathrm{B}}T}{|\mu|}\right) && \text{(B.17)}\\
&\approx \frac{2\pi L^2}{\lambda_T^2}\mathcal{D} && \text{(B.18)}\\
&\approx N. && \text{(B.19)}
\end{aligned}$$

Almost all the atoms are considered when limiting $\boldsymbol{p}$ to an amplitude lower than $2mk_{\mathrm{B}}T$, and we can therefore neglect the momenta exceeding $2mk_{\mathrm{B}}T$. The momentum distribution is then simply given by equation B.15. Its Fourier transform in two dimensions is a modified Bessel function of the second kind, denoted as K_0. Therefore we have

$$G_1(\mathbf{0}, \boldsymbol{r}) = \frac{1}{(2\pi\lambda_T)^2} K_0\left(\frac{|\boldsymbol{r}|}{\ell}\right), \tag{B.20}$$

with

$$\ell = \frac{\hbar}{\sqrt{2m|\mu|}}. \tag{B.21}$$

C

DETAILS ON THE INTERFEROMETRIC MEASUREMENTS OF g_1

In this appendix are summarized all the curves that we have measured to probe the first-order correlation function g_1 of a 2D Bose gas across the BKT transition, and that are discussed in Chapter 6.

The curves are shown in logarithmic graphs on Fig. C.1. Each of them is fitted with a power law. The same curves are shown in semi-logarithmic graphs on Fig. C.2, and each of them is fitted with an exponential decay.

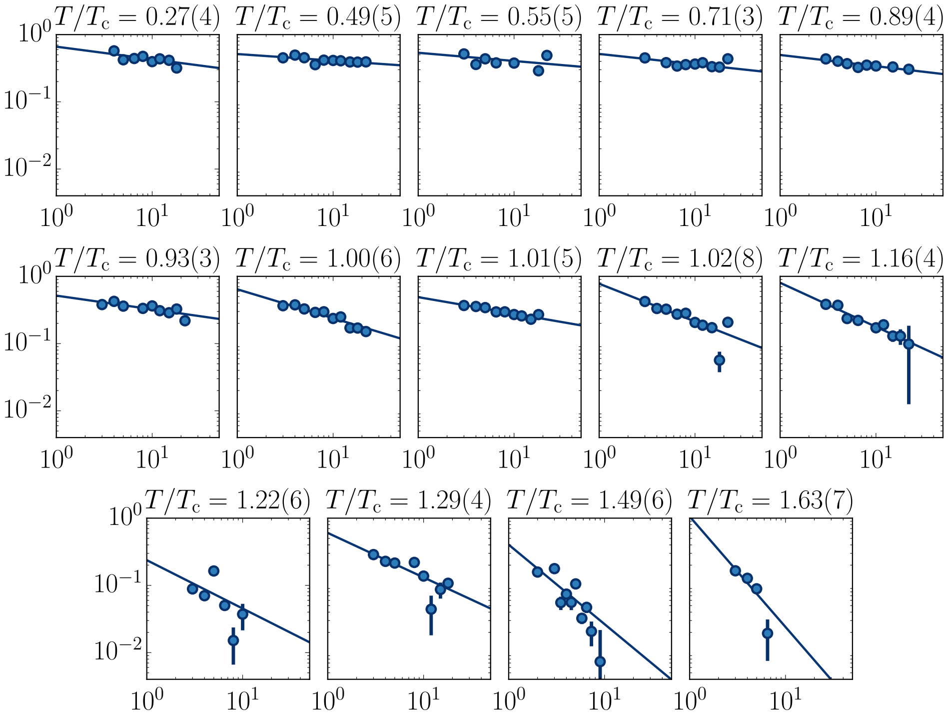

Figure C.1: The contrast C is plotted as a function of the distance d_l (in micrometers) between the two lines that interfere. The value of T/T_c is written on top of each graph. The horizontal and vertical scales are the same for all the graphs. The curves are presented with their power-law fit, represented as solid lines.

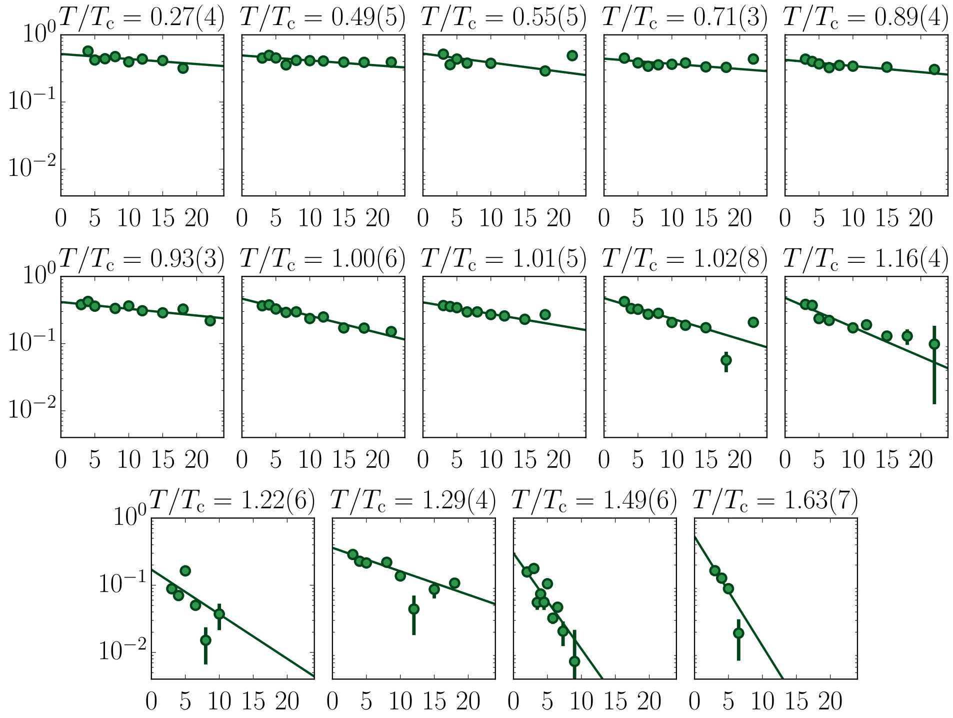

Figure C.2: The same data as Fig. C.1 are shown in semi-logarithmic graphs. The horizontal axis represents d_l in micrometers, and the vertical one represents the contrast $C(d_l)$. The horizontal and vertical scales are the same for all graphs. The exponential fit of each curve is shown as a solid line.

D

DETAILS ON THE SCALING LAWS OF THE 2D BOSE GAS

D.1 FREE GROSS-PITAEVSKII EQUATION

I prove here that an expansion, as presented in 7.2.1.2, keeps the free GPE (equation 7.15) invariant. The function ψ' is defined as stated in equation 7.20. The different terms of the GPE are expressed in terms of the initial function ψ and coordinates $\boldsymbol{r}$ and t:

$$\begin{aligned} \mathrm{i}\hbar\frac{\partial\psi'}{\partial t'} = &\bigg[\mathrm{i}\hbar(\gamma t+1)^2\gamma\psi - \frac{m}{2}(\gamma t+1)\gamma^2\boldsymbol{r}^2\psi - \frac{\hbar^2}{2m}(\gamma t+1)^3\boldsymbol{\nabla}^2\psi \\ &+ \frac{\hbar^2}{m}\tilde{g}N(\gamma t+1)^3|\psi|^2\psi + m(\gamma t+1)\gamma^2\boldsymbol{r}^2\psi \\ &+ \mathrm{i}\hbar(\gamma t+1)^2\gamma\boldsymbol{r}\cdot\boldsymbol{\nabla}\psi\bigg]\exp\left(-\frac{\mathrm{i}m\gamma\boldsymbol{r}^2}{2\hbar(\gamma t+1)}\right), \end{aligned} \tag{D.1}$$

$$\begin{aligned} \frac{\hbar^2}{2m}\boldsymbol{\nabla}'^2\psi' = &\bigg[-\mathrm{i}\hbar(\gamma t+1)^2\gamma\psi - \mathrm{i}\hbar(\gamma t+1)^2\gamma\boldsymbol{r}\cdot\boldsymbol{\nabla}\psi - \frac{m}{2}(\gamma t+1)\gamma\boldsymbol{r}^2\psi \\ &+ \frac{\hbar^2}{2m}(\gamma t+1)^3\boldsymbol{\nabla}^2\psi\bigg]\exp\left(-\frac{\mathrm{i}m\gamma\boldsymbol{r}^2}{2\hbar(\gamma t+1)}\right), \end{aligned} \tag{D.2}$$

$$-\frac{\hbar^2}{m}\tilde{g}N|\psi'|^2\psi' = -\frac{\hbar^2}{m}\tilde{g}N(\gamma t+1)^3|\psi|^2\psi\,\exp\left(-\frac{\mathrm{i}m\gamma\boldsymbol{r}^2}{2\hbar(\gamma t+1)}\right). \tag{D.3}$$

In the first term we have used the GPE that the wave function ψ fulfils.

The sum of these three terms is equal to zero, which means that the wave function ψ' is indeed a solution of the same Gross-Pitaevskii equation.

D.2 GROSS-PITAEVSKII EQUATION WITH A HARMONIC TRAP

I prove here the different properties of the GPE with a harmonic trap in the reverse order compared to their presentation in the main text. First, in D.2.1, I demonstrate how a solution of an equation with a time-dependent trap frequency can be derived from the solution of an equation with a time-independent trap frequency. Then, in D.2.2, I use it to link the solution of the free GPE (which has a fixed trap frequency $\omega = 0$) to the solution of a GPE with a fixed trap frequency. Finally, in D.2.3, I derive the Lie group of the GPE with a harmonic trap by using the Lie group of the free GPE and the link between these two equations.

D.2.1 *General case: a variable trap frequency*

Let ψ_1 be a solution of the equation

$$\mathrm{i}\hbar\frac{\partial\psi}{\partial t}+\frac{\hbar^2}{2m}\boldsymbol{\nabla}^2\psi-\frac{\hbar^2}{m}\tilde{g}N|\psi|^2\psi-\frac{1}{2}m\omega^2\boldsymbol{r}^2\psi=0. \tag{D.4}$$

We consider the function

$$\psi_2(\boldsymbol{r}',t')=f_{\tilde{\omega}}(\boldsymbol{r},t)\psi_1(\boldsymbol{r},t), \tag{D.5}$$

with

$$\boldsymbol{r}'=\frac{\boldsymbol{r}}{\lambda_{\tilde{\omega}}(t)}, \tag{D.6}$$

$$t'=\int_0^t\frac{\mathrm{d}u}{\lambda_{\tilde{\omega}}^2(u)}, \tag{D.7}$$

$$f_{\tilde{\omega}}=\lambda_{\tilde{\omega}}(t)\exp\left(-\frac{\mathrm{i}m\dot{\lambda}_{\tilde{\omega}}\boldsymbol{r}^2}{2\hbar\lambda_{\tilde{\omega}}}\right), \tag{D.8}$$

where the function $\lambda_{\tilde{\omega}}$ is a solution of the differential equation

$$\ddot{\lambda}=\frac{\omega^2(t)}{\lambda^3}-\omega^2\lambda. \tag{D.9}$$

The function $\tilde{\omega}(t)$ is any smooth function.

Let us prove that ψ_2 is a solution of the equation

$$\mathrm{i}\hbar\frac{\partial\psi}{\partial t}+\frac{\hbar^2}{2m}\boldsymbol{\nabla}^2\psi-\frac{\hbar^2}{m}\tilde{g}N|\psi|^2\psi-\frac{1}{2}m\omega^2\boldsymbol{r}^2\psi=0. \tag{D.10}$$

We express each of the terms of equation D.10:

$$\begin{aligned}\mathrm{i}\hbar\frac{\partial\psi_2}{\partial t'}=&\Big[\mathrm{i}\hbar\dot{\lambda}_{\tilde{\omega}}\lambda_{\tilde{\omega}}^2\psi_1+\frac{m}{2}\ddot{\lambda}_{\tilde{\omega}}\lambda_{\tilde{\omega}}^2\boldsymbol{r}^2\psi_1+\frac{m}{2}\dot{\lambda}_{\tilde{\omega}}^2\lambda_{\tilde{\omega}}\boldsymbol{r}^2\psi_1\\&-\frac{\hbar^2}{2m}\lambda_{\tilde{\omega}}^3\boldsymbol{\nabla}^2\psi_1+\frac{\hbar^2}{m}\,\tilde{g}N\lambda_{\tilde{\omega}}^3|\psi_1|^2\psi_1+\frac{m\omega^2}{2}\lambda_{\tilde{\omega}}^3\boldsymbol{r}^2\psi_1\\&+m\dot{\lambda}_{\tilde{\omega}}^2\lambda_{\tilde{\omega}}\boldsymbol{r}^2\psi_1+\mathrm{i}\hbar\dot{\lambda}_{\tilde{\omega}}\lambda_{\tilde{\omega}}^2\,\boldsymbol{r}\cdot\boldsymbol{\nabla}\psi_1\Big]\exp\left(-\frac{\mathrm{i}m\dot{\lambda}_{\tilde{\omega}}\boldsymbol{r}^2}{2\hbar\lambda_{\tilde{\omega}}}\right),\end{aligned} \tag{D.11}$$

$$\begin{aligned}\frac{\hbar^2}{2m}\boldsymbol{\nabla}'^2\psi_2=&-\Big[\mathrm{i}\hbar\dot{\lambda}_{\tilde{\omega}}\lambda_{\tilde{\omega}}^2\psi_1+\frac{m}{2}\dot{\lambda}_{\tilde{\omega}}^2\lambda_{\tilde{\omega}}\boldsymbol{r}^2\psi_1+\mathrm{i}\hbar\dot{\lambda}_{\tilde{\omega}}\lambda_{\tilde{\omega}}^2\,\boldsymbol{r}\cdot\boldsymbol{\nabla}\psi_1\\&-\frac{\hbar^2}{2m}\lambda_{\tilde{\omega}}^3\boldsymbol{\nabla}^2\psi_1\Big]\exp\left(-\frac{\mathrm{i}m\dot{\lambda}_{\tilde{\omega}}\boldsymbol{r}^2}{2\hbar\lambda_{\tilde{\omega}}}\right),\end{aligned} \tag{D.12}$$

$$-\frac{\hbar^2}{m}\tilde{g}N|\psi_2|^2\psi_2=-\frac{\hbar^2}{m}\tilde{g}N\lambda_{\tilde{\omega}}^3|\psi_1|^2\psi_1\,\exp\left(-\frac{\mathrm{i}m\dot{\lambda}_{\tilde{\omega}}\boldsymbol{r}^2}{2\hbar\lambda_{\tilde{\omega}}}\right), \tag{D.13}$$

$$-\frac{m}{2}\omega^2(t)\,\boldsymbol{r}'^2\psi_2=-\frac{m}{2}\frac{\omega^2(t)}{\lambda_{\tilde{\omega}}}\,\boldsymbol{r}^2\psi_1\,\exp\left(-\frac{\mathrm{i}m\dot{\lambda}_{\tilde{\omega}}\boldsymbol{r}^2}{2\hbar\lambda_{\tilde{\omega}}}\right). \tag{D.14}$$

The sum of these four terms above is equal to zero if and only if

$$\frac{m}{2}\left(\ddot{\lambda}_{\tilde{\omega}}\lambda_{\tilde{\omega}}^2+\omega^2\lambda_{\tilde{\omega}}^3-\frac{\omega^2(t)}{\lambda_{\tilde{\omega}}}\right)\boldsymbol{r}^2\psi_1=0, \tag{D.15}$$

which is the case if λ satisfies equation D.9.

D.2.2 *Particular case: a constant trap frequency*

We apply the previous section with $\omega = 0$ and $\tilde{\omega}(t) = \omega_0$ which is a constant. The equation D.9 is now

$$\ddot{\lambda} = \frac{\omega_0^2}{\lambda^3}. \tag{D.16}$$

We integrate it a first time with the initial conditions $\dot{\lambda}(0) = 0$ and $\lambda(0) = 1$:

$$\dot{\lambda}^2 = \omega_0^2 \left(1 - \frac{1}{\lambda^2}\right), \tag{D.17}$$

which then integrates in

$$\lambda(t) = \sqrt{1 + \omega_0^2 t^2}. \tag{D.18}$$

The relation D.7 between the times is then

$$t' = \int_0^t \frac{\mathrm{d}u}{1 + \omega_0^2 u^2}, \tag{D.19}$$

which means that

$$\tan\big(\omega_0 t'\big) = \omega_0 t. \tag{D.20}$$

With this we have demonstrated the link between the free GPE and the GPE with a harmonic trap of frequency ω_0.

D.2.3 *Invariant transformations*

Since the solutions of the free GPE can be mapped onto the solutions of the GPE with a harmonic trap, the Lie group of the two equations are homeomorphic. We can use the expression of the transformations of the first group along with the link between the two equations to deduce the expression of the transformations of the second group. We prove here the equations 7.39, 7.40 and 7.41.

Let $\psi_{0,1}(\boldsymbol{r}, t)$ a solution of the free GPE. A transformation $\mathcal{T}_{\alpha,\beta,\gamma,\delta}$ with parameters α, β, γ, δ allows us to construct another solution of this equation, as defined in equations 7.22 and 7.23. Thanks to the transformation $\mathcal{T}_{0,\omega}$ defined in equations 7.59 to 7.63, we can then construct two wave functions $\psi_{\omega,1}(\boldsymbol{\rho}, \tau)$ and $\psi_{\omega,2}(\boldsymbol{\rho}', \tau')$ that are solutions of the GPE with a harmonic trap with frequency ω. We only need to express the coordinates of $\boldsymbol{\rho}', \tau'$ in terms of the coordinates $\boldsymbol{\rho}, \tau$ and to determine how to transform $\psi_{\omega,1}$ into $\psi_{\omega,2}$. This scheme is summarised on Fig. D.1.

We start with the rescaling of time. We have three equations to combine:

$$\tan\big(\omega\tau'\big) = \omega t', \tag{D.21}$$

$$t' = \frac{\alpha t + \beta}{\gamma t + \delta}, \tag{D.22}$$

$$\tan(\omega\tau) = \omega t. \tag{D.23}$$

We get directly

$$\tan\big(\omega\tau'\big) = \frac{\alpha \tan(\omega\tau) + \beta\omega}{\frac{\gamma}{\omega}\tan(\omega\tau) + \delta}. \tag{D.24}$$

$$\begin{tikzcd}
\psi_{0,1}(\boldsymbol{r},t) \arrow[r, "\mathcal{T}_{\alpha,\beta,\gamma,\delta}"] \arrow[d, "\mathcal{T}_{0,\omega}"'] & \psi_{0,2}(\boldsymbol{r}',t') \arrow[d, "\mathcal{T}_{0,\omega}"] \\
\psi_{\omega,1}(\boldsymbol{\rho},\tau) \arrow[r, "?"'] & \psi_{\omega,2}(\boldsymbol{\rho}',\tau')
\end{tikzcd}$$

Figure D.1: Determining the Lie-Bäcklund transformations of the GPE with a harmonic potential. We use the Bäcklund transformation $\mathcal{T}_{0,\omega}$ that links this equation to the free GPE, and the Lie-Bäcklund transformations of this free GPE.

We define the new parameters $\tilde{\alpha} = \alpha$, $\tilde{\beta} = \beta\omega$, $\tilde{\gamma} = \gamma/\omega$ and $\tilde{\delta} = \delta$, which satisfy the constraint $\tilde{\alpha}\tilde{\delta} - \tilde{\beta}\tilde{\gamma} = 1$ and give

$$\tan\bigl(\omega\tau'\bigr) = \frac{\tilde{\alpha}\tan(\omega\tau) + \tilde{\beta}}{\tilde{\gamma}\tan(\omega\tau) + \tilde{\delta}}, \tag{D.25}$$

which proves equation 7.42, which is equivalent to equation 7.40 with the assumption that τ' is a continuous and monotonous function.

We continue with the rescaling of space. We have three equations as well:

$$\boldsymbol{\rho}' = \frac{\boldsymbol{r}'}{(1+\omega^2 t'^2)^{1/2}}, \tag{D.26}$$

$$\boldsymbol{r}' = \frac{\boldsymbol{r}}{\gamma t + \delta}, \tag{D.27}$$

$$\boldsymbol{\rho} = \frac{\boldsymbol{r}}{(1+\omega^2 t^2)^{1/2}}. \tag{D.28}$$

We translate them in terms of τ instead of t and t':

$$\boldsymbol{\rho}' = \frac{\left(\frac{\gamma}{\omega}\tan(\omega\tau) + \delta\right)\boldsymbol{r}'}{\left[\left(\alpha\tan(\omega\tau) + \beta\omega\right)^2 + \left(\frac{\gamma}{\omega}\tan(\omega\tau) + \delta\right)^2\right]^{1/2}}, \tag{D.29}$$

$$\boldsymbol{r}' = \frac{\boldsymbol{r}}{\frac{\gamma}{\omega}\tan(\omega\tau) + \delta}, \tag{D.30}$$

$$\boldsymbol{\rho} = \frac{\boldsymbol{r}}{(1+\tan^2(\omega\tau))^{1/2}}. \tag{D.31}$$

And we finally combine them to get, with the parameters $\tilde{\alpha}, \tilde{\beta}, \tilde{\gamma}, \tilde{\delta}$:

$$\rho' = \frac{\boldsymbol{\rho}}{\lambda(\tau)}, \tag{D.32}$$

with

$$\lambda(\tau) = \left[\Bigl(\tilde{\alpha}\sin(\omega\tau) + \tilde{\beta}\cos(\omega\tau)\Bigr)^2 + \Bigl(\tilde{\gamma}\sin(\omega\tau) + \tilde{\delta}\cos(\omega\tau)\Bigr)^2\right]^{1/2} \tag{D.33}$$

which demonstrates equation 7.39.

Finally, we prove the expression of the function $f(\boldsymbol{\rho},\tau)$ in equation 7.41. From the definitions of $f_{0,\omega}$ (equation 7.63) and $f_{\gamma,\delta}$ (equation 7.23), we have

$$\psi_{\omega,2} = f(\boldsymbol{\rho},\tau)\psi_{\omega,1} \tag{D.34}$$

with

$$\begin{aligned} f(\boldsymbol{\rho},\tau) &= \frac{f_{0,\omega}(\boldsymbol{r}',t')\,f_{\gamma,\delta}(\boldsymbol{r},t)}{f_{0,\omega}(\boldsymbol{r},t)} && \text{(D.35)} \\ &= \frac{(1+\omega^2t'^2)^{1/2}(\gamma t+\delta)}{(1+\omega^2t^2)^{1/2}} \exp\left[-\frac{im}{2\hbar}\left(\frac{\omega^2t'\boldsymbol{r}'^2}{1+\omega^2t'^2}+\frac{\gamma\boldsymbol{r}^2}{\gamma t+\delta}-\frac{\omega^2t\boldsymbol{r}^2}{1+\omega^2t^2}\right)\right]. && \text{(D.36)} \end{aligned}$$

With the new parameters $\tilde{\alpha},\tilde{\beta},\tilde{\gamma},\tilde{\delta}$ and with the previous relations between the times t,t',τ and the spatial coordinates $\boldsymbol{r},\boldsymbol{r}',\boldsymbol{\rho}$, we get

$$\begin{aligned} f(\boldsymbol{\rho},\tau) = {} & \frac{\left[1+\left(\frac{\tilde{\alpha}\tan(\omega\tau)+\tilde{\beta}}{\tilde{\gamma}\tan(\omega\tau)+\tilde{\delta}}\right)^2\right]^{1/2}\left[\tilde{\gamma}\tan(\omega\tau)+\tilde{\delta}\right]}{(1+\tan^2(\omega\tau))^{1/2}} \\ & \times\exp\left[-\frac{im\boldsymbol{\rho}^2}{2\hbar}\left(\frac{\frac{\tilde{\alpha}\omega\tan(\omega\tau)+\tilde{\beta}\omega}{\tilde{\gamma}\tan(\omega\tau)+\tilde{\delta}}(1+\tan^2(\omega\tau))}{1+\left(\frac{\tilde{\alpha}\tan(\omega\tau)+\tilde{\beta}}{\tilde{\gamma}\tan(\omega\tau)+\tilde{\delta}}\right)^2}+\frac{\omega\tilde{\gamma}(1+\tan^2(\omega\tau))}{\tilde{\gamma}\tan(\omega\tau)+\tilde{\delta}}-\omega\tan(\omega\tau)\right)\right]. \end{aligned} \tag{D.37}$$

One can show after a tedious but easy calculation that

$$f(\boldsymbol{\rho},\tau) = \lambda(\tau)\exp\left(-\frac{im\frac{\mathrm{d}\lambda}{\mathrm{d}\tau}\boldsymbol{\rho}^2}{2\hbar\lambda(\tau)}\right). \tag{D.38}$$

This demonstrates equation 7.41 and ends the proof.

D.3 HYDRODYNAMIC EQUATIONS

I demonstrate here how one can deduce a solution of a GPE with parameters ω, $\tilde{g}_2$, N_2 from the solution of a GPE with parameters ω, $\tilde{g}_1$, N_1 in the hydrodynamic regime.

In this regime, the GPE is equivalent to the two equations

$$\frac{\partial n}{\partial t} + \boldsymbol{\nabla}\cdot(n\boldsymbol{v}) = 0, \tag{D.39}$$

$$\frac{\partial \boldsymbol{v}}{\partial t} + \boldsymbol{\nabla}\left(\frac{1}{2}m\boldsymbol{v}^2+\frac{\hbar^2}{m}\tilde{g}n+\frac{1}{2}m\omega^2\boldsymbol{r}^2\right) = 0. \tag{D.40}$$

Let $n_1(\boldsymbol{r},t), \boldsymbol{v}_1(\boldsymbol{r},t)$ be a solution of these equations for the parameters ω, $\tilde{g}_1$, N_1. Then one can easily check that the functions

$$n'(\boldsymbol{r}',t') = \mu^2 n_1(\boldsymbol{r},t), \tag{D.41}$$

$$\boldsymbol{v}'(\boldsymbol{r}',t') = \mu\boldsymbol{v}_1(\boldsymbol{r},t), \tag{D.42}$$

where $\boldsymbol{r}'=\boldsymbol{r}$ and $t'=t/\mu$, are a solution of the GPE with parameters $\mu\omega$, $\tilde{g}_2$, N_2, where $\tilde{g}_2N_2=\mu^2\tilde{g}_1N_1$.

We can then apply a transformation on this solution to obtain a solution of the GPE with parameters ω, $\tilde{g}_2$, N_2. This transformation is given by equations 7.64 to 7.68, with $\omega_2 = \omega$ and $\omega_1 = \mu\omega$.

This transformation acts on n' and $\boldsymbol{v}'$ which are transformed into $n_2(\boldsymbol{r}'', t'')$ and $\boldsymbol{v}_2(\boldsymbol{r}'', t'')$ with

$$n_2(\boldsymbol{r}'', t'') = \mu^2 \lambda_{\mu\omega,\omega}^2(t') n_1(\boldsymbol{r}, t), \tag{D.43}$$

$$\boldsymbol{v}_2(\boldsymbol{r}'', t'') = \mu \lambda_{\mu\omega,\omega}(t')\, \boldsymbol{v}_1(\boldsymbol{r}, t) - \mu \frac{\mathrm{d}\lambda_{\mu\omega,\omega}}{\mathrm{d}t'} \tag{D.44}$$

and

$$\boldsymbol{r}'' = \frac{\boldsymbol{r}}{\lambda_{\mu\omega,\omega}(t')}, \tag{D.45}$$

$$\tan\big(\omega_2 t''\big) = \frac{1}{\mu} \tan\left(\frac{\mu\omega t}{\mu}\right). \tag{D.46}$$

These formula are exactly the same as equations 7.87 to 7.91, since

$$\lambda_{\mu\omega,\omega}(t') = \left[\frac{1}{\mu^2} \sin^2(\omega t) + \cos^2(\omega t)\right]^{1/2}. \tag{D.47}$$

E

PUBLICATIONS

In the following pages are reproduced the publications that I have contributed to during my PhD thesis and which are not discussed in this manuscript.

PHYSICAL REVIEW A **95**, 013632 (2017)

Loading and compression of a single two-dimensional Bose gas in an optical accordion

J. L. Ville,[1] T. Bienaimé,[2] R. Saint-Jalm,[1] L. Corman,[3] M. Aidelsburger,[1] L. Chomaz,[4] K. Kleinlein,[1] D. Perconte,[5]
S. Nascimbène,[1] J. Dalibard,[1] and J. Beugnon[1,*]

[1]*Laboratoire Kastler Brossel, Collège de France, CNRS, ENS-PSL Research University, UPMC-Sorbonne Universités,*
11 place Marcelin-Berthelot, 75005 Paris, France
[2]*INO-CNR BEC Center and Dipartimento di Fisica, Università di Trento, 38123 Povo, Italy*
[3]*Institute for Quantum Electronics, ETH Zurich, 8093 Zurich, Switzerland*
[4]*Institut für Experimentalphysik, Universität Innsbruck, Technikerstraße 25, 6020 Innsbruck, Austria*
[5]*Unité Mixte de Physique, CNRS, Thales, Université Paris-Sud, Université Paris-Saclay, 91767 Palaiseau, France*

(Received 23 November 2016; published 27 January 2017)

The experimental realization of two-dimensional (2D) Bose gases with a tunable interaction strength is an important challenge for the study of ultracold quantum matter. Here we report on the realization of an optical accordion creating a lattice potential with a spacing that can be dynamically tuned between 11 and 2 μm. We show that we can load ultracold ^{87}Rb atoms into a single node of this optical lattice in the large spacing configuration and then decrease nearly adiabatically the spacing to reach a strong harmonic confinement with frequencies larger than $\omega_z/2\pi$ =10 kHz. Atoms are trapped in an additional flat-bottom in-plane potential that is shaped with a high resolution. By combining these tools we create custom-shaped uniform 2D Bose gases with tunable confinement along the transverse direction and hence with a tunable interaction strength.

DOI: 10.1103/PhysRevA.95.013632

I. INTRODUCTION

Thanks to their high degree of isolation from the environment and the rich toolbox developed from atomic physics, quantum gases are ideal platforms to study strongly correlated systems [1] or to develop new metrology devices [2]. A key ingredient is the development of custom-shaped optical potentials allowing one to confine atoms in tunable geometries. Atoms are routinely trapped in low-dimensional setups, optical lattices, or, as recently demonstrated, flat-bottom potentials for three-dimensional (3D) [3] and two-dimensional (2D) [4,5] gases.

Low-dimensional systems are of particular interest for several reasons. The role of thermal and quantum fluctuations is enhanced compared to 3D and leads to rich physics such as the existence of the Berezinskii-Kosterlitz-Thouless superfluid phase in two dimensions [6,7]. When placed in (artificial) magnetic fields, they can give rise to topological phases of matter similar to those appearing in the quantum Hall effect [8]. From a more technical point of view, 2D systems, now routinely used in "atomic microscope" experiments [9,10], are well suited to implement high-resolution imaging or trap shaping with a resolution typically better than 1 μm, without being limited by a short focal depth or line-of-sight integration.

In 2D cold atomic clouds the interparticle interactions are characterized by a dimensionless parameter $\tilde{g} = \sqrt{8\pi}a/\ell_z$, where a is the s-wave scattering length and ℓ_z is the harmonic oscillator length along the strongly confining direction [11]. Varying the confinement (hence ℓ_z) thus opens the possibility of controlling the interaction strength for a fixed value of a and eventually entering the strongly interacting regime for large values of $\tilde{g}$ [12,13].

One of the challenges of realizing 2D systems is to load a large fraction of an initial (3D) Bose-Einstein condensate (BEC) in a single highly anisotropic trap with relatively weak confinement in the xy plane and a strong one along the third (z) direction. A possible approach consists of making a single potential minimum using either phase plates, creating a node of intensity of blue-detuned light [14], or a tightly focused red-detuned single beam [15]. Another approach consists of making an optical lattice by crossing two interfering beams at a fixed angle. In that case, the lattice spacing and hence the achievable strength of the confinement along the z axis are limited by the requirement of a single node loading [16,17]. Yet another possibility is to use a small-spacing lattice, load several planes, and then remove atoms in all the planes but one [18]. This procedure may lead to an important atom loss that is detrimental for exploring large systems. Single-plane 2D Bose gases have also been demonstrated in radio-frequency-dressed magnetic traps with a moderate transverse confinement [19] or in more complex setups involving an evanescent optical field close to a dielectric surface [20].

In this paper we create a single 2D cloud with a large number of atoms and a tunable confinement using a so-called "optical accordion." It consists of loading atoms in a single node of a large-spacing lattice and then increasing the angle between the two interfering beams to make the confinement stronger. This technique has been demonstrated optically, but not implemented on an atomic cloud, in Refs. [21,22] and used to increase the spacing of a lattice trapping ultracold atoms [23]. Compression of quantum gases has been reported in Ref. [24] using a different technique involving a reflexion on a dielectric surface. It has also recently been mentioned in Ref. [25], without any technical detail or study of the compression process. In this work we demonstrate single-plane loading and a fivefold increase of the trapping frequency of a Bose gas in an optical accordion and study the adiabaticity of the compression stage. With far-detuned light and moderate power we obtain clouds of 10^5 ^{87}Rb atoms confined with frequencies $\omega_z/2\pi$ higher than 10 kHz. We show that this compression can be realized in about 100 ms with a small

---

[*] beugnon@lkb.ens.fr

amount of additional heating compared to the ideal adiabatic evolution. These experiments are carried out with a flat-bottom in-plane potential.

II. ACCORDION OPTICAL SETUP

The design of our accordion lattice is inspired from [22] and depicted in Fig. 1(a). A single laser beam of wavelength $\lambda = 532$ nm is split by a pair of polarizing beam splitters (PBSs) into two parallel beams propagating along the y axis. These two beams cross in the focal plane of a lens, and their interference forms a one-dimensional (1D) optical lattice. The position of the incoming beam on the PBSs is moved thanks to a motorized translation stage. This position controls the distance between the two beams reflected by the PBSs, hence the angle between the beams in the focal plane and the fringe spacing. The relative phase between the two beams, which determines the absolute position of the fringes, is controlled by a piezoelectric stack glued on the mirror reflecting the top beam. The two beams are transmitted through a common polarizing beam-splitter cube positioned just before the lens [not shown in Fig. 1(a)] to ensure that they have identical polarization. In this work we use an elliptical beam with measured waists at atom positions of $w_x = 88(2)\,\mu$m and $w_z = 38(6)\,\mu$m in the horizontal and vertical directions, respectively. The uncertainty corresponds to the standard deviation of the measurement for the different lattice spacings studied here. The choice of these values for the waists results from the compromise between getting the highest intensity with the available power and having a large enough horizontal waist to get a uniform confinement over the sample size (see next section) and a large enough vertical one to ensure a robust overlap between the two beams when changing the lattice spacing, as discussed below.

In our setup we change the full angle θ between the two interfering beams from 3° to 15°. The maximum angle is limited by the available numerical aperture on this axis, and the minimum angle is constrained by the finite size of the beams, which should not be clipped by the edges of the PBSs. We measure the lattice period i resulting from the interference of the two beams by imaging the intensity pattern in the atom plane on a camera, and we obtain the results shown in Fig. 1(b). By translating the initial beam by 11.5 mm, we vary i from 11.0(1) to 1.9(1) μm. The data points are fitted by

$$i = \frac{\lambda}{2}\sqrt{1+[f/(d+d_0)]^2}, \qquad (1)$$

where d is the displacement of the stage from the position giving our largest lattice period. Here, d_0 is an arbitrary offset, and f is the focal length of the lens.

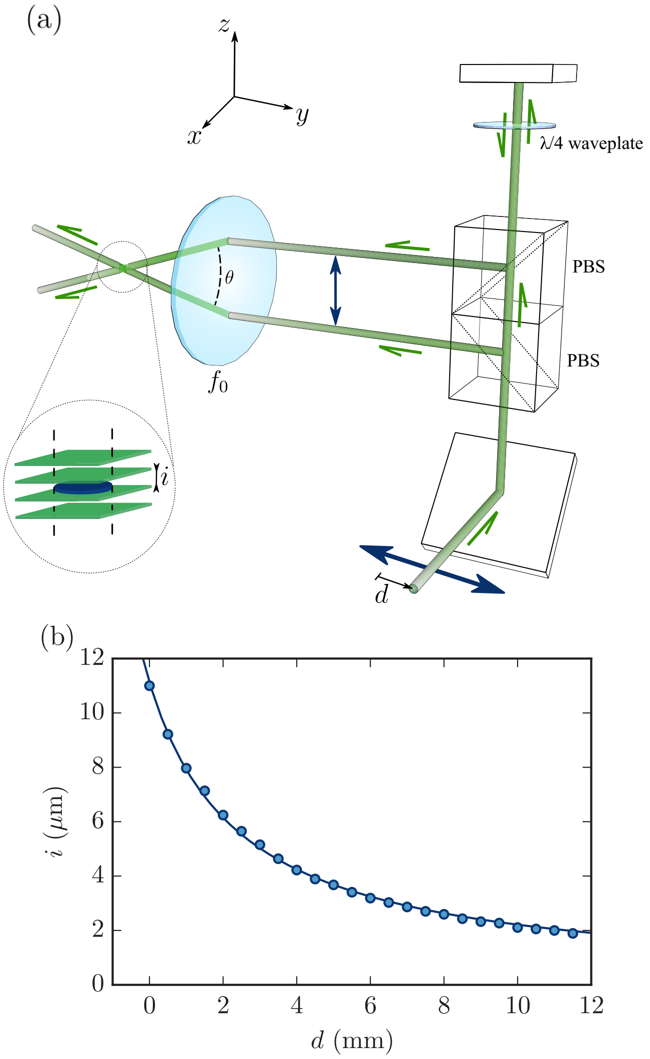

FIG. 1. (a) Sketch of the optical design allowing one to change the angle between the two interfering beams as proposed in [22]. The initial beam is moved (bottom arrow) by a distance d with a motorized translation stage (model LS-110 from PI miCos) that changes the distance between the two beams reflected by the polarizing beam splitters (PBS) of 25 mm size. These two beams are then focused on the atomic cloud by an aspherical 2-inch-diameter lens of focal length $f_0 = 100$ mm. The top beam is reflected on a mirror glued on a piezoelectric stack and goes twice through a quarter-wave plate. (b) Measured lattice spacing i of the vertical lattice at the atom position for different positions d of the translation stage. The data points are fitted by Eq. (1) with f and d_0 as free parameters. We obtain $f = 103(1)$ mm and $d_0 = 2.46(3)$ mm. The one-standard-deviation errors obtained from the fit on the measured lattice spacing are smaller than the size of the points.

The main challenge for realizing the accordion lattice is to avoid displacements of the beams in the focal plane when changing their angle. A large displacement of the two beams decreases their overlap and leads to a lower lattice depth and hence to a reduction of the trapping frequency or even to atom loss. In our setup, the main limitation is the imperfect quality of the lens. For instance, spherical aberrations and surface irregularities induce variations of the beam positions. We have tested standard achromatic doublets and an aspherical lens (Asphericon A50-100) and have found that the displacement is much smaller for the aspherical lens [26]. We show in Fig. 2 the positions of the centers of both beams in the z direction. The beams move by typically less than 20 μm in both directions, justifying our choice of $w_z = 39$ μm. We measure a displacement with a similar amplitude along the horizontal axis. We note that this motion of relatively small amplitude of the beams could induce irregular variations of the

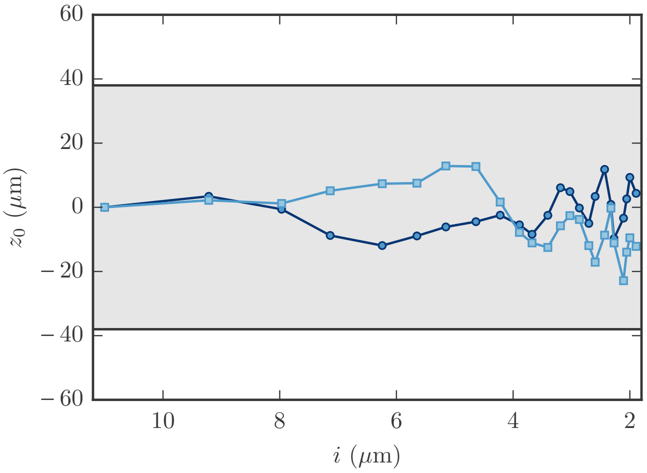

FIG. 2. Variation of the vertical positions z_0 with respect to their initial positions of the two interfering beams for different values of the lattice spacing i. Squares (circles) correspond to the bottom (top) beam. The shaded area corresponds to $\pm w_z$, where w_z is the averaged measured vertical waist over all the lattice spacings.

trap depth and center that may induce heating when changing the lattice spacing as discussed in Sec. IV.

III. MAKING A UNIFORM 2D BOSE GAS

We now describe the experimental system and the procedure used to realize 2D uniform gases. A sketch of the setup is shown in Fig. 3. We use two identical microscope objectives (numerical aperture of 0.45) above and below a glass cell. The bottom objective is used for absorption imaging of the cloud on a CCD camera with a typical resolution of 1 μm. The top objective allows us to image, with a similar resolution and a magnification of $1/70$, a trapping potential programmed on a digital micromirror device (DMD). This spatial light modulator is an array of 1024×784 square mirrors of size 13.8 μm. The orientation of each of these mirrors can be chosen between two states. In this work, all the mirrors are set in a state reflecting light towards the atomic cloud except the ones from a central disk-shaped area whose image in the atomic plane has a radius of 20 μm. The DMD reflects a blue-detuned beam at a wavelength of 532 nm with a maximum power of about 300 mW and a waist of 45 μm at the atom position. These parameters correspond to a maximum potential height at the edge of the disk of $k_B \times 4$ μK. In all the experiments described in the following, atoms are confined in the optical potential created by the combination of this box-potential beam and the accordion beams described in the previous section. The cloud is imaged using standard absorption imaging techniques either along the vertical axis or along the horizontal axis common with the accordion beams.

To load the 2D box potential we first prepare a 3D BEC using standard methods. We start from a 3D magneto-optical trap of ^{87}Rb atoms which contains 10^9 atoms. After cooling, compression, and optical pumping into the $F = 1$ manifold we load the atoms in the $F = 1$, $m_F = -1$ state in a magnetic quadrupole trap realized by a pair of conical coils along the vertical axis. After compression we proceed to forced evaporative cooling using a radio-frequency field ramp. Afterward, we decompress the magnetic trap to load atoms in an optical dipole trap consisting of two beams operating at a wavelength around 1064 nm and crossing at a right angle in the horizontal plane. Their vertical and horizontal waists are, respectively, 30 and 90 μm, and the depth potential is calculated to be around 70 μK. We then lower the trap depth to realize forced evaporative cooling, and we get almost pure BECs with typically 3×10^5 atoms.

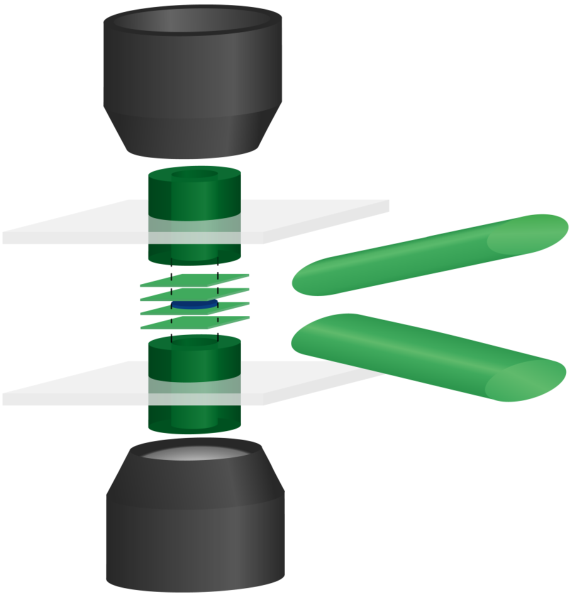

FIG. 3. Sketch of the experimental setup. The vacuum cell, simply depicted here as two horizontal glass plates, is surrounded by a pair of identical microscope objectives with a numerical aperture of 0.45. Atoms (in blue in the center) are trapped in the combination of blue-detuned dipole traps. Confinement along the vertical direction is realized by the interference of two beams at an angle (on the right) that create the accordion lattice. In-plane confinement is ensured by imaging the surface of a DMD on the atomic plane thanks to the top microscope objective. Here we created a disk-shaped uniform potential. This trap is loaded from a 3D BEC.

We now detail the loading of the 3D BEC in the box potential. We first ramp the box potential beam to full power in 300 ms. We then compress the BEC vertically to obtain a robust single-plane loading by increasing the power of one of the red-detuned dipole trap beams back to its maximum initial value in 125 ms while decreasing the other dipole trap power to zero. We then ramp the power of the accordion beams to their maximal value of 325 mW per beam in 25 ms with a maximum spacing of the accordion lattice of 11 μm. Finally, we ramp off the crossed dipole trap beams. The global spatial phase of the accordion lattice is adjusted thanks to the piezoelectric stack to get a dark fringe centered on the initial position of the atomic cloud. The optical alignment of the accordion beams is optimized so as to load the atoms in a fringe which is not moving when compressing the accordion lattice. We can then reliably load the atoms in a single plane [see Fig. 4(a)] [27]. Further evaporative cooling can be performed by lowering the power of the box potential beam and/or of the accordion beam to reach the 2D regime for which the thermal energy and the

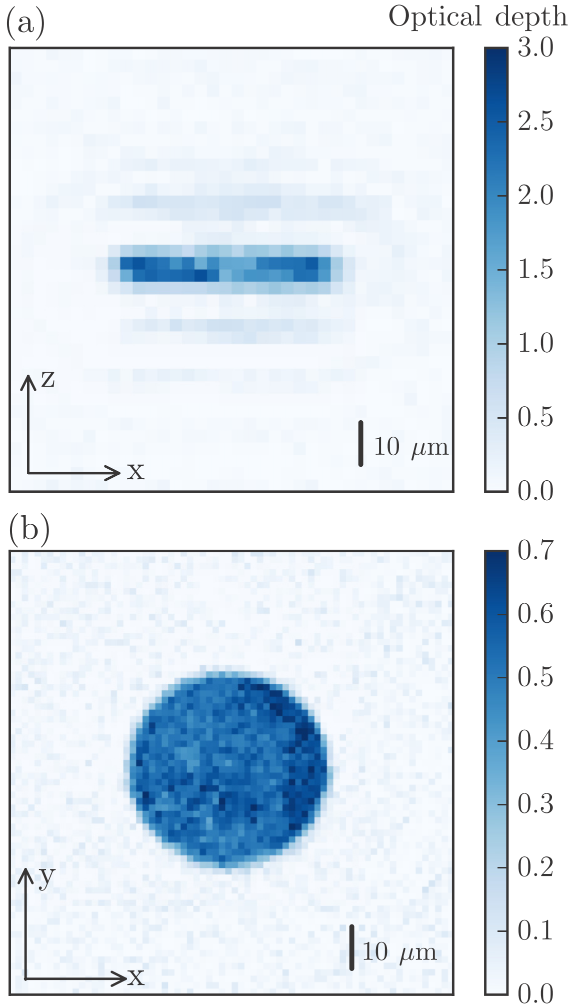

FIG. 4. *In situ* absorption images of the trapped cloud before compression with $\omega_z/2\pi = 2.1$ kHz and $T = 800$ nK. The cloud diameter is 40 μm. To avoid saturation of the absorption signal, we transfer, using a microwave field, only a small fraction of the 10^5 atoms from the $F = 1$ state to the $F = 2$ state before imaging atoms in $F = 2$. (a) Side view (transferred fraction: 100%, average of five pictures). The weak signals above and below the main cloud are fringes due to the propagation of light through our dense sample. We have checked that their position is independent of the lattice spacing of the accordion lattice. (b) Top view (transferred fraction: 2.4%, average of 35 pictures).

interaction energy are smaller than $\hbar\omega_z$. A typical picture of the cloud taken along the vertical axis is presented in Fig. 4(b).

IV. COMPRESSION IN THE ACCORDION

The main feature of this setup is the possibility to compress the gas along the z direction once the atoms are loaded in a single node of the lattice. In this section we describe our characterization of the compression process starting from atoms loaded in the largest-spacing configuration. First, we measure the oscillation frequency of the cloud in the vertical direction for different lattice spacings at maximum power. This frequency is determined as follows. We excite the center-of-mass motion of the cloud along the z direction by suddenly changing the power in the accordion beams, we let the cloud oscillate, and, finally, we measure the vertical position of the atomic cloud after a short free expansion. The trapping frequency is given by a sinusoidal fit of the data. The results are shown in Fig. 5. By compressing the lattice spacing from 11 to 2 μm we observe an increase of the oscillation frequency from 2.15(5) to 11.2(3) kHz. We also plot in Fig. 5 the expected frequency calculated with the measured power, waists, and lattice spacing. Our measurements are consistently below this calculation. We attribute this effect to the inaccurate calibration of the beam waists and powers and the imperfect overlap of the beams.

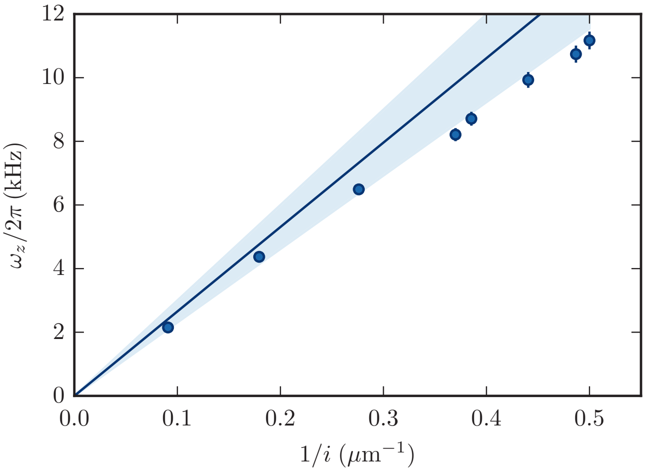

FIG. 5. Measured oscillation frequency along the vertical direction for different lattice spacings. The solid line is the calculated frequency with the independently measured parameters of the beams, and the shaded area corresponds to the uncertainty on the calibration of the beam parameters. The error bars represent the standard deviation given by the fit algorithm on the measured frequency and are close to the size of the data points and not visible for the low frequencies.

We now discuss the effect of compression on the cloud's temperature T, which is measured with a method detailed in Appendix A. In order to avoid evaporation of atoms during this compression, we first proceed to a cooling stage. It consists of lowering the power of the in-plane confining laser to evaporate the cloud and then setting it back to its initial value. After this evaporation cooling, we typically obtain $N = 3 \times 10^4$ atoms in the large-spacing lattice at a temperature of $T_0 = 180$ nK. With these parameters, the total 2D phase-space density, defined as $\mathcal{D} = N\lambda_T^2/A$, with A being the disk area and λ_T being the thermal de Broglie wavelength, is $\mathcal{D} = 4.8$, which corresponds to a noncondensed gas [5]. We then compress the cloud to various final vertical confinements at a constant velocity of the translation stage (90 mm/s) within 0.13 s while keeping the overall sequence duration constant. We show in Fig. 6(a) the measured final temperature (blue circles) for various final trapping frequencies. We observe a significant increase in the cloud's temperature by a factor of about 2 for the largest final frequency. The atom number is unchanged during this compression, and thus it rules out any evaporation process.

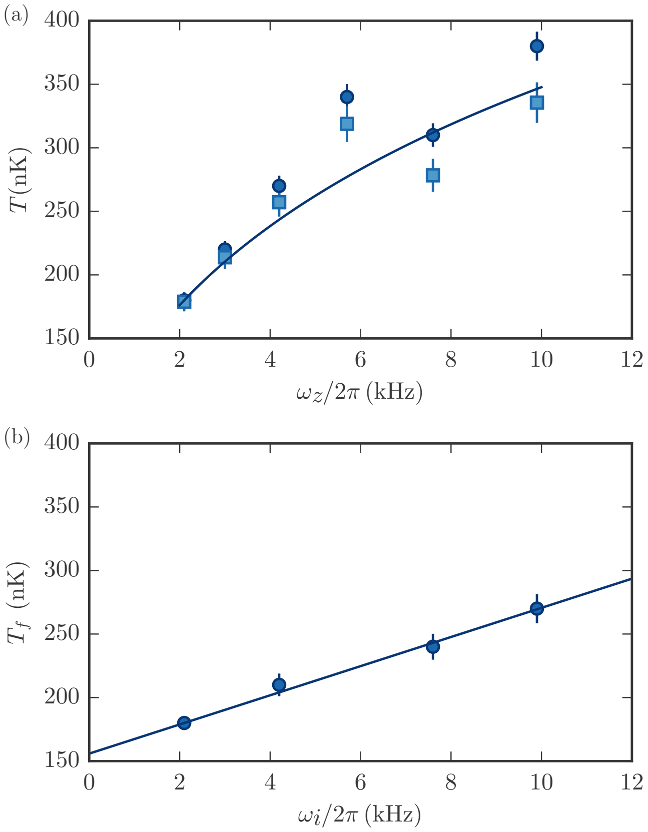

FIG. 6. Compression in the optical accordion. (a) Temperature measured after compression to a final frequency ω_z (circles) and corrected by the fit of the measured heating displayed in (b) (squares). The solid line is a calculation for an adiabatic compression of an ideal Bose gas with our trap geometry (see Appendix B). (b) Temperature T_f measured after a compression to the intermediate frequency ω_i and decompression to the initial frequency. The solid line is a linear fit to the data. The measured heating is divided by 2 before subtraction to the data in (a), considering that the heating for a full cycle is two times larger than the heating for the single compression.

The measured increase of temperature during the compression process could have two origins. (i) It could simply result from the change in density of states in a purely adiabatic process [solid line in Fig. 6(a)]. (ii) There may be an additional heating process due to imperfections in the trap compression as discussed in Sec. II. In order to test the adiabaticity of the process we realize a compression up to a given intermediate frequency ω_i followed by a decompression to the initial frequency. The measured final temperatures T_f are reported in Fig. 6(b). For a purely adiabatic compression-decompression cycle we expect no increase in temperature. We observe a deviation from adiabaticity which can reach 90 nK for a full compression-decompression sequence or, assuming the same amount of additional heating for compression and decompression, 45 nK for the compression stage. This heating remains small compared to the 150 nK increase in temperature expected for a purely adiabatic process as described in the next paragraph. This heating varies approximately linearly with the target frequency ω_i. We have measured a similar heating for lower velocities of the translation stage.

To further explore the origin of the temperature increase observed here, we compare our results to the prediction for adiabatic compression of an ideal Bose gas confined in our trap geometry. The result of this calculation, detailed in Appendix B and applied to the measured initial temperature and frequency, is shown in Fig. 6(a) as a solid line. We also show the measured temperatures corrected by half the heating measured for the compression-decompression cycle [Fig. 6(b)] as squares. They are in good agreement with the calculated temperature. We conclude that the deviation from adiabaticity in our experimental setup leads to an additional heating that remains small compared to the increase of temperature expected in the adiabatic case.

V. OUTLOOK: AN ADJUSTABLE INTERACTION STRENGTH

We have realized a 2D uniform Bose gas with a tunable confinement. As discussed in the Introduction, in such gases the role of interactions is described, up to logarithmic corrections [11], by the dimensionless parameter $\tilde{g} = \sqrt{8\pi}a/\ell_z$, where $\ell_z = \sqrt{\hbar/(m\omega_z)}$ is the harmonic oscillator ground-state length for a particle of mass m in the harmonic potential of frequency ω_z. Tuning the confinement thus allows one to control the strength of interaction in such systems without tuning the scattering length via a Feshbach resonance [13] or adding an in-plane lattice potential to control the effective mass of the atoms [12]. In our setup, by varying $\omega_z/2\pi$ between 1 and 11 kHz by tuning the lattice spacing or the laser power, we can adjust $\tilde{g}$ between 0.08 and 0.26. Obtaining such comparatively large values of $\tilde{g}$ is of great interest for realizing strongly correlated states for which the gap between the ground state and the excited states usually scales linearly with $\tilde{g}$ [28]. The demonstration of such an optical accordion is thus a significant step in this direction.

Our system is compatible with the realization of flat-bottom potentials with a shape that can be changed, potentially in a dynamic way, thanks to the use of DMDs. Our system is thus an ideal platform to study in- and out-of-equilibrium many-body physics in two-dimensional systems. Another asset of this geometry is the possibility to realize evaporative cooling with this accordion lattice. In the usual evaporation schemes a particle is evaporated when it has a high enough energy and when it reaches a position in the trap where it could be lost (like the edge of the box potential in the work described here). In this situation temperature gradients might be created in the sample. Lowering the depth of the accordion lattice by decreasing its intensity or by adding a magnetic field gradient allows for an evaporation independent of the atom position and could lead to more efficient evaporative cooling. This feature is particularly interesting when studying quench cooling of 2D quantum gases [5].

ACKNOWLEDGMENTS

We thank Z. Hadzibabic for fruitful discussions. This work is supported by DIM NanoK, ANR (ANR-12-BLANAGAFON), and ERC (Synergy UQUAM). L.C. acknowledges the support from DGA. M.A. is supported within the Marie Curie Project BosQuanTran of the European Commission.

J.L.V. and T.B. contributed equally to this work.

APPENDIX A: TEMPERATURE MEASUREMENT

The temperatures reported in the main text were measured using the following procedure. Immediately after loading the atoms in the optical box potential, we send a short pulse of a microwave field that transfers a small fraction of about 10% of the atoms from the $|1\rangle = |F = 1, m = -1\rangle$ state to the $|2\rangle = |F = 2, m = -2\rangle$ state. We then proceed to forced evaporation by lowering the power of the box potential beam and realize the experimental sequences discussed in the main text. We assume that the atoms in state $|2\rangle$ thermalize with the main cloud of atoms in $|1\rangle$. By choosing the fraction of atoms in state $|2\rangle$ to be small enough we always prevent the formation of a Bose-Einstein condensate in this state. To extract the temperature of the sample we release the atoms from the trap and image the density distribution of atoms in state $|2\rangle$ integrated along the vertical direction and after a time-of-flight of 8.7 ms. For each point we average typically 10 images with the same experimental conditions.

We compare the radially averaged profile of these distributions to a numerically computed profile considering an ideal gas with an initial velocity distribution given by the Bose distribution and an initial uniform position in the box potential and assuming an expansion without any interparticle interaction. The theoretical profile has two free parameters, the temperature T and the fugacity z, which we optimize to obtain the best fit to the experimental data points. With our signal-to-noise ratio, there is a continuous set of (z,T) that fits almost equally well a given experimental profile, making a robust estimate of the temperature difficult. We circumvent this issue by using the independently measured atom number as an additional input parameter to compute $z(T)$, leaving T as the only free parameter.

From the distribution of temperature measurements for a fixed experimental sequence, we estimate that the one-standard-deviation statistical error bars on the temperature measurement are around ±3% of the measured temperature. The main source of uncertainty is given by the uncertainty on the atom number that we use to estimate the temperature. In our range of parameters, the estimated uncertainty of 25% in the atom number calibration leads to an uncertainty of about 15% in the temperature. In the main text, we display error bars corresponding to only the ±3% statistical uncertainty.

APPENDIX B: ADIABATIC COMPRESSION

We consider a gas of noncondensed bosons of mass m confined in the xy plane in a box potential of surface A and along the vertical direction in a harmonic potential of frequency ω_z. We set $\rho_0 = mA/(2\pi\hbar^2)$ for the in-plane density of states and $z_j = z\exp(-j\beta\hbar\omega_z)$, where z is the gas fugacity, $\beta = 1/k_BT$, and j is the integer labeling the jth state of the vertical harmonic oscillator. The average occupation number $\bar{n}_{j,k}$ of a given energy state with an in-plane wave number k is

$$\bar{n}_{j,k} = \left\{ z^{-1} \exp\left[\beta \left(j\hbar\omega_z + \frac{\hbar^2 k^2}{2m} \right) - 1 \right] \right\}^{-1}. \quad \text{(B1)}$$

Introducing the polylogarithm function $g_\alpha(z) = \sum_{k=1}^{\infty} z^k/k^\alpha$, we compute N_j, J_j, and S_J, which are, respectively, the atom number, the grand-canonical potential, and the entropy of state j.

$$\begin{aligned} N_j &= \rho_0 k_B T g_1(z_j), \\ J_j &= -\rho_0 (k_B T)^2 g_2(z_j), \\ S_j &= -\left.\frac{\partial J_j}{\partial T}\right|_{\mu,\omega_z} = \rho_0 k_B T[2g_2(z_j) - g_1(z_j)\ln(z_j)]. \quad \text{(B2)} \end{aligned}$$

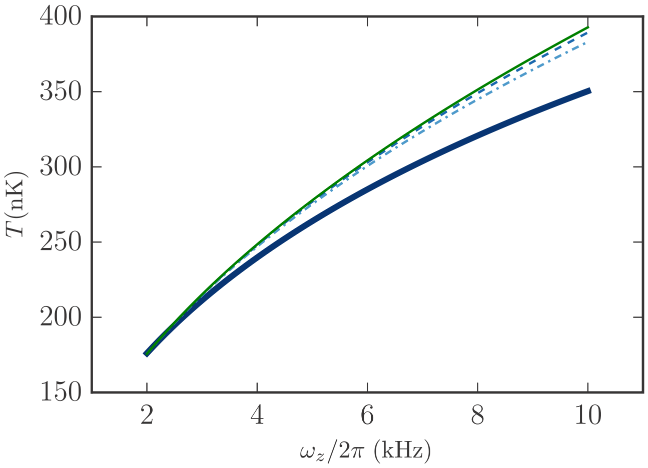

FIG. 7. Adiabatic compression. We show, for an initial temperature of 180 nK and an initial frequency of 2.1 kHz, the temperature increase during compression calculated numerically for different models. The thick solid line corresponds to the bosonic case. The green solid line is given by an analytical result obtained in the classical case with a weak confinement along z and scales as $\omega_z^{1/2}$. The dashed line and the dot-dashed line are associated with the fermionic and the Maxwell-Boltzmann statistics cases, respectively.

We compute the temperature evolution for an adiabatic compression by evaluating, for each value of the final compression frequency ω_z, the temperature and the fugacity, keeping $S = \sum_j S_j$ and $N = \sum_j N_j$ constant. The result of this calculation is shown in the main text in Fig. 6 and is reproduced in Fig. 7.

The previous calculation can be straightforwardly extended to fermionic statistics and to the classical Maxwell-Boltzmann statistics by replacing $g_\alpha(z)$ by $f_\alpha(z) = -g_\alpha(-z)$ and by z, respectively. The results for these cases are also represented in Fig. 7 as a dotted line and a dot-dashed line respectively, and show that, in all cases, the increase in temperature during adiabatic compression is larger than for the bosonic case. Indeed, Bose statistics leads to a larger population of the low-lying states of the vertical harmonic oscillator than the classical distribution and thus to a smaller increase of temperature when increasing the confinement frequency.

Finally, we also plot in Fig. 7 an analytical result obtained for the classical Maxwell-Boltzmann statistics but assuming a weak confinement along the vertical direction ($\beta\hbar\omega_z \ll 1$). In this case the 3D density of states is given by $\rho(\varepsilon) = \rho_0/(\hbar\omega_z)\,\varepsilon$, and the entropy reads

$$S/(Nk_B) = 3 + \ln[\rho_0(k_BT)^2/(N\hbar\omega_z)]. \tag{B3}$$

An adiabatic compression thus leads to an increase in temperature as $T \propto \sqrt{\omega_z}$, which corresponds to the green solid line shown in Fig. 7 and which is very close to the numerical calculation for the Maxwell-Boltzmann statistics. We note that in the experiments presented here the fugacity is close to 1 and the Maxwell-Boltzmann approximation is clearly not valid.

[1] I. Bloch, J. Dalibard, and W. Zwerger, Rev. Mod. Phys. **80**, 885 (2008).

[2] A. Cronin, J. Schmiedmayer, and D. Pritchard, Rev. Mod. Phys. **81**, 1051 (2009).

[3] A. L. Gaunt, T. F. Schmidutz, I. Gotlibovych, R. P. Smith, and Z. Hadzibabic, Phys. Rev. Lett. **110**, 200406 (2013).

[4] L. Corman, L. Chomaz, T. Bienaimé, R. Desbuquois, C. Weitenberg, S. Nascimbène, J. Dalibard, and J. Beugnon, Phys. Rev. Lett. **113**, 135302 (2014).

[5] L. Chomaz, L. Corman, T. Bienaimé, R. Desbuquois, C. Weitenberg, S. Nascimbène, J. Beugnon, and J. Dalibard, Nat. Commun. **6**, 6162 (2015).

[6] V. L. Berezinskii, Sov. Phys. JETP **34**, 610 (1972).

[7] J. Kostlerlitz and D. Thouless, J. Phys. C **6**, 1181 (1973).

[8] J. Dalibard, F. Gerbier, G. Juzeliūnas, and P. Öhberg, Rev. Mod. Phys. **83**, 1523 (2011).

[9] W. Bakr, J. Gillen, A. Peng, S. Fölling, and M. Greiner, Nature (London) **462**, 74 (2009).

[10] J. F. Sherson, C. Weitenberg, M. Endres, M. Cheneau, I. Bloch, and S. Kuhr, Nature (London) **467**, 68 (2010).

[11] Z. Hadzibabic and J. Dalibard, Riv. Nuovo Cimento **34**, 389 (2011).

[12] L.-C. Ha, C.-L. Hung, X. Zhang, U. Eismann, S.-K. Tung, and C. Chin, Phys. Rev. Lett. **110**, 145302 (2013).

[13] P. A. Murthy, I. Boettcher, L. Bayha, M. Holzmann, D. Kedar, M. Neidig, M. G. Ries, A. N. Wenz, G. Zürn, and S. Jochim, Phys. Rev. Lett. **115**, 010401 (2015).

[14] S. P. Rath, T. Yefsah, K. J. Günter, M. Cheneau, R. Desbuquois, M. Holzmann, W. Krauth, and J. Dalibard, Phys. Rev. A **82**, 013609 (2010).

[15] P. Cladé, C. Ryu, A. Ramanathan, K. Helmerson, and W. D. Phillips, Phys. Rev. Lett. **102**, 170401 (2009).

[16] N. Gemelke, X. Zhang, C.-L. Hung, and C. Chin, Nature (London) **460**, 995 (2009).

[17] M. G. Ries, A. N. Wenz, G. Zürn, L. Bayha, I. Boettcher, D. Kedar, P. A. Murthy, M. Neidig, T. Lompe, and S. Jochim, Phys. Rev. Lett. **114**, 230401 (2015).

[18] S. Stock, Z. Hadzibabic, B. Battelier, M. Cheneau, and J. Dalibard, Phys. Rev. Lett. **95**, 190403 (2005).

[19] K. Merloti, R. Dubessy, L. Longchambon, A. Perrin, P.-E. Pottie, V. Lorent, and H. Perrin, New J. Phys. **15**, 033007 (2013).

[20] J. I. Gillen, W. S. Bakr, A. Peng, P. Unterwaditzer, S. Fölling, and M. Greiner, Phys. Rev. A **80**, 021602 (2009).

[21] R. A. Williams, J. D. Pillet, S. Al-Assam, B. Fletcher, M. Shotter, and C. J. Foot, Opt. Express **16**, 16977 (2008).

[22] T. Li, H. Kelkar, D. Medellin, and M. Raizen, Opt. Express **16**, 5465 (2008).

[23] S. Al-Assam, R. A. Williams, and C. J. Foot, Phys. Rev. A **82**, 021604 (2010).

[24] M. Miranda, A. Nakamoto, Y. Okuyama, A. Noguchi, M. Ueda, and M. Kozuma, Phys. Rev. A **86**, 063615 (2012).

[25] D. Mitra, P. T. Brown, P. Schauß, S. S. Kondov, and W. S. Bakr, Phys. Rev. Lett. **117**, 093601 (2016).

[26] The variations of the beam position and angle induced by the motion of the translation stage were found to be less important than the defects of the tested lenses.

[27] We compensate the slow drift of the lattice by a feedback on the piezoelectric stack after each experimental sequence.

[28] N. Cooper, Adv. Phys. **57**, 539 (2008).

Relaxation Dynamics in the Merging of N Independent Condensates

M. Aidelsburger, J. L. Ville, R. Saint-Jalm, S. Nascimbène, J. Dalibard, and J. Beugnon
Laboratoire Kastler Brossel, Collège de France, CNRS, ENS-PSL Research University,
UPMC-Sorbonne Universités, 11 place Marcelin-Berthelot, 75005 Paris, France

(Received 7 May 2017; revised manuscript received 26 September 2017; published 6 November 2017)

Controlled quantum systems such as ultracold atoms can provide powerful platforms to study nonequilibrium dynamics of closed many-body quantum systems, especially since a complete theoretical description is generally challenging. In this Letter, we present a detailed study of the rich out-of-equilibrium dynamics of an adjustable number N of uncorrelated condensates after connecting them in a ring-shaped optical trap. We observe the formation of long-lived supercurrents and confirm the scaling of their winding number with N in agreement with the geodesic rule. Moreover, we provide insight into the microscopic mechanism that underlies the smoothening of the phase profile.

DOI: 10.1103/PhysRevLett.119.190403

Thermalization of closed out-of-equilibrium many-body systems lies at the heart of statistical physics. Because of the recent progress in the preparation of well-controlled isolated quantum systems, this question can now be revisited in a quantum context [1]. Whereas most systems are expected to reach thermal equilibrium, nontrivial situations can occur in integrable systems [2], in the presence of disorder [3] or due to the formation of long-lived topological defects [4,5]. Out-of-equilibrium dynamics are also central to the study of dynamical crossings of phase transitions. Indeed, the divergence of the relaxation time at the critical point for a second-order phase transition entails that the system cannot follow adiabatically the external perturbation. The relaxation dynamics can be used in that case to determine the critical exponents of the phase transition [5].

A rich situation occurs when N condensates, characterized by independent initial phase factors, are coupled together. Let us consider, for instance, the case where the condensates are placed along a ring and connections are suddenly established between neighboring condensates. One expects that, after some transient dynamics, stochastic metastable supercurrents are formed. This ring geometry was put forward by Zurek in a seminal paper [6] drawing a parallel between laboratory experiments with liquid helium and classes of early universe theories. More recently this gedankenexperiment inspired experiments with superconducting loops [7–9] and cold atoms [10]. A key ingredient of Zurek's study is the relation between the winding number of the supercurrent and the number of initial condensates N according to the *geodesic rule*. In essence, it enables a computation of the winding number based on the minimization of the kinetic energy of the system.

In this Letter we investigate the relaxation dynamics of up to $N = 12$ uncorrelated Bose-Einstein condensates (BECs) after merging them in a ring-shaped optical trap. We measure the statistical distribution of metastable supercurrents and relate their emergence to the evolution of the

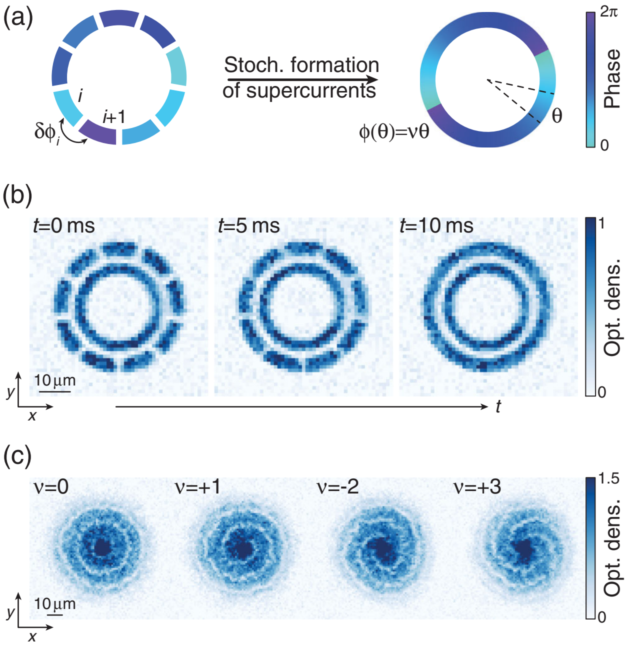

FIG. 1. Experimental protocol. (a) Illustration of the experimental sequence. An annular trap is partitioned into N segments of equal length. Uncorrelated BECs are prepared in these segments with random phase differences $\delta\phi_i$, $i = 1, \ldots, N$, between adjacent condensates. After merging into a single annular condensate, supercurrents with winding number $\nu \in \mathbb{Z}$ are formed. (b) *In situ* density distribution in the ring trap for $N = 9$ at different times t during the merging. The outer ring has a mean radius of 19.5 μm and a width of 5 μm. The inner ring serves as a phase reference for the detection as described in the main text. It has a mean radius of 13 μm and a width of 4 μm. Each image is an average over 5 or 6 experimental realizations. (c) Matter-wave interference after a 2D time of flight (TOF) of 6 ms. The chirality of the pattern and the number of spiral arms reveal the winding number ν of the supercurrent in the outer ring.

phase defects generated at the boundaries of the BECs. The experimental protocol is depicted in Fig. 1(a). Initially the condensates are characterized by random phase differences $\delta\phi_i$ $(i = 1, \ldots, N)$ between condensates i and $i+1$, that can lead to a net phase accumulation around the ring after merging [Fig. 1(b)]. Because of the single-valuedness of the wave function, the phase winding around the ring has to be equal to $2\pi\nu$, with winding number $\nu \in \mathbb{Z}$. This corresponds to the formation of supercurrents with quantized velocities, which we detect through matter-wave interference [Fig. 1(c)] with an additional ring-shaped condensate with uniform phase [10,11]. Our results show that the magnitude of the supercurrent scales in quantitative agreement with the geodesic rule. This extends earlier works on the merging of two [12] and three [13] condensates in a harmonic trap and on the dynamics of a large number of condensates in a two-dimensional (2D) optical lattice [14]. Complementary results have been obtained with a large number of Josephson junctions, where the scaling with N appears to be modified compared to the one studied in our work [7]. Additionally we explore the underlying dynamics by merging pairs of neighboring condensates. First, we study it globally by monitoring the evolution of the winding-number distribution as a function of time. Second, we detect local phase defects and study their dynamics in a time-resolved manner. The observed relaxation time scales are compatible with the evolution of solitonlike phase defects.

The experiment started by loading a cold cloud of $1.4(2) \times 10^5$ ^{87}Rb atoms in the $|F = 1, m_F = 0\rangle$ state into a pancake-type dipole trap with tight harmonic confinement along the vertical direction, $\omega_z = 2\pi \times 1.58(1)$ kHz, and negligible confinement in the xy-plane [15,16]. The in-plane trap was shaped using a digital micromirror device (DMD) in direct imaging with an optical resolution of ~ 1 μm to create a uniform double-ring trap as illustrated in Fig. 1(b). All experimental studies were performed in the outer ring, which was partitioned into several segments, while the inner ring served as a uniform phase reference for detection [10,11]. The distance between the segments as well as between the two rings was $2.5(2)$ μm, defined as the full width at half maximum of the density dip in the measured *in situ* distributions [Fig. 1(b)]. This separation is large enough to enable the formation of uncorrelated condensates [16].

After 2 s evaporative cooling, we reached a final temperature of $T < 20$ nK, thereby entering the quasi-2D regime $k_B T < \hbar\omega_z$, with k_B the Boltzmann constant and $\hbar$ the reduced Planck constant. The upper temperature limit of 20 nK is the smallest detectable temperature using our calibration method. This corresponds to 2D phase-space densities $\mathcal{D} = \lambda_T^2 n > 80$ deeply in the superfluid regime [18]; here $n = 36(4)/\mu\text{m}^2$ is the 2D atomic density, $\lambda_T = \hbar\sqrt{2\pi/(m k_B T)}$ the thermal wavelength and m the mass of one atom.

Subsequently, we merged the BECs in the outer ring within 10 ms by decreasing the width of the potential barriers [Fig. 1(b)] using our dynamically configurable DMD. The velocity at which the barriers were closed was chosen small compared to the speed of sound c_0 in order to prevent the formation of shock waves and high-energy excitations [19,20]. For our experimental parameters $c_0 = \sqrt{n g_{2D}/m} \approx 1.4(1)$ mm/s, where $g_{2D} = g_{3D}/(\sqrt{2\pi} l_z)$ is the 2D interaction parameter, $g_{3D} = 4\pi\hbar^2 a/m$, $a = 5.3$ nm the scattering length, and $l_z = \sqrt{\hbar/(m\omega_z)} = 0.27$ μm the harmonic oscillator length.

After a typical relaxation time of 0.5 s, we detected the phase winding after 2D time of flight by releasing the in-plane confinement abruptly while keeping the vertical one. We recorded the resulting interference pattern after 6 ms using standard absorption imaging along the z direction [Fig. 1(c)]. The chirality of the pattern and the number of spiral arms are a direct measure of the winding number ν of the supercurrent that was formed in the outer ring [10,11]. In an independent calibration measurement we found that

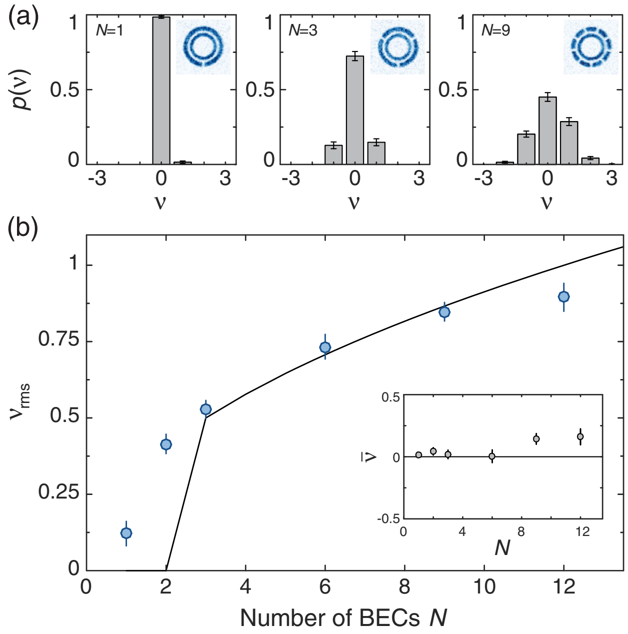

FIG. 2. Formation of supercurrents as a function of the number of BECs N. (a) Probability distributions $p(\nu)$ for $N = 1$, 3 and 9 obtained from $\mathcal{M} = 202$, 238, and 388 measurements, respectively. The insets display *in situ* images before the merging averaged over 4–6 realizations. (b) Measured rms width ν_{rms} of the probability distributions as a function of N. Each data point consists of $\mathcal{M} > 200$ independent measurements. The corresponding mean values $\bar{\nu}$ are displayed in the inset. The solid line is the predicted scaling given in Eq. (1). All error bars display the combined uncertainty from the experimental determination of the winding number and the statistical error due to a finite number of measurements $\mathcal{M}$, which was evaluated using a bootstrapping approach.

the probability of creating a supercurrent in the inner ring was $\lesssim 0.6\%$ [16].

Each repetition of the experiment results in a different set of random phase differences $\delta\phi_i$ that leads to the formation of a supercurrent with winding number $\nu = \sum_{i=1}^{N} \delta\phi_i/(2\pi)$, where $-\pi < \delta\phi_i \leq \pi$. The interval for the phase differences $\delta\phi_i$ is chosen according to the geodesic rule, which expresses the fact that the system tends to minimize the absolute value of the relative phase between neighboring condensates due to energetic reasons [21,22]. By repeating the measurement $\mathcal{M}$ times we extracted the corresponding probability distributions $p(\nu)$ as illustrated in Fig. 2(a). We observe an increase of the probability for nonzero winding numbers with N resulting in a broadening of the distribution. The measured center $\bar{\nu} = \sum_\nu p(\nu)\nu$ and rms width $\nu_{\mathrm{rms}} = \sqrt{\mathcal{M}/(\mathcal{M}-1)\sum_\nu p(\nu)(\nu-\bar{\nu})^2}$ of the individual distributions are depicted in Fig. 2(b).

Ideally the smallest number of domains that allows for the formation of topological defects is three. In this case the probabilities $p_{\mathrm{th}}(\nu)$ can be computed following simple arguments [13,23]. There are three possible cases: if $\delta\phi_1 + \delta\phi_2 > \pi$, the total sum of all phase differences has to amount to 2π, if $\delta\phi_1 + \delta\phi_2 < -\pi$ the total sum amounts to -2π and for all other cases it vanishes. The resulting probabilities are $p_{\mathrm{th}}(+1) = p_{\mathrm{th}}(-1) = 1/8$, which is compatible with our experimental results $p(+1) = 0.15(2)$ and $p(-1) = 0.13(2)$ displayed in Fig. 2(a). In general the probability distribution is determined by the Euler-Frobenius distribution [24] and we obtain

$$\nu_{\mathrm{rms}}(N) = \begin{cases} 0, & \text{if } N < 3 \\ \frac{1}{2\sqrt{3}}\sqrt{N}, & \text{if } N \geq 3. \end{cases} \qquad (1)$$

The distribution is symmetric around $\nu = 0$, with $\bar{\nu} = 0$, which is in agreement with our experimental data obtained for small N [Fig. 2(b)]. For $N \geq 9$ there seems to be a small systematic shift to positive values.

Our experimental results shown in Fig. 2(b) are in agreement with the predicted scaling for $N \geq 3$. There is a discrepancy for $N = 1$, where we measure a nonzero probability for the formation of supercurrents $p(\nu \neq 0) = 1.5(8)\%$. We attribute this to phase fluctuations of the condensate due to finite temperature effects, which are enhanced for larger systems. We tested that reducing the radius of the condensate by one-third significantly reduces the probability for nonzero winding numbers. For $N \geq 3$ thermal fluctuations are not expected to have a large influence because the length of the condensates is smaller. Regarding the case of $N = 2$ we found that this particular configuration was very sensitive to the alignment of our trap. Small trap inhomogeneities had a significant impact on the obtained distributions.

For the largest number of condensates $N = 12$ we measure slightly smaller values than expected, most likely due to an increased sensitivity to experimental imperfections and overlapping time scales. If the merging of the BECs is performed too slowly, there are two main effects that can lead to a reduction of ν_{rms}. If supercurrents are already formed during the merging, their lifetime could be reduced substantially due to the presence of residual weak potential barriers [25]. At the same time an asynchronous merging of the barriers could effectively reduce the total number of initial condensates, if the phase of neighboring condensates homogenizes before the merging is complete. We have investigated this in more detail for $N = 9$ and found a significant reduction of the winding numbers for merging times larger than 50 ms [16]. Both effects are expected to be more critical for increasing N.

We typically wait 0.5 s after merging the condensates before detecting the supercurrents. This waiting time is short compared to the lifetime of the supercurrents in our trap [16]. Indeed we observe no significant decay of the supercurrents for waiting times on the order of 10 s. On the other hand it is long enough to let the system relax to a steady state with a smoothened phase profile, without a significant number of defects in the interference pattern.

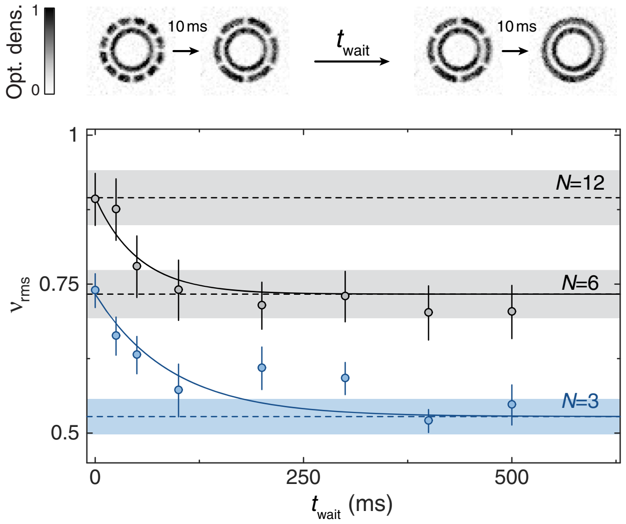

FIG. 3. Relaxation dynamics from N to $N/2$ condensates, when merging them in two successive steps. The *in situ* images above the main graph illustrate the experimental sequence for $N = 12$. Each image is an average over five individual measurements. The main graph depicts our experimental results for $N = 12$ (black) and $N = 6$ (blue). Each data point consists of $\mathcal{M} > 200$ measurements. The corresponding mean values $\bar{\nu}$ are shown in the Supplemental Material [16]. The error bars depict the uncertainty obtained from our finite number of measurements $\mathcal{M}$ and the experimental uncertainty in the determination of the winding numbers. The dashed lines indicate the measured values shown in Fig. 2(b) and the shaded areas illustrate the corresponding error bars. The solid lines are fits of exponential functions $f_j(t_{\mathrm{wait}}) = A_j e^{-t_{\mathrm{wait}}/\tau_j} + B_j$, $j = \{6, 12\}$, to our data, where τ_j is the only free fit parameter and the other variables are determined by the dashed lines extracted from Fig. 2(b).

In order to gain a deeper insight into the underlying relaxation dynamics, we performed two separate experiments. First, we probed the evolution of the winding number distribution by merging the BECs on the ring in two successive steps. The sequence started by merging pairs of neighboring condensates within 10 ms to reduce the number of condensates by a factor of 2, then we let the system relax for a variable time t_{wait} and subsequently merged the remaining $N/2$ condensates in 10 ms into a single annular BEC (Fig. 3). After an additional evolution time of 0.5 s we detected the probability distributions $p(\nu)$ using the detection method explained above.

We identify two limiting cases for the data shown in Fig. 3. If there is no additional wait time ($t_{\mathrm{wait}} = 0$) between the two merging steps, the system has not enough time to relax and the probability distribution resembles the one discussed in Fig. 2, where all condensates were merged in a single step. On the other hand, if t_{wait} is longer than the relaxation time, the phase of neighboring condensates homogenizes after the first step, so that we effectively reduce the number of initial phase domains to $N/2$ and the distribution approaches the one for $N/2$ initial BECs merged in a single step. The measurements were performed for $N = 12$ and $N = 6$ and the dashed lines indicate the limiting cases explained above. In order to extract a time scale for the relaxation, we fit an exponential decay to each of the two data sets. The amplitude and offset of the fitting function are determined by the data points displayed in Fig. 2(b). One can infer two different time scales $\tau_{12} = 52(17)$ ms and $\tau_6 = 90(30)$ ms associated with the relaxation dynamics, which most likely depend on the spatial extent of the condensates, that differ by almost a factor of 2 for the two data sets.

In a second set of measurements we focus on the microscopic relaxation dynamics via the time-resolved detection of local phase defects. We merged two condensates and probed the evolution of the phase profile through interference with a reference condensate [Fig. 4(a)]. The length of each condensate is comparable to the length of one segment studied in the relaxation dynamics discussed above for $N = 6$. At short times ($\sim$1 ms), we observe a phase defect in the center of the fringes, at the original position of the potential barrier [Fig. 4(b)]. With increasing time more phase defects appear and also start to propagate. After 5 ms the number of defects decays and we find an almost uniform distribution of their positions [26]. At long times (>100 ms) almost all defects have disappeared in agreement with the results displayed in Fig. 3.

We interpret the observed dynamics by the formation of dark solitons at the position of the potential barrier, whereby their shape depends on the random phase differences between neighboring condensates [27–29]. Subsequently, the generated excitations propagate, interact with each other, and eventually decay [29,30] to form a steady state with a smoothened phase profile [Figs. 3(b) and 3(c)]. Note, that the lifetime of solitonic excitations is typically short for 3D systems but can be strongly enhanced in low-dimensional geometries [31–33]. The propagation speed of dark solitons depends on their depth and is at maximum equal to the speed of sound c_0, which is compatible with the observed relaxation time scales. The round-trip time at c_0 in the ring trap is about 90 ms for the configuration studied in Fig. 2.

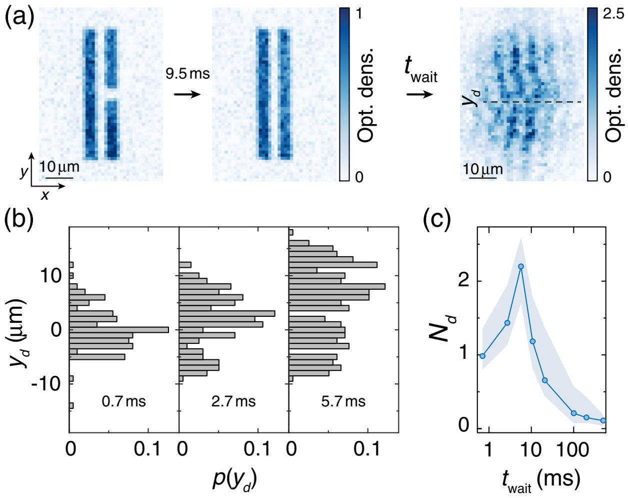

FIG. 4. Defect dynamics. (a) *In situ* density distribution of two line-shaped condensates (first two images) with dimensions 50 μm × 5 μm before and after the merging (averaged over four individual realizations). The condensates are separated by 3 μm. After merging the condensates in 9.5 ms the system evolves for a variable time t_{wait}. Phase defects are detected by matter-wave interference after TOF (image on the right) [16]. A typical image for $t_{\mathrm{wait}} = 0.7$ ms is depicted on the right. The phase defect at position y_d is highlighted by the dashed line. (b) Position distribution $p(y_d)$ of the phase defects as a function of the waiting time t_{wait} evaluated from 200 individual measurements. The histograms are normalized by the total number of measurements. Phase dislocations are detected, if the phase difference between neighboring pixels (corresponds to 1.16 μm in the atomic plane) is larger than 0.3π [16]. (c) Mean number of phase defects N_d as a function of time. The data were evaluated using a threshold of 0.3π. The shaded area illustrates the sensitivity due to this analysis (upper bound: 0.16π; lower bound: 0.43π).

In conclusion, we have reported the first quantitative study of the $\sqrt{N}$ scaling as predicted by the geodesic rule and show that the underlying relaxation dynamics is consistent with the formation of solitonlike defects. Future experiments could benefit from phase-imprinting techniques [27–29] to study the dynamics in a fully deterministic manner. In particular, it would be interesting to study the dynamics as a function of temperature and geometry.

We thank W. D. Phillips and S. Stringari for insightful discussions. This work was supported by DIM NanoK and

ERC (Synergy UQUAM). This project has received funding from the European Union's Horizon 2020 research and innovation program under the Marie Sklodowska-Curie Grant Agreement No. 703926.

[1] J. Eisert, M. Friesdorf, and C. Gogolin, Quantum many-body systems out of equilibrium, Nat. Phys. **11**, 124 (2015).

[2] T. Langen, T. Gasenzer, and J. Schmiedmayer, Prethermalization and universal dynamics in near-integrable quantum systems, J. Stat. Mech. (2016), P064009 (2016).

[3] R. Nandkishore and D. A. Huse, Many-body localization and thermalization in quantum statistical mechanics, Annu. Rev. Condens. Matter Phys. **6**, 15 (2015).

[4] T. Kibble, Phase-transition dynamics in the lab and the universe, Phys. Today **60**, 47 (2007).

[5] A. Del Campo and W. H. Zurek, Universality of phase transition dynamics: Topological defects from symmetry breaking, Int. J. Mod. Phys. B **29**, 1430018 (2014).

[6] W. H. Zurek, Cosmological experiments in superfluid helium?, Nature (London) **317**, 505 (1985).

[7] R. Carmi, E. Polturak, and G. Koren, Observation of Spontaneous Flux Generation in a Multi-Josephson-Junction Loop, Phys. Rev. Lett. **84**, 4966 (2000).

[8] R. Monaco, J. Mygind, and R. J. Rivers, Zurek-Kibble Domain Structures: The Dynamics of Spontaneous Vortex Formation in Annular Josephson Tunnel Junctions, Phys. Rev. Lett. **89**, 080603 (2002).

[9] R. Monaco, J. Mygind, R. J. Rivers, and V. P. Koshelets, Spontaneous fluxoid formation in superconducting loops, Phys. Rev. B **80**, 180501 (2009).

[10] L. Corman, L. Chomaz, T. Bienaimé, R. Desbuquois, C. Weitenberg, S. Nascimbène, J. Dalibard, and J. Beugnon, Quench-Induced Supercurrents in an Annular Bose Gas, Phys. Rev. Lett. **113**, 135302 (2014).

[11] S. Eckel, F. Jendrzejewski, A. Kumar, C. J. Lobb, and G. K. Campbell, Interferometric Measurement of the Current-Phase Relationship of a Superfluid Weak Link, Phys. Rev. X **4**, 031052 (2014).

[12] G. B. Jo, J. H. Choi, C. A. Christensen, T. A. Pasquini, Y. R. Lee, W. Ketterle, and D. E. Pritchard, Phase-Sensitive Recombination of Two Bose-Einstein Condensates on an Atom Chip, Phys. Rev. Lett. **98**, 180401 (2007).

[13] D. R. Scherer, C. N. Weiler, T. W. Neely, and B. P. Anderson, Vortex Formation by Merging of Multiple Trapped Bose-Einstein Condensates, Phys. Rev. Lett. **98**, 110402 (2007).

[14] V. Schweikhard, S. Tung, and E. A. Cornell, Vortex Proliferation in the Berezinskii-Kosterlitz-Thouless Regime on a Two-Dimensional Lattice of Bose-Einstein Condensates, Phys. Rev. Lett. **99**, 030401 (2007).

[15] J. L. Ville, T. Bienaimé, R. Saint-Jalm, L. Corman, M. Aidelsburger, L. Chomaz, K. Kleinlein, D. Perconte, S. Nascimbène, J. Dalibard *et al.*, Loading and compression of a single two-dimensional Bose gas in an optical accordion, Phys. Rev. A **95**, 013632 (2017).

[16] See Supplemental Material at http://link.aps.org/supplemental/10.1103/PhysRevLett.119.190403, which includes Ref. [17], for a detailed description of the experimental sequence, calibration measurements for the phase reference of the inner ring, measurements on the random phase difference between neighboring condensates, lifetime measurements of the supercurrents, mean values $\bar{\nu}$ of the distribution for the data depicted in Fig. 3, and details about the experimental sequence and data analysis for the results displayed in Fig. 4.

[17] R. T. Bailey, Estimation from Zero-Failure Data, Risk Analysis **17**, 375 (1997).

[18] According to the Mermin-Wagner theorem there is no true long-range order in low-dimensional systems; however, for our experimental parameters the characteristic correlation length exceeds the size of the condensate by several orders of magnitude, which enables the formation of a Bose-Einstein condensate.

[19] J. J. Chang, P. Engels, and M. A. Hoefer, Formation of Dispersive Shock Waves by Merging and Splitting Bose-Einstein Condensates, Phys. Rev. Lett. **101**, 170404 (2008).

[20] R. Meppelink, S. B. Koller, J. M. Vogels, P. van der Straten, E. D. van Ooijen, N. R. Heckenberg, H. Rubinsztein-Dunlop, S. A. Haine, and M. J. Davis, Observation of shock waves in a large Bose-Einstein condensate, Phys. Rev. A **80**, 043606 (2009).

[21] T. W. B. Kibble and A. Vilenkin, Phase equilibration in bubble collisions, Phys. Rev. D **52**, 679 (1995).

[22] S. Rudaz, A. M. Srivastava, and S. Varma, Probing gauge string formation in a superconducting phase transition, Int. J. Mod. Phys. B **14**, 1591 (1999).

[23] M. Bowick, L. Chandar, E. A. Schiff, and A. M. Srivastava, The cosmological kibble mechanism in the laboratory: string formation in liquid crystals, Science **263**, 943 (1994).

[24] S. Janson, Euler-Frobenius numbers and rounding, Online J. Anal. Comb. **8** (2013).

[25] A. Ramanathan, K. C. Wright, S. R. Muniz, M. Zelan, W. T. Hill III, C. J. Lobb, K. Helmerson, W. D. Phillips, and G. K. Campbell, Superflow in a Toroidal Bose-Einstein Condensate: An Atom Circuit with a Tunable Weak Link, Phys. Rev. Lett. **106**, 130401 (2011).

[26] The asymmetry in the position distribution of the phase defects [third panel of Fig. 4(b)] is due to a bias in the contrast of the interference fringes.

[27] S. Burger, K. Bongs, S. Dettmer, W. Ertmer, K. Sengstock, A. Sanpera, G. V. Shlyapnikov, and M. Lewenstein, Dark Solitons in Bose-Einstein Condensates, Phys. Rev. Lett. **83**, 5198 (1999).

[28] J. Denschlag, J. E. Simsarian, D. L. Feder, C. W. Clark, L. A. Collins, J. Cubizolles, L. Deng, E. W. Hagley, K. Helmerson, W. P. Reinhardt *et al.*, Generating solitons by phase engineering of a Bose-Einstein condensate, Science **287**, 97 (2000).

[29] C. Becker, S. Stellmer, P. Soltan-Panahi, S. Dörscher, M. Baumert, E.-M. Richter, J. Kronjäger, K. Bongs, and K. Sengstock, Oscillations and interactions of dark and dark–bright solitons in Bose–Einstein condensates, Nat. Phys. **4**, 496 (2008).

[30] E. A. Kuznetsov and S. K. Turitsyn, Instability and collapse of solitons in media with a defocusing nonlinearity, Sov. Phys. JETP **67**, 1583 (1988).

[31] C. Becker, K. Sengstock, P. Schmelcher, P. G. Kevrekidis, and R. Carretero-González, Inelastic collisions of solitary waves in anisotropic Bose–Einstein condensates: sling-shot events and expanding collision bubbles, New J. Phys. **15**, 113028 (2013).

[32] G. Lamporesi, S. Donadello, S. Serafini, F. Dalfovo, and G. Ferrari, Spontaneous creation of Kibble–Zurek solitons in a Bose–Einstein condensate, Nat. Phys. **9**, 656 (2013).

[33] S. Donadello, S. Serafini, T. Bienaimé, F. Dalfovo, G. Lamporesi, and G. Ferrari, Creation and counting of defects in a temperature-quenched Bose-Einstein condensate, Phys. Rev. A **94**, 023628 (2016).

PHYSICAL REVIEW A **96**, 053629 (2017)

Transmission of near-resonant light through a dense slab of cold atoms

L. Corman,[*] J. L. Ville, R. Saint-Jalm, M. Aidelsburger,[†] T. Bienaimé, S. Nascimbène, J. Dalibard, and J. Beugnon[‡]
Laboratoire Kastler Brossel, Collège de France, CNRS, ENS-PSL Research University, UPMC-Sorbonne Universités,
11 place Marcelin-Berthelot, 75005 Paris, France

(Received 30 June 2017; revised manuscript received 4 October 2017; published 27 November 2017)

The optical properties of randomly positioned, resonant scatterers is a fundamentally difficult problem to address across a wide range of densities and geometries. We investigate it experimentally using a dense cloud of rubidium atoms probed with near-resonant light. The atoms are confined in a slab geometry with a subwavelength thickness. We probe the optical response of the cloud as its density and hence the strength of the light-induced dipole-dipole interactions are increased. We also describe a theoretical study based on a coupled dipole simulation which is further complemented by a perturbative approach. This model reproduces qualitatively the experimental observation of a saturation of the optical depth, a broadening of the transition, and a blueshift of the resonance.

DOI: 10.1103/PhysRevA.96.053629

I. INTRODUCTION

The interaction of light with matter is a fundamental problem which is relevant for simple systems, such as an atom strongly coupled to photons [1–3], as well as for complex materials, whose optical properties provide information on their electronic structure and geometry [4]. This interaction can also be harnessed to create materials and devices with tailored properties, from quantum information systems such as memories [5] and nanophotonic optical isolators [6] to solar cells combining highly absorptive materials with transparent electrodes [7].

The slab geometry is especially appropriate to study light-matter interaction [8,9]. In the limit of a monolayer, two-dimensional (2D) materials exhibit fascinating optical properties. For simple direct band gap 2D semiconductors, the single-particle band structure implies that the transmission coefficient takes a universal value [10,11]. This was first measured for single-layer graphene samples [12], which have an optical transmission independent of the light frequency in the eV range, $|\mathcal{T}|^2 = 1 - \pi\alpha$, where α is the fine-structure constant [13,14]. The same value was recovered in InAs semiconductors [15]. This universality does not hold for more complex 2D materials, for instance when the Coulomb interaction plays a more important role [16].

Atomic gases represent in many respects an ideal test bed for investigating light-matter interaction. First, they can be arranged in regular arrays [17,18] or randomly placed [19] to tailor the optical properties of the system. Second, an atom always scatters light, in contrast with solid-state materials where the optical excitation can be absorbed and dissipated in a nonradiative way. Even for thin and much more dilute samples than solid-state systems, strong attenuation of the transmission can be observed at resonance. Third, inhomogeneous Doppler broadening can be made negligible using ultracold atomic clouds. Finally, the geometry and the density of the gases can be varied over a broad range.

In the dilute limit, such that the three-dimensional (3D) atomic density ρ and the light wave number k verify $\rho k^{-3} \ll 1$, and for low optical depths, a photon entering the atomic medium does not recurrently interact with the same atom. Then, for a two-level atom, the transmission of a resonant probe beam propagating along the z axis is given by the Beer-Lambert law: $|\mathcal{T}|^2 = e^{-\sigma_0 \int \rho\, dz}$, where $\sigma_0 = 6\pi k^{-2}$ is the light cross section at the optical resonance [20]. At larger densities the transmission is strongly affected by the light-induced dipole-dipole coupling between neighboring atoms.

Modification of the atomic resonance line shape or super- and subradiance in dilute (but usually optically dense) and cold atomic samples have been largely investigated experimentally [21–30]. Recently, experiments have been performed in the dense regime studying nanometer-thick hot vapors [31] and mesoscopic cold clouds [32–35]. Interestingly, it has been found that the mean-field Lorentz-Lorenz shift is absent in cold systems where the scatterers remain fixed during the measurement. A small redshift is still observed for dense clouds in Refs. [32,34] but could be specific to the geometry of the system.

Achieving large densities is concomitant with a vanishingly small transmission $\mathcal{T}$. It is therefore desirable to switch to a 2D or thin slab geometry in order to investigate the physical consequences of these resonant interaction effects at the macroscopic level. Using a 2D geometry also raises a fundamental question inspired by the monolayer semiconductor case: can the light extinction through a plane of randomly positioned atoms be made arbitrarily large when increasing the atom density or does it remain finite, potentially introducing a maximum of light extinction through 2D random atomic samples independent of the atomic species of identical electronic spin?

In this article, we study the transmission of nearly resonant light through uniform slabs of atoms. We report experiments realized on a dense layer of atoms with a tunable density and thickness. For dense clouds, the transmission is strongly enhanced compared to the one expected from the single-atom

---

[*] Also at Institute for Quantum Electronics, ETH Zurich, 8093 Zurich, Switzerland.

[†] Also at Fakultät für Physik, Ludwig-Maximilians-Universität München, Schellingstr. 4, 80799 Munich, Germany.

[‡] beugnon@lkb.ens.fr

response. We also observe a broadening and a blueshift of the resonance line on the order of the natural linewidth. This blueshift contrasts with the mean-field Lorentz-Lorenz redshift and is a signature of the stronglycorrelated regime reached in our system because of dipole-dipole interactions [36]. In addition, we observe deviations of the resonance line shape from the single-atom Lorentzian behavior, especially in the wings where the transmission decays more slowly. We model this system with coupled dipole simulations complemented by a perturbative approach which qualitatively supports our observations. After describing our experimental system in Sec. II, we investigate theoretically light scattering for the geometry explored in the experiment in Sec. III. In Sec. IV we present our experimental results and compare them with theory. We conclude in Sec. V.

II. EXPERIMENTAL METHODS

A. Cloud preparation

We prepare a cloud of ^{87}Rb atoms with typically $N = 1.3(2) \times 10^5$ atoms in the $|F = 1, m_F = -1\rangle$ state. The atoms are confined in an all-optical trap, described in more detail in [37], with a strong harmonic confinement in the vertical direction z with frequency $\omega_z/2\pi = 2.3(2)$ kHz leading to a Gaussian density profile along this direction. The transverse confinement along the x and y directions is produced by a flat-bottom disk-shaped potential of diameter $2R = 40\ \mu$m. For our initial cloud temperature $\simeq$300 nK, there is no extended phase coherence in the cloud [38]. Taking into account this finite temperature, we compute for an ideal Bose gas a rms thickness $\Delta z = 0.25(1)\ \mu$m, or equivalently $k\Delta z = 2.0(1)$. This situation corresponds to $nk^{-2} \approx 1.5$, where $n = N/(\pi R^2)$ is the surface density and to a maximum density $\rho k^{-3} \approx 0.3$ at the trap center along z where ρ is the volume density. We tune the number of atoms that interact with light by partially transferring them to the $|F = 2, m_F = -2\rangle$ state using a resonant microwave transition. Atoms in this state are sensitive to the probe excitation, contrary to the ones in the $|F = 1, m_F = -1\rangle$ state. In this temperature range the Doppler broadening is about three orders of magnitude smaller than the natural linewidth of the atomic transition.

The cloud thickness is varied in a controlled way using mainly the following two techniques. (i) Varying the vertical harmonic confinement by modifying the laser power in the blue-detuned lattice that traps the atoms, thus changing its frequency from $\omega_z/2\pi = 1.1(2)$ kHz to $\omega_z/2\pi = 2.3(2)$ kHz. Using the ideal Bose gas statistics in the tight harmonic trap, for a gas of $N = 1.3(2) \times 10^5$ atoms at a temperature of $T \simeq 300$ nK, this corresponds to rms thicknesses between 0.3 μm and 0.6 μm. (ii) Allowing the atoms to expand for a short time after all traps have been switched off. The extent of the gas in the xy direction does not vary significantly during the time of flight (duration between 0.7 ms and 4.7 ms). In that case, the rms thickness varies between 3 μm and 25 μm. For the densest clouds, the thickness is also influenced by the measurement itself. Indeed, the light-induced dipole-dipole forces between atoms lead to an increase of the size of the cloud during the probing. In the densest case, we estimate from measurements of the velocity distribution after an excitation with a duration of $\tau = 10\ \mu$s that the thickness averaged over the pulse duration is increased by $\sim$20%. In some experiments, in which the signal is large enough, we limit this effect by reducing the probe duration τ to 3 μs.

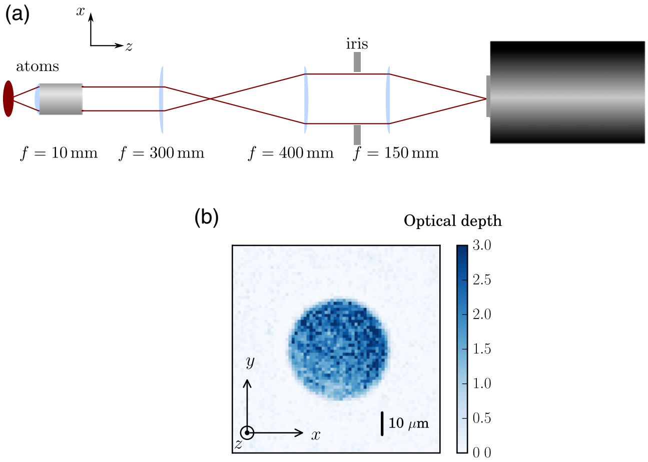

FIG. 1. (a) Schematic representation of the imaging setup. The atoms are confined by a single, disk-shaped potential which is imaged using a microscope objective onto a back-illuminated CCD camera. The numerical aperture of the system is limited to $\approx$0.2 using an iris in the Fourier plane of the atoms to limit the collected fluorescence light. (b) Typical *in situ* image obtained on a back illuminated CCD camera of the in-plane density distribution averaged over three individual measurements. For this example, the atom surface density is $n = 25\ \mu\text{m}^{-2}$. We extract a region of interest with uniform density for our analysis with a typical area of 200 μm^2.

B. Transmission measurement

We probe the response of the cloud by measuring the transmission of a laser beam propagating along the z direction (See Fig. 1). The light is linearly polarized along the x axis and tuned close to the $|F = 2\rangle \rightarrow |F' = 3\rangle$ D_2 transition. The duration of the light pulse is fixed to 10 μs for most experiments and we limit the imaging intensity I to the weakly saturating regime with $0.075 < I/I_{\text{sat}} < 0.2$, where $I_{\text{sat}} \simeq 1.67$ mW/cm^2 is the resonant saturation intensity. We define $\Delta\nu$ as the detuning of the laser beam with respect to the single-atom resonance. The cloud intensity transmission $|\mathcal{T}|^2$ is extracted by comparing images with and without atoms and we compute the optical depth $D = -\ln|\mathcal{T}|^2$ (see Sec. II C). The numerical aperture of the optical system is limited on purpose to minimize the collection of fluorescence light from directions different from the propagation direction of the light beam.

C. Computation of the optical depth

We extract the optical depth (D) of the clouds by comparing pictures with and without atoms. The readout noise on the count number N_{count} is $dN_{\text{count}} \sim 5$ per pixel. We subtract from these images equivalent pictures without any imaging pulse to remove the background counts and obtain two pictures M_{with} and M_{without}. The typical noise on the count number per pixel is thus $dN = \sqrt{2}\,dN_{\text{count}} \sim 7$.

The magnification of the optical system is 11.25, leading to an effective pixel size in the plane of the atoms of 1.16 μm. The typical mean number of counts per pixel accumulated during the 10 μs imaging pulse is 80 on the picture without atoms. We optimize the signal-to-noise ratio by summing all the pixels in the region of interest for M_{with} and M_{without}. This yields a total count number in the picture with atoms N_{with} and without atoms N_{without} from which we compute the optical depth: $D = -\ln(N_{\text{with}}/N_{\text{without}})$. The region of interest varies with the time of flight of the cloud. This region is a disk that ensures that we consider a part of the cloud with approximately constant density (with 15% rms fluctuations), comprising typically 200 pixels. With these imaging parameters we can reliably measure optical depths up to 4 but we conservatively fit only data for which $D < 3$. At low densities, the statistical error on D due to the readout noise is about 0.01. At $D \sim 3$, it reaches 0.12.

D. Atom number calibration

As demonstrated in this article, dipole-dipole interactions strongly modify the response of the atomic cloud to resonant light and make an atom number calibration difficult. In this work, we measure the atom number with absorption imaging for different amounts of atoms transferred by a coherent microwave field from the $|F = 1, m_F = -1\rangle$ "dark" state to the $|F = 2, m_F = -2\rangle$ state in which the atoms are resonant with the linearly polarized probe light. We perform resonant Rabi oscillations for this coherent transfer and fit the measured atom number as a function of time by a sinus square function. We select points with an optical depth below 1, to limit the influence of dipole-dipole interactions. This corresponds to small microwave pulse area or to an area close to a 2π pulse, to make the fit more robust. From the measured optical depth D, we extract $nk^{-2} = (15/7)D/(6\pi)$. The factor 7/15 corresponds to the average of equally weighted squared Clebsch-Gordan coefficients for linearly polarized light resonant with the $F = 2$ to $F' = 3$ transition. This model does not take into account possible optical pumping effects that could lead to an unequal contribution from the different transitions and hence a systematic error on the determination of the atom number.

E. Experimental protocol

Our basic transmission measurements consist in scanning the detuning $\Delta\nu$ close to the $F = 2$ to $F' = 3$ resonance ($|\Delta\nu| < 30$ MHz) and in measuring the optical depth at a fixed density. The other hyperfine levels $F' = 2,1,0$ of the excited $5P_{3/2}$ level play a negligible role for this detuning range. The position of the single-atom resonance is independently calibrated using a dilute cloud. The precision on this calibration is of 0.03 Γ_0, where $\Gamma_0/2\pi = 6.1$ MHz is the atomic linewidth. The measured resonance curves are fitted with a Lorentzian function:

$$\Delta\nu \mapsto D_{\max}/[1 + 4(\Delta\nu - \nu_0)^2/\Gamma^2]. \tag{1}$$

This function captures well the central shape of the curve for thin gases, as seen in the examples of Fig. 2. When increasing the atomic density we observe a broadening of the line $\Gamma > \Gamma_0$, a nonlinear increase of the maximal optical depth $D_{\max}$, and a blueshift $\nu_0 > 0$. In Sec. IV we present the evolution of these fitted parameters for different densities and thicknesses. Note that in our analysis all points with values of D above 3 are discarded to avoid potential systematic errors. Whereas this threshold has little influence for thin clouds (as shown in Fig. 2) for which the maximal optical depths are not large compared to the threshold, for thick gases this typically removes the measurements at detunings smaller than $1.5\Gamma_0$. Hence, in this case, we consider the amplitude and the width of the fits to be not reliable and we use the position of the maximum of the resonance ν_0 with caution.

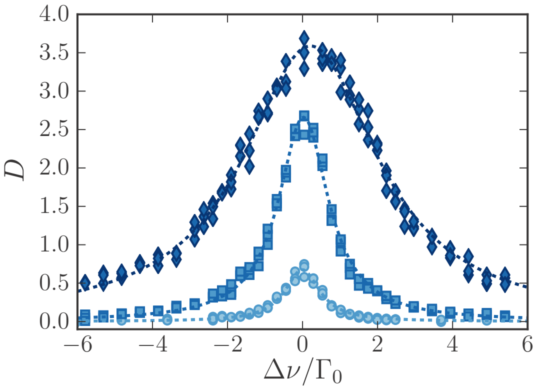

FIG. 2. Example of resonance curves. Symbols represent the experimental data and the corresponding dashed lines are Lorentzian fits. All curves are taken with the cloud thickness $k\Delta z = 2.4(6)$ and for surface densities of $nk^{-2} = 0.06(1)$ (circles), 0.38(6) (squares), and 1.5(2) (diamonds). The errors on the fitted parameters are determined using a basic bootstrap analysis, repeating the fitting procedure 100 times on a set of random points drawn from the original set of data, of the same length as this original set.

We investigate the dependence of the fit parameters $D_{\max}$, Γ, and ν_0 for different atomic clouds in Sec. IV. These results are compared to the prediction from a theoretical model that we describe in the following section.

III. THEORETICAL DESCRIPTION

Light scattering by a dense sample of emitters is a complex many-body problem and it is quite challenging to describe. The slab geometry is a textbook situation which has been largely explored. A recent detailed study of the slab geometry can be found in Ref. [39]. We focus in this section first on a perturbative approach which is valid for low enough densities. We then report coupled dipole simulations following the method presented in [19] but extended with a finite-size scaling approach to address the situation of large slabs. We also discuss the regime of validity for these two approaches.

A. Perturbative approach

We describe here a semianalytical model accounting for the multiple scattering of light by a dilute atom sample, inspired from Ref. [40]. By taking into account multiple scattering processes between atom pairs, it provides the first correction to the Beer-Lambert law when decreasing the mean distance l between nearest neighbors towards k^{-3}.

1. Index of refraction of a homogeneous system

In Ref. [40], the index of refraction of a homogeneous dilute atomic gas was calculated, taking into account the first nonlinear effects occurring when increasing the volume atom density. The small parameter governing the perturbative expansion is ρk^{-3}, where ρ is the atom density. At second order in ρk^{-3} two physical effects contribute to the refraction index, namely the effect of the quantum statistics of atoms on their position distribution and the dipole-dipole interactions occurring between nearby atoms after one photon absorption. Here we expect the effect of quantum statistics to remain small, and thus neglect it hereafter (see Ref. [41] for a recent measurement of this effect). Including the effect of multiple scattering processes between atom pairs, one obtains the following expression for the refractive index:

$$n_r = 1 + \frac{\alpha\rho}{1 - \alpha\rho/3 + \beta\rho}, \tag{2}$$

$$\beta = -\int d\mathbf{r}\left[\frac{\alpha^2\mathbf{G}'^2 + \alpha^3\mathbf{G}'^3 e^{-ikz}}{1 - \alpha^2\mathbf{G}'^2}\right]_{xx}(\mathbf{r}), \tag{3}$$

where we introduced the atom polarizability $\alpha = 6\pi i k^{-3}/(1 - 2i\delta/\Gamma)$ and the Green function $[\mathbf{G}]$ of an oscillating dipole,

$$\begin{aligned}\mathbf{G}_{\alpha\beta}(\mathbf{r}) &= -\frac{1}{3}\delta(\mathbf{r})\delta_{\alpha\beta} + \mathbf{G}'_{\alpha\beta}(\mathbf{r}),\\ \mathbf{G}'_{\alpha\beta}(\mathbf{r}) &= -\frac{k^3}{4\pi}\frac{e^{ikr}}{kr}\left[\left(1 + \frac{3i}{kr} - \frac{3}{(kr)^2}\right)\frac{r_\alpha r_\beta}{r^2}\right.\\ &\quad\left. - \left(1 + \frac{i}{kr} - \frac{1}{(kr)^2}\right)\delta_{\alpha\beta}\right],\end{aligned} \tag{4}$$

in which retardation effects are neglected [42]. Note that for a thermal atomic sample of Doppler width larger than Γ, we expect an averaging of the coherent term β to zero due to the random Doppler shifts. When setting $\beta = 0$ in Eq. (2) we recover the common Lorentz-Lorenz shift of the atomic resonance [43]. We plot in Fig. 3 the imaginary part of the index of refraction as a function of the detuning δ, for a typical atom density used in the experiment (solid line), and compare with the single-atom response with (dotted line) and without (dashed line) Lorentz-Lorenz correction. The resonance line is modified by dipole-dipole interactions and we observe a blueshift of the position of the maximum of the resonance [44].

2. Transmission through an infinite slab with a Gaussian density profile

In order to account more precisely for the light absorption occurring in the experiment, we extend the perturbative analysis of light scattering to inhomogeneous atom distributions, for which the notion of index of refraction may not be well defined. The atom distribution is modeled by an average density distribution $\rho(z)$ of infinite extent along x and y, and depending on z only, as $\rho(z) = \rho_0 \exp[-z^2/(2\Delta z^2)]$. We describe the propagation of light along z in the atomic sample. The incoming electric field is denoted as $E_0 e^{i(kz-\omega t)}\mathbf{e_x}$. The total electric field, written as $\mathbf{E}(z)e^{-i\omega t}$, is given by the sum of the incoming field and the field radiated by the excited atomic dipoles:

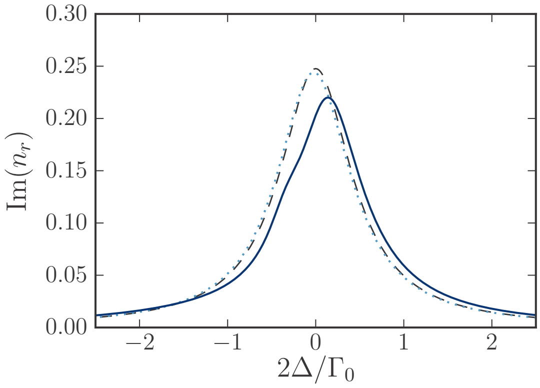

FIG. 3. Imaginary part of the index of refraction of a homogeneous atomic sample of density $\rho k^{-3} \simeq 0.026$. The three curves correspond to the absorption of independent atoms (dashed black line), to the resonance line taking into account the Lorentz-Lorenz correction (dotted blue line), and to the perturbative analysis discussed in the text (solid black line), which takes into account multiple scattering of photons between pairs of atoms [40].

$$\mathbf{E}(z) = E_0 e^{ikz}\mathbf{e_x} + \int d^3\mathbf{r}'\,\rho(z')\frac{[\mathbf{G}(\mathbf{r}-\mathbf{r}')]}{\epsilon_0}\mathbf{d}(z'), \tag{5}$$

where $\mathbf{d}(z)$ is the dipole amplitude of an atom located at z and ϵ_0 is the vacuum permittivity. The integral over x and y can be performed analytically, leading to the expression

$$\mathbf{E}(z) = E_0 e^{ikz}\mathbf{e_x} + \frac{ik}{2\epsilon_0}\int dz'\,\rho(z')e^{ik|z-z'|}\mathbf{d}_\perp(z'), \tag{6}$$

where $\mathbf{d}_\perp(z)$ is the dipole amplitude projected in the x,y plane.

The dipole amplitude can be calculated from the atom polarizability α and the electric field at the atom position. Taking into account multiple light scattering between atom pairs, we obtain a self-consistent expression for the dipole amplitude, valid up to first order in atom density, as $\mathbf{d}(z) = d(z)\mathbf{e_x}$, with

$$\begin{aligned}d(z) = \alpha\epsilon_0 E_0 e^{ikz} &+ \int d\mathbf{r}'\,\rho(z')\left\{\left[\frac{\alpha\mathbf{G}}{1-\alpha^2\mathbf{G}^2}\right]_{xx}(\mathbf{r}-\mathbf{r}')d(z')\right.\\ &\left. + \left[\frac{\alpha^2\mathbf{G}^2}{1-\alpha^2\mathbf{G}^2}\right]_{xx}(\mathbf{r}-\mathbf{r}')d(z)\right\}.\end{aligned} \tag{7}$$

Note that the dipole amplitude also features a component along z, but it would appear in the perturbative expansion in the atom density at higher orders.

The electric field and dipole amplitude are numerically computed by solving the linear system (6) and (7). The optical depth is then calculated as $D = -\ln(|E(z)|^2/|E_0|^2)$ for $z \gg \Delta z$. The results of this approach will be displayed and quantitatively compared to coupled dipole simulations in the next subsection.

B. Coupled dipole simulations

1. Methods

Our second approach to simulate the experiments follows the description in Ref. [19] and uses a coupled dipole model.

We consider atoms with a $J = 0$ to $J = 1$ transition. For a given surface density n and thickness Δz we draw the positions of the N atoms with a uniform distribution in the xy plane and a Gaussian distribution along the z direction. The number of atoms and hence the disk radius is varied to perform finite-size scaling. For a given detuning and a linear polarization along x of the incoming field, we compute the steady-state value of each dipole $\boldsymbol{d}_j$ which is induced by the sum of the contributions from the laser field and from all the other dipoles in the system. The second contribution is obtained thanks to the tensor Green function $\mathbf{G}$ giving the field radiated at position $\mathbf{r}$ by a dipole located at origin.

Practically, the values of the N dipoles are obtained by numerically solving a set of $3N$ linear equations, which limits the atom number to a few thousands, a much lower value than in the experiment (where we have up to 10^5 atoms). From the values of the dipoles we obtain the transmission $\mathcal{T}$ of the sample:

$$\mathcal{T} = 1 - \frac{i}{2}\sigma\frac{nk^{-2}}{N}\sum_j \frac{k^3}{6\pi\epsilon_0 E_L} d_{j,x} e^{-ikz_j}, \qquad (8)$$

where z_j is the vertical coordinate of the jth atom, E_L the incoming electric field, and $d_{j,x}$ is the x component of the dipole of the jth atom. From the transmission, we compute the optical depth $D = -\ln|\mathcal{T}|^2$ and fit the resonance line with a Lorentzian line shape to extract, as for the experimental results, the maximum, the position, and the width of the line.

As the number of atoms used in the simulations is limited, it is important to verify the result of the simulations is independent of the atom number. In this work, we are mostly interested in the response of an infinitely large system in the xy plane. It is indeed the situation considered in the perturbative approach and in the experimental system for which the diameter is larger than $300k^{-1}$ and where finite-size effects should be small. The atom number in the simulations is typically two orders of magnitude lower than in the experiment and finite-size effects could become important. For instance, some diffraction effects due to the sharp edge of the disk could play a role [39]. Consequently, we varied the atom number in the simulations and observed, for simulated clouds with small radii, a significant dependence of the simulation results on the atom number. We have developed a finite-size scaling approach to circumvent this limitation. We focus in the following on transmission measurements as in the experiment.

We show two examples of this finite-size scaling approach for $k\Delta z = 1.6$ in Fig. 4 and $k\Delta z = 80$ in Fig. 5. For low enough surface densities, the results of the simulations (maximal optical depth, width, shift, etc.) for different atom numbers in the simulation are aligned, when plotted as a function of $1/\sqrt{N_{\text{sim}}}$, and allow for the desired finite-size scaling. All the results presented in this section and in Sec. IV [45] are obtained by taking the extrapolation to an infinite system size, which corresponds to the offset of the linear fit in Figs. 4 and 5.

Interestingly, we observe in Fig. 4 for a thin cloud that considering a finite-size system only leads to a small underestimate of the blueshift of the resonance. However, for thicker slabs, such as in Fig. 5, we get, for finite systems, a small redshift and a narrowing of the line. Considering our experimental system, we have $1/\sqrt{N} \approx 0.003$, leading to a small correction according to the fits in Fig. 5. However, for such thick systems we are able to simulate only systems with low nk^{-2}, typically 0.1, whereas we can reach densities 15 times larger in the experiment, which could enhance finite-size effects. Simulation of thick and optically dense slabs is thus challenging and the crossover between the thin slab situation explored in this article and the thick regime is an interesting perspective of this work.

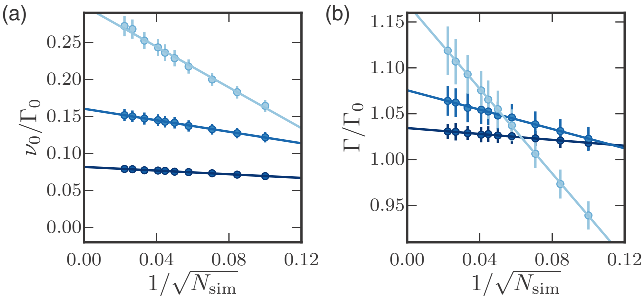

FIG. 4. Example of finite-size scaling to determine (a) the position of the maximum of the resonance and (b) the width of the resonance. Here $k\Delta z = 1.6$ and (from bottom to top) $nk^{-2} = 0.05$, 0.11, and 0.21. Simulations are repeated for different atom number N_{sim}. The number of averages ranges from 75 (left points, $N_{\text{sim}} = 2000$) to 25 000 (right points, $N_{\text{sim}} = 100$). When plotting the shift as a function of $1/\sqrt{N_{\text{sim}}} \propto 1/R$, and for low enough densities, data points are aligned and allow for a finite-size scaling. Vertical error bars represent the standard error obtained when averaging the results over many random atomic distributions.

2. *Role of the thickness and density of the cloud*

We now investigate the results of coupled dipole simulations for different densities and thicknesses of the atomic cloud. We limit the study to low densities, for which the finite-size scaling approach works. It is important to note that the computed line shapes deviate significantly from a Lorentzian shape and become asymmetric. Consequently

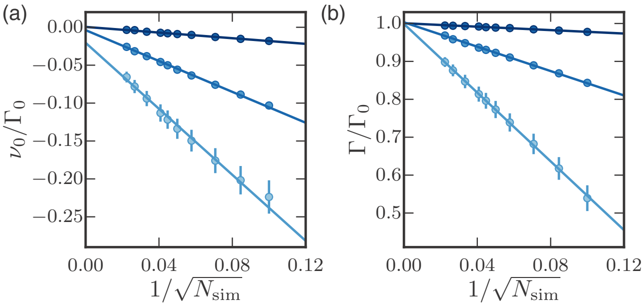

FIG. 5. Example of finite-size scaling to determine (a) the position of the maximum of the resonance ν_0 and (b) the width Γ of the resonance. Here, $k\Delta z = 80$ and (from top to bottom) $nk^{-2} = 0.027$, 0.08, and 0.13. Simulations are repeated for different atom number N_{sim}. The number of averages ranges from 75 (left points, $N_{\text{sim}} = 2000$) to 25 000 (right points, $N_{\text{sim}} = 100$). Vertical error bars represent the standard error obtained when averaging the result over many random atomic distributions.

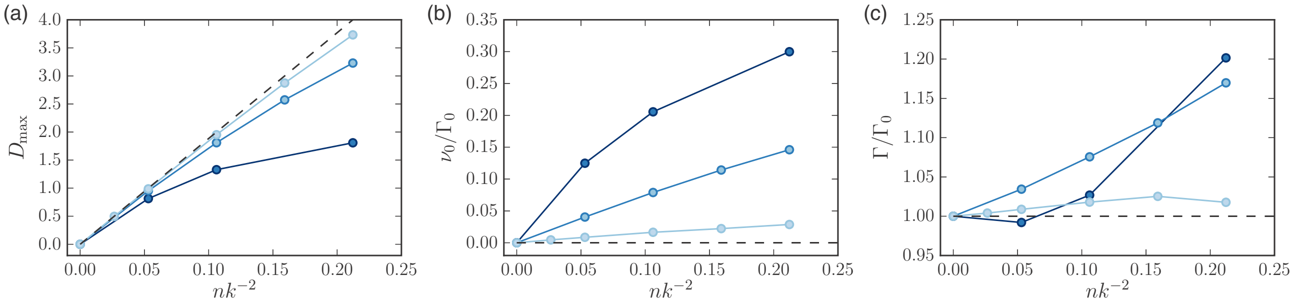

FIG. 6. Coupled dipole simulations for different thicknesses. (a) Maximal optical depth; (b) position of the maximum of the line; (c) width of the resonance line. We report results for $k\Delta z = 0$, 1.6, and 8, the darkest lines corresponding to the smallest thicknesses. The black dashed lines correspond to the single-atom response.

there is not a unique definition for the center of the line and for its width. In our analysis, we fit the resonance lines around their maximum with a typical range of $\pm 0.5\,\Gamma$. The shift thus corresponds to a variation of the position of the maximum of the line and the "width" characterizes the curvature of the line around its maximum. The results of these fits are reported in Fig. 6 as a function of surface density for different thicknesses. In these plots, we observe the same features as qualitatively described in Sec. II: a decrease of the maximal optical depth with respect to the single-atom response [Fig. 6(a)], a blueshift of the position of the maximum [Fig. 6(b)], and a broadening of the line [Fig. 6(c)]. For a fixed thickness, these effects increase with surface density and for a fixed surface density they are more pronounced for lower thicknesses. Note that we only explore here surface densities lower than 0.25 which is quite lower than the maximum experimental value ($\sim$1.5). Whereas our finite-size scaling approach can be well extended for very thin systems ($k\Delta z < 1$) it fails for thick and optically dense systems [46].

3. Comparison with the perturbative model

The perturbative approach is limited to low densities $\rho k^{-3} \ll 1$ but it gives the response of an infinitely expanded cloud in the transverse direction. Coupled dipole simulations can in principle address arbitrarily large densities but the number of atoms considered in a simulation is limited, and thus for a given density the size of the system is limited. Coupled dipole simulations are thus more relevant for thin and dense samples and the perturbative approach more suited for nonzero thickness samples.

In Fig. 7 we choose two illustrative examples to confirm, in the regime where both models could be used, that these two approaches are in quantitative agreement. In Fig. 7(a) we compare the maximum optical depth as a function of surface density for three different thicknesses. The perturbative approach is typically valid, for this set of thicknesses, up to $nk^{-2} \sim 0.1$. We investigate the shift of the position of the maximum in Fig. 7(b). We report, as a function of the inverse thickness ($1/k\Delta z$), the slope γ of the shift with density, $\nu_0 = \gamma nk^{-2}$, computed for surface densities below 0.1. The dotted line is the result from the perturbative approach, the solid line corresponds to coupled dipole simulations, and the dash-dotted line to the result for zero thickness. The perturbative approach approximates well coupled dipole simulations. This result also confirms that the finite-size scaling approach provides a good determination of the response of an infinite system in the xy direction.

We have identified in this section the specific features of the transmission of light through a dense slab of atoms. We focus here on the transmission coefficient to show that we

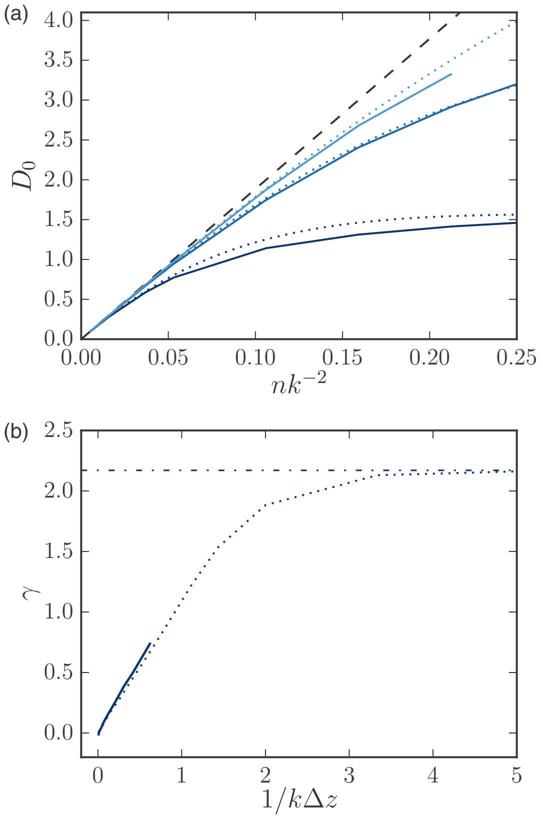

FIG. 7. Comparison between the coupled dipole simulations and the perturbative model. (a) Behavior of the optical depth at the single-atom resonance D_0 with surface density for different thicknesses ($k\Delta z = 0$, 1.6, and 3.2, from bottom to top). Coupled dipole simulations are shown as solid lines, perturbative approach as dotted lines, and the dashed line is the Beer-Lambert prediction. (b) Slope γ of the blueshift $\nu_0 = \gamma nk^{-2}$ as a function of the inverse thickness $1/k\Delta z$. The solid line is the result of the coupled dipole model, the dash-dotted line is the zero-thickness coupled dipole result ($1/k\Delta z \to \infty$), and the dotted line is the perturbative model.

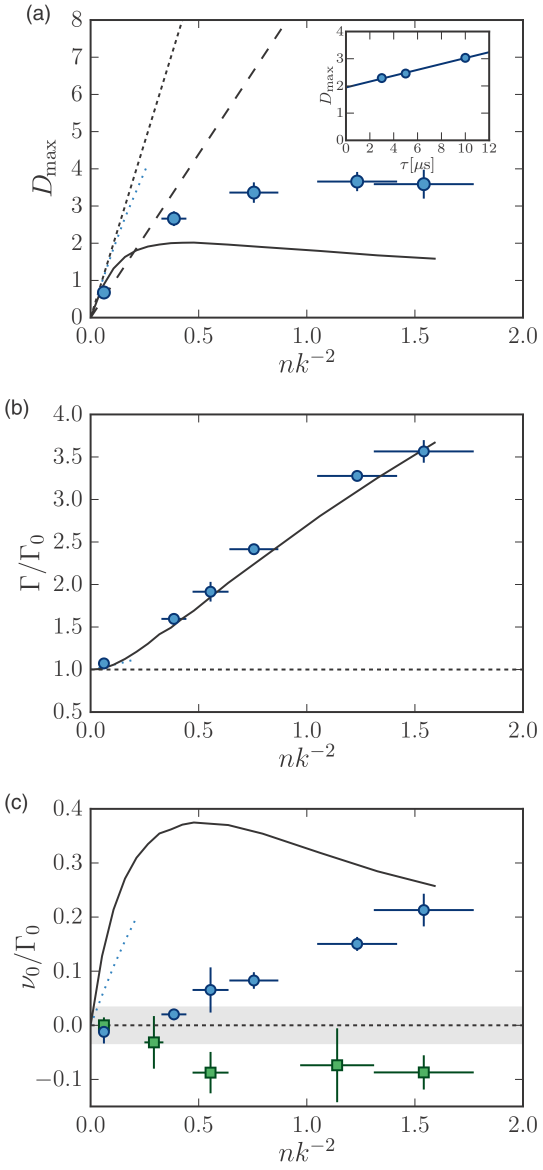

FIG. 8. Maximum optical depth (a), broadening (b), and frequency shift (c) of the resonance line for our thinnest samples with $k\Delta z = 2.4(6)$ (circles) and for thicker samples with $k\Delta z = 30(8)$ (squares). In (a) the shaded area represents the uncertainty in the frequency calibration of the single-atom resonance. In (a) and (b), the dark black solid (light blue dotted) line is the prediction of the coupled dipole model for $k\Delta z = 0$ ($k\Delta z = 2.4$) in its accessible range of densities. The dashed lines represent the single-atom response.

observe the same features in the experiment and we will make a quantitative comparison between our experimental findings and the results obtained with coupled dipole simulations. Our theoretical analysis is complemented by a study of the reflection coefficient of a strictly 2D gas detailed in Appendix.

IV. EXPERIMENTAL RESULTS

We show in Fig. 8 the results of the experiments introduced in Sec. II. The fitted $D_{\max}$ for different surface densities is shown in Fig. 8(a). We compare these results to the Beer-Lambert prediction (narrow dashes) $D_{\rm BL} = n\sigma_0$ and to the same prediction corrected by a factor 7/15 (large dashes). This factor is the average of the Clebsch-Gordan coefficients relevant for π-polarized light tuned close to the $|F = 2\rangle \to |F' = 3\rangle$ transition and, as discussed previously, it is included in the calibration of the atom number. At large surface densities, we observe an important deviation from this corrected Beer-Lambert prediction: we measure that $D_{\max}$ seems to saturate around $D_{\max} \approx 3.5$, whereas $D_{\rm BL} \approx 13$ [47]. We also show the prediction of the coupled dipole model, as a solid line for the full range of surface densities at $k\Delta z = 0$ and as a dotted line for the numerically accessible range of surface densities at $k\Delta z = 2.4$. The coupled dipole simulation at $k\Delta z = 0$ shows the same trend as in the experiment but with $D_{\max}$ now bounded by 2. A reason could be the nonzero thickness of the atomic slab. In order to test this hypothesis, we investigated the influence of probing duration for the largest density. For such a density we could decrease the pulse duration while keeping a good enough signal-to-noise ratio [see inset in Fig. 2(b)]. For a shorter probing duration, hence for a smaller expansion of the cloud, $D_{\max}$ decreases, in qualitative agreement with the expected effect of the finite thickness.

The saturation of the optical depth with density is a counterintuitive feature. It shows that increasing the surface density of an atomic layer does not lead to an increase of its optical depth. Coupled dipole simulations at $k\Delta z = 0$ even show that the system becomes slightly more transparent as the surface density is increased. This behavior may be explained qualitatively by the broadening of the distribution of resonance frequencies of the eigenmodes of this many-body system. A dense system scatters light for a large range of detunings but the cross section at a given detuning saturates or becomes lower as the surface density is increased.

We display in Fig. 8(b) the width Γ of the Lorentzian fits for $k\Delta z = 2.4(6)$ along with coupled dipole simulation results [46]. We observe a broadening of the resonance line up to more than $3\Gamma_0$. This broadening is confirmed by the simulation results for $k\Delta z = 0$ (solid line). Note that the exact agreement with the experimental data should be considered as coincidental. The range on which we can compute the broadening for $k\Delta z = 2.4$ (light dotted line) is too small to discuss a possible agreement.

We show in Fig. 8(c) the evolution of ν_0 with density. A blueshift, reaching $0.2\Gamma_0$ for the largest density, is observed. At the largest density, an even larger shift is observed when decreasing the pulse duration ($\approx 0.4\Gamma_0$, not shown here). We also display the result of the coupled dipole model for the cases $k\Delta z = 2.4$ and $k\Delta z = 0$. Both simulations confirm the blueshift but predict a different behavior and a larger effect. In addition, we show the variation of ν_0 for a thick cloud with $k\Delta z = 30(8)$. In that case we observe a marginally significant redshift [48].

The experimental observation of a blueshift is in stark contrast, both in amplitude and in sign, with the mean-field prediction of the Lorentz-Lorenz redshift $\nu_0^{\rm MF}/\Gamma_0 = -\pi\rho k^{-3} = -\sqrt{\pi/2}\, nk^{-2}/(k\Delta z)$, written here at the center of the cloud along z. The failure of the Lorentz-Lorenz prediction for cold atom systems has already been observed and discussed for instance in Refs. [30,34,36]. As discussed with the perturbative approach in Sec. III, the Lorentz-Lorenz contribution is still present but it is (over)compensated by multiple scattering effects for a set of fixed scatterers. In hot vapors, where the Doppler effect is large, the contribution of multiple scattering vanishes and thus the Lorentz-Lorenz contribution alone is observed. The related cooperative Lamb shift has been recently demonstrated in hot vapor of atoms confined in a thin slab in Ref. [31]. In the cold regime where scatterers are fixed, such effects are not expected [39]. However, in these recent studies with dense and cold samples a small redshift is still observed [30,34,36]. This difference on the sign of the frequency shift with respect to the results obtained in this work may be explained by residual inhomogeneous broadening induced by the finite temperature or the diluteness of the sample in Ref. [30] and by the specific geometry in Ref. [34], where the size of the atomic cloud is comparable to λ and where diffraction effects may play an important role. As discussed in Sec. III, our observation of a blueshift is a general result which applies to the infinite slab. It is robust to a wide range of thicknesses and density, and while we computed it theoretically for a two-level system, it also shows up experimentally in a more complex atomic level structure. It was also predicted in Ref. [39] but for a uniform distribution along the z axis instead of the Gaussian profile considered in this work, and also discussed in [44]. Consequently, we believe that it is an important and generic feature of light scattering in a extended cloud of fixed randomly distributed scatterers.

Finally, we compare the line shape of the resonance with the Lorentzian shape expected for a single atom. We measure for $nk^{-2} = 1.5(2)$, the optical depth at large detunings, and for various cloud thicknesses. We fit it with a power law on the red-detuned (blue-detuned) frequency interval with exponent η_r (η_b) as shown, for two examples, in Fig. 9(a). If the behavior were indeed Lorentzian, the exponents should be -2 in the limit of large detuning. As seen in Fig. 4(c), for the thinnest gases, the fitted exponents are significantly different from the expected value and can reach values up to -1.3, showing the strong influence of dipole-dipole interactions in our system. We show the result of coupled dipole simulations for $k\Delta z = 0$ in Fig. 4(b) along with their power-law fit. We extract the exponents $\eta_r = -0.36(1)$ and $\eta_b = -0.70(1)$ that are reported as solid lines in Fig. 4(c). Our experimental results interpolate between the single-atom case and the simulated 2D situation.

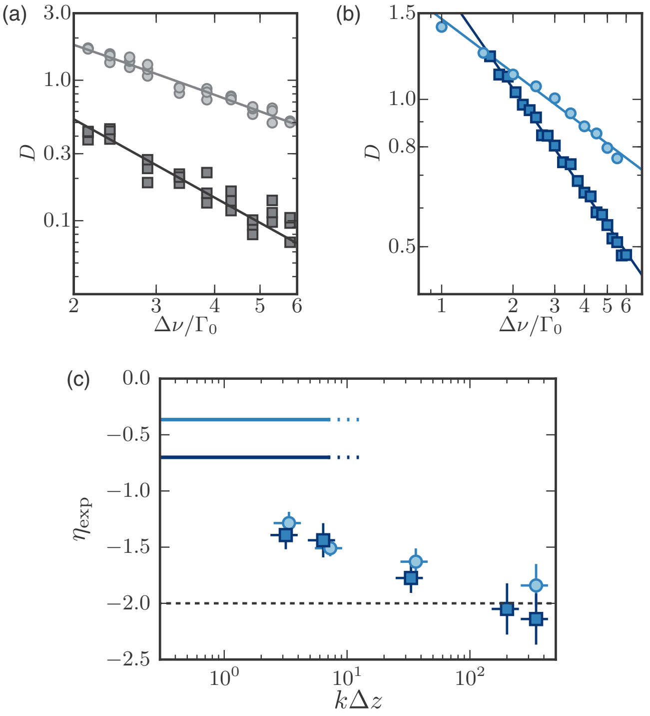

FIG. 9. Non-Lorentzian wings of the resonance line. (a) Two examples of the scaling of optical depth with $\Delta\nu$ (blue side), in log-log scale, for $k\Delta z = 2.4(6)$ (circles) and for $k\Delta z = 350(90)$ (squares) and their power-law fit. (b) Coupled dipole simulations at zero thickness and for $nk^{-2} = 1.5(2)$. The optical depth is plotted as a function of detuning (minus the detuning) from the resonance line, for the blue (circles) [red (squares)] side. The solid lines are power-law fits. (c) Experimental results for $nk^{-2} = 1.5(2)$. Circles (squares) represent the fitted exponents η_r (η_b) to the far-detuned regions of the resonance line on the red and blue side, respectively. The fit function is $\Delta\nu \mapsto D(\Delta\nu) = A\,(\Delta\nu - \nu_0)^\eta$. The error on the fitted exponents is also determined using a bootstrap analysis. The horizontal dashed black line ($\eta = -2$) emphasizes the expected asymptotic value for low densities for a Lorentzian line (at large detunings).

V. CONCLUSION

In summary we have studied the transmission of a macroscopic dense slab of atoms with uniform in-plane density and a transverse Gaussian density distribution. We observed a strong reduction of the maximum optical density and a broadening of the resonance line. More surprisingly, we showed the presence of a large blueshift of the resonance line and a deviation from Lorentzian behavior in the wings of the resonance line. These results are qualitatively confirmed by coupled dipole simulations and a perturbative approach of this scattering problem. We also confirm the difficulty already observed to obtain a quantitative agreement between coupled dipole simulations and experimental results in the dense regime [32,34]. Possible explanations for this discrepancy are (i) residual motion of the atoms during the probing due to the strong light-induced dipole-dipole interactions, (ii) a too large intensity used in the experiment which goes beyond the validity of the coupled dipole approach, and (iii) the influence of the complex atomic level structure. We were careful in this work to limit the influence of the two first explanations and the last possibility is likely to be the main limitation. The complex level structure leads to optical pumping effects during the probing and thus the scattering cross section of the sample is not well defined. A simple way to take into account the level structure is, as discussed in Sec. IV, to renormalize the scattering cross section by the average of the Clebsch-Gordan coefficients involved in the process. For ^{87}Rb atoms this amounts to the factor 7/15 already discussed earlier. However, this is a crude approximation which neglects optical pumping effects during scattering and whose validity in the dense regime is not clear. Two approaches can be considered to remove this limitation. First, one can use another atomic species such as strontium or ytterbium bosonic isotopes which have a spin singlet ground state and in which almost exact two-level systems are available for some optical transitions.

Scattering experiments on strontium clouds have been reported [25,30,49] but they did not explore the dense regime tackled in this work. The comparison with theory thus relies on modeling their inhomogeneous density distribution accurately. Second, an effective two-level system can be created in the widely used alkali-metal atoms by imposing a strong magnetic field which could separate the different transitions by several times the natural linewidth as demonstrated in some recent experiments on three-level systems [50,51]. This method could be in principle applied on our setup to create an effective two-level system and could help one to understand the aforementioned discrepancies.

Finally, we note that this article focuses on the steady-state transmission of a cloud illuminated by a uniform monochromatic beam. The slab geometry that we have developed here is of great interest for comparison between theory and experiments and our work opens interesting perspectives for extending this study to time-resolved experiments, to fluorescence measurements, or to spatially resolved propagation of light studies.

ACKNOWLEDGMENTS

We thank Vitaly Kresin, Klaus Mølmer, Janne Ruostekoski, Markus Greiner, Zoran Hadzibabic, and Wilhelm Zwerger for fruitful discussions. This work is supported by DIM NanoK, ERC (Synergy UQUAM). L.C. acknowledges the support from DGA. This project has received funding from the European Union's Horizon 2020 research and innovation programme under the Marie Skłodowska-Curie grant agreement No. 703926.

APPENDIX: REFLECTION COEFFICIENT OF A 2D GAS

Thanks to their large scattering cross section at resonance, arrays of atoms can be used to emit light with a controlled spatial pattern [52]. A single-atom mirror has been demonstrated [53] and, more generally, regular two-dimensional arrays of atoms have been considered for realizing controllable light absorbers [17] or mirrors [18] with atomic-sized thicknesses. For the disordered atomic samples considered in this article the strong decrease of the transmission because of dipole-dipole interactions could lead to a large reflection coefficient. For a strictly two-dimensional gas we show as a solid line in Fig. 10 the result of the coupled dipole model for the intensity reflection coefficient $|\mathcal{R}|^2$ at resonance and at normal incidence as a function of density. This intensity reflection coefficient has a behavior with density similar to the optical depth D (dotted line). The relation between these two quantities depends on the relative phase between the incoming and the reflected field. For a transmitted field in phase with the incident field we find, using the boundary condition $\mathcal{R}+\mathcal{T}=1$, a lower bound for this reflection coefficient, $|\mathcal{R}|^2 \geqslant (1-|\mathcal{T}|)^2$, shown as a dashed line in Fig. 10. The intensity reflection coefficient is close to this lower bound in the regime explored in this work. The maximum computed value for the reflection coefficient is close to 40%, which shows that a single disordered layer of individual atoms can significantly reflect an incoming light beam [54]. Note that for a non-2D sample light can be diffused at any angle. For our experimental thickness and the relevant densities the reflection coefficient is in practice much lower than the above prediction.

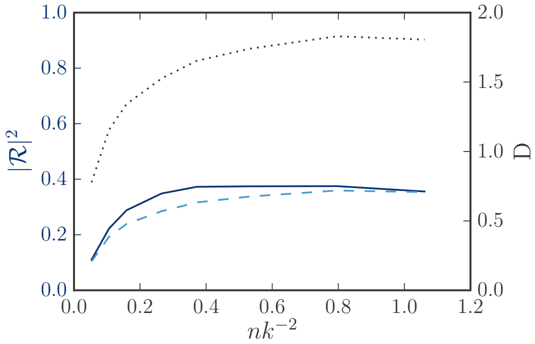

FIG. 10. Intensity reflection coefficient as a function of surface density for $k\Delta z = 0$ (solid line). For comparison we show the corresponding optical depth D (dotted line, right axis) and the lower bound for the reflection coefficient deduced from this optical depth (dashed line).

---

[1] C. Cohen-Tannoudji, J. Dupont-Roc, G. Grynberg, and P. Thickstun, *Atom-photon Interactions: Basic Processes and Applications* (Wiley Online Library, New York, 1992).

[2] J.-M. Raimond and S. Haroche, *Exploring the Quantum* (Oxford University Press, Oxford, 2006).

[3] P. W. H. Pinkse, T. Fischer, P. Maunz, and G. Rempe, Trapping an atom with single photons, Nature (London) **404**, 365 (2000).

[4] X. Ling, H. Wang, S. Huang, F. Xia, and M.S. Dresselhaus, The renaissance of black phosphorus, Proc. Natl. Acad. Sci. U.S.A. **112**, 4523 (2015).

[5] B. Gouraud, D. Maxein, A. Nicolas, O. Morin, and J. Laurat, Demonstration of a Memory for Tightly Guided Light in an Optical Nanofiber, Phys. Rev Lett. **114**, 180503 (2015).

[6] C. Sayrin, C. Junge, R. Mitsch, B. Albrecht, D. O'Shea, P. Schneeweiss, J. Volz, and A. Rauschenbeutel, Nanophotonic Optical Isolator Controlled by the Internal State of Cold Atoms, Phys. Rev. X **5**, 041036 (2015).

[7] L. Britnell, R. M. Ribeiro, A. Eckmann, R. Jalil, B. D. Belle, A. Mishchenko, Y.-J. Kim, R. V. Gorbachev, T. Georgiou, S. V. Morozov, A. N. Grigorenko, A. K. Geim, C. Casiraghi, A. H. Castro Neto, and K. S. Novoselov, Strong light-matter interactions in heterostructures of atomically thin films, Science **340**, 1311 (2013).

[8] A. Damascelli, Z. Hussain, and Z.-X. Shen, Angle-resolved photoemission studies of the cuprate superconductors, Rev. Mod. Phys. **75**, 473 (2003).

[9] J. Braun, The theory of angle-resolved ultraviolet photoemission and its applications to ordered materials, Rep. Prog. Phys. **59**, 1267 (1996).

[10] T. Stauber, D. Noriega-Pérez, and J. Schliemann, Universal absorption of two-dimensional systems, Phys. Rev. B **91**, 115407 (2015).

[11] D. J. Merthe and V. V. Kresin, Transparency of graphene and other direct-gap two-dimensional materials, Phys. Rev. B **94**, 205439 (2016).

[12] K. S. Novoselov, A. K. Geim, S. V. Morozov, D. Jiang, Y. Zhang, S. V. Dubonos, I. V. Grigorieva, and A. A. Firsov, Electric field effect in atomically thin carbon films, Science **306**, 666 (2004).

[13] R. R. Nair, P. Blake, A. N. Grigorenko, K. S. Novoselov, T. J. Booth, T. Stauber, N. M. R. Peres, and A. K. Geim, Fine structure constant defines visual transparency of graphene, Science **320**, 1308 (2008).

[14] K. F. Mak, M. Y. Sfeir, Y. Wu, C. H. Lui, J. A. Misewich, and T. F. Heinz, Measurement of the Optical Conductivity of Graphene, Phys. Rev. Lett. **101**, 196405 (2008).

[15] H. Fang, H. A. Bechtel, E. Plis, M. C. Martin, S. Krishna, E. Yablonovitch, and A. Javey, Quantum of optical absorption in two-dimensional semiconductors, Proc. Natl. Acad. Sci. U.S.A. **110**, 11688 (2013).

[16] G. Eda and S. A. Maier, Two-dimensional crystals: managing light for optoelectronics, Acs Nano **7**, 5660 (2013).

[17] R. J. Bettles, S. A. Gardiner, and C. S. Adams, Enhanced Optical Cross Section Via Collective Coupling of Atomic Dipoles in a 2D Array, Phys. Rev. Lett. **116**, 103602 (2016).

[18] E. Shahmoon, D. S. Wild, M. D. Lukin, and S. F. Yelin, Cooperative Resonances in Light Scattering from Two-Dimensional Atomic Arrays, Phys. Rev. Lett. **118**, 113601 (2017).

[19] L. Chomaz, L. Corman, T. Yefsah, R. Desbuquois, and J. Dalibard, Absorption imaging of a quasi-two-dimensional gas: a multiple scattering analysis, New J. Phys. **14**, 055001 (2012).

[20] T. Yefsah, R. Desbuquois, L. Chomaz, K. J. Günter, and J. Dalibard, Exploring the Thermodynamics of a Two-Dimensional Bose Gas, Phys. Rev. Lett. **107**, 130401 (2011).

[21] T. Bienaimé, S. Bux, E. Lucioni, P. W. Courteille, N. Piovella, and R. Kaiser, Observation of a Cooperative Radiation Force in the Presence of Disorder, Phys. Rev. Lett. **104**, 183602 (2010).

[22] S. Balik, A. L. Win, M. D. Havey, I. M. Sokolov, and D. V. Kupriyanov, Near-resonance light scattering from a high-density ultracold atomic ^{87}Rb gas, Phys. Rev. A **87**, 053817 (2013).

[23] Z. Meir, O. Schwartz, E. Shahmoon, D. Oron, and R. Ozeri, Cooperative Lamb Shift in a Mesoscopic Atomic Array, Phys. Rev. Lett. **113**, 193002 (2014).

[24] K. Kemp, S. J. Roof, M. D. Havey, I. M. Sokolov, and D. V. Kupriyanov, Cooperatively enhanced light transmission in cold atomic matter, arXiv:1410.2497.

[25] C. C. Kwong, T. Yang, M. S. Pramod, K. Pandey, D. Delande, R. Pierrat, and D. Wilkowski, Cooperative Emission of a Coherent Superflash of Light, Phys. Rev. Lett. **113**, 223601 (2014).

[26] A. Goban, C.-L. Hung, J. D. Hood, S.-P. Yu, J. A. Muniz, O. Painter, and H. J. Kimble, Superradiance for Atoms Trapped Along a Photonic Crystal Waveguide, Phys. Rev. Lett. **115**, 063601 (2015).

[27] M. O. Araújo, I. Krešić, R. Kaiser, and W. Guerin, Superradiance in a Large and Dilute Cloud of Cold Atoms in the Linear-Optics Regime, Phys. Rev. Lett. **117**, 073002 (2016).

[28] S. J. Roof, K. J. Kemp, M. D. Havey, and I. M. Sokolov, Observation of Single-Photon Superradiance and the Cooperative Lamb Shift in an Extended Sample of Cold Atoms, Phys. Rev. Lett. **117**, 073003 (2016).

[29] W. Guerin, M. O. Araújo, and R. Kaiser, Subradiance in a Large Cloud of Cold Atoms, Phys. Rev. Lett. **116**, 083601 (2016).

[30] S. L. Bromley, B. Zhu, M. Bishof, X. Zhang, T. Bothwell, J. Schachenmayer, T. L. Nicholson, R. Kaiser, S. F. Yelin, M. D. Lukin, A. M. Rey, and J. Ye, Collective atomic scattering and motional effects in a dense coherent medium, Nat. Commun. **7** 11039 (2016).

[31] J. Keaveney, A. Sargsyan, U. Krohn, I. G. Hughes, D. Sarkisyan, and C. S. Adams, Cooperative Lamb Shift in an Atomic Vapor Layer of Nanometer Thickness, Phys. Rev. Lett. **108**, 173601 (2012).

[32] J. Pellegrino, R. Bourgain, S. Jennewein, Y. R. P. Sortais, A. Browaeys, S. D. Jenkins, and J. Ruostekoski, Observation of Suppression of Light Scattering Induced by Dipole-Dipole Interactions in a Cold-Atom Ensemble, Phys. Rev. Lett. **113**, 133602 (2014).

[33] S. D. Jenkins, J. Ruostekoski, J. Javanainen, R. Bourgain, S. Jennewein, Y. R. P. Sortais, and A. Browaeys, Optical Resonance Shifts in the Fluorescence of Thermal and Cold Atomic Gases, Phys. Rev. Lett. **116**, 183601 (2016).

[34] S. Jennewein, M. Besbes, N. J. Schilder, S. D. Jenkins, C. Sauvan, J. Ruostekoski, J.-J. Greffet, Y. R. P. Sortais, and A. Browaeys, Coherent Scattering of Near-Resonant Light by a Dense Microscopic Cold Atomic Cloud, Phys. Rev. Lett. **116**, 233601 (2016).

[35] S. D. Jenkins, J. Ruostekoski, J. Javanainen, S. Jennewein, R. Bourgain, J. Pellegrino, Y. R. P. Sortais, and A. Browaeys, Collective resonance fluorescence in small and dense atom clouds: Comparison between theory and experiment, Phys. Rev. A **94**, 023842 (2016).

[36] J. Javanainen, J. Ruostekoski, Y. Li, and S.-M. Yoo, Shifts of a Resonance Line in a Dense Atomic Sample, Phys. Rev. Lett. **112**, 113603 (2014).

[37] J.-L. Ville, T. Bienaimé, R. Saint-Jalm, L. Corman, M. Aidelsburger, L. Chomaz, K. Kleinlein, D. Perconte, S. Nascimbène, J. Dalibard, and J. Beugnon, Loading and compression of a single two-dimensional Bose gas in an optical accordion, Phys. Rev. A **95**, 013632 (2017).

[38] The 2D phase-space density of the cloud is below the transverse condensation threshold as defined in [55] .

[39] J. Javanainen, J. Ruostekoski, Y. Li, and S.-M. Yoo, Exact electrodynamics versus standard optics for a slab of cold dense gas, Phys. Rev. A **96**, 033835 (2017).

[40] O. Morice, Y. Castin, and J. Dalibard, Refractive index of a dilute Bose gas, Phys. Rev. A **51**, 3896 (1995).

[41] P. C. Bons, R. de Haas, D. de Jong, A. Groot, and P. van der Straten, Quantum Enhancement of the Index of Refraction in a Bose-Einstein Condensate, Phys. Rev. Lett. **116**, 173602 (2016).

[42] P. W. Milonni and P. L. Knight, Retardation in the resonant interaction of two identical atoms, Phys. Rev. A **10**, 1096 (1974).

[43] J. Ruostekoski and J. Javanainen, Lorentz-Lorenz shift in a Bose-Einstein condensate, Phys. Rev. A **56**, 2056 (1997).

[44] N. Cherroret, D. Delande, and B. A. van Tiggelen, Induced dipole-dipole interactions in light diffusion from point dipoles, Phys. Rev. A **94**, 012702 (2016).

[45] Except for Fig. 9(b) for which simulations are performed for a fixed atom number of 2000.

[46] We guess that this is due to the limited atom number used in the simulation which prevents one from investigating a regime where the geometry of the simulated cloud has an aspect ratio similar to the experimental one.

[47] The observed saturation is not due to our detection procedure. In the fitting procedure, we only select points with a measured optical depth below 3 to avoid any bias.

[48] For thick clouds the expected optical depth of the cloud becomes larger than the maximal value we can detect. We then only fit the points with a measured optical depth below 3. From this fit we cannot estimate reliably the value of the maximum and width of the resonance line, but we can get an estimate of the "center" of the line which may deviate from the position of the maximum of the resonance for an asymmetric line shape.

[49] Y. Bidel, B. Klappauf, J. C. Bernard, D. Delande, G. Labeyrie, C. Miniatura, D. Wilkowski, and R. Kaiser, Coherent Light Transport in a Cold Strontium Cloud, Phys. Rev. Lett. **88**, 203902 (2002).

[50] D. J. Whiting, E. Bimbard, J. Keaveney, M. A. Zentile, C. S. Adams, and I. G. Hughes, Electromagnetically induced absorption in a nondegenerate three-level ladder system, Opt. Lett. **40**, 4289 (2015).

[51] D. J. Whiting, J. Keaveney, C. S. Adams, and I. G. Hughes, Direct measurement of excited-state dipole matrix elements using electromagnetically induced transparency in the hyperfine Paschen-Back regime, Phys. Rev. A **93**, 043854 (2016).

[52] S. D. Jenkins and J. Ruostekoski, Controlled manipulation of light by cooperative response of atoms in an optical lattice, Phys. Rev. A **86**, 031602 (2012).

[53] G. Hétet, L. Slodička, M. Hennrich, and R. Blatt, Single Atom as a Mirror of an Optical Cavity, Phys. Rev. Lett. **107**, 133002 (2011).

[54] We have investigated here only the behavior at normal incidence. A full characterization of such an atomic mirror is beyond the scope of this work .

[55] L. Chomaz, L. Corman, T. Bienaimé, R. Desbuquois, C. Weitenberg, S. Nascimbene, J. Beugnon, and J. Dalibard, Emergence of coherence via transverse condensation in a uniform quasi-two-dimensional Bose gas, Nat. Commun. **6**, 6162 (2015).

PHYSICAL REVIEW A **97**, 061801(R) (2018)

Rapid Communications

Resonant-light diffusion in a disordered atomic layer

R. Saint-Jalm,[1] M. Aidelsburger,[1,*] J. L. Ville,[1] L. Corman,[1,†] Z. Hadzibabic,[2] D. Delande,[1] S. Nascimbene,[1] N. Cherroret,[1,‡] J. Dalibard,[1] and J. Beugnon[1,§]

[1]*Laboratoire Kastler Brossel, Collège de France, CNRS, ENS-PSL University, Sorbonne Université, 11 Place Marcelin Berthelot, 75005 Paris, France*

[2]*Cavendish Laboratory, University of Cambridge, J.J. Thomson Avenue, Cambridge CB3 0HE, United Kingdom*

(Received 12 February 2018; published 18 June 2018)

Light scattering in dense media is a fundamental problem of many-body physics, which is also relevant for the development of optical devices. In this work we investigate experimentally light propagation in a dense sample of randomly positioned resonant scatterers confined in a layer of subwavelength thickness. We locally illuminate the atomic cloud and monitor spatially resolved fluorescence away from the excitation region. We show that light spreading is well described by a diffusion process, involving many scattering events in the dense regime. For light detuned from resonance we find evidence that the atomic layer behaves as a graded-index planar waveguide. These features are reproduced by a simple geometrical model and numerical simulations of coupled dipoles.

DOI: 10.1103/PhysRevA.97.061801

Multiple scattering in disordered materials is currently the focus of intense investigations in many different contexts such as electron transport in solids [1], sound wave propagation [2], matter waves in optical potentials [3], and light propagation in dielectric materials [4]. Multiple light scattering is of paramount importance to understand light transport, for instance, in biological tissues, planetary atmospheres, or interstellar clouds [5]. In addition, the development of custom photonic materials allows one to engineer disordered materials in a controlled way and opens new applications in random lasing [6] or in the development of solar cells [7].

Cold atomic gases offer a unique platform to investigate light scattering. Due to the simple atomic level structure, all photons incident on the gas are scattered without absorption. Cooling techniques can bring the atoms to a temperature where their residual motion is so small that Doppler broadening is negligible. Additionally, the gas dimensionality can be changed rather easily by shaping the trapping potential. Finally, the tunability of the scattering cross section and the atomic density allows one to explore light scattering from the dilute to the dense regime.

In the multiple-scattering regime, light is scattered several times before exiting the material in random directions. In sufficiently dilute atomic clouds, this process is known to be well captured by a random-walk-type diffusive model [1]. This regime has been explored in several experiments, achieving, for instance, the observation of coherent backscattering [8,9], subradiant and superradiant modes [10–12], cooperative radiation pressure force [13], or collective light scattering [14,15]. At higher densities ρ where the product of the light wave number k and the interatomic spacing $\rho^{-1/3}$ becomes of the order of unity, the situation is still poorly understood. Indeed, scatterers are no longer independent of each other and significant induced dipole-dipole interactions occur [16–20]. These interactions are responsible for cooperative effects such as broadening and a shift of the resonance line [21–26].

Here we explore the phenomenon of multiple scattering of light in a dense and large cloud of atoms. In our ultracold sample the motion of the atoms is negligible on the timescale of the experiment, so they act as a gas of fixed, randomly distributed point scatterers. Atoms are confined in a layer geometry in the focal plane of a high-resolution imaging system, which allows us to inject light in a region with sharp boundaries and monitor its spreading away from this region [see Fig. 1(a)]. We observed that the fluorescence intensity, which measures the local photon escape rate, decays exponentially with the distance from the excitation zone. We show that this behavior is compatible with a two-dimensional (2D) diffusive model. For resonant light, we measured the decay length of the fluorescence signal as a function of the atomic density, all the way from the dilute to the dense regime. This decay length, or equivalently the escape radius of the photons, represents the distance the photons travel before escaping the sample. It decreases with increasing density and then saturates in the regime of high density where photons undergo a few tens of scattering events before leaving the cloud. For detuned light and in the dense regime, the photon escape rate is significantly modified in a way that suggests a light-guiding mechanism reminiscent of a graded-index planar waveguide. We also observed these phenomena in numerical simulations based on a model of coupled dipoles and explained them in a semiquantitative way by an analytical model of light guiding in an open, disordered 2D slab.

We use a dense layer of ^{87}Rb atoms as previously described in Refs. [26,27]. In the xy plane, we produce a uniform disk-shaped atomic layer of radius $R = 20\ \mu$m with a controllable surface density up to $\rho_{2D} = 135(15)\ \mu\text{m}^{-2}$ and a temperature

---

[*] Present address: Fakultät für Physik, Ludwig-Maximilians-Universität München, Schellingstraße 4, 80799 Munich, Germany.

[†] Present address: Institute for Quantum Electronics, ETH Zurich, 8093 Zurich, Switzerland.

[‡] cherroret@lkb.upmc.fr

[§] beugnon@lkb.ens.fr

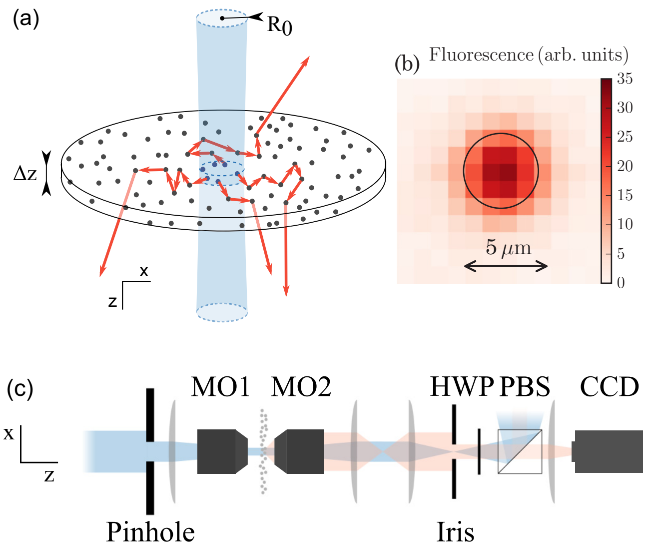

FIG. 1. Experimental setup. A layer of atoms is illuminated at its center with a resonant light beam of radius R_0. Photons initially emitted in the excitation region can be scattered several times in the atomic layer before exiting the system and being collected and imaged. (b) Typical fluorescence image at resonance and maximum density. The black circle, of diameter of $2R_0 = 5\ \mu$m, delineates the excitation region. Intensity is not uniform inside the excitation region partially because of finite optical resolution but also, and more importantly, because of the light diffusion process itself, as described in the text. (c) Schematic of the imaging system. A pinhole is imaged on the atomic cloud using a microscope objective (MO1). The atomic fluorescence is imaged on a camera (CCD) using a second and identical objective (MO2) and a set of lenses. Fluorescence is spatially filtered using an iris and the detected polarization is chosen by adjusting a combination of a half-wave plate (HWP) and a polarization beam splitter (PBS).

$T_0 = 270(10)$ nK. Atoms are strongly confined along the vertical z direction with an approximately Gaussian density distribution of rms thickness $\Delta z \approx 0.3\ \mu\mathrm{m} < \lambda_0$, with $\lambda_0 = 2\pi/k = 0.78\ \mu$m the resonant wavelength for the $|F = 2\rangle$ to $|F' = 3\rangle$ $D2$ transition of rubidium atoms. This corresponds to a maximum density at the center of the Gaussian profile of $\rho_{3\mathrm{D}}k^{-3} = 0.35(5)$ where $\rho_{3\mathrm{D}} = \rho_{2\mathrm{D}}/\sqrt{2\pi}\,\Delta z$.

We tune this density by varying the number of atoms in the $|F = 2, m_F = -2\rangle$ hyperfine ground state, which is sensitive to our light probe. The population in this state is controlled using partial transfer from the $|F = 1, m_F = -1\rangle$ state in which the atoms are initially spin polarized. As discussed in Ref. [26], dipole-dipole interactions play a dominant role at the densities achieved in our setup. Because of these interactions, the thickness of the cloud could increase, depending on its density, during the light excitation. We estimate that the effective cloud thickness, in the illuminated region, could reach a maximum value of 0.4 μm at the end of the excitation.

The atomic cloud is locally excited by light at a wavelength λ_0, propagating perpendicular to the atomic plane along the z axis, as illustrated in Fig. 1(a), and linearly polarized along x. In the illuminated region, the intensity of the beam is on the order of $7I_{\mathrm{sat}}$, where $I_{\mathrm{sat}} = 1.6\ \mathrm{mW\,cm^{-2}}$ is the saturation intensity for this transition (with a linewidth $\Gamma = 2\pi \times 6.0$ MHz).[1] The light beam profile on the atomic cloud is given by the image of a pinhole whose diameter on the atomic cloud is $2R_0 = 5\ \mu$m. The excitation duration is $\tau = 10\ \mu$s. The atomic fluorescence is collected, spatially filtered, and imaged on a CCD camera, as shown in Fig. 1(c). We detect only photons with a linear polarization perpendicular to the excitation polarization and block the residual light transmitted in the spatial mode of the incident beam. The optical resolution of our system ($\sim$1 μm) is characterized in the Supplemental Material [28]. Atoms outside the illuminated region are only excited by scattered light and experience a much lower intensity than in the illuminated region. Taking into account our collection and detection efficiencies, assuming that the scatterers are independent and that polarization is randomized for photons emitted from outside the excitation region, we obtain a rough estimate for the intensity experienced by atoms at 1 μm from the edge of the illuminated region of approximately $0.1I_{\mathrm{sat}}$. It is important to operate in this low-saturation regime to enable comparison with the simulations described below.

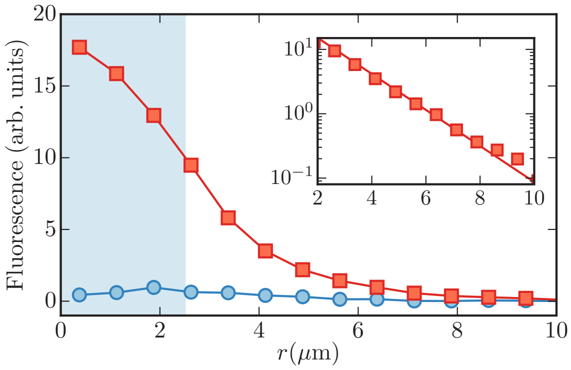

FIG. 2. Fluorescence decay. Binned and azimuthally averaged profile for the measured atomic fluorescence (squares). Circles show the small background signal observed without atoms. The shaded area represents the excitation region. Statistical errors bars due to photon counting are smaller than the size of the points. The solid lines are broken lines linking the points. The inset shows the same data outside the excitation region in a semilogarithmic plot to emphasize the exponential decay of the fluorescence signal. We attribute the deviation of the last two points from the exponential fit to the contribution from stray light. Data are averaged over 100 measurements.

We show in Fig. 1(b) a typical measurement of the atomic fluorescence signal integrated over the full duration of the excitation. The circle indicates the illuminated region. Photons are detected up to several microns away from this region. We show in Fig. 2 a binned and azimuthally averaged profile of the fluorescence image. There is a large ratio between the atomic signal and residual stray light over the explored experimental range. Outside the illuminated region we observe an exponential decay with distance of the atomic fluorescence

---

[1] The intensity we used is large enough to ensure that, even if our samples have large optical depths, the cloud is well excited for all positions along the z direction.

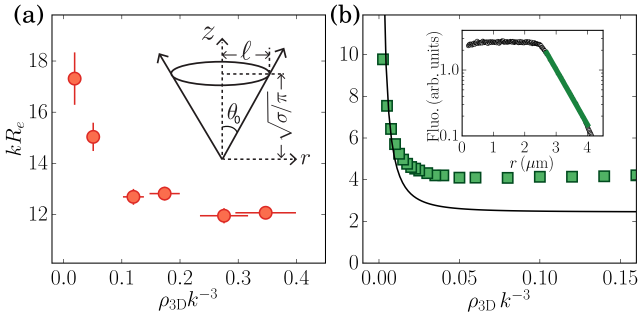

FIG. 3. (a) Measured escape radius R_e for different densities at resonance ($\Delta = 0$). Vertical error bars correspond to the standard deviation of the results of exponential fits to the data obtained with a bootstrap approach [29]. Each data set is obtained from the average of 100 measurements. Horizontal error bars represent the statistical uncertainty on the atom number. The inset shows the relevant parameters of the simple model described in the main text. (b) Escape radius R_e obtained from the analytical result of Eq. (4) (solid curve) and numerical simulations of a model of classical coupled dipoles (squares) as a function of density. Statistical error bars on R_e obtained from the fitting procedure of the coupled dipole simulations are smaller than the size of the points. The inset shows the fluorescence signal computed with coupled dipole simulations for $\rho_{3D}k^{-3} = 0.12$ and averaged over more than 1000 atomic distributions. The solid line is the exponential fit outside the illuminated region.

over almost two decades (see the inset in Fig. 2). The typical distance over which the photons travel is of a few microns.

We first focus on the experimental results for a resonant excitation. We fit the experimental fluorescence signal for various densities by Ae^{-r/R_e} and obtain the escape radius R_e as a function of density [see Fig. 3(a)]. The escape radius decreases for increasing densities and reaches an approximately constant value for $\rho_{3D}k^{-3} > 0.1$. The measurements in the low-density regime (lower values of $\rho_{3D}k^{-3}$) correspond to a single-scattering-event regime where a photon typically leaves the sample after the first scattering event outside the illuminated region. In this case the escape radius is on the order of the scattering mean free path $\ell = 1/\rho_{3D}\sigma$, where σ is the light cross section and we expect $R_e \sim \ell$, in agreement with the observed decrease of R_e with density.

In the opposite regime of large densities, photons are scattered several times before leaving the sample and we observe a saturation of the escape radius. It remains around $kR_e \approx 12$ while varying the density by a factor of about 3. We checked that this saturation is not due to the finite resolution of our imaging system, which allows us to measure spatial structures with a size below 1 μm ($kR_e \lesssim 8$). In this regime the system can be described by a diffusion model of light transport. In the steady-state regime, the light energy density $I(\mathbf{r})$ at a point $\mathbf{r}$ in the sample obeys a diffusion equation with losses

$$-D_0\nabla^2 I(\mathbf{r}) = -\gamma I(\mathbf{r}) + S(\mathbf{r}), \tag{1}$$

where D_0 is the diffusion constant, γ the escape rate of photons, and $S(\mathbf{r})$ the source term describing the laser excitation. We consider the situation where the source term is $S(\mathbf{r}) = S_0$ for $r < R_0$ and 0 otherwise. The solution of this equation in two dimensions is given by

$$I(\mathbf{r}) = \frac{S_0}{2\pi D_0}\iint_{|\mathbf{r}'|<R_0} K_0\left(\frac{|\mathbf{r}-\mathbf{r}'|}{R_e}\right)d^2r' \underset{r\gg R_0+R_e}{\propto} \frac{e^{-r/R_e}}{\sqrt{r}}, \tag{2}$$

where K_0 is the modified Bessel function of the second kind of order zero and $R_e = \sqrt{D_0/\gamma}$. Outside the illuminated region, at large r, the function $I(r)$ decays almost exponentially,[2] in agreement with our measurements. These results allow us to relate the measured photon escape radius R_e to the diffusion constant D_0 and to the escape rate γ that we cannot measure individually in a direct way. In this diffusive regime, the escape radius R_e can also be related to the microscopic parameters describing the propagation of a photon in a random-walk picture. Introducing p, the probability of escaping the cloud after a scattering event, and using ℓ, the (already defined) scattering mean free path, one gets, for large r,

$$R_e \sim \ell/\sqrt{p}. \tag{3}$$

We have developed a simple geometrical model to estimate the escape probability p and to explain the main features of the curve in Fig. 3(a). Consider an atom in a 2D gas emitting a photon as being placed at the center of a vertical cylinder of radius ℓ, corresponding to the typical distance to the next scatterer. The photon will escape the cloud if its emission angle θ_0 is small enough so that it would meet the next scatterer at a height larger than $\sqrt{\sigma/\pi}$. Emitted photons that escape the medium are then effectively contained within a cone of half angle θ_0 [see the inset of Fig. 3(a)]. This gives a probability $p \sim 2\times 2\pi(1-\cos\theta_0)/4\pi$ with $\tan\theta_0 = \ell/\sqrt{\sigma/\pi}$ and in turn

$$kR_e = \frac{k\ell}{\sqrt{1-(1+\ell^2\pi/\sigma)^{-1/2}}}. \tag{4}$$

We display Eq. (4) computed for the resonant scattering cross section $3\lambda_0^2/2\pi$ in Fig. 3(b) (solid line). At large densities, $p \sim \ell^2\pi/2\sigma$ so that R_e becomes independent of the density and much larger than the mean free path. This saturation of R_e with increasing density thus stems from the compensation of two antagonistic effects: (i) the decrease of ℓ, which tends to make the escape radius smaller, and (ii) the decrease of p. The extension of Eq. (3) to low densities (large ℓ) is consistent with $R_e \propto \ell$ and this simple model thus reproduces roughly the behavior of the ensemble of the experimental points.

Using the random-walk picture and this estimate of p, we find that the typical number of scattering events before a photon leaves the sample is $N_{\text{scatt}} = 1/p = 2\sigma/\pi\ell^2$. Considering an atomic density of $\rho_{3D}k^{-3} = 0.07$, in the plateau of Fig. 3(b) but not too large so that ℓ could still be interpreted with the classical picture of a mean free path, we get a typical value of about 20 scattering events. This value justifies the diffusion model and confirms that we investigate experimentally a steady-state situation (the total duration of a photon random walk, approximately equal to $N_{\text{scatt}}\Gamma^{-1}$, is much shorter than the duration τ of the illumination pulse).

---

[2] We neglect the $\sqrt{r}$ dependence, which has almost no influence on the shape of the signal in the range of distance we explore in this work.

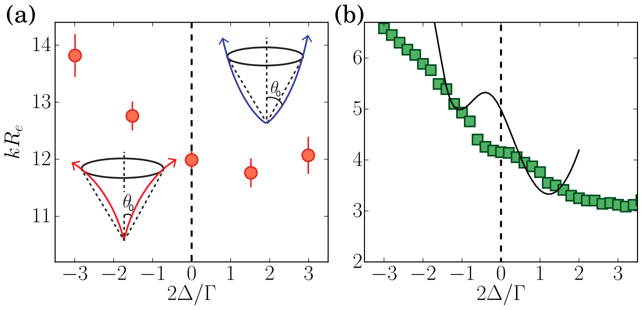

FIG. 4. Escape radius versus detuning. (a) Experimental results obtained for a dense cloud with $\rho_{3D}k^{-3} \simeq 0.35$. The insets show the bending of the trajectories which depends on the sign of the detuning. The dashed lines in the insets correspond to the maximal emission angle a photon leaving the sample could have without considering the bending effect. Taking into account the bending effect, this maximal angle is smaller for negative detuning and larger for positive detunings. Each point is the average result of 100 measurements. (b) Escape radius computed from a numerical model of coupled dipoles (squares), with the escape radius $R_e = \ell/\sqrt{1-\cos\theta_0}$ obtained by solving Eq. (5) for θ_0 (solid line). All theory curves are computed for the largest density we are able to handle $\rho_{3D}k^{-3} = 0.1$. Statistical error bars obtained from the fitting procedure for the coupled dipole simulations are smaller than the size of the points.

As shown in Fig. 3(b), the variation of escape radius with density is also reproduced by numerical simulations based on the method of coupled dipoles. As described in Ref. [30], we model our atomic system by a random ensemble of randomly positioned classical coupled dipoles (with the transition from $J=0$ to $J=1$) in a layer geometry with the same thickness as in the experiment. We compute the exact radiated field from these dipoles for a given excitation field taking into account simultaneously all effects related to dipole-dipole interactions and interferences. Fluorescence signals are obtained from the modulus square of each dipole and escape radii from an exponential fit to the fluorescence signal in the range from $r_1 = 2.7\ \mu$m to $r_2 = 4\ \mu$m, where r is the distance from the center. For each density we adapt the atom number in the simulations (from 100 up to 4000) and the number of repetitions over which the result of the simulations are averaged (from 20 to more than 10^5).

The two models that we have developed are in good agreement with each other. However, although these predictions qualitatively reproduce the measurements in Fig. 3(a), note the difference by a factor approximately equal to 3 between the scales of the two graphs. Possible reasons for this difference are discussed below.

An interesting feature of atomic systems is the possibility to change dramatically the response of the system by varying the detuning Δ of the excitation light with respect to the resonance. We report in Fig. 4(a) the influence of the detuning on the experimental escape radius R_e for the cloud of highest density. We observe a clear asymmetry around $\Delta = 0$: The escape radius is larger for negative than for positive detunings, which indicates that photons are escaping more easily the sample when $\Delta > 0$. Clearly, the results of Fig. 4(a) cannot be explained by the dependence of Eq. (4) on Δ, which originates only from the photon scattering cross section by a single atom and is thus symmetric with respect to $\Delta = 0$.

We attribute the asymmetry mainly to a refractive-index gradient effect and we developed a simple model to describe this effect. We approximate the atomic slab by a continuous medium with a spatially varying index of refraction $n(z)$ along the vertical direction and use the low-density expression for this index: $n(z) = 1 - [6\pi\rho_{3D}(z)\Delta/\Gamma]/[k^3(1+4\Delta^2/\Gamma^2)]$. It is thus either larger than one below the resonance ($\Delta < 0$) or lower than one above the resonance ($\Delta > 0$). In our system, the density distribution $\rho_{3D}(z)$ has an approximately Gaussian shape with a maximum at $z = 0$ leading to a gradient of the index of refraction. For negative detuning, $n(z)$ decreases with $|z|$ from the center of the cloud. This gives rise to a phenomenon of light guiding close to the one encountered in optical waveguides, explaining qualitatively why the escape radius gets larger. For $\Delta > 0$, the opposite effect is expected, with a decrease of the escape radius.

More quantitatively, the effect of the refractive-index gradient on R_e can be estimated by modifying the geometrical picture of the inset in Fig. 3(a) to account for the *bending* of photon trajectories that escape the layer, as illustrated in the insets of Fig. 4(a) for $\Delta > 0$ and $\Delta < 0$. For negative detunings, this bending leads to a decrease of the maximum value of the emission angle θ_0 for which a photon leaves the cloud. Similarly, it leads to an increase of θ_0 for positive detunings. The principle of the calculation is the following. We compute the equation for the trajectory $z(r)$ of a photon emitted in $z = 0$ and $r = 0$ and determine the emission angle θ_0 that fulfills the escape condition

$$z(\ell) = \sqrt{\sigma/\pi}, \tag{5}$$

where $\sigma = (3\lambda_0^2/2\pi)/(1+4\Delta^2/\Gamma^2)$. To find $z(r)$, we use the low-density expression of $n(z)$ given above and approximate the density profile $\rho_{3D}(z)$ of the atomic layer by an inverted parabola. Details of the calculation and complementary data for other densities are available in the Supplemental Material [28]. The escape radius obtained from this model is displayed in Fig. 4(b) as a function of Δ and shows a significant asymmetric behavior with detuning.

A similar asymmetry is also visible in our numerical simulations of coupled dipoles [see Fig. 4(b)]. Note that differences show up between the numerical simulations and our geometrical model. In particular, the simulations display a weaker variation with Δ than the one predicted by Eq. (5). This effect could be attributed to light-induced dipole-dipole interactions between atoms. These interactions are known to give rise to a broadening and a blueshift of the line [26], present in the simulations but not taken into account in Eq. (5). More generally, cooperative effects could be taken into account by modifying also the mean free path and the cross section, which are fundamental parameters of our model. Calculation of these parameters in the dense regime is however a difficult task that we leave for future work.

Since the measured escape radii are on the order of the optical wavelength, their measurement is rather challenging. We discuss two possible experimental limitations for this measurement. First, the finite resolution of the imaging system leads to an overestimate of the escape radius, but our setup benefits from a good spatial resolution, and we estimate that this correction should be at most on the order of 10%. Second, light-induced forces caused by dipole-dipole interactions are strong when operating in the dense regime. We have thus chosen the duration of the excitation short enough to limit the atomic motion while being long enough to probe the steady-state regime. With these parameters dipole-dipole interactions still lead to a small increase of the cloud size along the vertical axis. This increase of the cloud thickness (only in the illuminated region where the scattering rate is large) could favor the propagation of photons to a larger distance. For a pulse duration twice as long,[3] we observed an increase of the escape radius R_e by about 20%.

Both the coupled dipole simulations and the geometrical model predict a variation of R_e with density and detuning qualitatively similar to the experimental results, but with a factor ∼3 difference in the absolute value for R_e. A possible explanation for this discrepancy is the complex level structure of the rubidium atom. For instance, the averaging of the Clebsch-Gordan coefficients over all possible π transitions relevant for our incident linearly polarized light should at least lead to a correction of the effective single-atom scattering cross section which is not taken into account in our expression of the mean free path ℓ.[4] Taking into account this level structure on the determination of R_e requires complex simulations beyond the scope of this article [25]. An alternative approach would be to reproduce this study with atomic species like ytterbium and strontium, which present well-isolated $J = 0$ to $J = 1$ transitions. One could also couple our method for producing thin slabs with the method to isolate an effective two-level system in a multilevel atom discussed in Refs. [31–33] and based on the large Zeeman effect produced by an external magnetic field.

In summary, we have explored the diffusion of light in a dense and extended sample of fixed scatterers. Experiments with cold atomic systems are usually limited to lower densities. Still, the dense regime was explored in Refs. [23–25], but with a microscopic sample where light propagation cannot be investigated, and also in Ref. [21], but with a hot and thus Doppler-broadened cloud. Complementary studies on light transport in photonic planar waveguides have also been reported, for instance, in Ref. [34]. However, our system reveals a unique combination of multiple scattering, high densities, and guiding effects which can be tuned rather easily. Our experiment paves the way to a deeper understanding of the propagation of light in dense samples and possibly on the role of interference-induced (localization) effects in this geometry [35,36]. Indeed, while the observation of photon localization is still elusive [35], presumably due to the vector nature of light detrimental to interference [36], the problem could be circumvented in a 2D system illuminated by a light field linearly polarized perpendicular to the disordered plane. Our atomic system could constitute a good candidate for that objective, using the escape radius, which is directly controlled by the diffusion coefficient, as a probe for localization [37].

This work was supported by DIM NanoK, ERC (Synergy UQUAM). This project has received funding from the European Union's Horizon 2020 research and innovation program under the Marie Skłodowska-Curie Grant Agreement No. 703926. We thank S. Gigan for fruitful discussions. N.C. thanks A. Browaeys for discussions on cooperative effects and the Agence Nationale de la Recherche (Grant No. ANR-14-CE26-0032 LOVE) for financial support. Z.H. acknowledges support from EPSRC (Grant No. EP/N011759/1) and Sorbonne Université.

---

[3] The amplitude of the signal becomes too low for shorter pulses.

[4] An average with equal weight on all the transitions gives a cross section decreased by a factor 7/15 but neglects any optical pumping effects during the excitation. The scattering cross section should also be modified to take into account the spectrum of the photons emitted by the illuminated region. Indeed, as the Rabi frequency of our excitation beam is on the order of Γ, we expect a modification of the fluorescence spectrum.

[1] E. Akkermans and G. Montambaux, *Mesoscopic Physics of Electrons and Photons* (Cambridge University Press, Cambridge, 2007).

[2] H. Hu, A. Strybulevych, J. H. Page, S. E. Skipetrov, and B. A. van Tiggelen, Localization of ultrasound in a three-dimensional elastic network, Nat. Phys. **4**, 945 (2008).

[3] A. Aspect and M. Inguscio, Anderson localization of ultracold atoms, Phys. Today **62**(8), 30 (2009).

[4] M. C. W. van Rossum and T. M. Nieuwenhuizen, Multiple scattering of classical waves: Microscopy, mesoscopy, and diffusion, Rev. Mod. Phys. **71**, 313 (1999).

[5] H. C. van de Hulst, *Multiple Light Scattering: Tables, Formulas, and Applications* (Elsevier, Amsterdam, 2012).

[6] D. S. Wiersma, The physics and applications of random lasers, Nat. Phys. **4**, 359 (2008).

[7] D. S. Wiersma, Disordered photonics, Nat. Photon. **7**, 188 (2013).

[8] G. Labeyrie, F. de Tomasi, J.-C. Bernard, C. A. Müller, C. Miniatura, and R. Kaiser, Coherent Backscattering of Light by Cold Atoms, Phys. Rev. Lett. **83**, 5266 (1999).

[9] Y. Bidel, B. Klappauf, J. C. Bernard, D. Delande, G. Labeyrie, C. Miniatura, D. Wilkowski, and R. Kaiser, Coherent Light Transport in a Cold Strontium Cloud, Phys. Rev. Lett. **88**, 203902 (2002).

[10] S. J. Roof, K. J. Kemp, M. D. Havey, and I. M. Sokolov, Observation of Single-Photon Superradiance and the Cooperative Lamb Shift in an Extended Sample of Cold Atoms, Phys. Rev. Lett. **117**, 073003 (2016).

[11] W. Guerin, M. O. Araújo, and R. Kaiser, Subradiance in a Large Cloud of Cold Atoms, Phys. Rev. Lett. **116**, 083601 (2016).

[12] M. O. Araújo, I. Krešić, R. Kaiser, and W. Guerin, Superradiance in a Large and Dilute Cloud of Cold Atoms in the Linear-Optics Regime, Phys. Rev. Lett. **117**, 073002 (2016).

[13] T. Bienaimé, S. Bux, E. Lucioni, P. W. Courteille, N. Piovella, and R. Kaiser, Observation of a Cooperative Radiation Force in the Presence of Disorder, Phys. Rev. Lett. **104**, 183602 (2010).

[14] S. Balik, A. L. Win, M. D. Havey, I. M. Sokolov, and D. V. Kupriyanov, Near-resonance light scattering from a high-density ultracold atomic ^{87}Rb gas, Phys. Rev. A **87**, 053817 (2013).

[15] S. L. Bromley, B. Zhu, M. Bishof, X. Zhang, T. Bothwell, J. Schachenmayer, T. L. Nicholson, R. Kaiser, S. F. Yelin, M. D. Lukin, A. M. Rey, and J. Ye, Collective atomic scattering and motional effects in a dense coherent medium, Nat. Commun. **7**, 11039 (2016).

[16] R. H. Lehmberg, Radiation from an N-atom system. I. General formalism, Phys. Rev. A **2**, 883 (1970).

[17] R. Friedberg, S. R. Hartmann, and J. T. Manassah, Frequency shifts in emission and absorption by resonant systems ot two-level atoms, Phys. Rep. **7**, 101 (1973).

[18] M. Gross and S. Haroche, Superradiance: An essay on the theory of collective spontaneous emission, Phys. Rep. **93**, 301 (1982).

[19] O. Morice, Y. Castin, and J. Dalibard, Refractive index of a dilute Bose gas, Phys. Rev. A **51**, 3896 (1995).

[20] N. Cherroret, D. Delande, and B. A. van Tiggelen, Induced dipole-dipole interactions in light diffusion from point dipoles, Phys. Rev. A **94**, 012702 (2016).

[21] J. Keaveney, A. Sargsyan, U. Krohn, I. G. Hughes, D. Sarkisyan, and C. S. Adams, Cooperative Lamb Shift in An Atomic Vapor Layer of Nanometer Thickness, Phys. Rev. Lett. **108**, 173601 (2012).

[22] J. Javanainen, J. Ruostekoski, Y. Li, and S. M. Yoo, Shifts of a Resonance Line in a Dense Atomic Sample, Phys. Rev. Lett. **112**, 113603 (2014).

[23] J. Pellegrino, R. Bourgain, S. Jennewein, Y. R. P. Sortais, A. Browaeys, S. D. Jenkins, and J. Ruostekoski, Observation of Suppression of Light Scattering Induced by Dipole-Dipole Interactions in a Cold-Atom Ensemble, Phys. Rev. Lett. **113**, 133602 (2014).

[24] S. Jennewein, M. Besbes, N. J. Schilder, S. D. Jenkins, C. Sauvan, J. Ruostekoski, J.-J. Greffet, Y. R. P. Sortais, and A. Browaeys, Coherent Scattering of Near-Resonant Light by a Dense Microscopic Cold Atomic Cloud, Phys. Rev. Lett. **116**, 233601 (2016).

[25] S. D. Jenkins, J. Ruostekoski, J. Javanainen, R. Bourgain, S. Jennewein, Y. R. P. Sortais, and A. Browaeys, Optical Resonance Shifts in the Fluorescence of Thermal and Cold Atomic Gases, Phys. Rev. Lett. **116**, 183601 (2016).

[26] L. Corman, J. L. Ville, R. Saint-Jalm, M. Aidelsburger, T. Bienaimé, S. Nascimbène, J. Dalibard, and J. Beugnon, Transmission of near-resonant light through a dense slab of cold atoms, Phys. Rev. A **96**, 053629 (2017).

[27] J. L. Ville, T. Bienaimé, R. Saint-Jalm, L. Corman, M. Aidelsburger, L. Chomaz, K. Kleinlein, D. Perconte, S. Nascimbène, J. Dalibard, and J. Beugnon, Loading and compression of a single two-dimensional Bose gas in an optical accordion, Phys. Rev. A **95**, 013632 (2017).

[28] See Supplemental Material at http://link.aps.org/supplemental/10.1103/PhysRevA.97.061801 for description of the calibration of the imaging setup, the derivation of the semi-analytical model, and supplementary data for the models.

[29] E. Bradley, Better bootstrap confidence intervals, J. Am. Stat. Assoc. **82**, 171 (1987).

[30] L. Chomaz, L. Corman, T. Yefsah, R. Desbuquois, and J. Dalibard, Absorption imaging of a quasi-two-dimensional gas: A multiple scattering analysis, New J. Phys. **14**, 055001 (2012).

[31] S. E. Skipetrov and I. M. Sokolov, Magnetic-Field-Driven Localization of Light in a Cold-Atom Gas, Phys. Rev. Lett. **114**, 053902 (2015).

[32] D. J. Whiting, E. Bimbard, J. Keaveney, M. A. Zentile, C. S. Adams, and I. G. Hughes, Electromagnetically induced absorption in a nondegenerate three-level ladder system, Opt. Lett. **40**, 4289 (2015).

[33] D. J. Whiting, J. Keaveney, C. S. Adams, and I. G. Hughes, Direct measurement of excited-state dipole matrix elements using electromagnetically induced transparency in the hyperfine Paschen-Back regime, Phys. Rev. A **93**, 043854 (2016).

[34] F. Riboli, F. Uccheddu, G. Monaco, N. Caselli, F. Intonti, M. Gurioli, and S. E. Skipetrov, Tailoring Correlations of the Local Density of States in Disordered Photonic Materials, Phys. Rev. Lett. **119**, 043902 (2017).

[35] S. E. Skipetrov and J. H. Page, Red light for Anderson localization, New J. Phys. **18**, 021001 (2016).

[36] S. E. Skipetrov and I. M. Sokolov, Absence of Anderson Localization of Light in a Random Ensemble of Point Scatterers, Phys. Rev. Lett. **112**, 023905 (2014).

[37] N. Cherroret and S. E. Skipetrov, Microscopic derivation of self-consistent equations of Anderson localization in a disordered medium of finite size, Phys. Rev. E **77**, 046608 (2008).

PHYSICAL REVIEW LETTERS **121,** 145301 (2018)

Featured in Physics

Sound Propagation in a Uniform Superfluid Two-Dimensional Bose Gas

J. L. Ville, R. Saint-Jalm, É. Le Cerf, M. Aidelsburger,[*] S. Nascimbène, J. Dalibard, and J. Beugnon[†]
Laboratoire Kastler Brossel, Collège de France, CNRS, ENS-PSL University, Sorbonne Université,
11 Place Marcelin Berthelot, 75005 Paris, France

(Received 5 April 2018; published 3 October 2018)

In superfluid systems several sound modes can be excited, such as, for example, first and second sound in liquid helium. Here, we excite running and standing waves in a uniform two-dimensional Bose gas and we characterize the propagation of sound in both the superfluid and normal regimes. In the superfluid phase, the measured speed of sound is in good agreement with the prediction of a two-fluid hydrodynamic model, and the weak damping is well explained by the scattering with thermal excitations. In the normal phase we observe a stronger damping, which we attribute to a departure from hydrodynamic behavior.

DOI: 10.1103/PhysRevLett.121.145301

Propagation of sound waves is at the heart of our understanding of quantum fluids. In liquid helium, the celebrated two-fluid model was confirmed by the observation of first and second sound modes [1,2]. There, first sound stands for the usual sound appellation, namely, a density wave for which normal and superfluid fractions oscillate in phase. Second sound corresponds to a pure entropy wave with no perturbation in density (normal and superfluid components oscillating out of phase), and is generally considered as conclusive evidence of superfluidity.

Sound wave propagation is also central to the study of dilute quantum gases, providing information on thermodynamic properties, relaxation mechanisms, and superfluid behavior. In ultracold strongly interacting Fermi gases, the existence of first and second sound modes in the superfluid phase was predicted [3] and observed in experiments [4,5], with a behavior similar to liquid helium. In three-dimensional (3D) weakly interacting Bose-Einstein condensates (BECs), one still expects two branches of sound with speeds $c^{(1)} > c^{(2)}$ but the nature of first and second sound is strongly modified because of their large compressibility [6]. At zero temperature the gas is fully superfluid and the only relevant mode corresponds to Bogoliubov excitations, i.e., density oscillations. At nonzero temperature, an isothermal density perturbation is expected to excite mostly the second sound mode, propagating at a velocity approximately proportional to the square root of the superfluid fraction [6,7]. This contrasts to the usual picture for liquid helium where second sound is excited via local heating [1,2]. Sound waves in an elongated 3D BEC were observed in Refs. [8–10] in a regime where the sound speed remains close to the Bogoliubov sound speed.

The study of sound propagation can be very insightful for two-dimensional (2D) Bose fluids, where superfluidity does not result from a Bose-Einstein condensation, but occurs instead via a Berezinskii-Kosterlitz-Thouless (BKT) transition [11]. This transition is associated with a jump of the superfluid density but as the transition is of infinite order, the jump cannot be revealed by the thermodynamic properties of the fluid. However, the presence of a superfluid component is predicted to lead to two distinct sound modes, whose velocities $c_{\mathrm{HD}}^{(1)}$ and $c_{\mathrm{HD}}^{(2)}$ were calculated within a hydrodynamic model in Refs. [12,13]. These velocities are functions of the superfluid density and thus both exhibit a discontinuity associated with the superfluid jump at the critical point. In particular, the second sound velocity is expected to remain nonzero just below the critical point of the superfluid to normal transition and to disappear just above. Experimentally, 2D Bose fluids were first realized with liquid helium films adsorbed on a substrate [14]; in this case the presence of the substrate blocks the motion of the normal component and thus prevents the investigation of such phenomena.

In this Letter, we report on the first observation of sound propagation in a 2D Bose fluid. We observe a single density sound mode both in the superfluid and normal regimes. Deep in the superfluid regime, the measured sound speed agrees well with the Bogoliubov prediction. We measure a weak damping rate compatible with Landau damping, a fundamental mechanism for the understanding of collective modes of superfluids at finite temperature [15]. For higher temperatures, we observe a decrease of the sound velocity consistent with the second sound speed variation predicted in Ref. [12] from two-fluid hydrodynamics. The damping of sound increases with temperature and, above the critical point, we still observe strongly damped density waves with no discernable discontinuity at the critical point. The discrepancy with the two-fluid model predictions could be due to a departure from hydrodynamic behavior.

Our experimental setup has been described in Refs. [16,17] and more details can be found in Ref. [18]. Briefly, we confine ^{87}Rb atoms in the $|F = 1, m = 0\rangle$ ground state into a 2D rectangular box potential

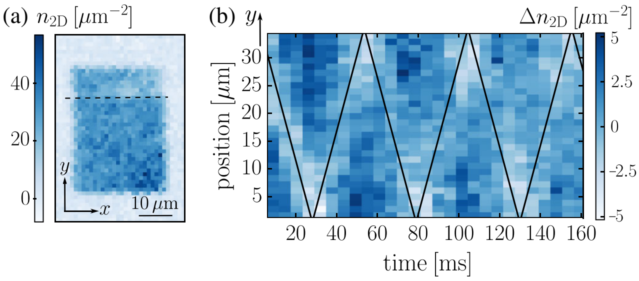

FIG. 1. Experimental protocol and observation of propagating waves. (a) Absorption image of the cloud perturbed by a local additional potential. The excitation is delimited by the horizontal dashed line and depletes the atomic density by a factor around 1/3. (b) Example of time evolution of the variation of the density profile n_{2D} with respect to its spatial mean value (integrated along x) obtained after abruptly removing the additional potential. For this example $T/T_c = 0.37(12)$ and $n_{2D} = 29(3)\ \mu\mathrm{m}^{-2}$. The position of the dip is fitted by a triangle function (black solid line) which gives, $c = 1.49(3)$ mm/s.

of size $L_x \times L_y = 30(1) \times 38(1)\ \mu$m [see Fig. 1(a)]. The confinement along the vertical z direction can be approximated by a harmonic potential of frequency $\omega_z/(2\pi) = 4.59(4)$ kHz. We always operate in the quasi-2D regime where interaction and thermal energies are smaller than $\hbar\omega_z$. The gas is characterized by the effective coupling constant $g = \hbar^2\tilde{g}/m = (\hbar^2/m)\sqrt{8\pi}a_s/\ell_z$, where a_s is the s-wave scattering length, $\ell_z = \sqrt{\hbar/(m\omega_z)}$, and m the atomic mass [11]. We operate here in the weakly interacting regime: $\tilde{g} = 0.16(1)$. In the quasi-2D regime and for a given $\tilde{g}$, the equilibrium state of the cloud is only characterized by a dimensionless combination of T and n_{2D}, thanks to an approximate scale invariance [11]. In the following we use the ratio T/T_c, where $T_c = 2\pi n_{2D}\hbar^2/[mk_B \ln(380/\tilde{g})]$ is the calculated critical temperature for the BKT phase transition [25]. In this work, we study Bose gases from the highly degenerate regime ($T/T_c \approx 0.2$) to the normal regime ($T/T_c \approx 1.4$).

We first investigate propagating waves which we excite by a density perturbation. Prior to evaporative cooling in the box potential, we apply to the cloud a repulsive potential, which creates a density dip on one side of the rectangle [see Fig. 1(a)]. The extension of this dip is about 1/4 of the length of the box and its amplitude is chosen so that the density in this region is decreased by a factor of 1/3. After equilibration, we abruptly remove the additional potential and monitor the propagation of this density dip. We show in Fig. 1(b) a typical time evolution of the density profile integrated along the transverse direction to the perturbation for a strongly degenerate gas. In this regime, the density perturbation propagates at constant speed and bounces several times off the walls of the box. Using the calibrated size of the box, we extract a speed $c = 1.49(3)$ mm/s. This value is slightly lower than the Bogoliubov sound speed $c_B = \sqrt{gn_{2D}/m} = 1.6(1)$ mm/s expected at zero temperature for the measured density $n_{2D} = 29(3)\ \mu\mathrm{m}^{-2}$. The measured speed is also close to the second sound mode velocity $c_{\mathrm{HD}}^{(2)} = 1.4(1)$ mm/s, estimated from two-fluid hydrodynamics at our experimental value of $T/T_c = 0.37(12)$ [12]. The first sound, expected to propagate at a much higher speed $c_{\mathrm{HD}}^{(1)} = 3.3(3)$ mm/s [12], does not appear in our measurements that feature a single wave front only. The absence of first sound in our experiments can be explained by its very small coupling to isothermal density excitations in a weakly interacting gas [12].

In order to probe the role of the cloud degeneracy on the sound wave propagation, we vary both n_{2D} and T. For each configuration, we excite the cloud with the protocol described above, while adjusting the intensity of the depleting laser beam to keep the density dip around 1/3 of nonperturbed density. At lower degeneracies, sound waves are strongly damped and the aforementioned measurements of the density dip position become inadequate. We thus focus on the time evolution of the lowest-energy mode [26]. We decompose the density profiles integrated along x as

$$n(y,t) = \bar{n} + \sum_{j=1}^{\infty} A_j(t)\ \cos(j\pi y/L_y), \qquad (1)$$

where $\bar{n}$ is the average density along y and the A_j are the amplitudes of the modes. The choice of the cosine basis ensures the cancellation of the velocity field on the edges of the box. Our excitation protocol mainly couples to the lowest energy modes. We keep the excitation to a low value to be in the linear regime while still observing a clear signal for the lowest-energy mode, which in return provides a too weak signal for a quantitative analysis of higher modes [27]. For each duration of the evolution, we compute the overlap of the atomic density profile with the lowest-energy mode. Examples of the time evolution of the normalized amplitude $\tilde{A}_1(t) = A_1(t)/A_1(0)$ for different degrees of degeneracy are shown in Fig. 2. We observe damped oscillations with a damping rate increasing with T/T_c. We fit the experimental data by an exponentially damped sinusoidal curve $e^{-\Gamma t/2}[\Gamma/2\omega \sin(\omega t) + \cos(\omega t)]$ to determine the energy damping rate Γ and the frequency ω [28]. We then determine the speed of sound $c = L_y\omega/\pi$ and the quality factor of this mode $Q = 2\omega/\Gamma$.

We consolidate all our measurements of speed of sound and quality factors in Fig. 3. To facilitate comparison with theory, we show in Fig. 3(a) the values of c normalized to c_B. The non-normalized results are reported in Ref. [18] for completeness. In the temperature range $T \lesssim 0.9T_c$, we measure weakly damped density oscillations, corresponding to a well-defined sound mode ($Q \gtrsim 10$). In this regime, we observe a significant decrease by about ≈25% of the sound velocity for increasing values of T/T_c. The

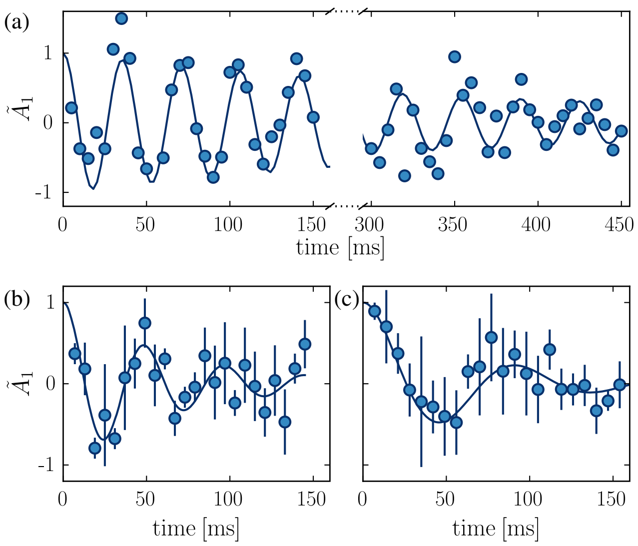

FIG. 2. Time evolution of the normalized amplitude of the lowest-energy mode for (a) $T/T_c = 0.21(11)$, (b) $T/T_c = 0.95(5)$, (c) $T/T_c = 1.38(18)$. The solid line is a fit of an exponentially damped sinusoidal oscillation. For (b) and (c) graphs, each data point is the average of three measurements and the error bars represent the associated standard deviation. In (a) each point corresponds to a single measurement.

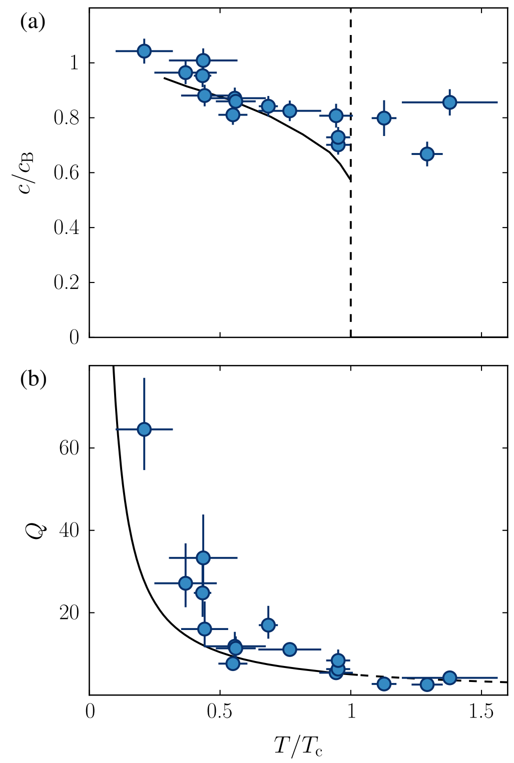

FIG. 3. Speed of sound and quality factor. (a) Measured speed of sound c normalized to c_B. The vertical dashed line shows the position of the critical point. The solid line shows the result from the two-fluid hydrodynamic model applied to the 2D Bose gas [12]. A fit to the data points below T_c by this hydrodynamic model with a free multiplicative factor shows that the measurements are globally 3% above the theoretical prediction. This could correspond to a 6% systematic error in the calibration of $n_{\rm 2D}$ used to determine $c_B \propto n_{\rm 2D}^{1/2}$. Our estimated uncertainty on $n_{\rm 2D}$ is on the order of 11% (see Ref. [18]) and our measurements are thus compatible with the predicted value of the speed of second sound $c_{\rm HD}^{(2)}$. (b) Quality factor $Q = 2\omega/\Gamma$ of the lowest-energy mode. The solid line is the prediction for Landau damping [30] (continued as a dashed line for $T > T_c$). For both graphs, the error bars represent the statistical uncertainty extracted from the fitting procedures used to determine c, Γ and T/T_c.

measured velocities agree well with the prediction from two-fluid hydrodynamics [12] combined with the equation of state of the 2D Bose gas [29]. According to the analysis of Ref. [12] for weakly interacting gases, the change of speed of sound is mainly due to the variation of the superfluid fraction $f_{\rm s}$ from ≈ 1 at $T = 0$ to ≈ 0.5 close to $T = T_c$ with the approximate scaling $c_{\rm HD}^{(2)} \propto f_{\rm s}^{1/2}$ [13]. We note the absence of a discernable discontinuity of sound velocity at T_c, in disagreement with the two-fluid hydrodynamic approach.

In order to explain this disagreement, we first note that collective excitations in ultracold Bose gases can be of different nature depending on the relative amplitude of mean-field effects and collisions between particles [9,31,32]. In the very degenerate regime $T \ll T_c$, the system is naturally described within quantum hydrodynamics [33], where interactions between particles occur via a mean-field energy $E_{\rm int}$. This is valid for $\omega \ll E_{\rm int}/\hbar$, which is satisfied for our setup. In this regime we expect sound waves propagating at c_B, as observed in the experiment. For larger temperatures, but still below T_c, the normal fraction becomes significant. In order to use an hydrodynamic two-fluid model in that case, the local equilibrium condition also requires $\omega \ll \Gamma_{\rm coll}$, where $\Gamma_{\rm coll} = \hbar\tilde{g}^2 n/(2m)$ is the collision rate [34]. The same condition holds for the single fluid case above T_c. The opposite "collisionless" regime has been recently studied in Refs. [35,36]. It also leads to the existence of a sound mode, originating solely from mean-field interactions described, e.g., by a Landau-Vlasov kinetic equation. For $T \gtrsim T_c$ this collisionless sound mode has a velocity notably smaller than the hydrodynamic result and close to the prediction of Ref. [12] for the second sound velocity at T_c. For our data above T_c we estimate $\Gamma_{\rm coll}/\omega$ to be in the range 1.6–3.4, which indicates that we are in a crossover between these limiting hydrodynamic and collisionless regimes.

The distinction between the quantum hydrodynamics regime and the crossover regime ($\Gamma_{\rm coll} \sim \omega$) is supported by the study of the measured quality factors [see Fig. 3(b)]. For $T \ll T_c$, damping can be described at first order by the decay of low-lying collective excitations via scattering on thermal excitations [15,37], the so-called Landau damping

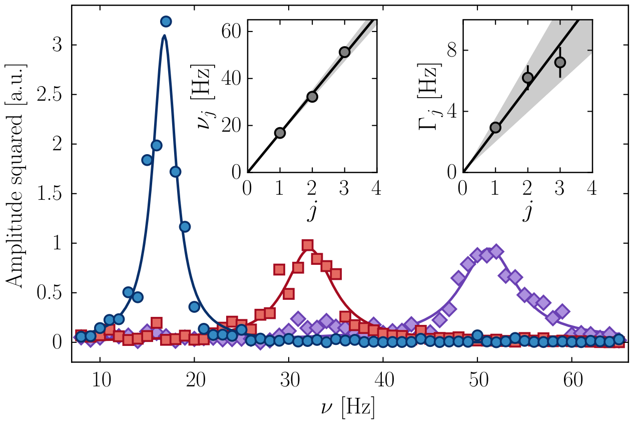

FIG. 4. Observation of standing waves in the box potential. Contribution of the three lowest-energy modes to the amplitude of the density modulation: $j = 1$ (circles), $j = 2$ (squares), $j = 3$ (diamonds). The solid lines are Lorentzian fits. The two insets show the resonance frequencies ν_j and the full widths at half maximum Γ_j resulting from these fits. The solid lines in the insets are linear fit to the data and the shaded areas represent the uncertainty on the fitted slope. From the slope $c/(2L_y)$ of the fit to the resonance frequencies, we find $c = 1.90(9)$ mm/s. For this specific experiment, the length of the cloud is $L_y = 57(1)$ μm and the degree of degeneracy is $T/T_c = 0.41(7)$.

mechanism. It predicts an increase of the quality factor when decreasing temperature due to the reduction of the number of thermal excitations available for scattering with the sound mode [38]. This perturbative approach is meaningful for large enough quality factors and does not take into account interactions between phonon modes. The solid line in Fig. 3(b) corresponds to Landau prediction for a 2D system [30]. It shows an overall good agreement with our data, even close to T_c, where it gradually looses its validity. Finally, above T_c, we measured low quality factors, showing that the observed sound mode is strongly damped, in agreement with the predictions of the collisionless sound mode [35].

In the highly degenerate regime, the low damping rate allows us to observe standing waves. To study them, we modulate sinusoidally the amplitude of the potential creating the dip of density on one edge of the box [39]. After ≈1 s we extract, for each frequency ν of the excitation, the amplitude of the (time-dependent) density modulation induced on the cloud (see Ref. [18] for details). We show in Fig. 4 the contribution of the three lowest-energy modes to the amplitude of the modulation as a function of the excitation frequency. For each mode j we observe a clear resonance peak centered at a frequency ν_j. We display in the insets the resonance frequencies and width of the modes. The ν_j's are equally spaced, as confirmed by the linear fit. In addition, the right inset shows the widths of the peaks. They also increase approximately linearly with j [40], meaning that the quality factor associated with these peaks is almost the same, as expected for Landau damping.

We focus in this work on a weakly interacting Bose gas which features a large compressibility compared to liquid helium or strongly interacting Fermi gases. A natural extension of this work would thus be to investigate second sound propagation for increasing interactions [13]. It would also be interesting to investigate first sound, e.g., by applying a localized temperature excitation [5]. During the completion of this work we were informed that a related study with a homogeneous 3D Fermi gas was currently performed at MIT [41].

This work is supported by DIM NanoK and ERC (Synergy UQUAM). This project has received funding from the European Union's Horizon 2020 research and innovation programme under the Marie Skłodowska-Curie Grant Agreement No. 703926. We thank S. Stringari, L. Pitaevskii, M. Ota, N. Proukakis, F. Dalfovo, F. Larcher, and P. C. M. Castilho for fruitful discussions, M. Villiers for experimental assistance, and F. Gerbier, R. Lopes, and M. Zwierlein for their reading of the manuscript.

J. L. V. and R. S. J. contributed equally to this work.

[*] Present address: Fakultät für Physik, Ludwig-Maximilians-Universität München, Schellingstr. 4, 80799 Munich, Germany.

[†] beugnon@lkb.ens.fr

[1] R. J. Donnelly, The two-fluid theory and second sound in liquid helium, Phys. Today **62**, 34 (2009).
[2] S. Balibar, The discovery of superfluidity, J. Low Temp. Phys. **146**, 441 (2007).
[3] E. Taylor, H. Hu, X.-J. Liu, L. P. Pitaevskii, A. Griffin, and S. Stringari, First and second sound in a strongly interacting Fermi gas, Phys. Rev. A **80**, 053601 (2009).
[4] J. Joseph, B. Clancy, L. Luo, J. Kinast, A. Turlapov, and J. E. Thomas, Measurement of Sound Velocity in a Fermi Gas Near a Feshbach Resonance, Phys. Rev. Lett. **98**, 170401 (2007).
[5] L. A. Sidorenkov, M. K. Tey, R. Grimm, Y.-H. Hou, L. Pitaevskii, and S. Stringari, Second sound and the superfluid fraction in a Fermi gas with resonant interactions, Nature (London) **498**, 78 (2013).
[6] A. Griffin and E. Zaremba, First and second sound in a uniform Bose gas, Phys. Rev. A **56**, 4839 (1997).
[7] A. Griffin, T. Nikuni, and E. Zaremba, *Bose-Condensed Gases at Finite Temperatures* (Cambridge University Press, Cambridge, England, 2009).
[8] M. R. Andrews, D. M. Kurn, H.-J. Miesner, D. S. Durfee, C. G. Townsend, S. Inouye, and W. Ketterle, Propagation of Sound in a Bose-Einstein Condensate, Phys. Rev. Lett. **79**, 553 (1997).
[9] D. M. Stamper-Kurn, H.-J. Miesner, S. Inouye, M. R. Andrews, and W. Ketterle, Collisionless and Hydrodynamic Excitations of a Bose-Einstein Condensate, Phys. Rev. Lett. **81**, 500 (1998).

[10] R. Meppelink, S. B. Koller, and P. van der Straten, Sound propagation in a Bose-Einstein condensate at finite temperatures, Phys. Rev. A **80**, 043605 (2009).

[11] Z. Hadzibabic and J. Dalibard, Two-dimensional Bose fluids: An atomic physics perspective, Riv. Nuovo Cimento **34**, 389 (2011).

[12] T. Ozawa and S. Stringari, Discontinuities in the First and Second Sound Velocities at the Berezinskii-Kosterlitz-Thouless Transition, Phys. Rev. Lett. **112**, 025302 (2014).

[13] M. Ota and S. Stringari, Second sound in a two-dimensional Bose gas: From the weakly to the strongly interacting regime, Phys. Rev. A **97**, 033604 (2018).

[14] D. J. Bishop and J. D. Reppy, Study of the Superfluid Transition in Two-Dimensional ^{4}He Films, Phys. Rev. Lett. **40**, 1727 (1978).

[15] L. P. Pitaevskii and S. Stringari, Landau damping in dilute Bose gases, Phys. Lett. A **235**, 398 (1997).

[16] J. L. Ville, T. Bienaimé, R. Saint-Jalm, L. Corman, M. Aidelsburger, L. Chomaz, K. Kleinlein, D. Perconte, S. Nascimbène, J. Dalibard, and J. Beugnon, Loading and compression of a single two-dimensional Bose gas in an optical accordion, Phys. Rev. A **95**, 013632 (2017).

[17] M. Aidelsburger, J. L. Ville, R. Saint-Jalm, S. Nascimbène, J. Dalibard, and J. Beugnon, Relaxation Dynamics in the Merging of N Independent Condensates, Phys. Rev. Lett. **119**, 190403 (2017).

[18] See Supplemental Materials at http://link.aps.org/supplemental/10.1103/PhysRevLett.121.145301 for methods and complementary results, which includes [19–24].

[19] L. Corman, J. L. Ville, R. Saint-Jalm, M. Aidelsburger, T. Bienaimé, S. Nascimbène, J. Dalibard, and J. Beugnon, Transmission of near-resonant light through a dense slab of cold atoms, Phys. Rev. A **96**, 053629 (2017).

[20] K. Hueck, N. Luick, L. Sobirey, J. Siegl, T. Lompe, and H. Moritz, Two-Dimensional Homogeneous Fermi Gases, Phys. Rev. Lett. **120**, 060402 (2018).

[21] A. Ramanathan, S. R. Muniz, K. C. Wright, R. P. Anderson, W. D. Phillips, K. Helmerson, and G. K. Campbell, Partial-transfer absorption imaging: A versatile technique for optimal imaging of ultracold gases, Rev. Sci. Instrum. **83**, 083119 (2012).

[22] M. F. Riedel, P. Böhi, Y. Li, T. W. Hänsch, A. Sinatra, and P. Treutlein, Atom-chip-based generation of entanglement for quantum metrology, Nature (London) **464**, 1170 (2010).

[23] V. Pastukhov, Damping of Bogoliubov excitations at finite temperatures, J. Phys. A **48**, 405002 (2015).

[24] P. C. Hohenberg and P. C. Martin, Microscopic theory of superfluid helium, Ann. Phys. (N.Y.) **34**, 291 (1965).

[25] N. Prokof'ev, O. Ruebenacker, and B. Svistunov, Critical Point of a Weakly Interacting Two-Dimensional Bose Gas, Phys. Rev. Lett. **87**, 270402 (2001).

[26] N. Navon, A. L. Gaunt, R. P. Smith, and Z. Hadzibabic, Emergence of a turbulent cascade in a quantum gas, Nature (London) **539**, 72 (2016).

[27] The study of the second spatial mode gives oscillation frequencies that are in good approximation twice larger than the lowest-energy mode and thus results in very similar speeds of sounds. However, the damping rate of this mode is also larger (see Fig. 4) and we cannot robustly estimate its lifetime for our deliberately weak excitation protocol.

[28] The choice of this oscillating function ensures a null derivative of the amplitude of the mode at $t = 0$, when the potential creating the density dip is removed. This behavior is expected from the continuity of the wave function and of its derivative describing the state of the gas at $t = 0$.

[29] N. Prokof'ev and B. Svistunov, Two-dimensional weakly interacting Bose gas in the fluctuation region, Phys. Rev. A **66**, 043608 (2002).

[30] M.-C. Chung and A. B. Bhattacherjee, Damping in 2D and 3D dilute Bose gases, New J. Phys. **11**, 123012 (2009).

[31] A. Griffin, Wen-Chin Wu, and S. Stringari, Hydrodynamic Modes in a Trapped Bose Gas above the Bose-Einstein Transition, Phys. Rev. Lett. **78**, 1838 (1997).

[32] D. Guéry-Odelin, F. Zambelli, J. Dalibard, and S. Stringari, Collective oscillations of a classical gas confined in harmonic traps, Phys. Rev. A **60**, 4851 (1999).

[33] L. Pitaevskii and S. Stringari, *Bose-Einstein Condensation and Superfluidity*, Vol. 164 (Oxford University Press, 2016).

[34] D. S. Petrov and G. V. Shlyapnikov, Interatomic collisions in a tightly confined Bose gas, Phys. Rev. A **64**, 012706 (2001).

[35] M. Ota, F. Larcher, F. Dalfovo, L. Pitaevskii, N. P. Proukakis, and S. Stringari, Collisionless Sound in a Uniform Two-Dimensional Bose Gas, following letter, Phys. Rev. Lett. **121**, 145302 (2018).

[36] A. Cappellaro, F. Toigo, and L. Salasnich, Collisionless Dynamics in Two-Dimensional Bosonic Gases, arXiv:1807.02541 [Phys. Rev. A (to be published)].

[37] R. Meppelink, S. B. Koller, J. M. Vogels, H. T. C. Stoof, and P. van der Straten, Damping of Superfluid Flow by a Thermal Cloud, Phys. Rev. Lett. **103**, 265301 (2009).

[38] Note that Beliaev damping, another mechanism for the decay of low-lying excitations, is absent for the first spatial mode of the box. Indeed, it corresponds to a decay of a low-lying excitation into two excitations with lower energies and thus does not exist for the lowest energy mode.

[39] Y.-H. Wang, A. Kumar, F. Jendrzejewski, R. M. Wilson, M. Edwards, S. Eckel, G. K. Campbell, and C. W. Clark, Resonant wave packets and shock waves in an atomtronic SQUID, New J. Phys. **17**, 125012 (2015).

[40] Because of the finite duration of the excitation (1 s), the width of the peaks is Fourier limited at a typical width of 1 Hz, which should be taken into account for a more quantitative analysis.

[41] M. Zwierlein (private communication).

F

RÉSUMÉ EN FRANÇAIS

Chapitre 1: Introduction

Ce travail de thèse est consacré à l'étude expérimentale de gaz de Bose bidimensionnels en faible interaction, et se concentre sur les propriétés de cohérence spatiale ainsi que sur les symétries fondamentales de ce système.

L'étude des symétries d'un système physique est en effet au cœur de la compréhension que l'on peut en avoir, et cette approche a apporté de nombreuses avancées dans des domaines variés de la physique au cours du dernier siècle. Le résultat le plus éclatant est dû à Emmy Noether qui a démontré que l'existence d'une symétrie continue procure à un système une quantité conservée au cours du temps [1]. Ces symétries continues peuvent être étudiées à la lumière de la théorie de Lie qui permet d'en comprendre la structure algébrique [5].

Le choix d'étudier un système de basse dimension spatiale peut se justifier par le fait que les systèmes à une ou deux dimensions présentent des symétries qui sont très riches [12], comme par exemple le groupe de symétrie conforme [14]. Les systèmes de basse dimension sont également susceptibles de présenter autant de quantités invariantes que de degrés de liberté, et l'étude de ces problèmes intégrables a été le sujet de nombreux travaux [16].

La thermodynamique d'un système est aussi affectée par le faible nombre de dimensions, comme l'illustre par exemple le théorème de Mermin-Wagner-Hohenberg. Ce théorème affirme qu'un ordre à longue portée ne peut s'établir à température non nulle dans un système à une ou deux dimensions d'espace présentant des interactions à courte portée [141, 142]. La raison en est que les fluctuations thermiques ont une importance accrue par rapport à une situation à trois dimensions (ou plus).

Une particularité s'ajoute avec l'existence d'une transition de phase topologique pour certains systèmes bidimensionnels. Cette transition, prédite par Berezinskii [25] ainsi que par Kosterlitz et Thouless [26], provient de l'appariement de défauts topologiques, les vortex, et non de la brisure spontanée d'une symétrie. Il s'agit d'une transition d'ordre infini qui a été intensivement étudiée [27]. Une propriété intéressante est la discontinuité de la fraction superfluide au point critique de la transition. Cette discontinuité est universelle et s'accompagne d'un changement de comportement à grande distance de la fonction de corrélation du premier ordre.

Le gaz de Bose à deux dimensions en faible interaction est sujet à cette transition de phase Berezinskii-Kosterlitz-Thouless (BKT) [38]. L'un des objectifs de cette thèse est de mesurer pour un gaz uniforme les propriétés de cohérence spatiale qui sont dues à la physique particulière de cette transition de phase. Le second objectif est de déterminer les symétries fondamentales de ce système lorsque celui-ci est soumis à un potentiel harmonique, ainsi que de mesurer les conséquences de ces symétries dites « dynamiques » sur l'évolution temporelle d'un gaz.

Le plan de cette thèse est le suivant. Dans un premier temps je présente le montage expérimental qui nous permet de produire des gaz de Bose uniformes à deux dimensions en faible interaction, de contrôler leur état, et de mesurer leurs propriétés. Dans une deuxième partie j'explique quelles sont les propriétés de cohérence spatiale de part et d'autre de la transition BKT, et je montre deux méthodes expérimentales qui visent à mesurer la fonction de corrélation du premier ordre. Dans une troisième et dernière partie, je présente les symétries dynamiques du gaz de Bose à deux dimensions et j'expose l'approche expérimentale qui nous permet de mettre en lumière les conséquences de ces symétries. Ces expériences, de façon surprenante, révèlent des propriétés dynamiques particulières de certains nuages pris dans des conditions initiales bien choisies: ces nuages ont une évolution temporelle qui semble être périodique.

PARTIE I: CRÉATION ET MANIPULATION DE GAZ DE BOSE EN DEUX DIMENSIONS

Chapitre 2: Le montage expérimental

Ce chapitre présente le protocole expérimental qui nous permet de refroidir des atomes de rubidium afin de créer des gaz de Bose à deux dimensions.

Les premières étapes sont des étapes standard dans la communauté des atomes froids et utilisent les méthodes de refroidissement par laser développées pendant ces dernières décennies. Une succession de pièges magnéto-optiques, d'évaporation dans un piège magnétique quadripolaire et d'évaporation dans un piège optique amène un échantillon d'atomes de rubidium jusqu'à un régime de dégénérescence quantique: un condensat de Bose-Einstein à trois dimensions est formé.

Une particularité de notre montage expérimental est l'utilisation d'un « accordéon optique » permettant de piéger ce condensat dans un site unique d'un réseau optique unidimensionnel de pas dynamiquement variable. La construction de cet accordéon a constitué le sujet de mon stage de Master, et son implémentation sur le dispositif expérimental s'est déroulée durant les premiers mois de ma thèse. Grâce à cet outil, nous pouvons capturer un grand nombre d'atomes (de l'ordre de 10^5) et leur imposer un confinement fort dans la direction verticale (z), ce qui crée une crêpe d'atomes dont la dynamique est gelée selon l'axe z. La taille verticale du nuage est inférieure au micromètre. Je développe dans le manuscrit de thèse certaines caractérisations de notre accordéon optique, comme par exemple le mécanisme de stabilisation spatiale du réseau optique.

Une deuxième particularité provient de la création de potentiels à fond plat dans le plan xy. La surface d'une matrice de micro-miroirs est imagée sur les atomes grâce à un objectif de microscope avec de la lumière répulsive et permet, grâce à la versatilité de cette matrice, de contrôler la géométrie du nuage d'atomes avec une grande résolution optique. La taille de nos échantillons est de l'ordre de 50 µm de diamètre.

La densité atomique des nuages ainsi créés peut être mesurée grâce à une imagerie par absorption utilisant un second objectif de microscope. Ces mesures permettent par exemple de caractériser le degré d'uniformité de la densité atomique. Un exemple d'images obtenues est montré sur la figure 2.8[1], et illustre la polyvalence de notre dispositif.

Les atomes de rubidium ont un degré interne de spin qui provient essentiellement du spin de leur électron de valence et du spin de leur noyau. L'état fondamental comporte deux niveaux séparés par environ 6, 8 GHz. Le niveau le plus bas ($F = 1$, où F désigne le spin total de l'atome) possède trois niveaux Zeeman ($m_F = -1, 0, 1$), et l'autre niveau ($F = 2$) en possède cinq ($m_F = -2, \cdots, 2$). L'énergie de ces niveaux Zeeman dépend du nombre quantique m_F, du facteur de Landé $g_F = \pm 1$ et du champ magnétique local B. Initialement les atomes sont tous dans l'état $F = 1, m_F = -1$, seul état piégé par le piège magnétique quadripolaire utilisé lors des étapes de refroidissement.

Durant ma thèse j'ai développé un outil inspiré de la thèse de K. Maussang [104] permettant d'effectuer des rotations cohérentes entre ces différents états de spin grâce à des impulsions micro-ondes. Je présente les détails techniques de cet outil dans le manuscrit. Une limitation importante que nous avons du surmonter provient du bruit magnétique du Métropolitain parisien, et nous avons pu compenser activement le champ magnétique local pour nous affranchir de ce bruit. Ces rotations de spin nous permettent de préparer les atomes dans un état interne différent de $F = 1, m_F = -1$, comme par exemple dans l'état $F = 1, m_F = 0$ qui est insensible au champ magnétique, ou dans un état superposé entre $F = 1, m_F = 0$ et $F = 2, m_F = 0$.

Enfin, l'équation d'état du gaz de Bose à deux dimensions reliant le potentiel chimique du gaz, sa température et sa densité dans l'espace des phases est détaillée. Une caractéristique de ce système est que ses propriétés thermodynamiques ne dépendent de son potentiel chimique et de sa température que via leur rapport. Nous avons développé une méthode expérimentale, inspirée de la référence [67] permettant de mesurer cette équation d'état, et une comparaison à des simulations de Monte-Carlo permettent d'en déduire la densité dans l'espace des phases de notre gaz, ainsi que le rapport T/T_c, où T_c est la température critique de la transition BKT. Le degré de dégénérescence du gaz peut être varié en modifiant la hauteur du potentiel optique de piégeage ou en retirant une fraction contrôlée des atomes du piège. Le rapport T/T_c peut ainsi être varié et mesuré de façon fiable entre environ 0,2 et 2. Il est ainsi possible de mesurer les propriétés du gaz de part et d'autre de la transition de phase.

---

[1] *Version française de la légende:* Images d'absorption de nuages atomiques dans différents types de potentiels à fond plat. La quantité tracée est la densité optique (OD) qui est proportionnelle à la densité atomique. La ligne noire représente une échelle de 20 µm. (a): Disque de rayon 20 µm. (b): Étoile inscrite dans un cercle de rayon 24 µm. (c): Soixante-douze nuages indépendants arrangés en un réseau de Kagomé. (d): Nuage ayant la forme plus exotique de la silhouette d'un cochon.

Chapitre 3: Réalisation de rotations de spin spatialement résolues

Les rotations de spin présentées dans le chapitre précédent sont effectuées grâce à des micro-ondes dont la longueur d'onde surpasse largement la taille de notre échantillon atomique. Ces rotations affectent donc les différentes régions du nuage de façon identique. J'ai développé durant ma thèse un outil permettant de réaliser des rotations de spin résolues spatialement. Il s'agit de faisceaux Raman qui permettent d'effectuer des transferts cohérents entre les deux états internes $F = 1, m_F = 0$ et $F = 2, m_F = 0$ de l'atome. Le profil d'intensité de ces faisceaux peut être façonné pour s'adresser à des régions du nuage bien choisies. Ce chapitre décrit cet outil et caractérise quelques uns de nos résultats.

Une première partie du chapitre détaille comment l'on peut changer l'état interne d'un atome par effet Raman. Deux faisceaux laser de fréquence différente et non-résonants avec les transitions électroniques du rubidium sont accordés pour que leur différence de fréquence corresponde à la différence d'énergie entre les deux états internes considérés. Un photon de l'un des lasers est diffusé par un atome dans le mode du second laser, et au cours de ce processus, l'atome change d'état interne. Ce changement d'état interne peut être accompagné d'un transfert d'impulsion selon l'angle d'incidence relatif des deux faisceaux laser. La longueur d'onde que nous avons choisie est précisément située entre les deux transitions électroniques principales du rubidium, de sorte à annuler le décalage lumineux différentiel entre le niveau $F = 1$ et le niveau $F = 2$.

Les deux faisceaux de fréquence différente sont issus d'un même laser qui est séparé en deux. L'un des faisceaux obtenus est modulé grâce à un modulateur électro-optique afin de décaler sa fréquence d'environ $6,8\,\mathrm{GHz}$. La fréquence des deux faisceaux est également décalée de quelques dizaines de mégahertz à l'aide de modulateurs acousto-optiques afin de prévenir tout effet d'interférence destructive entre les deux bandes latérales créées par le modulateur électro-optique, en suivant les conclusions de la référence [120]. On obtient ainsi deux faisceaux qui permettent, lorsque utilisés avec des polarisations orthogonales, de réaliser des rotations de spin entre les états $F = 1, m_F = 0$ et $F = 2, m_F = 0$.

Les deux faisceaux peuvent ensuite, au choix de l'expérimentateur, être envoyés sur les atomes avec le même mode spatial, en particulier avec des directions de propagation parallèles, ou bien être envoyés avec un angle d'incidence relatif non nul. Le premier cas correspond à un transfert d'impulsion nul, et le second permet un transfert d'impulsion non nul dans l'une des directions du plan atomique. La valeur de ce transfert d'impulsion peut être choisi sur une plage variable grâce à un accordéon optique, et correspond à un recul variant entre 0 et une vitesse supérieure à la vitesse du son du gaz, qui est de l'ordre de 1 ou $2\,\mathrm{mm/s}$.

Dans les deux cas, les deux faisceaux sont au préalable réfléchis sur la surface d'une matrice de micro-miroirs similaire à celle décrite dans le chapitre précédent, qui permet de façonner le profil d'intensité des deux faisceaux. Le plan de la matrice est optiquement conjugué au plan atomique, ce qui nous permet de sélectionner avec une précision de l'ordre du micromètre les zones du nuages qui sont affectés par ces rotations de spin.

Le reste du chapitre présente quelques uns des résultats obtenus lorsque l'on effectue ces rotations de spin localisées, et dans un premier temps lorsque le transfert d'impulsion est nul. Le contrôle cohérent de l'état de spin est démontré, et la fréquence de Rabi associée à ce contrôle est de l'ordre de quelques dizaines de kilohertz. La calibration de la taille effective de la matrice de micro-miroirs ainsi que la mise au focus de cette matrice sont présentées. La précision de nos faisceaux Raman tant dans le contrôle de l'état interne de spin que dans la sélection spatiale des atomes affectés est illustrée sur la figure 3.7[2]: initialement un gaz d'atomes dans l'état $F = 1, m_F = 0$ remplit un carré de côté 40 µm. Les faisceaux Raman illuminent deux lignes durant une durée correspondant à un transfert total vers l'état $F = 2, m_F = 0$. La figure présente les densités des deux états et montre le degré de précision avec lequel nous sommes capables de sélectionner une région du gaz et de contrôler l'état interne des atomes dans cette région.

Dans le cas où les deux faisceaux Raman ne sont pas co-propageants, nous avons pu calibrer le transfert d'impulsion attendu en observant la figure d'interférence statique obtenue lorsque ces faisceaux ont la même fréquence. Ce transfert d'impulsion est varié en déplaçant un seul miroir à l'aide d'une platine de translation, et est très reproductible. Je présente dans le manuscrit une expérience préliminaire où une fraction des atomes situés dans une petite région circulaire au centre du nuage est transférée dans l'état $F = 2, m_F = 0$ avec une certaine vitesse de recul. La dynamique de ces atomes est observée durant une centaine de millisecondes. Les atomes se déplacent vers le bord du nuage, rebondissent contre les murs du potentiel optique confinant le gaz, repartent dans la direction opposée et ainsi de suite. L'étalement de ces atomes augmente également au cours du temps, de sorte qu'après trois ou quatre rebonds, ils se diluent dans le nuage d'atomes dans l'état $F = 1$ et leur dynamique ne peut plus être observée par manque de signal. Cette expérience préliminaire démontre la richesse des phénomènes que l'on peut observer grâce à notre nouvel outil, et nous incite à nous diriger vers la physique des mélanges. Dans le cadre de cette thèse, les faisceaux Raman nous ne serviront cependant qu'à l'étude d'un gaz à une composante, comme par exemple dans le chapitre 6.

PARTIE II: MESURES DE LA FONCTION DE CORRÉLATION DU PREMIER ORDRE

Chapitre 4: Considérations théoriques

La physique de la transition BKT est bien illustrée par un modèle simple de physique statistique: le modèle XY. C'est en considérant ce modèle que cette transition de phase a été initialement découverte. Dans ce chapitre je présente les propriétés thermodynamiques de ce modèle et celles de la transition BKT. Je présente ensuite le cas du gaz de bosons en deux dimensions et comment

---

[2] *Version française de la légende:* Les atomes sont préparés dans un carré de côté 40 µm et dans l'état $F = 1, m_F = 0$. Les faisceaux Raman illuminent une zone délimitée par deux lignes de largeur 8 µm et dont les centres respectifs sont séparés de 18 µm pendant une durée correspondant à un transfert total vers l'état $F = 2, m_F = 0$. (a): Densité optique des atomes dans l'état $F = 1$. (b): Densité optique dans l'état $F = 2$. Le transfert est effectivement total dans la région des deux lignes, et la résolution spatiale des faisceaux est excellente.

il se relie au modèle XY à basse température. Enfin, j'aborde la question de l'observation de la physique BKT dans les laboratoires: différents systèmes sont réputés être décrits par cette physique, mais chacun présente des difficultés théoriques ou expérimentales pour mesurer les propriétés de cette transition de phase. La fin du chapitre passe brièvement en revue ces systèmes et les limitations des mesures qui ont été effectuées ces dernières années.

Le modèle XY consiste en un réseau bidimensionnel d'aimants qui peuvent s'orienter dans n'importe quelle direction du plan. Des interactions entre plus proches voisins sont ajoutées et favorisent énergétiquement les configurations où les aimants sont orientés dans la même direction. L'énergie d'interaction associée est notée J. À température nulle, le système se place dans l'état fondamental où tous les aimants sont alignés dans une même direction. Lorsque la température T augmente, les aimants dévient de cette direction commune. Le théorème de Mermin-Wagner-Hohenberg affirme que deux aimants arbitrairement lointains ont une corrélation arbitrairement faible dès que la température n'est pas nulle. Deux types d'excitations collectives sont mises en jeu et qui sont importantes pour comprendre la thermodynamique du système: les phonons et les vortex.

Une quantité importante pour mesurer l'ordre spatial est la fonction de corrélation du premier ordre $g_1(\boldsymbol{r})$, qui détermine le degré de corrélation entre la direction de deux aimants séparés par une certaine distance $\boldsymbol{r}$. Il est possible de déterminer cette fonction de corrélation dans la limite des températures très basses ($k_\mathrm{B}T \ll J$ où k_B est ma constante de Boltzmann) ou très hautes ($k_\mathrm{B}T \gg J$) grâce à des arguments simples. À haute température, $g_1(\boldsymbol{r})$ décroît exponentiellement avec la distance $\boldsymbol{r}$, et la longueur caractéristique de cette décroissance est plus petite que la distance entre aimants voisins dès que la température correspond à une énergie plus grande que l'énergie d'interaction. À basse température, la contribution des phonons est évaluée, et on peut montrer que la fonction de corrélation décroît avec la distance selon une loi algébrique: $g_1(\boldsymbol{r}) \propto r^{-\alpha}$ où l'exposant α augmente linéairement avec la température. On désigne ce type de décroissance de la cohérence par le terme d'« ordre à quasi-longue portée ».

Afin de déterminer comment l'on passe du régime de basse température au régime de haute température, il faut tenir compte de l'existence des vortex. Un vortex de charge topologique unité est une configuration où les aimants ont une orientation qui est orthoradiale par rapport au centre de ce vortex. La figure 4.1a[3] illustre une telle configuration. Un vortex peut « tourner » dans un sens ou dans l'autre, définissant le signe de sa charge topologique. Lorsque l'on somme la configuration de plusieurs vortex de charge topologique unité centrés sur le même point, on peut obtenir un vortex de charge topologique supérieure à 1. De tels vortex ont une énergie supérieure à celle de vortex spatialement séparés, et ne seront pas pris en compte. En revanche, les configurations contenant des paires de vortex de charge topologique respective +1 et −1 ont une contribution importante. Une telle configuration est illustrée sur la figure 4.1b.

---

[3] *Version française de la légende:* Deux configurations particulières du modèle XY. (a): Un vortex centré sur la croix rouge. L'orientation des aimants « tourne » dans le sens anti-horaire autour de ce centre, et le vortex a une charge topologique +1. (b): Une paire de vortex de charge topologique respective +1 et -1, et centrés respectivement autour de la croix et du cercle rouges.

Une analyse par un groupe de renormalisation permet de prendre en compte les principaux effets dus à la création de paires de vortex. On peut alors identifier une température critique T_c en dessous de laquelle il n'est pas favorable de créer des paires de vortex, et où le système conserve une cohérence décroissant algébriquement avec la distance. L'exposant de cette loi algébrique est compris entre 0 et 1/4. Au dessus de T_c, des paires de vortex apparaissent et cet ordre à quasi-longue portée disparaît au profit d'une décroissance exponentielle de la fonction de corrélation du premier ordre. Le fait que la transition de phase existe du fait de la création de paires de vortex explique pourquoi l'on parle de transition de phase topologique.

Un gaz de bosons en faible interaction peut être décrit par un champ classique complexe $\psi(\boldsymbol{r})$, et pour des densités dans l'espace des phases $\mathcal{D} \gtrsim 1$, l'amplitude de ce champ complexe est uniforme car des variations spatiales de cette amplitude ont un coût énergétique supérieur à l'énergie thermique disponible. On parle alors de régime pré-superfluide ou de quasi-condensat. Dans ce régime, seule la phase du champ $\psi(\boldsymbol{r})$ varie, et le système est similaire à une version continue du modèle XY. Cela explique pourquoi une transition de type BKT est présente pour un tel gaz. Sous la température critique, le gaz possède également une fraction superfluide n_s, associée à une densité superfluide dans l'espace des phases $\mathcal{D}_\mathrm{s} = n_\mathrm{s}\lambda_T^2$. Pour un système de taille infinie, cette fraction superfluide est discontinue à T_c. L'étude de la fonction de corrélation du premier ordre $g_1(\boldsymbol{r}) = \langle\psi^*(\boldsymbol{0})\psi(\boldsymbol{r})\rangle$ est intéressante, car l'exposant α de la loi algébrique décrivant sa décroissance est reliée à la densité superfluide dans l'espace des phases via $\alpha = 1/\mathcal{D}_\mathrm{s}$. Notamment au point critique, on trouve que $\alpha = 1/4$.

Plusieurs dispositifs expérimentaux ont été utilisés dans les dernières années pour explorer la transition de phase BKT, et notamment pour tenter de mesurer la fonction de corrélation du premier ordre $g_1(\boldsymbol{r})$:

- Des systèmes d'excitons-polaritons ont été étudiés (voir par exemple les références [159–161]). Cependant, ces systèmes possèdent des pertes importantes, et nécessitent d'être excités continûment par une source extérieure. L'existence d'une transition de phase de type BKT pour ces systèmes est débattue, et des mesures de la fonction de corrélation du premier ordre sont intéressantes dans le cadre de ces discussions.

- Des nuages d'atomes ultra-froids piégés dans un piège harmonique ont été étudiés (voir par exemple les références [144, 162, 163]). Le fait que la densité de ces nuages n'est pas uniforme modifie significativement le comportement de la fonction de corrélation du premier ordre et notamment change l'exposant de la loi algébrique décrivant sa décroissance en dessous de T_c.

Il est donc intéressant d'étudier des nuages atomiques qui sont à l'équilibre thermodynamique, et préparés dans des potentiels à fond plat pour mesurer des quantités directement comparables à la théorie BKT. Une différence notable avec cette théorie idéale est la taille finie des échantillons étudiés expérimentalement. L'effet de cette taille finie peut être évalué, et pour les paramètres de notre expérience, cet effet est suffisamment faible pour que des mesures puissent être comparées aux propriétés d'un système infini.

Les deux chapitres qui suivent sont consacrés à la présentation de mesures de la fonction de corrélation du premier ordre de part et d'autre de la température critique du système.

Chapitre 5: Mesures de cohérence en phase via la distribution d'impulsion

Ce chapitre détaille une première série de mesures qui vise à déterminer la fonction de corrélation du premier ordre $g_1(\boldsymbol{r})$. Cette fonction est en effet reliée à la distribution d'impulsion via une simple transformée de Fourier, à une convolution près, qui est due à la taille finie des échantillons étudiés.

Nous avons implémenté une méthode pour mesurer cette distribution d'impulsion, inspirée de la référence [163]. Cette méthode repose sur le fait qu'une particule quantique évoluant dans un potentiel harmonique de pulsation ω durant un quart de période a une distribution en position qui coïncide avec sa distribution d'impulsion initiale. La mesure de cette distribution en position s'effectue simplement grâce à une imagerie par absorption du nuage.

La séquence expérimentale est la suivante:

- Un nuage est préparé dans un potentiel optique ayant la forme d'un disque de rayon 20 µm. Ce nuage est à l'équilibre thermodynamique et sa température et son nombre d'atomes sont choisis pour que la densité dans l'espace des phases de ce nuage ait une valeur déterminée, que l'on mesure via l'équation d'état du gaz (voir Chapitre 2). Les atomes sont initalement dans l'état $F = 1, m_F = 0$.

- Un champ magnétique quadripolaire est créé, et induit un potentiel harmonique dans le plan xy pour des atomes dans l'état $F = 1, m_F = -1$. La pulsation de ce potentiel est $\omega \approx 2\pi \cdot 10\,\mathrm{Hz}$. Selon l'axe vertical z, ce champ magnétique crée un potentiel linéaire qui compense la gravité pour des atomes dans ce même état interne.

- À $t = 0$, une petite fraction des atomes est transférée de l'état $F = 1, m_F = 0$ vers l'état $F = 1, m_F = -1$ grâce à deux impulsions micro-ondes de fréquence et de durée bien choisies. Au même instant, les potentiels optiques créant le confinement des atomes sont éteints.

- Aux temps ultérieurs, les atomes qui sont restés dans l'état interne initial tombent sous l'effet de la gravité tandis que les atomes transférés lévitent. Ces deux différents nuages sont spatialement séparés au bout de quelques millisecondes. Les atomes dans l'état $F = 1, m_F = -1$ évoluent dans le potentiel harmonique, et si la densité atomique est suffisamment faible, les interactions sont négligeables, et cette évolution est la même que celle d'une particule unique.

- Au temps t, les atomes situés dans le plan initial sont transférés vers l'état $F = 2, m_F = 0$ pour être imagés. Seule une fraction des atomes sont imagés, car le nuage s'étend également selon la direction verticale. La tranche imagée a une épaisseur inférieure à la profondeur de champ de notre imagerie.

Dans un premier temps je caractérise l'évolution des atomes dans le potentiel harmonique. La taille du nuage dans le plan xy permet de constater que ce potentiel n'est pas isotrope, mais cette anisotropie est corrigée grâce à une paire de bobines auxiliaire orientée selon l'axe y et branchée en configuration anti-Helmholtz. Le fait que les interactions peuvent être négligées durant l'évolution du gaz est expérimentalement vérifiée en mesurant sa distribution spatiale après une demi-période d'évolution: on s'attend à mesurer $\psi(\boldsymbol{r}, T/2) = \psi(-\boldsymbol{r}, 0)$, et c'est ce que l'on obtient.

La distribution spatiale des atomes mesurée après un quart de période d'évolution ($t = T/4$) est la convolution entre la transformée de Fourier de la fonction de corrélation du premier ordre et d'une fonction dépendant de la taille et de la forme du nuage initial. Plus la portée des corrélations de phase est petite, plus cette taille sera grande. De même, plus le nuage initial est petit, plus la taille du nuage à $t = T/4$ sera grande. Cette dernière affirmation est bien confirmée expérimentalement. Cependant la présence de cette convolution dans le signal mesuré nous empêche de remonter à la fonction de corrélation $g_1(\boldsymbol{r})$ avec une précision satisfaisante, notamment pour pouvoir mesurer l'exposant d'une loi algébrique ou pour discriminer une décroissance algébrique d'une décroissance exponentielle, ceci s'expliquant également par la faible étendue spatiale sur laquelle le signal atomique est détectable.

Dans ces conditions, la seule observable qui soit quantitativement mesurable est l'extension spatiale du nuage après un quart de période d'évolution dans le piège harmonique. Cette taille dépend de la portée de la cohérence de phase du nuage d'atomes, de son extension initiale ainsi que, dans une moindre mesure, de la résolution optique de notre système d'imagerie. Ces deux derniers facteurs étant fixés, on peut varier la densité dans l'espace des phases du nuage initial et observer l'évolution de cette observable.

La figure 5.6[4] présente la demi-largeur à mi-hauteur σ_{H} du nuage à $t = T/4$. Cette largeur varie peu lorsque la température du gaz reste sous la température critique, mais elle augmente significativement lorsque T est au dessus de T_{c}, ce qui indique que la portée de la cohérence en phase décroît lorsque la température est augmentée. En prenant compte la taille initiale du nuage et la résolution de notre système d'imagerie, on constate que, en dessous de T_{c}, ces mesures sont compatibles avec une fonction de corrélation $g_1(\boldsymbol{r})$ qui décroît algébriquement avec un exposant α compris entre 0 et 0,3, et avec une décroissance exponentielle dont la longueur caractéristique surpasse la dimension initiale du gaz. Lorsque la température croît au dessus de T_{c}, ces mesures sont compatibles avec une décroissance algébrique d'exposant α qui croît de 0,2 à environ 1, ainsi qu'avec une décroissance exponentielle de longueur caractéristique qui décroît de plus de 40 à quelques micromètres. Cela démontre qu'en franchissant la température critique, le gaz perd en cohérence de phase à l'échelle de son extension spatiale.

---

[4] *Version française de la légende:* Demi-largeur à mi-hauteur du nuage après un quart de période dans un potentiel harmonique. Le rapport T/T_{c} est varié. Lorsqu'il est inférieur à 1, la largeur mesurée reste autour de 1.3 µm, et lorsqu'il est supérieur à 1, cette largeur augmente jusqu'à environ 2 µm.

Ces mesures ne peuvent malheureusement pas fournir de conclusions plus précises, et il nous faut employer une autre méthode de mesure afin de mieux connaître la fonction de corrélation $g_1(\boldsymbol{r})$ de part et d'autre de la transition de phase. C'est ce qui est développé dans le chapitre qui suit.

Chapitre 6: Mesures de la fonction de corrélation par interférométrie atomique

Nous avons développé une méthode qui nous permet de mesurer plus directement la fonction de corrélation $g_1(\boldsymbol{r})$. Cette méthode utilise de façon cruciale les faisceaux Raman présentés dans le chapitre 3, et est similaire à une expérience de fentes d'Young. Elle repose sur l'interférence de deux régions distantes de $\boldsymbol{r}$ du gaz d'atomes, et le contraste moyen de la figure d'interférence obtenue est directement $g_1(\boldsymbol{r})$. Dans ce chapitre je présente cette méthode ainsi qu'une analyse préliminaire des mesures effectuées.

La séquence expérimentale est la suivante:

- Un nuage est préparé dans un potentiel ayant la forme d'un carré de côté 40 µm. Tout comme dans le chapitre précédent, le rapport T/T_c, ou de façon équivalente la densité dans l'espace des phases $\mathcal{D}$, est choisi et fixé. L'état interne des atomes est $F=1, m_F=0$.
- La totalité du nuage est transféré dans l'état $F=2, m_F=0$ grâce à une impulsion micro-ondes. Une fraction des atomes compris dans la région formée par deux bandes de largeur 4 µm et distantes de d est de nouveau transférée dans l'état $F=1, m_F=0$ grâce à nos faisceaux Raman. La géométrie de la région en question est très similaire à celle présentée sur la figure 3.7.
- À $t=0$, une impulsion laser résonante avec la transition $F=2 \to F'=3$ est envoyée selon la direction verticale sur les atomes. Seuls les atomes dans l'état $F=2$ absorbent des photons, et l'énergie de recul associée à ces absorptions est suffisante pour les chasser du potentiel de piégeage. Ne restent dans le potentiel optique que les atomes dans l'état $F=1$.
- Ces atomes s'étendent dans le plan xy. Après une certaine durée d'expansion, les atomes issus de chacune des deux bandes initiales interfèrent. Lorsque la période de la figure d'interférence est de l'ordre de 4 à 5 µm, une image par absorption est enregistrée.

On effectue cette même séquence expérimentale une centaine de fois, et la moyenne des figures d'interférences obtenues a un contraste qui correspond à $g_1(d)$. Cette affirmation est confirmée par un calcul analytique négligeant l'énergie d'interaction lors de l'expansion des deux bandes, ce qui est justifié étant donnée la densité d'atomes initialement transférés.

Une caractérisation approfondie de l'expansion d'une et de deux bandes d'atomes est présentée dans le manuscrit et correspond qualitativement à ce que l'on attend théoriquement.

Le contraste moyen d'une figure d'interférence peut-être déterminé à partir d'un nombre fini de réalisations expérimentales. On peut alors varier la distance d entre les deux bandes d'atomes qui interfèrent. Typiquement, d est variée entre 3 et 20 µm. On observe que la cohérence de phase diminue lorsque cette distance augmente, et que cette diminution est d'autant plus importante que le rapport T/T_c est élevé. La faible gamme de distances d qui peut être explorée ne nous permet pas d'affirmer avec certitude que $g_1(d)$ suit une loi algébrique ou exponentielle, cependant on peut déterminer les meilleurs paramètres permettant de décrire cette fonction par de telles lois.

La figure 6.8[5] montre comment ces paramètres optimaux dépendent de T/T_c, et constitue le résultat central de ce chapitre. En dessous de la température critique, nos mesures sont compatibles avec une loi algébrique d'exposant compris entre 0 et 1/4. Cet exposant croît avec la température, et est proche de prédictions obtenues par des simulations Monte-Carlo [110]. Les mesures sont également compatibles avec une loi exponentielle de longueur caractéristique surpassant la taille de notre échantillon, et qui diminue légèrement lorsque T s'approche de T_c. Lorsque la température augmente au delà de T_c, la décroissance de la cohérence de phase est compatible avec une loi algébrique d'exposant qui croît au delà de 1/4, et avec une loi exponentielle dont la longueur caractéristique est inférieure à la taille totale du système et décroît jusqu'à atteindre quelques micromètres.

Ces mesures représentent une avancée importante pour l'étude expérimentale des propriétés d'équilibre de systèmes présentant une transition de phase de type BKT. Il subsiste cependant quelques points qui nécessitent d'être éclaircis pour confirmer la validité de nos résultats: l'influence de la résolution de notre système d'imagerie sur le contraste des figures d'interférence, l'éventuelle réduction de ce contraste due à la fluctuation du nombre d'atomes dans les bandes qui interfèrent, l'effet qu'a la largeur non nulle de ces bandes, ou encore l'effet des interactions au début de l'expansion des atomes qui interfèrent.

PARTIE III: SYMÉTRIES DYNAMIQUES DU GAZ DE BOSE EN DEUX DIMENSIONS

Chapitre 7: Éléments de théorie sur les symétries dynamiques

Les symétries d'un système physique correspondent aux transformations d'espace, de temps et des variables décrivant le problème qui laissent invariant ce système. Par exemple, de nombreux problèmes physiques possèdent des symétries spatiales comme l'invariance par translation ou l'invariance par rotation, et des symétries temporelles comme l'invariance par translation dans le temps. Des symétries plus subtiles qui font intervenir à la fois les variables d'espace et de temps peuvent aussi exister, et sont appelées symétries dynamiques. Un exemple important est la symétrie dynamique du problème de Kepler décrivant le mouvement d'une planète autour de son étoile, symétrie qui conduit à l'invariance dans le temps du vecteur de Laplace-Runge-Lenz.

---

[5] *Version française de la légende:* La décroissance avec la distance d du contraste de la figure d'interférence de deux bandes initialement distantes de d peut être décrite par une décroissance algébrique ou une décroissance exponentielle. (a): L'exposant α de la loi algébrique décrivant le mieux nos mesures est tracée en fonction de T/T_c. La ligne continue représente la prédiction $\alpha = 1/\mathcal{D}_s$. (b): La longueur caractéristique ℓ de la loi exponentielle décrivant le mieux nos mesures est tracée en fonction de T/T_c.

Dans ce chapitre je détaille quelques éléments de la théorie permettant un traitement mathématique de ces symétries. J'expose ensuite les symétries dynamiques du gaz de Bose à deux dimensions en faible interaction et certaines de leurs conséquences importantes.

Les symétries d'un système sont définies plus formellement par l'ensemble des transformations qui laissent invariante l'action de ce système, ou de façon équivalente l'équation d'Euler-Lagrange décrivant la dynamique du système. L'ensemble de ces transformations forment un groupe qui, dans de nombreux cas, est aussi une variété différentielle. On appelle ces groupes des groupes de Lie, et, dans le contexte des symétries d'un système physique, leurs éléments sont appelés des transformations de Lie-Bäcklund. Des objets importants pour décrire un groupe de Lie sont ses générateurs infinitésimaux. Ces générateurs forment une algèbre appelée algèbre de Lie. La structure algébrique du groupe de Lie est résumée dans la donnée des commutateurs entre les éléments de cette algèbre de Lie.

On peut adopter un point de vue différent sur les transformations de Lie-Bäcklund d'un système. Lorsque ces transformations sont appliquées sur une solution de l'équation d'Euler-Lagrange du système, on obtient une autre solution de cette équation. L'ensemble des solutions de cette équation possède donc la même structure de groupe de Lie.

Une généralisation de ces concepts permet d'établir des liens entre deux systèmes physiques différents. S'il existe une transformation qui, appliquée à l'action du premier système, permet d'obtenir celle du second système, alors les groupes de Lie des deux systèmes sont identiques, et en particulier leur structure algébrique est la même. Une telle transformation reliant deux systèmes physiques est appelée une transformation de Bäcklund. En adoptant le second point de vue, il est possible de déduire les solutions de l'équation d'Euler-Lagrange du second système à partir de la connaissance de celles de l'équation du premier système. Conceptuellement, la capacité de tisser un tel lien entre deux systèmes physiques différents est très intéressant, car la compréhension de l'un permet d'éclairer la compréhension que l'on a de l'autre.

La seconde partie du chapitre est consacrée à la détermination du groupe de Lie d'un gaz de N bosons à deux dimensions en faible interaction, dans deux situations distinctes: dans un potentiel extérieur nul, et dans un potentiel extérieur harmonique. Cette discussion est très similaire à celle que l'on trouve dans les références [190, 192]: il s'agit de trouver les symétries dynamiques de l'équation de Schrödinger pour le champ classique décrivant la fonction d'onde des atomes. Cette équation possède un terme non-linéaire dû aux interactions, et porte également le nom d'équation de Gross-Pitaevskii.

Que le potentiel extérieur soit uniforme ou harmonique, le groupe de Lie possède toujours douze générateurs infinitésimaux. Neuf d'entre eux proviennent de symétries qui sont peu intéressantes, comme par exemple celui associé à l'invariance par rotation. Les trois derniers forment un sous-groupe dont la structure est plus riche. Ces trois générateurs sont liés à l'invariance par translation temporelle, l'invariance par dilatation spatio-temporelle, et l'invariance par une transformation appelée « expansion ». La structure algébrique associée à ces trois générateurs est celle du groupe $\mathrm{SO}(2,1)$.

Dans le cas où un potentiel harmonique est présent, cette structure a une conséquence remarquable: l'énergie potentielle du système a une évolution temporelle exactement sinusoïdale, de fréquence double de la fréquence du potentiel harmonique. Cette propriété n'est pas surprenante si les atomes n'interagissent pas, mais elle l'est bien plus dans notre cas où ils interagissent via une interaction de contact qui introduit un terme non-linéaire dans l'équation d'Euler-Lagrange.

Enfin, les deux cas considérés, avec ou sans potentiel harmonique extérieur, sont deux systèmes physiques qui peuvent être reliés via une transformation de Bäcklund. Ils sont donc décrits par la même physique, et l'on peut déduire l'évolution d'un nuage atomique dans un potentiel harmonique de son évolution libre. De façon plus générale, on peut connaître l'évolution de ce nuage atomique évoluant dans un potentiel harmonique dont la fréquence peut varier dans le temps de façon arbitraire. Les symétries dynamiques de chacun des cas permet également de relier entre elles les évolutions de deux nuages initiaux de forme identique, possédant le même nombre d'atomes, mais de taille initiale différente.

Lorsque les nuages atomiques se situent dans le régime hydrodynamique, qui correspond à la limite où la longueur de cicatrisation du gaz est très faible devant la dimension du gaz, une symétrie supplémentaire apparaît. Dans cette limite, il existe en effet des transformations de Bäcklund reliant deux systèmes atomiques ayant un nombre d'atomes N différent, ou de façon équivalente un paramètre d'interaction différent.

En combinant ce résultat avec le précédent, on en déduit que la connaissance de l'évolution de N atomes dans un potentiel harmonique de fréquence donnée et interagissant avec un certain paramètre d'interaction permet de connaître l'évolution d'un nombre différent d'atomes dans un potentiel harmonique de fréquence différente, éventuellement variable, et interagissant avec un paramètre d'interaction différent, et ce tant que les nuages restent dans le régime hydrodynamique.

Ce résultat est frappant du fait de la présence d'un terme non-linéaire dans l'équation d'évolution du système qui, *a priori*, empêche de relier l'évolution d'un système de N atomes à celle d'un système possédant un nombre différent d'atomes. Cela est permis grâce à la présence de symétries particulières du système.

Chapitre 8: Approche expérimentale des symétries dynamiques

Ce chapitre est consacré à l'étude expérimentale des conséquences de l'existence des symétries dynamiques pour un gaz de bosons à deux dimensions en faible interaction. Il s'agit donc de vérifier expérimentalement les résultats théoriques du chapitre précédent. Connaissant l'évolution d'un gaz donné dans des conditions expérimentales données, ces résultats permettent de déduire l'évolution d'un gaz de forme initiale identique, mais de taille initiale différente, avec un nombre d'atomes différents, un paramètre d'interaction différent, et une fréquence du potentiel harmonique extérieur différent.

La séquence expérimentale est très similaire à celle du chapitre 5:

- Un gaz est préparé dans un potentiel à fond plat et dont on peut choisir la forme. Sa température est fixée à une valeur la plus basse possible, et correspond à un rapport $T/T_\mathrm{c} < 0,3$. Initialement, ce gaz est au repos.
- À $t = 0$, le confinement optique dans le plan est éteint, et le confinement vertical est maintenu. Il y a deux choix pour le potentiel externe auquel est soumis le gaz. Soit les atomes sont transférés dans l'état $F = 1, m_F = -1$ et sont soumis à un potentiel harmonique similaire à celui du chapitre 5, soit ils restent dans l'état $F = 1, m_F = 0$ et le potentiel extérieur est uniforme.
- Après une évolution pendant la durée t dans le potentiel choisi, on mesure la distribution spatiale des atomes grâce à notre imagerie par absorption.

Avec ces images nous pouvons déterminer le nombre d'atomes du gaz, le premier et le second moment de la distribution spatiale, ainsi que l'énergie d'interaction du gaz. Dans le cas d'une évolution dans un potentiel harmonique, le second moment de la distribution permet d'obtenir l'énergie potentielle du gaz.

La première conséquence de la symétrie dynamique est l'évolution sinusoïdale de cette énergie potentielle. On vérifie effectivement que cette énergie oscille avec une fréquence double de la fréquence du potentiel harmonique.

La deuxième vérification que l'on fait est la correspondance entre l'évolution d'un gaz initialement au repos en présence d'un potentiel uniforme et celle du même gaz en présence d'un potentiel harmonique. La mesure de l'évolution temporelle de la distribution spatiale d'un gaz initial dans ces deux cas permet de reconstruire expérimentalement les lois d'échelles sur le temps et l'espace qui permettent de relier les deux évolutions. Les lois d'échelle que l'on obtient sont en excellent accord avec la prédiction théorique déterminée au chapitre précédent.

La troisième expérience permet de relier, dans le régime hydrodynamique, l'évolution de deux gaz initialement au repos de forme et de taille initiales identiques, avec une fréquence de potentiel harmonique identique, mais possédant un nombre d'atomes différent. Ici encore, les résultats expérimentaux sont en très bon accord avec la théorie.

De façon intéressante, la taille d'un nuage après une évolution d'un quart de période dans un potentiel harmonique dépend du nombre d'atomes dans ce nuage. Dans le cas d'un nuage dans le régime hydrodynamique dont la forme initiale est un triangle équilatéral, l'énergie cinétique du gaz est négligeable après une évolution d'un quart de période, et la taille du nuage est proportionnelle à son nombre d'atomes. Cette propriété remarquable fournit une méthode simple et robuste pour calibrer l'imagerie par absorption et déterminer précisément le nombre d'atomes que l'on mesure. Le résultat de cette méthode est compatible avec une méthode de calibration utilisée antérieurement, mais qui était bien plus longue à mettre en place. Les particularités d'une forme initiale triangulaire sont détaillées dans le chapitre suivant.

Enfin, la dernière vérification permet d'explorer le dernier paramètre pertinent: la taille initiale du gaz. On relie ici l'évolution de deux gaz de taille initiale et de nombre d'atomes différents, avec la même fréquence du potentiel harmonique. Ceci est également réalisé dans le régime hydrodynamique. Ces expériences sont illustrées par la figure 8.9[6], où l'évolution de la distribution spatiale des deux gaz initiaux est montrée. Les lois d'échelles expérimentales et théoriques coïncident également.

Ce chapitre permet de valider les prédictions théoriques du chapitre précédent, et montre que, dans le régime hydrodynamique, l'évolution d'un gaz initialement au repos est universelle dans la mesure où elle ne dépend que de la forme initiale du gaz. Sa taille initiale, son nombre d'atomes, le paramètre d'interaction et la fréquence du potentiel harmonique extérieur n'introduisent que des lois d'échelle sur l'espace et le temps par rapport à cette dynamique universelle.

Chapitre 9: Solutions périodiques de l'équation de Gross-Pitaevskii à deux dimensions

L'étude de l'équation de Gross-Pitaevskii à deux dimensions est pertinente dans d'autres domaines de la physique que celui des atomes froids. En effet, elle peut également décrire la propagation d'une onde électromagnétique dans une fibre optique non-linéaire, ou dans un gaz thermique dilué d'atomes qui joue le rôle de milieu propagateur non-linéaire. Dans ces deux cas, la variable temporelle de l'équation correspond à la variable d'espace dans la direction de propagation de l'onde. Plus généralement, cette équation est une des équations emblématiques de la physique non-linéaire, et ses propriétés intéressent tout autant les physiciens que les mathématiciens.

Les équations différentielles non-linéaires peuvent présenter des propriétés remarquables, comme par exemple l'équation de sine-Gordon. Cette équation possède des solutions appelées « solitons », qui sont des solutions qui se propagent sans se déformer. D'autres solutions sont appelés des solitons à respirations. Ces solutions se propagent en ayant un comportement oscillatoire.

Pour l'équation de Schrödinger à une dimension, des solitons et des solitons à respirations existent et sont observés expérimentalement. Pour l'équation de Schrödinger à deux dimensions, aucune solution de ce type n'a été prédite à notre connaissance.

En observant l'évolution temporelle de différents nuages dans un potentiel harmonique de pulsation ω, deux formes spécifiques semblent avoir un comportement particulier: un gaz dont la distribution initiale est celle d'un triangle

---

[6] *Version française de la légende:* Évolution de deux gaz de même forme initiale, mais de taille différente et ayant un nombre d'atomes différents. Les deux nuages évoluent dans un potentiel harmonique de même pulsation ω. (a): Le gaz initial possède $3,7(3) \cdot 10^4$ atomes et les atomes remplissent initialement un carré de côté $27,0(5)$ µm de façon uniforme. (b): Le gaz initial possède $5,4(3) \cdot 10^4$ atomes et les atomes remplissent initialement un carré de côté $36,8(5)$ µm de façon uniforme. Les deux évolutions semblent similaires, à ceci près que la taille respective des nuages n'est pas la même, et que deux distributions spatiales similaires ne sont pas nécessairement obtenues à des temps identiques. Ces mesures de densité permettent cependant de reconstruire les lois d'échelle spatiale et temporelle qui relient ces deux évolutions.

équilatéral rempli uniformément, et un gaz dont la distribution initiale est celle d'un disque rempli uniformément. Dans les deux cas, le gaz se trouve dans le régime hydrodynamique.

Dans le premier cas, l'évolution du gaz est présenté sur la figure 9.1[7]. Le nombre indiqué au dessus de chaque image correspond au rapport entre le temps d'évolution t dans le potentiel harmonique et la période du potentiel $T = 2\pi/\omega$. On constate que l'évolution du nuage semble être périodique de période $T/2$. De façon surprenante, le gaz semble retrouver une forme triangulaire à $t = T/4$, inversée par rapport à la forme initiale. Au bout d'un certain temps d'évolution, la forme triangulaire du gaz est moins marquée, ce qui peut être dû à des imperfections expérimentales, à des effets dus à la température, ou au fait que cette évolution n'est pas périodique.

Dans le second cas, on constate que le nuage a une évolution qui semble être périodique de période $2T$. Dans ce cas également, les données expérimentales ne permettent pas d'affirmer avec certitude que cette évolution est effectivement périodique.[8]

Lorsque diverses autres formes initiales remplies uniformément sont testées, on n'observe pas le même comportement, du moins sur les deux premières périodes. Nous avons essayé les polygones réguliers à n côtés jusque $n = 6$, ainsi qu'un triangle isocèle rectangle.

Afin de savoir plus précisément si les deux formes déterminées ont effectivement une évolution périodique, une étude numérique est menée pour simuler un système à température nulle. Un exemple d'une simulation numérique est montrée sur la figure 9.6[9] où l'évolution d'un gaz initialement triangulaire est calculée sur une grille de taille 512 × 512 de $t = 0$ jusqu'à $t = 3T$.

Ces simulations numériques sont effectuées sur des grilles dont le nombre de pixels peut être augmenté jusqu'à une certaine valeur au delà de laquelle les calculs numériques deviennent trop longs, ici 1024 × 1024. On peut également simuler différents gaz initiaux qui se trouvent de plus en plus dans le régime hydrodynamique. Les simulations permettent un accès à une information plus complète que les données expérimentales, puisque ces dernières ne nous renseignent que sur l'amplitude de la fonction d'onde du gaz, tandis que les simulations nous donnent également accès à sa phase. L'observable qui nous intéresse est ainsi le produit scalaire entre la fonction d'onde initiale et la fonction d'onde au temps correspondant à la période supposée de la forme étudiée. Cette observable n'est pas accessible avec nos mesures expérimentales.

---

[7] *Version française de la légende:* Images expérimentales de l'évolution dans un potentiel harmonique d'un gaz remplissant initialement un triangle équilatéral de façon uniforme et au repos. Au bout d'une demi-période dans ce potentiel ($t/T = 0,5$), la distribution spatiale semble identique à la distribution initiale. Ce motif se répète plusieurs fois, indiquant que cette évolution est périodique.

[8] Il est à noter que, en l'absence d'interactions, tout nuage évolue périodiquement dans le potentiel avec une période T. En présence d'interactions, l'existence d'orbites périodiques de période différente de T serait ainsi surprenante.

[9] *Version française de la légende:* Un exemple de simulation numérique sur une grille de taille 512 × 512. La fonction d'onde initiale est l'état fondamental d'un potentiel triangulaire en présence d'interactions. La possible périodicité de l'évolution est claire, et correspond à ce que l'on observe expérimentalement.

Dans les deux cas qui nous intéresse, ce produit scalaire est proche de 1, au mieux à moins de 5‰. Il se rapproche de 1 lorsque l'on augmente le nombre de pixels et que l'on augmente le « degré d'hydrodynamicité » du gaz. Ceci ne constitue pas une preuve de la périodicité de l'évolution de ces formes, mais donnent une bonne indication que cette évolution se rapproche d'une évolution périodique lorsque le gaz se trouve de plus en plus dans le régime hydrodynamique.

Nous n'avons pas trouvé de preuve mathématique qui pourrait établir que l'une ou l'autre des formes étudiées évoluent effectivement de façon périodique dans un potentiel harmonique. Certaines pistes peuvent être explorées, mais n'ont abouti à aucun résultat, du moins lors de nos tentatives limitées dans le temps. Cela n'exclut en rien qu'une voie vers une telle preuve puisse être découverte.

Ces résultats expérimentaux et numériques, s'ils sont confirmés par des simulations plus poussées et éventuellement par des démonstrations mathématiques rigoureuses, seraient à la fois surprenants et intéressants pour de nombreux domaines de la physique et pour les mathématiciens qui étudient les équations différentielles non-linéaires. L'équation de Schrödinger non-linéaire à deux dimensions pourrait ainsi rejoindre la famille restreinte des équations possédant des solutions de type « solitons ».

Chapitre 10: Conclusion et perspectives

Cette thèse explore certaines caractéristiques de l'équilibre thermique et de la dynamique hors équilibre de gaz de bosons à deux dimensions en faible interaction. Les résultats présentés constituent une avancée importante pour ces deux thématiques.

Les mesures de cohérence de phase de part et d'autre de la transition BKT apportent une confirmation solide de la théorie découverte il y a quarante-cinq ans, bien que les résultats présentés dans ce manuscrit soient préliminaires et nécessitent probablement la confirmation qu'ils ne sont pas sujets à certains biais systématiques. Ces mesures pourraient à l'avenir être complétées par des expériences de trempe où le système est subitement amené sous la température critique et où la dynamique pourrait être sondée grâce à l'accès à la fonction de corrélation du premier ordre.

Les expériences concernant les symétries dynamiques permettent d'établir solidement les résultats théoriques déjà connus relatifs à l'équation de Schrödinger non-linéaire à deux dimensions. Elles montrent aussi la possible existence de solitons à respiration pour cette équation, qui n'avaient jusque maintenant pas été prédits ni observés. De nombreuses questions se posent à leur sujet: leur existence est-elle reliée aux symétries dynamiques du système ? D'autres systèmes possédant les mêmes symétries dynamiques, telles que le gaz de fermions unitaire à trois dimensions, possèdent-ils des solitons similaires ? Et que deviennent les solitons de notre système lorsque les interactions sont augmentées jusqu'au point où les symétries dynamiques ne sont plus valables ?

Les outils expérimentaux développés au cours de cette thèse ouvrent également tout un champ d'expériences mettant en jeu des mélanges d'espèces de spin, en particulier les états $F = 1, m_F = 0$ et $F = 2, m_F = 0$. Ces deux espèces ne sont pas miscibles, et l'on peut par exemple étudier la dynamique de leur séparation lorsqu'elles sont initialement superposées. L'utilisation des rotations de spin résolues spatialement, présentées dans le chapitre 3, permet également de mesurer la relation de dispersion de Bogoliubov de ce système à deux composantes. Ces mesures sont actuellement en cours.

Dans un futur plus ou moins proche, il sera également possible d'étudier sur notre système expérimental la dynamique de quelques atomes dans un état de spin lorsqu'ils sont immergés dans un gaz d'atomes ayant l'autre état de spin. De telles expériences permettront peut-être d'atteindre un régime où la dynamique de ces atomes est décrite par un modèle de mouvement brownien quantique.

BIBLIOGRAPHY

[1] E. Noether. “Invariante Variationsprobleme.” In: *Nachrichten von der Gesellschaft der Wissenschaften zu Göttingen, Mathematisch-Physikalische Klasse* 1918 (1918), pp. 235–257 (cited on pages 1, 109, 227).

[2] J. D. Jackson. *Classical Electrodynamics.* Third edition. John Wiley & Sons, 1999 (cited on page 1).

[3] David J. Gross. “Gauge theory - Past, Present and Future?” In: *Chinese Journal of Physics* 30.7 (1992), p. 955 (cited on page 1).

[4] George Bluman and Sukeyuki Kumei. *Symmetries and Differential Equations.* Applied Mathematical Sciences. New York: Springer-Verlag, 1989 (cited on pages 1, 112).

[5] Peter J. Olver. *Applications of Lie Groups to Differential Equations.* 2nd ed. Graduate Texts in Mathematics. New York: Springer-Verlag, 1993 (cited on pages 1, 111, 227).

[6] Harold H. Rogers. “Symmetry transformations of the classical Kepler problem.” In: *Journal of Mathematical Physics* 14.8 (Aug. 1973), pp. 1125–1129 (cited on pages 1, 111).

[7] W. Pauli. “Über das Wasserstoffspektrum vom Standpunkt der neuen Quantenmechanik.” In: *Zeitschrift für Physik* 36.5 (May 1926), pp. 336–363 (cited on page 1).

[8] M. Bander and C. Itzykson. “Group Theory and the Hydrogen Atom (I).” In: *Reviews of Modern Physics* 38.2 (Apr. 1966), pp. 330–345 (cited on page 1).

[9] V. Fock. “Zur Theorie des Wasserstoffatoms.” In: *Zeitschrift für Physik* 98.3 (Mar. 1935), pp. 145–154 (cited on page 1).

[10] Theodor Kaluza. “Zum Unitätsproblem der Physik.” In: *Sitzungsberichte der Königlich Preußischen Akademie der Wissenschaften (Berlin)* (1921), pp. 966–972 (cited on page 1).

[11] E. Cremmer, B. Julia, and J. Scherk. “Supergravity in theory in 11 dimensions.” In: *Physics Letters B* 76.4 (June 1978), pp. 409–412 (cited on page 1).

[12] R. Jackiw. “Dynamical symmetry of the magnetic vortex.” In: *Annals of Physics* 201.1 (July 1990), pp. 83–116 (cited on pages 1, 227).

[13] David E. Blair. *Inversion Theory and Conformal Mapping.* American Mathematical Society, 2000 (cited on page 1).

[14] Paul Ginsparg. “Applied Conformal Field Theory.” In: *Fields, Strings and Critical Phenomena.* Edited by E. Brézin and J. Zinn-Justin. Elsevier Science & Technology, 1989 (cited on pages 1, 227).

[15] A. S. Fokas. “Symmetries and Integrability.” In: *Studies in Applied Mathematics* 77.3 (1987), pp. 253–299 (cited on page 1).

[16] Vladimir E. Zakharov. *What Is Integrability?* Springer Series in Nonlinear Dynamics. Springer Berlin Heidelberg, 1991 (cited on pages 1, 227).

[17] Stefano Lepri, Roberto Livi, and Antonio Politi. "Thermal conduction in classical low-dimensional lattices." In: *Physics Reports* 377.1 (Apr. 2003), pp. 1–80 (cited on page 1).

[18] Tobias Brandes (Ed.) *Low-Dimensional Systems.* Lecture Notes in Physics. Springer Berlin Heidelberg, 2000 (cited on page 1).

[19] K. v. Klitzing, G. Dorda, and M. Pepper. "New Method for High-Accuracy Determination of the Fine-Structure Constant Based on Quantized Hall Resistance." In: *Physical Review Letters* 45.6 (Aug. 1980), pp. 494–497 (cited on page 1).

[20] V. J. Goldman and B. Su. "Resonant Tunneling in the Quantum Hall Regime: Measurement of Fractional Charge." In: *Science* 267.5200 (Feb. 1995), pp. 1010–1012 (cited on page 1).

[21] L. Saminadayar, D. C. Glattli, Y. Jin, and B. Etienne. "Observation of the $e/3$ Fractionally Charged Laughlin Quasiparticle." In: *Physical Review Letters* 79.13 (Sept. 1997), pp. 2526–2529 (cited on page 1).

[22] R. de Picciotto, M. Reznikov, M. Heiblum, V. Umansky, G. Bunin, and D. Mahalu. "Direct observation of a fractional charge." In: *Nature* 389.6647 (Sept. 1997), p. 162 (cited on page 1).

[23] K. S. Novoselov, A. K. Geim, S. V. Morozov, D. Jiang, M. I. Katsnelson, I. V. Grigorieva, S. V. Dubonos, and A. A. Firsov. "Two-dimensional gas of massless Dirac fermions in graphene." In: *Nature* 438.7065 (Nov. 2005), p. 197 (cited on page 1).

[24] Yuanbo Zhang, Yan-Wen Tan, Horst L. Stormer, and Philip Kim. "Experimental observation of the quantum Hall effect and Berry's phase in graphene." In: *Nature* 438.7065 (Nov. 2005), p. 201 (cited on page 1).

[25] V. L. Berezinskii. "Destruction of long-range order in one-dimensional and two-dimensional systems possessing a continuous symmetry group. II. Quantum systems." In: *Soviet Physics JETP* 34.3 (1972), pp. 610–616 (cited on pages 1, 57, 227).

[26] J. M. Kosterlitz and D. J. Thouless. "Ordering, metastability and phase transitions in two-dimensional systems." In: *Journal of Physics C: Solid State Physics* 6.7 (Apr. 1973), pp. 1181–1203 (cited on pages 1, 57, 61, 227).

[27] Jorge V. José. *40 Years of Berezinskii-Kosterlitz-Thouless Theory.* World Scientific, 2013 (cited on pages 2, 227).

[28] D. J. Bishop and J. D. Reppy. "Study of the superfluid transition in two-dimensional ^{4}He films." In: *Physical Review B* 22.11 (Dec. 1980), pp. 5171–5185 (cited on page 2).

[29] D. J. Resnick, J. C. Garland, J. T. Boyd, S. Shoemaker, and R. S. Newrock. "Kosterlitz-Thouless Transition in Proximity-Coupled Superconducting Arrays." In: *Physical Review Letters* 47.21 (Nov. 1981), pp. 1542–1545 (cited on page 2).

[30] Richard F. Voss and Richard A. Webb. “Phase coherence in a weakly coupled array of 20 000 Nb Josephson junctions.” In: *Physical Review B* 25.5 (Mar. 1982), pp. 3446–3449 (cited on page 2).

[31] S. P. Benz, M. S. Rzchowski, M. Tinkham, and C. J. Lobb. “Critical currents in frustrated two-dimensional Josephson arrays.” In: *Physical Review B* 42.10 (Oct. 1990), pp. 6165–6171 (cited on page 2).

[32] Zheng Han, Adrien Allain, Hadi Arjmandi-Tash, Konstantin Tikhonov, Mikhail Feigel’man, Benjamin Sacépé, and Vincent Bouchiat. “Collapse of superconductivity in a hybrid tin–graphene Josephson junction array.” In: *Nature Physics* 10.5 (May 2014), pp. 380–386 (cited on page 2).

[33] A. F. Hebard and A. T. Fiory. “Evidence for the Kosterlitz-Thouless Transition in Thin Superconducting Aluminum Films.” In: *Physical Review Letters* 44.4 (Jan. 1980), pp. 291–294 (cited on page 2).

[34] K. Epstein, A. M. Goldman, and A. M. Kadin. “Vortex-Antivortex Pair Dissociation in Two-Dimensional Superconductors.” In: *Physical Review Letters* 47.7 (Aug. 1981), pp. 534–537 (cited on page 2).

[35] A. F. Hebard and A. T. Fiory. “Critical-Exponent Measurements of a Two-Dimensional Superconductor.” In: *Physical Review Letters* 50.20 (May 1983), pp. 1603–1606 (cited on page 2).

[36] F. Gallet, S. Balibar, and E. Rolley. “The roughening transition of crystal surfaces. II. experiments on static and dynamic properties near the first roughening transition of hcp ^{4}He.” In: *Journal de Physique* 48.3 (Mar. 1987), pp. 369–377 (cited on page 2).

[37] V. Schweikhard, S. Tung, and E. A. Cornell. “Vortex Proliferation in the Berezinskii-Kosterlitz-Thouless Regime on a Two-Dimensional Lattice of Bose-Einstein Condensates.” In: *Physical Review Letters* 99.3 (July 2007), p. 030401 (cited on pages 2, 57).

[38] Z. Hadzibabic and J. Dalibard. “Two-dimensional Bose fluids: An atomic physics perspective.” In: *Rivista del Nuovo Cimento* 34 (2011), p. 389 (cited on pages 2, 29, 68, 73, 227).

[39] L. D. Landau. “Theory of superfluidity of Helium-II.” In: *Zhurnal Eksperimentalnoi i Teoreticheskoi Fiziki* 11 (Dec. 1941), p. 592 (cited on page 2).

[40] Claude Cohen-Tannoudji and David Guéry-Odelin. *Advances in atomic physics: An overview.* Jan. 2011 (cited on page 2).

[41] C. J. Pethick and H. Smith. *Bose-Einstein Condensation in Dilute Gases.* Cambridge University Press, 2002 (cited on pages 2, 161).

[42] Bose. “Plancks Gesetz und Lichtquantenhypothese.” In: *Zeitschrift für Physik* 26.1 (Dec. 1924), pp. 178–181 (cited on page 2).

[43] A. Einstein. “Quantentheorie des einatomigen idealen Gases.” In: *S. B. Preuss. Akad. Wiss. phys.-math. Klasse* (1924) (cited on page 2).

[44] M. H. Anderson, J. R. Ensher, M. R. Matthews, C. E. Wieman, and E. A. Cornell. “Observation of Bose-Einstein Condensation in a Dilute Atomic Vapor.” In: *Science* 269.5221 (July 1995), pp. 198–201 (cited on page 2).

[45] K. B. Davis, M. O. Mewes, M. R. Andrews, N. J. van Druten, D. S. Durfee, D. M. Kurn, and W. Ketterle. “Bose-Einstein Condensation in a Gas of Sodium Atoms.” In: *Physical Review Letters* 75.22 (Nov. 1995), pp. 3969–3973 (cited on page 2).

[46] E. Fermi. “Zur Quantelung des idealen einatomigen Gases.” In: *Zeitschrift für Physik* 36.11 (Nov. 1926), pp. 902–912 (cited on page 2).

[47] B. DeMarco and D. S. Jin. “Onset of Fermi Degeneracy in a Trapped Atomic Gas.” In: *Science* 285.5434 (Sept. 1999), pp. 1703–1706 (cited on page 2).

[48] I. Bloch, T. W. Hänsch, and T. Esslinger. “Measurement of the spatial coherence of a trapped Bose gas at the phase transition.” In: *Nature* 403.6766 (Jan. 2000), p. 166 (cited on pages 2, 57, 89).

[49] David E. Pritchard. “Cooling Neutral Atoms in a Magnetic Trap for Precision Spectroscopy.” In: *Physical Review Letters* 51.15 (Oct. 1983), pp. 1336–1339 (cited on page 2).

[50] Rudolf Grimm, Matthias Weidemüller, and Yurii B. Ovchinnikov. “Optical Dipole Traps for Neutral Atoms.” In: *Advances In Atomic, Molecular, and Optical Physics* 42 (Jan. 2000). Ed. by Benjamin Bederson and Herbert Walther, pp. 95–170 (cited on page 2).

[51] Immanuel Bloch. “Ultracold quantum gases in optical lattices.” In: *Nature Physics* 1.1 (Oct. 2005), p. 23 (cited on page 2).

[52] J. Sebby-Strabley, M. Anderlini, P. S. Jessen, and J. V. Porto. “Lattice of double wells for manipulating pairs of cold atoms.” In: *Physical Review A* 73.3 (Mar. 2006), p. 033605 (cited on page 2).

[53] Leticia Tarruell, Daniel Greif, Thomas Uehlinger, Gregor Jotzu, and Tilman Esslinger. “Creating, moving and merging Dirac points with a Fermi gas in a tunable honeycomb lattice.” In: *Nature* 483.7389 (Mar. 2012), pp. 302–305 (cited on page 2).

[54] Gyu-Boong Jo, Jennie Guzman, Claire K. Thomas, Pavan Hosur, Ashvin Vishwanath, and Dan M. Stamper-Kurn. “Ultracold Atoms in a Tunable Optical Kagome Lattice.” In: *Physical Review Letters* 108.4 (Jan. 2012), p. 045305 (cited on page 2).

[55] A. Görlitz, J. M. Vogels, A. E. Leanhardt, C. Raman, T. L. Gustavson, J. R. Abo-Shaeer, A. P. Chikkatur, S. Gupta, S. Inouye, T. Rosenband, and W. Ketterle. “Realization of Bose-Einstein Condensates in Lower Dimensions.” In: *Physical Review Letters* 87.13 (Sept. 2001), p. 130402 (cited on page 2).

[56] K. Merloti, R. Dubessy, L. Longchambon, A. Perrin, P.-E. Pottie, V. Lorent, and H. Perrin. “A two-dimensional quantum gas in a magnetic trap.” In: *New Journal of Physics* 15.3 (Mar. 2013), p. 033007 (cited on page 2).

[57] József Fortágh and Claus Zimmermann. “Magnetic microtraps for ultracold atoms.” In: *Reviews of Modern Physics* 79.1 (Feb. 2007), pp. 235–289 (cited on page 2).

[58] Juliette Billy, Vincent Josse, Zhanchun Zuo, Alain Bernard, Ben Hambrecht, Pierre Lugan, David Clément, Laurent Sanchez-Palencia, Philippe Bouyer, and Alain Aspect. “Direct observation of Anderson localization of matter waves in a controlled disorder.” In: *Nature* 453.7197 (June 2008), pp. 891–894 (cited on page 2).

[59] Alexander L. Gaunt, Tobias F. Schmidutz, Igor Gotlibovych, Robert P. Smith, and Zoran Hadzibabic. “Bose-Einstein Condensation of Atoms in a Uniform Potential.” In: *Physical Review Letters* 110.20 (May 2013), p. 200406 (cited on pages 2, 24).

[60] S. Inouye, M. R. Andrews, J. Stenger, H.-J. Miesner, D. M. Stamper-Kurn, and W. Ketterle. “Observation of Feshbach resonances in a Bose–Einstein condensate.” In: *Nature* 392.6672 (Mar. 1998), p. 151 (cited on page 3).

[61] C. Menotti, M. Lewenstein, T. Lahaye, and T. Pfau. “Dipolar interaction in ultracold atomic gases.” In: *AIP Conference Proceedings* 970.1 (Jan. 2008), pp. 332–361 (cited on page 3).

[62] Kristian Baumann, Christine Guerlin, Ferdinand Brennecke, and Tilman Esslinger. “Dicke quantum phase transition with a superfluid gas in an optical cavity.” In: *Nature* 464.7293 (July 2010), pp. 1301–1306 (cited on page 3).

[63] Immanuel Bloch, Jean Dalibard, and Wilhelm Zwerger. “Many-body physics with ultracold gases.” In: *Reviews of Modern Physics* 80.3 (July 2008), pp. 885–964 (cited on page 3).

[64] Laura Corman. “The two-dimensional Bose Gas in box potentials.” PhD thesis. PSL Research University, June 2016 (cited on pages 3, 11, 16).

[65] Jean-Loup Ville. “Quantum gases in box potentials: Sound and light in bosonic Flatland.” PhD thesis. PSL Research University, Apr. 2018 (cited on pages 3, 11, 16, 24, 138).

[66] Biswaroop Mukherjee, Zhenjie Yan, Parth B. Patel, Zoran Hadzibabic, Tarik Yefsah, Julian Struck, and Martin W. Zwierlein. “Homogeneous Atomic Fermi Gases.” In: *Physical Review Letters* 118.12 (Mar. 2017), p. 123401 (cited on pages 3, 24).

[67] Klaus Hueck, Niclas Luick, Lennart Sobirey, Jonas Siegl, Thomas Lompe, and Henning Moritz. “Two-Dimensional Homogeneous Fermi Gases.” In: *Physical Review Letters* 120.6 (Feb. 2018), p. 060402 (cited on pages 3, 24, 32, 229).

[68] Guillaume Gauthier, Stuart S. Szigeti, Matthew T. Reeves, Mark Baker, Thomas A. Bell, Halina Rubinsztein-Dunlop, Matthew J. Davis, and Tyler W. Neely. “An atomtronic oscillator circuit for quantum gases.” In: *arXiv:1903.04086 [cond-mat, physics:quant-ph]* (Mar. 2019). arXiv: 1903.04086 (cited on pages 3, 24).

[69] M. Aidelsburger, J.L. Ville, R. Saint-Jalm, S. Nascimbène, J. Dalibard, and J. Beugnon. “Relaxation Dynamics in the Merging of N Independent Condensates.” In: *Physical Review Letters* 119.19 (Nov. 2017), p. 190403 (cited on pages 3, 25).

[70] S. Jennewein, M. Besbes, N. J. Schilder, S. D. Jenkins, C. Sauvan, J. Ruostekoski, J.-J. Greffet, Y. R. P. Sortais, and A. Browaeys. "Coherent Scattering of Near-Resonant Light by a Dense Microscopic Cold Atomic Cloud." In: *Physical Review Letters* 116.23 (June 2016), p. 233601 (cited on page 3).

[71] L. Chomaz, L. Corman, T. Yefsah, R. Desbuquois, and J. Dalibard. "Absorption imaging of a quasi-two-dimensional gas: a multiple scattering analysis." In: *New Journal of Physics* 14.5 (May 2012), p. 055001 (cited on page 3).

[72] Nicolas Cherroret, Dominique Delande, and Bart A. van Tiggelen. "Induced dipole-dipole interactions in light diffusion from point dipoles." In: *Physical Review A* 94.1 (July 2016), p. 012702 (cited on page 3).

[73] Mark D. Lee, Stewart D. Jenkins, and Janne Ruostekoski. "Stochastic methods for light propagation and recurrent scattering in saturated and nonsaturated atomic ensembles." In: *Physical Review A* 93.6 (June 2016), p. 063803 (cited on page 3).

[74] J. Keaveney, A. Sargsyan, U. Krohn, I. G. Hughes, D. Sarkisyan, and C. S. Adams. "Cooperative Lamb Shift in an Atomic Vapor Layer of Nanometer Thickness." In: *Physical Review Letters* 108.17 (Apr. 2012), p. 173601 (cited on page 4).

[75] S. Balik, A. L. Win, M. D. Havey, I. M. Sokolov, and D. V. Kupriyanov. "Near-resonance light scattering from a high-density ultracold atomic ^{87}Rb gas." In: *Physical Review A* 87.5 (May 2013), p. 053817 (cited on page 4).

[76] S. L. Bromley, B. Zhu, M. Bishof, X. Zhang, T. Bothwell, J. Schachenmayer, T. L. Nicholson, R. Kaiser, S. F. Yelin, M. D. Lukin, A. M. Rey, and J. Ye. "Collective atomic scattering and motional effects in a dense coherent medium." In: *Nature Communications* 7 (Mar. 2016), p. 11039 (cited on page 4).

[77] P. C. Bons, R. de Haas, D. de Jong, A. Groot, and P. van der Straten. "Quantum Enhancement of the Index of Refraction in a Bose-Einstein Condensate." In: *Physical Review Letters* 116.17 (Apr. 2016), p. 173602 (cited on page 4).

[78] J. Pellegrino, R. Bourgain, S. Jennewein, Y. R. P. Sortais, A. Browaeys, S. D. Jenkins, and J. Ruostekoski. "Observation of Suppression of Light Scattering Induced by Dipole-Dipole Interactions in a Cold-Atom Ensemble." In: *Physical Review Letters* 113.13 (Sept. 2014), p. 133602 (cited on page 4).

[79] S. D. Jenkins, J. Ruostekoski, J. Javanainen, S. Jennewein, R. Bourgain, J. Pellegrino, Y. R. P. Sortais, and A. Browaeys. "Collective resonance fluorescence in small and dense atom clouds: Comparison between theory and experiment." In: *Physical Review A* 94.2 (Aug. 2016), p. 023842 (cited on page 4).

[80] W. H. Zurek. "Cosmological experiments in superfluid helium?" In: *Nature* 317.6037 (Oct. 1985), p. 505 (cited on page 4).

[81] Jérôme Beugnon and Nir Navon. “Exploring the Kibble–Zurek mechanism with homogeneous Bose gases.” In: *Journal of Physics B: Atomic, Molecular and Optical Physics* 50.2 (Jan. 2017), p. 022002 (cited on page 4).

[82] A. Ramanathan, K. C. Wright, S. R. Muniz, M. Zelan, W. T. Hill, C. J. Lobb, K. Helmerson, W. D. Phillips, and G. K. Campbell. “Superflow in a Toroidal Bose-Einstein Condensate: An Atom Circuit with a Tunable Weak Link.” In: *Physical Review Letters* 106.13 (Mar. 2011), p. 130401 (cited on page 4).

[83] C. Schenke, A. Minguzzi, and F. W. J. Hekking. “Nonadiabatic creation of macroscopic superpositions with strongly correlated one-dimensional bosons in a ring trap.” In: *Physical Review A* 84.5 (Nov. 2011), p. 053636 (cited on page 4).

[84] K. C. Wright, R. B. Blakestad, C. J. Lobb, W. D. Phillips, and G. K. Campbell. “Driving Phase Slips in a Superfluid Atom Circuit with a Rotating Weak Link.” In: *Physical Review Letters* 110.2 (Jan. 2013), p. 025302 (cited on page 4).

[85] F. Jendrzejewski, S. Eckel, N. Murray, C. Lanier, M. Edwards, C. J. Lobb, and G. K. Campbell. “Resistive Flow in a Weakly Interacting Bose-Einstein Condensate.” In: *Physical Review Letters* 113.4 (July 2014), p. 045305 (cited on page 4).

[86] B. T. Seaman, M. Krämer, D. Z. Anderson, and M. J. Holland. “Atomtronics: Ultracold-atom analogs of electronic devices.” In: *Physical Review A* 75.2 (Feb. 2007), p. 023615 (cited on page 4).

[87] Davit Aghamalyan, Marco Cominotti, Matteo Rizzi, Davide Rossini, Frank Hekking, Anna Minguzzi, Leong-Chuan Kwek, and Luigi Amico. “Coherent superposition of current flows in an atomtronic quantum interference device.” In: *New Journal of Physics* 17.4 (Apr. 2015), p. 045023 (cited on page 4).

[88] M. R. Andrews, D. M. Kurn, H.-J. Miesner, D. S. Durfee, C. G. Townsend, S. Inouye, and W. Ketterle. “Propagation of Sound in a Bose-Einstein Condensate.” In: *Physical Review Letters* 79.4 (July 1997), pp. 553–556 (cited on page 4).

[89] D. M. Stamper-Kurn, H.-J. Miesner, S. Inouye, M. R. Andrews, and W. Ketterle. “Collisionless and Hydrodynamic Excitations of a Bose-Einstein Condensate.” In: *Physical Review Letters* 81.3 (July 1998), pp. 500–503 (cited on page 4).

[90] J. Joseph, B. Clancy, L. Luo, J. Kinast, A. Turlapov, and J. E. Thomas. “Measurement of Sound Velocity in a Fermi Gas near a Feshbach Resonance.” In: *Physical Review Letters* 98.17 (Apr. 2007), p. 170401 (cited on page 4).

[91] R. Meppelink, S. B. Koller, and P. van der Straten. “Sound propagation in a Bose-Einstein condensate at finite temperatures.” In: *Physical Review A* 80.4 (Oct. 2009), p. 043605 (cited on page 4).

[92] Leonid A. Sidorenkov, Meng Khoon Tey, Rudolf Grimm, Yan-Hua Hou, Lev Pitaevskii, and Sandro Stringari. “Second sound and the superfluid fraction in a Fermi gas with resonant interactions.” In: *Nature* 498.7452 (June 2013), pp. 78–81 (cited on page 4).

[93] Tomoki Ozawa and Sandro Stringari. “Discontinuities in the First and Second Sound Velocities at the Berezinskii-Kosterlitz-Thouless Transition.” In: *Physical Review Letters* 112.2 (Jan. 2014), p. 025302 (cited on page 4).

[94] Miki Ota, Fabrizio Larcher, Franco Dalfovo, Lev Pitaevskii, Nick P. Proukakis, and Sandro Stringari. “Collisionless Sound in a Uniform Two-Dimensional Bose Gas.” In: *Physical Review Letters* 121.14 (Oct. 2018), p. 145302 (cited on pages 5, 33, 69).

[95] Katharina Kleinlein. *Setting up a new experiment for investigating artificial magnetism of two-dimensional Bose gases.* Masterarbeit. Ludwig-Maximilians-Universität, 2014 (cited on page 11).

[96] L. Corman, J. L. Ville, R. Saint-Jalm, M. Aidelsburger, T. Bienaimé, S. Nascimbène, J. Dalibard, and J. Beugnon. “Transmission of near-resonant light through a dense slab of cold atoms.” In: *Physical Review A* 96.5 (Nov. 2017), p. 053629 (cited on page 16).

[97] R. Saint-Jalm, M. Aidelsburger, J. L. Ville, L. Corman, Z. Hadzibabic, D. Delande, S. Nascimbene, N. Cherroret, J. Dalibard, and J. Beugnon. “Resonant-light diffusion in a disordered atomic layer.” In: *Physical Review A* 97.6 (June 2018), p. 061801 (cited on page 16).

[98] T. C. Li, H. Kelkar, D. Medellin, and M. G. Raizen. “Real-time control of the periodicity of a standing wave: an optical accordion.” In: *Optics Express* 16.8 (Apr. 2008), pp. 5465–5470 (cited on page 17).

[99] R. A. Williams, J. D. Pillet, S. Al-Assam, B. Fletcher, M. Shotter, and C. J. Foot. “Dynamic optical lattices: two-dimensional rotating and accordion lattices for ultracold atoms.” In: *Optics Express* 16.21 (Oct. 2008), pp. 16977–16983 (cited on page 17).

[100] S. Al-Assam, R. A. Williams, and C. J. Foot. “Ultracold atoms in an optical lattice with dynamically variable periodicity.” In: *Physical Review A* 82.2 (Aug. 2010), p. 021604 (cited on page 17).

[101] M. Miranda, A. Nakamoto, Y. Okuyama, A. Noguchi, M. Ueda, and M. Kozuma. “All-optical transport and compression of ytterbium atoms into the surface of a solid immersion lens.” In: *Physical Review A* 86.6 (Dec. 2012), p. 063615 (cited on page 17).

[102] J. L. Ville, T. Bienaimé, R. Saint-Jalm, L. Corman, M. Aidelsburger, L. Chomaz, K. Kleinlein, D. Perconte, S. Nascimbène, J. Dalibard, and J. Beugnon. “Loading and compression of a single two-dimensional Bose gas in an optical accordion.” In: *Physical Review A* 95.1 (Jan. 2017), p. 013632 (cited on page 19).

[103] L. Corman, L. Chomaz, T. Bienaimé, R. Desbuquois, C. Weitenberg, S. Nascimbène, J. Dalibard, and J. Beugnon. “Quench-Induced Supercurrents in an Annular Bose Gas.” In: *Physical Review Letters* 113.13 (Sept. 2014), p. 135302 (cited on pages 24, 160).

[104] Kenneth Maussang. “Etats comprimés atomiques sur puce à atomes.” PhD thesis. Université Pierre et Marie Curie - Paris VI, Sept. 2010 (cited on pages 27, 229).

[105] Daniel S. Fisher and P. C. Hohenberg. “Dilute Bose gas in two dimensions.” In: *Physical Review B* 37.10 (Apr. 1988), pp. 4936–4943 (cited on pages 29, 31).

[106] Nikolay Prokof’ev, Oliver Ruebenacker, and Boris Svistunov. “Critical Point of a Weakly Interacting Two-Dimensional Bose Gas.” In: *Physical Review Letters* 87.27 (Dec. 2001), p. 270402 (cited on page 29).

[107] Tarik Yefsah, Rémi Desbuquois, Lauriane Chomaz, Kenneth J. Günter, and Jean Dalibard. “Exploring the Thermodynamics of a Two-Dimensional Bose Gas.” In: *Physical Review Letters* 107.13 (Sept. 2011), p. 130401 (cited on page 30).

[108] Rémi Desbuquois, Tarik Yefsah, Lauriane Chomaz, Christof Weitenberg, Laura Corman, Sylvain Nascimbène, and Jean Dalibard. “Determination of Scale-Invariant Equations of State without Fitting Parameters: Application to the Two-Dimensional Bose Gas Across the Berezinskii-Kosterlitz-Thouless Transition.” In: *Physical Review Letters* 113.2 (July 2014), p. 020404 (cited on page 30).

[109] Chen-Lung Hung, Xibo Zhang, Nathan Gemelke, and Cheng Chin. “Observation of scale invariance and universality in two-dimensional Bose gases.” In: *Nature* 470.7333 (Feb. 2011), pp. 236–239 (cited on page 30).

[110] Nikolay Prokof’ev and Boris Svistunov. “Two-dimensional weakly interacting Bose gas in the fluctuation region.” In: *Physical Review A* 66.4 (Oct. 2002), p. 043608 (cited on pages 30, 31, 68, 69, 237).

[111] Lev Pitaevskii and Sandro Stringari. *Bose-Einstein Condensation and Superfluidity.* Oxford University Press, 2016 (cited on pages 31, 57, 125, 162).

[112] Mark J. H. Ku, Ariel T. Sommer, Lawrence W. Cheuk, and Martin W. Zwierlein. “Revealing the Superfluid Lambda Transition in the Universal Thermodynamics of a Unitary Fermi Gas.” en. In: *Science* 335.6068 (Feb. 2012), pp. 563–567 (cited on page 32).

[113] J.L. Ville, R. Saint-Jalm, É. Le Cerf, M. Aidelsburger, S. Nascimbène, J. Dalibard, and J. Beugnon. “Sound Propagation in a Uniform Superfluid Two-Dimensional Bose Gas.” In: *Physical Review Letters* 121.14 (Oct. 2018), p. 145301 (cited on pages 33, 52, 69).

[114] Zanyar Movasaghi, Shazza Rehman, and Dr Ihtesham U. Rehman. “Raman Spectroscopy of Biological Tissues.” In: *Applied Spectroscopy Reviews* 42.5 (Sept. 2007), pp. 493–541 (cited on page 35).

[115] Ji-Xin Cheng and X. Sunney Xie. “Vibrational spectroscopic imaging of living systems: An emerging platform for biology and medicine.” In: *Science* 350.6264 (Nov. 2015), aaa8870 (cited on page 35).

[116] Holly J. Butler, Lorna Ashton, Benjamin Bird, Gianfelice Cinque, Kelly Curtis, Jennifer Dorney, Karen Esmonde-White, Nigel J. Fullwood, Benjamin Gardner, Pierre L. Martin-Hirsch, Michael J. Walsh, Martin R. McAinsh, Nicholas Stone, and Francis L. Martin. “Using Raman spectroscopy to characterize biological materials.” In: *Nature Protocols* 11.4 (Apr. 2016), p. 664 (cited on page 35).

[117] F. Tuinstra and J. L. Koenig. “Raman Spectrum of Graphite.” In: *The Journal of Chemical Physics* 53.3 (Aug. 1970), pp. 1126–1130 (cited on page 35).

[118] Andrea C. Ferrari and Denis M. Basko. “Raman spectroscopy as a versatile tool for studying the properties of graphene.” In: *Nature Nanotechnology* 8.4 (Apr. 2013), pp. 235–246 (cited on page 35).

[119] C. Monroe, D. M. Meekhof, B. E. King, S. R. Jefferts, W. M. Itano, D. J. Wineland, and P. Gould. “Resolved-Sideband Raman Cooling of a Bound Atom to the 3D Zero-Point Energy.” In: *Physical Review Letters* 75.22 (Nov. 1995), pp. 4011–4014 (cited on page 35).

[120] I. Dotsenko, W. Alt, S. Kuhr, D. Schrader, M. Müller, Y. Miroshnychenko, V. Gomer, A. Rauschenbeutel, and D. Meschede. “Application of electro-optically generated light fields for Raman spectroscopy of trapped cesium atoms.” In: *Applied Physics B* 78.6 (Apr. 2004), pp. 711–717 (cited on pages 35, 39, 230).

[121] Paul Hamilton, Matt Jaffe, Justin M. Brown, Lothar Maisenbacher, Brian Estey, and Holger Müller. “Atom Interferometry in an Optical Cavity.” In: *Physical Review Letters* 114.10 (Mar. 2015), p. 100405 (cited on page 36).

[122] J. Stenger, S. Inouye, A. P. Chikkatur, D. M. Stamper-Kurn, D. E. Pritchard, and W. Ketterle. “Bragg Spectroscopy of a Bose-Einstein Condensate.” In: *Physical Review Letters* 82.23 (June 1999), pp. 4569–4573 (cited on page 36).

[123] Igor Gotlibovych, Tobias F. Schmidutz, Alexander L. Gaunt, Nir Navon, Robert P. Smith, and Zoran Hadzibabic. “Observing properties of an interacting homogeneous Bose-Einstein condensate: Heisenberg-limited momentum spread, interaction energy, and free-expansion dynamics.” In: *Physical Review A* 89.6 (June 2014), p. 061604 (cited on pages 36, 43).

[124] Y.-J. Lin, K. Jiménez-García, and I. B. Spielman. “Spin–orbit-coupled Bose–Einstein condensates.” In: *Nature* 471.7336 (Mar. 2011), pp. 83–86 (cited on page 36).

[125] Pengjun Wang, Zeng-Qiang Yu, Zhengkun Fu, Jiao Miao, Lianghui Huang, Shijie Chai, Hui Zhai, and Jing Zhang. “Spin-Orbit Coupled Degenerate Fermi Gases.” In: *Physical Review Letters* 109.9 (Aug. 2012), p. 095301 (cited on page 36).

[126] Lawrence W. Cheuk, Ariel T. Sommer, Zoran Hadzibabic, Tarik Yefsah, Waseem S. Bakr, and Martin W. Zwierlein. “Spin-Injection Spectroscopy of a Spin-Orbit Coupled Fermi Gas.” In: *Physical Review Letters* 109.9 (Aug. 2012), p. 095302 (cited on page 36).

[127] M. F. Andersen, C. Ryu, Pierre Cladé, Vasant Natarajan, A. Vaziri, K. Helmerson, and W. D. Phillips. "Quantized Rotation of Atoms from Photons with Orbital Angular Momentum." In: *Physical Review Letters* 97.17 (Oct. 2006), p. 170406 (cited on page 36).

[128] K. C. Wright, L. S. Leslie, and N. P. Bigelow. "Optical control of the internal and external angular momentum of a Bose-Einstein condensate." In: *Physical Review A* 77.4 (Apr. 2008), p. 041601 (cited on page 36).

[129] K. C. Wright, L. S. Leslie, A. Hansen, and N. P. Bigelow. "Sculpting the Vortex State of a Spinor BEC." In: *Physical Review Letters* 102.3 (Jan. 2009), p. 030405 (cited on page 36).

[130] A. P. Chikkatur, A. Görlitz, D. M. Stamper-Kurn, S. Inouye, S. Gupta, and W. Ketterle. "Suppression and Enhancement of Impurity Scattering in a Bose-Einstein Condensate." In: *Physical Review Letters* 85.3 (July 2000), pp. 483–486 (cited on page 52).

[131] E. G. M. van Kempen, S. J. J. M. F. Kokkelmans, D. J. Heinzen, and B. J. Verhaar. "Interisotope Determination of Ultracold Rubidium Interactions from Three High-Precision Experiments." In: *Physical Review Letters* 88.9 (Feb. 2002), p. 093201 (cited on page 54).

[132] Artur Widera, Fabrice Gerbier, Simon Fölling, Tatjana Gericke, Olaf Mandel, and Immanuel Bloch. "Precision measurement of spin-dependent interaction strengths for spin-1 and spin-2 ^{87}Rb atoms." In: *New Journal of Physics* 8.8 (Aug. 2006), pp. 152–152 (cited on pages 54, 161).

[133] P. A. Altin, G. McDonald, D. Döring, J. E. Debs, T. H. Barter, J. D. Close, N. P. Robins, S. A. Haine, T. M. Hanna, and R. P. Anderson. "Optically trapped atom interferometry using the clock transition of large ^{87}Rb Bose–Einstein condensates." In: *New Journal of Physics* 13.6 (June 2011), p. 065020 (cited on pages 54, 161).

[134] Lev Landau and Evguéni Lifchitz. *Physique Théorique : Physique Statistique.* 4ème éd. Moscou; Paris: Ellipses, May 1995 (cited on page 57).

[135] Neil W. Ashcroft and N. David Mermin. *Physique des solides.* EDP sciences, 2002 (cited on page 57).

[136] P. C. Hohenberg and B. I. Halperin. "Theory of dynamic critical phenomena." In: *Reviews of Modern Physics* 49.3 (July 1977), pp. 435–479 (cited on page 57).

[137] H. Eugene Stanley. "Scaling, universality, and renormalization: Three pillars of modern critical phenomena." In: *Reviews of Modern Physics* 71.2 (Mar. 1999), S358–S366 (cited on page 57).

[138] Michael E. Fisher. "The renormalization group in the theory of critical behavior." In: *Reviews of Modern Physics* 46.4 (Oct. 1974), pp. 597–616 (cited on page 57).

[139] H. E. Stanley. "Dependence of Critical Properties on Dimensionality of Spins." In: *Physical Review Letters* 20.12 (Mar. 1968), pp. 589–592 (cited on page 57).

[140] T. Donner, S. Ritter, T. Bourdel, A. Öttl, M. Köhl, and T. Esslinger. "Critical Behavior of a Trapped Interacting Bose Gas." In: *Science* 315.5818 (Mar. 2007), pp. 1556–1558 (cited on pages 57, 89).

[141] N. D. Mermin and H. Wagner. "Absence of Ferromagnetism or Antiferromagnetism in One- or Two-Dimensional Isotropic Heisenberg Models." In: *Physical Review Letters* 17.22 (Nov. 1966), pp. 1133–1136 (cited on pages 57, 227).

[142] P. C. Hohenberg. "Existence of Long-Range Order in One and Two Dimensions." In: *Physical Review* 158.2 (June 1967), pp. 383–386 (cited on pages 57, 227).

[143] Jürg Fröhlich and Thomas Spencer. "The Kosterlitz-Thouless transition in two-dimensional abelian spin systems and the Coulomb gas." In: *Communications in Mathematical Physics* 81.4 (1981), pp. 527–602 (cited on page 57).

[144] P. Cladé, C. Ryu, A. Ramanathan, K. Helmerson, and W. D. Phillips. "Observation of a 2D Bose Gas: From Thermal to Quasicondensate to Superfluid." In: *Physical Review Letters* 102.17 (Apr. 2009), p. 170401 (cited on pages 57, 68, 70, 72, 233).

[145] S. Tung, G. Lamporesi, D. Lobser, L. Xia, and E. A. Cornell. "Observation of the Presuperfluid Regime in a Two-Dimensional Bose Gas." In: *Physical Review Letters* 105.23 (Dec. 2010), p. 230408 (cited on pages 57, 75).

[146] T. Plisson, B. Allard, M. Holzmann, G. Salomon, A. Aspect, P. Bouyer, and T. Bourdel. "Coherence properties of a two-dimensional trapped Bose gas around the superfluid transition." In: *Physical Review A* 84.6 (Dec. 2011), p. 061606 (cited on page 57).

[147] Jae-yoon Choi, Sang Won Seo, and Yong-il Shin. "Observation of Thermally Activated Vortex Pairs in a Quasi-2D Bose Gas." In: *Physical Review Letters* 110.17 (Apr. 2013), p. 175302 (cited on page 57).

[148] John B. Kogut. "An introduction to lattice gauge theory and spin systems." In: *Reviews of Modern Physics* 51.4 (Oct. 1979), pp. 659–713 (cited on pages 58, 62).

[149] Michel Le Bellac. *Des phénomènes critiques aux champs de jauge.* Savoirs actuels. Editions du CNRS, 1990 (cited on pages 58, 59, 61, 62, 68).

[150] Jean Dalibard. *Fluides quantiques de basse dimension et transition de Kosterlitz-Thouless.* Cours du Collège de France, 2017 (cited on pages 59, 61, 64).

[151] J. M. Kosterlitz. "The critical properties of the two-dimensional xy model." In: *Journal of Physics C: Solid State Physics* 7.6 (Mar. 1974), pp. 1046–1060 (cited on pages 62, 64).

[152] Jorge V. José, Leo P. Kadanoff, Scott Kirkpatrick, and David R. Nelson. "Renormalization, vortices, and symmetry-breaking perturbations in the two-dimensional planar model." In: *Physical Review B* 16.3 (Aug. 1977), pp. 1217–1241 (cited on page 62).

[153] M. Naraschewski and R. J. Glauber. “Spatial coherence and density correlations of trapped Bose gases.” In: *Physical Review A* 59.6 (June 1999), pp. 4595–4607 (cited on page 65).

[154] A. I. Safonov, S. A. Vasilyev, I. S. Yasnikov, I. I. Lukashevich, and S. Jaakkola. “Observation of Quasicondensate in Two-Dimensional Atomic Hydrogen.” In: *Physical Review Letters* 81.21 (Nov. 1998), pp. 4545–4548 (cited on page 68).

[155] Petter Minnhagen and G. G. Warren. “Superfluid density of a two-dimensional fluid.” In: *Physical Review B* 24.5 (Sept. 1981), pp. 2526–2532 (cited on page 68).

[156] Krzysztof Gawryluk and Mirosław Brewczyk. “Signatures of a universal jump in the superfluid density of a two-dimensional Bose gas with a finite number of particles.” In: *Physical Review A* 99.3 (Mar. 2019), p. 033615 (cited on pages 68, 101).

[157] D. J. Bishop and J. D. Reppy. “Study of the Superfluid Transition in Two-Dimensional ^{4}He Films.” In: *Physical Review Letters* 40.26 (June 1978), pp. 1727–1730 (cited on page 69).

[158] Miki Ota and Sandro Stringari. “Second sound in a two-dimensional Bose gas: From the weakly to the strongly interacting regime.” In: *Physical Review A* 97.3 (Mar. 2018), p. 033604 (cited on page 69).

[159] Georgios Roumpos, Michael Lohse, Wolfgang H. Nitsche, Jonathan Keeling, Marzena Hanna Szymańska, Peter B. Littlewood, Andreas Löffler, Sven Höfling, Lukas Worschech, Alfred Forchel, and Yoshihisa Yamamoto. “Power-law decay of the spatial correlation function in exciton-polariton condensates.” In: *Proceedings of the National Academy of Sciences* 109.17 (Apr. 2012), pp. 6467–6472 (cited on pages 70, 71, 89, 233).

[160] Wolfgang H. Nitsche, Na Young Kim, Georgios Roumpos, Christian Schneider, Martin Kamp, Sven Höfling, Alfred Forchel, and Yoshihisa Yamamoto. “Algebraic order and the Berezinskii-Kosterlitz-Thouless transition in an exciton-polariton gas.” In: *Physical Review B* 90.20 (Nov. 2014), p. 205430 (cited on pages 70, 71, 89, 233).

[161] Davide Caputo, Dario Ballarini, Galbadrakh Dagvadorj, Carlos Sánchez Muñoz, Milena De Giorgi, Lorenzo Dominici, Kenneth West, Loren N. Pfeiffer, Giuseppe Gigli, Fabrice P. Laussy, Marzena H. Szymańska, and Daniele Sanvitto. “Topological order and thermal equilibrium in polariton condensates.” In: *Nature Materials* 17.2 (Feb. 2018), pp. 145–151 (cited on pages 70, 71, 89, 233).

[162] Zoran Hadzibabic, Peter Krüger, Marc Cheneau, Baptiste Battelier, and Jean Dalibard. “Berezinskii–Kosterlitz–Thouless crossover in a trapped atomic gas.” In: *Nature* 441.7097 (June 2006), p. 1118 (cited on pages 70–72, 233).

[163] P. A. Murthy, I. Boettcher, L. Bayha, M. Holzmann, D. Kedar, M. Neidig, M. G. Ries, A. N. Wenz, G. Zürn, and S. Jochim. “Observation of the Berezinskii-Kosterlitz-Thouless Phase Transition in an Ultracold Fermi Gas.” In: *Physical Review Letters* 115.1 (June 2015), p. 010401 (cited on pages 70, 72, 75, 86, 233, 234).

[164] Iacopo Carusotto and Cristiano Ciuti. “Quantum fluids of light.” In: *Reviews of Modern Physics* 85.1 (Feb. 2013), pp. 299–366 (cited on page 70).

[165] Hui Deng, Hartmut Haug, and Yoshihisa Yamamoto. “Exciton-polariton Bose-Einstein condensation.” In: *Reviews of Modern Physics* 82.2 (May 2010), pp. 1489–1537 (cited on page 70).

[166] A. Zamora, L. M. Sieberer, K. Dunnett, S. Diehl, and M. H. Szymańska. “Tuning across Universalities with a Driven Open Condensate.” In: *Physical Review X* 7.4 (Oct. 2017), p. 041006 (cited on pages 70, 71).

[167] Jonathan Keeling, Lukas M. Sieberer, Ehud Altman, Leiming Chen, Sebastian Diehl, and John Toner. “Superfluidity and Phase Correlations of Driven Dissipative Condensates.” In: *Universal Themes of Bose-Einstein Condensation.* Edited by Nick P. Proukakis, David W. Snoke and Peter B. Littlewood. Cambridge University Press, 2017 (cited on page 70).

[168] G. Dagvadorj, J. M. Fellows, S. Matyjaśkiewicz, F. M. Marchetti, I. Carusotto, and M. H. Szymańska. “Nonequilibrium Phase Transition in a Two-Dimensional Driven Open Quantum System.” In: *Physical Review X* 5.4 (Nov. 2015), p. 041028 (cited on page 71).

[169] Na Young Kim, Wolfgang H. Nitsche, and Yoshihisa Yamamoto. “Berezinskii-Kosterlitz-Thouless Phase of a Driven-Dissipative Condensate.” In: *Universal Themes of Bose-Einstein Condensation.* Edited by Nick P. Proukakis, David W. Snoke and Peter B. Littlewood. Cambridge University Press, 2017 (cited on page 71).

[170] Anatoli Polkovnikov, Ehud Altman, and Eugene Demler. “Interference between independent fluctuating condensates.” In: *Proceedings of the National Academy of Sciences* 103.16 (Apr. 2006), pp. 6125–6129 (cited on page 71).

[171] Igor Boettcher and Markus Holzmann. “Quasi-long-range order in trapped two-dimensional Bose gases.” In: *Physical Review A* 94.1 (July 2016), p. 011602 (cited on page 72).

[172] P. A. Murthy, D. Kedar, T. Lompe, M. Neidig, M. G. Ries, A. N. Wenz, G. Zürn, and S. Jochim. “Matter-wave Fourier optics with a strongly interacting two-dimensional Fermi gas.” In: *Physical Review A* 90.4 (Oct. 2014), p. 043611 (cited on pages 75, 77).

[173] I. Shvarchuck, Ch. Buggle, D. S. Petrov, K. Dieckmann, M. Zielonkowski, M. Kemmann, T. G. Tiecke, W. von Klitzing, G. V. Shlyapnikov, and J. T. M. Walraven. “Bose-Einstein Condensation into Nonequilibrium States Studied by Condensate Focusing.” In: *Physical Review Letters* 89.27 (Dec. 2002), p. 270404 (cited on page 75).

[174] A. H. van Amerongen, J. J. P. van Es, P. Wicke, K. V. Kheruntsyan, and N. J. van Druten. “Yang-Yang Thermodynamics on an Atom Chip.” In: *Physical Review Letters* 100.9 (Mar. 2008), p. 090402 (cited on page 75).

[175] J. J. P. van Es, P. Wicke, A. H. van Amerongen, C. Rétif, S. Whitlock, and N. J. van Druten. “Box traps on an atom chip for one-dimensional quantum gases.” In: *Journal of Physics B: Atomic, Molecular and Optical Physics* 43.15 (July 2010), p. 155002 (cited on page 75).

[176] Thibaut Jacqmin, Bess Fang, Tarik Berrada, Tommaso Roscilde, and Isabelle Bouchoule. “Momentum distribution of one-dimensional Bose gases at the quasicondensation crossover: Theoretical and experimental investigation.” In: *Physical Review A* 86.4 (Oct. 2012), p. 043626 (cited on page 75).

[177] E. W. Hagley, L. Deng, M. Kozuma, M. Trippenbach, Y. B. Band, M. Edwards, M Doery, P. S. Julienne, K. Helmerson, S. L. Rolston, and W. D. Phillips. “Measurement of the Coherence of a Bose-Einstein Condensate.” In: *Physical Review Letters* 83.16 (Oct. 1999), pp. 3112–3115 (cited on page 89).

[178] Nir Navon, Alexander L. Gaunt, Robert P. Smith, and Zoran Hadzibabic. “Critical dynamics of spontaneous symmetry breaking in a homogeneous Bose gas.” In: *Science* 347.6218 (Jan. 2015), pp. 167–170 (cited on page 89).

[179] R. P. Feynman. “Space-Time Approach to Non-Relativistic Quantum Mechanics.” In: *Reviews of Modern Physics* 20.2 (Apr. 1948), pp. 367–387 (cited on page 90).

[180] M. R. Andrews, C. G. Townsend, H.-J. Miesner, D. S. Durfee, D. M. Kurn, and W. Ketterle. “Observation of Interference Between Two Bose Condensates.” en. In: *Science* 275.5300 (Jan. 1997), pp. 637–641 (cited on page 97).

[181] P. Comaron, F. Larcher, F. Dalfovo, and N. P. Proukakis. “Quench dynamics of an ultracold two-dimensional Bose gas.” In: *Physical Review A* 100.3 (Sept. 2019), p. 033618 (cited on pages 101, 160).

[182] R. Saint-Jalm, P. C. M. Castilho, É. Le Cerf, B. Bakkali-Hassani, J.-L. Ville, S. Nascimbene, J. Beugnon, and J. Dalibard. “Dynamical Symmetry and Breathers in a Two-Dimensional Bose Gas.” In: *Physical Review X* 9.2 (May 2019), p. 021035 (cited on page 107).

[183] Athanassios S. Fokas. “Invariants, Lie-Bäcklund operators and Bäcklund transformations.” Ph.D. thesis. California Institute of Technology, 1979 (cited on page 110).

[184] Jean-Marc Lévy-Leblond. “Conservation Laws for Gauge-Variant Lagrangians in Classical Mechanics.” In: *American Journal of Physics* 39.5 (May 1971), pp. 502–506 (cited on page 111).

[185] G. E. Prince and C. J. Eliezer. “On the Lie symmetries of the classical Kepler problem.” In: *Journal of Physics A: Mathematical and General* 14.3 (Mar. 1981), pp. 587–596 (cited on page 111).

[186] R. K. Dodd, H. C. Morris, J. C. Eilbeck, and J. D. Gibbon. *Solitons And Nonlinear Wave Equations.* Academic Press, 1982 (cited on pages 112, 143).

[187] Y. Castin. “Simple theoretical tools for low dimension Bose gases.” In: *Journal de Physique IV (Proceedings)* 116 (Oct. 2004), pp. 89–132 (cited on page 113).

[188] Barry R. Holstein. “Anomalies for pedestrians.” In: *American Journal of Physics* 61.2 (Feb. 1993), pp. 142–147 (cited on page 113).

[189] Maxim Olshanii, Hélène Perrin, and Vincent Lorent. “Example of a Quantum Anomaly in the Physics of Ultracold Gases.” In: *Physical Review Letters* 105.9 (Aug. 2010), p. 095302 (cited on page 113).

[190] U. Niederer. “The maximal kinematical invariance group of the free Schrödinger equation.” In: *Helvetica Physica Acta* 45.5 (1972), p. 802 (cited on pages 114, 115, 238).

[191] V. Bargmann. “Irreducible Unitary Representations of the Lorentz Group.” In: *Annals of Mathematics* 48.3 (1947), pp. 568–640 (cited on page 116).

[192] U. Niederer. “The maximal kinematical invariance group of the harmonic oscillator.” In: *Helvetica Physica Acta* 46.2 (1973), p. 191 (cited on pages 117, 118, 127, 238).

[193] L. P. Pitaevskii and A. Rosch. “Breathing modes and hidden symmetry of trapped atoms in two dimensions.” In: *Physical Review A* 55.2 (Feb. 1997), R853–R856 (cited on page 118).

[194] F. Chevy, V. Bretin, P. Rosenbusch, K. W. Madison, and J. Dalibard. “Transverse Breathing Mode of an Elongated Bose-Einstein Condensate.” In: *Physical Review Letters* 88.25 (June 2002), p. 250402 (cited on page 119).

[195] Enrico Vogt, Michael Feld, Bernd Fröhlich, Daniel Pertot, Marco Koschorreck, and Michael Köhl. “Scale Invariance and Viscosity of a Two-Dimensional Fermi Gas.” In: *Physical Review Letters* 108.7 (Feb. 2012), p. 070404 (cited on page 119).

[196] Y. Castin and R. Dum. “Bose-Einstein Condensates in Time Dependent Traps.” In: *Physical Review Letters* 77.27 (Dec. 1996), pp. 5315–5319 (cited on page 120).

[197] Yu. Kagan, E. L. Surkov, and G. V. Shlyapnikov. “Evolution of a Bose-condensed gas under variations of the confining potential.” In: *Physical Review A* 54.3 (Sept. 1996), R1753–R1756 (cited on page 120).

[198] Pijush K. Ghosh. “Conformal symmetry and the nonlinear Schrödinger equation.” In: *Physical Review A* 65.1 (Dec. 2001), p. 012103 (cited on page 120).

[199] Félix Werner and Yvan Castin. “Unitary gas in an isotropic harmonic trap: Symmetry properties and applications.” In: *Physical Review A* 74.5 (Nov. 2006), p. 053604 (cited on page 120).

[200] Vladimir Gritsev, Peter Barmettler, and Eugene Demler. "Scaling approach to quantum non-equilibrium dynamics of many-body systems." In: *New Journal of Physics* 12.11 (Nov. 2010), p. 113005 (cited on page 120).

[201] John R. Ray and James L. Reid. "More exact invariants for the time-dependent harmonic oscillator." In: *Physics Letters A* 71.4 (May 1979), pp. 317–318 (cited on page 121).

[202] C. Rogers and W. K. Schief. "Multi-component Ermakov Systems: Structure and Linearization." In: *Journal of Mathematical Analysis and Applications* 198.1 (Feb. 1996), pp. 194–220 (cited on page 121).

[203] S. Carillo and F. Zullo. "Ermakov–Pinney and Emden–Fowler Equations: New Solutions from Novel Bäcklund Transformations." In: *Theoretical and Mathematical Physics* 196.3 (Sept. 2018), pp. 1268–1281 (cited on page 121).

[204] E. A. Kuznetsov, M. Yu Kagan, and A. V. Turlapov. "Expansion of the strongly interacting superfluid Fermi gas: symmetries and self-similar regimes." In: *arXiv:1903.04245 [cond-mat]* (Mar. 2019). arXiv: 1903.04245 (cited on page 121).

[205] Stephen Wiggins. *Introduction to Applied Nonlinear Dynamical Systems and Chaos*. Springer Science & Business Media, Oct. 2003 (cited on page 143).

[206] Daniel Kaplan and Leon Glass. *Understanding Nonlinear Dynamics*. Springer Science & Business Media, Dec. 2012 (cited on page 143).

[207] Steven H. Strogatz. *Nonlinear Dynamics and Chaos: With Applications to Physics, Biology, Chemistry, and Engineering*. Avalon Publishing, Aug. 2014 (cited on page 143).

[208] Robert M. May. "Simple mathematical models with very complicated dynamics." In: *Nature* 261.5560 (June 1976), p. 459 (cited on page 143).

[209] Edward N. Lorenz. "Deterministic Nonperiodic Flow." In: *Journal of the Atmospheric Sciences* 20.2 (Mar. 1963), pp. 130–141 (cited on page 143).

[210] Robert W. Boyd. *Nonlinear Optics*. Elsevier, May 2008 (cited on page 143).

[211] John Grue. *Waves and Nonlinear Processes in Hydrodynamics*. Springer, July 2012 (cited on page 143).

[212] Alfred Seeger, Hans Donth, and Albert Kochendörfer. "Theorie der Versetzungen in eindimensionalen Atomreihen." In: *Zeitschrift für Physik* 134.2 (Apr. 1953), pp. 173–193 (cited on page 143).

[213] G. L. Lamb. "Propagation of ultrashort optical pulses." In: *Physics Letters A* 25.3 (Aug. 1967), pp. 181–182 (cited on page 143).

[214] Dodd R. K., Bullough R. K., and Ursell Fritz Joseph. "Bäcklund transformations for the sine–Gordon equations." In: *Proceedings of the Royal Society of London. A. Mathematical and Physical Sciences* 351.1667 (Dec. 1976), pp. 499–523 (cited on page 143).

[215] British Association for the Advancement of Science. and British Association for the Advancement of Science. *Report of the British Association for the Advancement of Science.* Vol. 14th Meeting (1845). London., 1844 (cited on page 144).

[216] V. F. Zakharov and A. B. Shabat. “Exact Theory of Two-dimensional Self-focusing and One-dimensional Self-modulation of Wave in Nonlinear Media.” In: *JETP* 34.1 (1972), p. 62 (cited on page 144).

[217] L. F. Mollenauer, R. H. Stolen, and J. P. Gordon. “Experimental Observation of Picosecond Pulse Narrowing and Solitons in Optical Fibers.” In: *Physical Review Letters* 45.13 (Sept. 1980), pp. 1095–1098 (cited on page 144).

[218] J. S. Aitchison, A. M. Weiner, Y. Silberberg, M. K. Oliver, J. L. Jackel, D. E. Leaird, E. M. Vogel, and P. W. E. Smith. “Observation of spatial optical solitons in a nonlinear glass waveguide.” In: *Optics Letters* 15.9 (May 1990), pp. 471–473 (cited on page 144).

[219] M. Sich, D. N. Krizhanovskii, M. S. Skolnick, A. V. Gorbach, R. Hartley, D. V. Skryabin, E. A. Cerda-Méndez, K. Biermann, R. Hey, and P. V. Santos. “Observation of bright polariton solitons in a semiconductor microcavity.” In: *Nature Photonics* 6.1 (Jan. 2012), pp. 50–55 (cited on page 144).

[220] A. M. Weiner, J. P. Heritage, R. J. Hawkins, R. N. Thurston, E. M. Kirschner, D. E. Leaird, and W. J. Tomlinson. “Experimental Observation of the Fundamental Dark Soliton in Optical Fibers.” In: *Physical Review Letters* 61.21 (Nov. 1988), pp. 2445–2448 (cited on page 144).

[221] J. Denschlag, J. E. Simsarian, D. L. Feder, Charles W. Clark, L. A. Collins, J. Cubizolles, L. Deng, E. W. Hagley, K. Helmerson, W. P. Reinhardt, S. L. Rolston, B. I. Schneider, and W. D. Phillips. “Generating Solitons by Phase Engineering of a Bose-Einstein Condensate.” In: *Science* 287.5450 (Jan. 2000), pp. 97–101 (cited on page 144).

[222] D. H. Peregrine. “Water waves, nonlinear Schrödinger equations and their solutions.” In: *The ANZIAM Journal* 25.1 (July 1983), pp. 16–43 (cited on page 144).

[223] Cong Zhang, JuanFen Wang, Ren Gao, LingZhen Yang, and ZhaoXiao Zhang. “Generation and control of Akhmediev breathers in fiber laser.” In: *Optik* 179 (Feb. 2019), pp. 700–707 (cited on page 144).

[224] B. Kibler, J. Fatome, C. Finot, G. Millot, G. Genty, B. Wetzel, N. Akhmediev, F. Dias, and J. M. Dudley. “Observation of Kuznetsov-Ma soliton dynamics in optical fibre.” In: *Scientific Reports* 2 (June 2012), p. 463 (cited on page 144).

[225] Hao Xiong and Ying Wu. “Optomechanical Akhmediev Breathers.” In: *Laser & Photonics Reviews* 12.7 (2018), p. 1700305 (cited on page 144).

[226] N. Akhmediev, A. Ankiewicz, and M. Taki. “Waves that appear from nowhere and disappear without a trace.” In: *Physics Letters A* 373.6 (Feb. 2009), pp. 675–678 (cited on page 144).

[227] B. Kibler, J. Fatome, C. Finot, G. Millot, F. Dias, G. Genty, N. Akhmediev, and J. M. Dudley. "The Peregrine soliton in nonlinear fibre optics." In: *Nature Physics* 6.10 (Oct. 2010), pp. 790–795 (cited on page 144).

[228] A. Chabchoub, N. P. Hoffmann, and N. Akhmediev. "Rogue Wave Observation in a Water Wave Tank." In: *Physical Review Letters* 106.20 (May 2011), p. 204502 (cited on page 144).

[229] H. Bailung, S. K. Sharma, and Y. Nakamura. "Observation of Peregrine Solitons in a Multicomponent Plasma with Negative Ions." In: *Physical Review Letters* 107.25 (Dec. 2011), p. 255005 (cited on page 144).

[230] V. N. Serkin, Akira Hasegawa, and T. L. Belyaeva. "Nonautonomous Solitons in External Potentials." In: *Physical Review Letters* 98.7 (Feb. 2007), p. 074102 (cited on page 144).

[231] V. N. Serkin, Akira Hasegawa, and T. L. Belyaeva. "Solitary waves in nonautonomous nonlinear and dispersive systems: nonautonomous solitons." In: *Journal of Modern Optics* 57.14-15 (Aug. 2010), pp. 1456–1472 (cited on page 144).

[232] W. H. Hui and J. Hamilton. "Exact solutions of a three-dimensional nonlinear Schrödinger equation applied to gravity waves." In: *Journal of Fluid Mechanics* 93.1 (July 1979), pp. 117–133 (cited on page 144).

[233] Xiang Liu, Kale Beckwitt, and Frank Wise. "Two-dimensional optical spatiotemporal solitons in quadratic media." In: *Physical Review E* 62.1 (July 2000), pp. 1328–1340 (cited on page 144).

[234] William E. Torruellas, Zuo Wang, David J. Hagan, Eric W. VanStryland, George I. Stegeman, Lluís Torner, and Curtis R. Menyuk. "Observation of Two-Dimensional Spatial Solitary Waves in a Quadratic Medium." In: *Physical Review Letters* 74.25 (June 1995), pp. 5036–5039 (cited on page 144).

[235] S. Baluschev, A. Dreischuh, I. Velchev, S. Dinev, and O. Marazov. "Generation and evolution of two-dimensional dark spatial solitons." In: *Physical Review E* 52.5 (Nov. 1995), pp. 5517–5523 (cited on page 144).

[236] Tin-Lun Ho and Michael Ma. "Quasi 1 and 2d Dilute Bose Gas in Magnetic Traps: Existence of Off-Diagonal Order and Anomalous Quantum Fluctuations." In: *Journal of Low Temperature Physics* 115.1 (Apr. 1999), pp. 61–70 (cited on page 156).

[237] S. Stringari. "Dynamics of Bose-Einstein condensed gases in highly deformed traps." In: *Physical Review A* 58.3 (Sept. 1998), pp. 2385–2388 (cited on page 156).

[238] L. Mathey, Kenneth J. Günter, Jean Dalibard, and A. Polkovnikov. "Dynamic Kosterlitz-Thouless transition in two-dimensional Bose mixtures of ultracold atoms." In: *Physical Review A* 95.5 (May 2017), p. 053630 (cited on page 160).

[239] M. Holten, L. Bayha, A. C. Klein, P. A. Murthy, P. M. Preiss, and S. Jochim. "Anomalous Breaking of Scale Invariance in a Two-Dimensional Fermi Gas." In: *Physical Review Letters* 121.12 (Sept. 2018), p. 120401 (cited on page 160).

[240] T. Peppler, P. Dyke, M. Zamorano, I. Herrera, S. Hoinka, and C. J. Vale. "Quantum Anomaly and 2D-3D Crossover in Strongly Interacting Fermi Gases." In: *Physical Review Letters* 121.12 (Sept. 2018), p. 120402 (cited on page 160).

[241] Puneet A. Murthy, Nicolò Defenu, Luca Bayha, Marvin Holten, Philipp M. Preiss, Tilman Enss, and Selim Jochim. "Quantum scale anomaly and spatial coherence in a 2D Fermi superfluid." en. In: *Science* 365.6450 (July 2019), pp. 268–272 (cited on page 160).

[242] Johannes Hofmann. "Quantum Anomaly, Universal Relations, and Breathing Mode of a Two-Dimensional Fermi Gas." In: *Physical Review Letters* 108.18 (May 2012), p. 185303 (cited on page 161).

[243] Chao Gao and Zhenhua Yu. "Breathing mode of two-dimensional atomic Fermi gases in harmonic traps." In: *Physical Review A* 86.4 (Oct. 2012), p. 043609 (cited on page 161).

[244] Wilhelm Zwerger, ed. *The BCS-BEC Crossover and the Unitary Fermi Gas*. Lecture Notes in Physics. Berlin Heidelberg: Springer-Verlag, 2012 (cited on page 161).

[245] Fabian Grusdt and Eugene Demler. "New theoretical approaches to Bose polarons." In: *arXiv:1510.04934 [cond-mat]* (Oct. 2015). arXiv: 1510.04934 (cited on page 163).

[246] Aniello Lampo, Soon Hoe Lim, Miguel Ángel García-March, and Maciej Lewenstein. "Bose polaron as an instance of quantum Brownian motion." In: *Quantum* 1 (Sept. 2017), p. 30 (cited on page 163).

[247] Claude Cohen-Tannoudji, Bernard Diu, and Franck Laloë. *Mécanique quantique*. 1973 (cited on page 171).

[248] Daniel Adam Steck. *Rubidium 87 D Line Data*. 2003 (cited on pages 171, 172).

This document was typeset using the typographical look-and-feel `classicthesis` developed by André Miede and Ivo Pletikosić. The style was inspired by Robert Bringhurst's seminal book on typography "*The Elements of Typographic Style*". `classicthesis` is available for both LaTeX and LyX:

`https://bitbucket.org/amiede/classicthesis/`

RÉSUMÉ

Les propriétés thermodynamiques ainsi que l'évolution temporelle des systèmes bidimensionnels sont nettement différentes de celles de systèmes à trois dimensions. Ce travail de thèse présente des expériences réalisées avec des gaz ultrafroids uniformes de bosons en interaction faible, et confinés à deux dimensions d'espace. Ces expériences permettent de mettre en lumière certains traits caractéristiques de l'équilibre thermique et de la dynamique hors équilibre des systèmes à deux dimensions. Un expérimentateur travaillant avec des atomes froids possède une boîte à outils très fournie: la géométrie, la température, l'état interne des atomes sont très bien contrôlés, et de nombreuses méthodes permettant d'étudier leurs propriétés sont disponibles. En particulier, nous travaillons avec des gaz de densité uniforme dont la géométrie peut être choisie à volonté. Je décris l'installation expérimentale et les outils à notre disposition dans une première partie. Dans une deuxième partie, je présente une série d'expériences concernant la transition de phase Berezinskii-Kosterlitz-Thouless d'un gaz de Bose bidimensionnel. Il s'agit d'une transition de phase topologique pour laquelle le système présente un ordre à quasi-longue portée en dessous de la température critique. Nous avons développé deux méthodes expérimentales pour sonder cet ordre à quasi-longue portée. Dans une troisième et dernière partie, je détaille les symétries qui sous-tendent la dynamique d'un gaz proche d'une température nulle dans un piège harmonique. Ces symétries sont les symétries cachées de l'équation de Schrödinger non-linéaire, qui décrit plusieurs autres systèmes physiques. Nous avons testé ces symétries expérimentalement, et nous avons également observé des formes dont l'évolution est périodique dans un potentiel harmonique en présence de non-linéarités. Ces formes géométriques pourraient constituer un nouveau type de solutions périodiques de cette équation non-linéaire.

MOTS CLÉS

Condensats de Bose-Einstein, gaz bidimensionnels, ordre en phase, symétrie dynamique

ABSTRACT

The thermodynamic properties and the dynamical behaviour of two-dimensional systems differ notably from the ones in three dimensions. This work presents experiments performed with ultracold clouds of uniform weakly interacting bosons confined in two dimensions of space. These experiments explore some specific features of the thermodynamics and the out-of equilibrium dynamics of two-dimensional systems. Working with ultracold atoms provides the experimentalist with a rich toolbox: geometry, temperature and internal state of the system are well controlled, and various methods to investigate their properties are available. In particular we work with uniform Boses gases in highly tunable geometries. I describe the set-up and our experimental toolbox in a first part. In a second part I present experiments to investigate the Berezinskii-Kosterlitz-Thouless transition of a two-dimensional Bose gas. It is a topological phase transition for which the system displays a quasi-long range order below the critical temperature. We have developed two experimental schemes to probe this quasi-long range order. In a third and final part I explain the symmetries that underlie the dynamics of a cloud near zero temperature in a harmonic potential. These symmetries are the hidden symmetries of the two-dimensional non-linear Schrödinger equation, which describes many other physical systems. We could probe these symmetries experimentally, and we also observed initial shapes whose evolution is periodic in a harmonic potential in the presence of a non-linearity. They could constitute new breathers of this non-linear equation.

KEYWORDS

Bose-Einstein condensates, two-dimensional gases, phase ordering, dynamical symmetry